

Investigation of Hot Streak Migration and Film Cooling Effects on Heat Transfer in Rotor/Stator Interacting Flows

2

AD-A250 688



N00140-88-C-0677 - Report 1
UTRC Report 91-29

Daniel J. Dorney Roger L. Davis
Computational & Design Methods

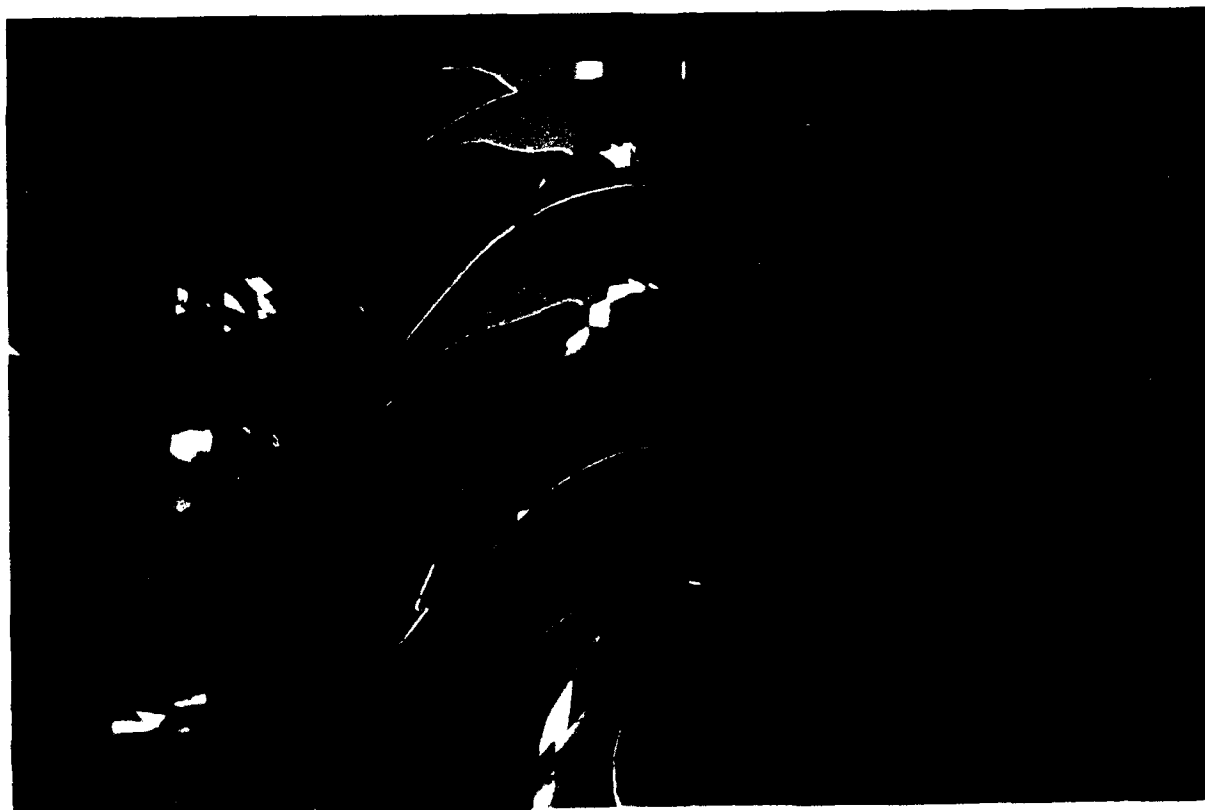
David E. Edwards
Physical & Mathematical Modeling
United Technologies Research Center

DTIC
ELECTE
JUN 08 1992
S D

DISTRIBUTION STATEMENT A

Approved for public release;
Distribution Unlimited

1 April 1992



92 5 26 097

Original contains color
plates. All DTIC reproductions
will be in black and
white.



UNITED
TECHNOLOGIES
RESEARCH
CENTER

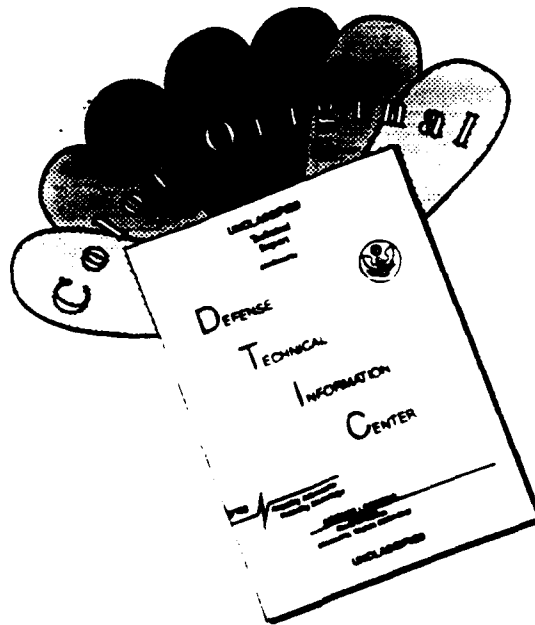
92-13889



AD-A250 688

REPORT DOCUMENTATION PAGE			Form Approved OMB No. 0704-0188	
<small>Please respond to this collection of information as indicated to reduce the burden of reporting. Send comments regarding this burden estimate or any other aspect of this collection of information, including suggestions for reducing this burden, to Washington Headquarters Services, Directorate for Information Operations and Reports, 1215 Jefferson Davis Highway, Suite 1204, Arlington, VA 22202-4302, and to the Office of Management and Budget, Paperwork Reduction Project (0704-0188), Washington, DC 20503.</small>				
1. AGENCY USE ONLY (Leave blank)		2. REPORT DATE April 1, 1992		3. REPORT TYPE AND DATES COVERED Final 1 Nov 88 - 1 April 92
4. TITLE AND SUBTITLE <i>Investigation of</i> Hot Streak Migration and Film Cooling Effects on the Heat Transfer in Rotor/Stator Interacting Flows - Report I			5. FUNDING NUMBERS Contract No. N00140-88-C-0677	
6. AUTHOR(S) D. J. Dorney, R. L. Davis, D. E. Edwards				
7. PERFORMING ORGANIZATION NAME(S) AND ADDRESS(ES) United Technologies Research Center 411 Silver Lane MS 129-20 East Hartford, CT 06108			8. PERFORMING ORGANIZATION REPORT NUMBER UTRC 91-29	
9. SPONSORING/MONITORING AGENCY NAME(S) AND ADDRESS(ES) Office of Naval Research/Naval Air Systems Command Department of the Navy 800 North Quincy St., Arlington, VA 22217-5000			10. SPONSORING/MONITORING AGENCY REPORT NUMBER	
11. SUPPLEMENTARY NOTES ADH200105 AD-B167302 This final report is associated with a video and user's manual. <i>See also ADH200104,</i>				
12a. DISTRIBUTION/AVAILABILITY STATEMENT Unclassified <i>Unlimited per DA, Lewis S/OA (1703-622-7443), 3 June 1992</i>			12b. DISTRIBUTION CODE A	
13. ABSTRACT (Maximum 200 words) Experimental data taken from gas turbine engines has shown that hot streaks exiting combustors can have a significant impact upon the secondary flow and wall temperature of the first stage turbine rotor. Understanding the secondary flow and heat transfer effects due to combustor hot streaks is essential to turbine designers attempting to optimize turbine cooling systems. A numerical investigation has been performed which addresses the issues of multi-blade count ratio and three-dimensionality effects on the prediction of combustor hot streak migration in a turbine stage. The two- and three-dimensional Navier-Stokes analyses developed by Rai et al are used to predict unsteady viscous rotor-stator interacting flow in the presence of a combustor hot streak with heat transfer and film cooling. Predicted results are presented for a two-dimensional 3-stator/4-rotor and a three-dimensional 1-stator/1-rotor simulations of streak migration through a turbine stage. Comparison of these results with experimental data demonstrates the capability of the three-dimensional procedure to capture most of the flow physics associated with hot streak migration including the effects of combustor hot streaks on turbine rotor surface temperatures.				
14. SUBJECT TERMS Combustor Hot Streak, Rotor/Stator Interaction, Unsteady Flow, Heat Transfer, Film Cooling, Navier-Stokes, Numerical Simulation			15. NUMBER OF PAGES 218	
			16. PRICE CODE	
17. SECURITY CLASSIFICATION OF REPORT Unclassified	18. SECURITY CLASSIFICATION OF THIS PAGE Unclassified	19. SECURITY CLASSIFICATION OF ABSTRACT Unclassified	20. LIMITATION OF ABSTRACT UL	

DISCLAIMER NOTICE



THIS DOCUMENT IS BEST QUALITY AVAILABLE. THE COPY FURNISHED TO DTIC CONTAINED A SIGNIFICANT NUMBER OF COLOR PAGES WHICH DO NOT REPRODUCE LEGIBLY ON BLACK AND WHITE MICROFICHE.

Investigation of Hot Streak Migration and Film Cooling Effects on Heat Transfer in Rotor/Stator Interacting Flows

**N00140-88-C-0677 - Report 1
UTRC Report 91-29**

**Daniel J. Dorney Roger L. Davis
Computational & Design Methods**

**David E. Edwards
Physical & Mathematical Modeling
United Technologies Research Center**

1 April 1992

**Prepared for
Naval Air Systems Command
AIR 931E, JP1 Rm. 424
Washington, DC 20361-9310**

**Turbo Propulsion Laboratory
Department of Aeronautics
Naval Post Graduate School
Monterey, CA 93940**

Contents

Acknowledgements	14
Nomenclature	15
Subscripts	16
1 Introduction	17
2 Numerical Procedure	20
2.1 Governing Equations	20
2.2 Integration Procedure	24
2.3 Turbulence/Transition Model	29
2.4 Boundary Conditions	33
3 Grid Generation	40
4 Visualization Technology	42
4.1 NASA's PLOT3D	43
4.2 UTRC's VISA	44
4.2.1 User Interface	45

4.2.2	Graphics	48
4.3	Intelligent Light's 3DV	50
4.4	Data Compression	51
5	Validation Test Cases	53
5.1	LSRR Stator	53
5.2	Energy Efficient Engine (E^3) Turbine Blade	58
5.3	Langston Cascade	59
6	Numerical Experiments	66
6.1	Experimental Apparatus	66
6.2	Adiabatic Simulations	67
6.2.1	Two-Dimensional Simulations	67
6.2.2	Three-Dimensional Simulations	77
6.3	Heat Transfer and Film Cooling Simulations	81
6.3.1	Two-Dimensional Simulations	81
6.3.2	Three-Dimensional Simulations	88
7	Scientific Visualization Results	92
7.1	2-D Adiabatic Hot Streak Simulation	93
7.2	3-D Adiabatic Hot Streak Simulation	94
7.3	2-D Hot Streak Simulation with Film Cooling	96

7.4 3-D Hot Streak Simulation with Film Cooling	97
---	----

8 Conclusions	99
---------------	----



Accession For	
NTIS GRA&I	<input checked="" type="checkbox"/>
DTIC TAB	<input type="checkbox"/>
Unannounced	<input type="checkbox"/>
Justification	
By _____	
Distribution/	
Availability Codes	
Dist	Avail and/or Special
A-1	

List of Figures

1	Angle definitions for film cooling applications	110
2	H-grid development	111
3	O-grid development	112
4	Flow diagram of user interface operation	113
5	System layout of VISA	114
6	Data compression of static temperature contours for a two-dimensional hot streak simulation	115
7	Computational grid for LSRR stator	116
8	Predicted pressure distributions for LSRR stator	117
9	Predicted skin friction distribution for LSRR stator	117
10	Predicted displacement thickness distribution for LSRR stator	118
11	Velocity profiles on pressure side of LSRR stator	118
12	Velocity profiles on suction side of LSRR stator	119
13	Predicted pressure distribution for LSRR stator with specified wall temperature	119
14	Predicted skin friction distribution for LSRR stator with specified wall tem- perature	120

15	Suction side skin friction distributions for LSRR stator with specified wall temperature	120
16	Predicted Stanton number distribution for LSRR stator	121
17	Predicted displacement thickness distribution for LSRR stator	121
18	Pressure surface velocity profiles for LSRR stator with specified wall temperature	122
19	Suction surface velocity profiles for LSRR stator with specified wall temperature	122
20	Pressure surface temperature profiles for 25% axial chord of LSRR stator . .	123
21	Pressure surface temperature profiles for 50% axial chord of LSRR stator . .	123
22	Pressure surface temperature profiles for 75% axial chord of LSRR stator . .	124
23	Suction surface temperature profiles for 25% axial chord of LSRR stator . . .	124
24	Suction surface temperature profiles for 50% axial chord of LSRR stator . . .	125
25	Suction surface temperature profiles for 75% axial chord of LSRR stator . . .	125
26	Predicted pressure distribution for LSRR stator with specified heat flux . . .	126
27	Wall temperature distribution for LSRR stator with specified heat flux . . .	126
28	Viscous computational grid for E^3 lightweight turbine blade	127
29	Pressure distribution for E^3 turbine blade, 10° incidence	128
30	Pressure distribution for E^3 turbine blade, 5° incidence	128
31	Pressure distribution for E^3 turbine blade, 0° incidence	129
32	Pressure distribution for E^3 turbine blade, -5° incidence	129
33	Pressure distribution for E^3 turbine blade, -10° incidence	130
34	Pressure distribution for E^3 turbine blade, -15° incidence	130

35	Velocity vectors for E^3 turbine blade at 10° positive incidence	131
36	Total pressure loss map for E^3 lightweight turbine blade	131
37	Exit flow angle and total pressure loss as a function of grid point density for Langston cascade	132
38	Blade-to-blade computational grid for Langston cascade	133
39	Static pressure coefficient distributions for Langston cascade	134
40	Predicted endwall static pressure coefficient contours for Langston cascade .	135
41	Experimental endwall static pressure coefficient contours for Langston cascade	136
42	Predicted suction surface static pressure coefficient contours for Langston cas- cade	137
43	Predicted pressure surface static pressure coefficient contours for Langston cascade	138
44	Experimental suction surface static pressure coefficient contours for Langston cascade	139
45	Experimental pressure surface static pressure coefficient contours for Langston cascade	140
46	Predicted suction surface limiting streamlines for Langston cascade	141
47	Experimental suction surface limiting streamlines for Langston cascade . . .	142
48	Predicted pressure surface limiting streamlines for Langston cascade	143
49	Experimental pressure surface experimental limiting streamlines for Langston cascade	144
50	Predicted endwall limiting streamlines for Langston cascade	145
51	Experimental endwall limiting streamlines for Langston cascade	146

52	Mid-span suction surface Stanton number distributions for Langston cascade	147
53	Mid-span pressure surface Stanton number distributions for Langston cascade	147
54	Predicted suction surface Stanton number contours for Langston cascade . .	148
55	Experimental suction surface Stanton number contours for Langston cascade	149
56	Predicted pressure surface Stanton number contours for Langston cascade . .	150
57	Experimental pressure surface Stanton number contours for Langston cascade	151
58	Predicted endwall Stanton number contours for Langston cascade	152
59	Experimental endwall Stanton number contours for Langston cascade	153
60	Gap-averaged total pressure coefficient distributions for Langston cascade . .	154
61	Predicted total pressure loss coefficient contours at exit of turbine passage .	155
62	Experimental total pressure loss coefficient contours at exit of turbine passage	156
63	Gap-averaged flow angle distributions for Langston cascade	157
64	Computational grid topology for 1-stator/1-rotor hot streak simulation . . .	158
65	Pressure history for midchord of LSRR stator	159
66	Pressure history for midchord of LSRR rotor	159
67	Temperature history for midchord of LSRR stator	160
68	Temperature history for midchord of LSRR rotor	160
69	Predicted and experimental blade loading for the LSRR stator	161
70	Predicted and experimental blade loading for the LSRR rotor	161
71	Pressure amplitude coefficient distribution for LSRR stator	162
72	Pressure amplitude coefficient distribution for LSRR rotor	162

73	Predicted and experimental time-averaged surface temperature for rotor . . .	163
74	Time-averaged static temperature contours for 3-stator/4-rotor hot streak simulation	164
75	Static temperature contours for 3-stator/4-rotor hot streak simulation	165
76	Computational grid for planar hot streak simulation	166
77	Predicted pressure coefficient distribution for the LSRR stator	167
78	Predicted and experimental pressure coefficient distributions for the LSRR rotor	167
79	Experimental time-averaged CO_2 contours for the LSRR rotor - planar hot streak	168
80	Predicted and experimental rotor surface temperatures for a planar hot streak	169
81	Predicted time-averaged temperature profiles for LSRR rotor - planar hot streak	169
82	Predicted and experimental rotor surface temperatures for a planar hot streak using new correlation	170
83	Static temperature contours in stator passage for three-dimensional hot streak simulations	171
84	Blade-to-blade computational grid for LSRR turbine	172
85	Temperature history at mid-span LSRR rotor surface - 2% span	173
86	Temperature history at mid-span LSRR rotor surface - 25% span	173
87	Temperature history at mid-span LSRR rotor surface - 50% span	174
88	Temperature history at mid-span LSRR rotor surface - 75% span	174
89	Temperature history at mid-span LSRR rotor surface - 98% span	175

90	Time-averaged pressure coefficient distribution for LSRR stator	176
91	Time-averaged pressure coefficient distribution for LSRR rotor	177
92	Pressure amplitude coefficient for mid-span stator section of LSRR	178
93	Pressure amplitude coefficient for mid-span rotor section of LSRR	179
94	Predicted and experimental time-averaged surface temperature for LSRR rotor mid-span section	179
95	Predicted time-averaged surface temperature contours for LSRR rotor	180
96	Experimental time-averaged surface temperature contours for LSRR rotor . .	180
97	Rotor pressure surface time-averaged temperature contours - adiabatic simulation	181
98	$T = 1.05$ Isotherm for adiabatic 3-D hot streak simulation (rotor suction side)	182
99	$T = 1.05$ Isotherm for adiabatic 3-D hot streak simulation (rotor pressure side)	183
100	Time-averaged velocity vectors in the vicinity of the film cooling hole	184
101	Rotor pressure surface time-averaged, maximum, and minimum coefficient distributions	184
102	Temperature coefficient distributions for film cooling simulation	185
103	Temperature coefficient distributions for film cooling simulations	185
104	Temperature coefficient distributions for film cooling simulations	186
105	Temperature coefficient distributions for film cooling simulations	187
106	Temperature coefficient distributions for film cooling simulations	187
107	Static temperature contours for LSRR turbine stage - heat flux, film cooling	188
108	Static temperature contours for LSRR turbine stage - heat flux, film cooling	189

109	Time-averaged temperature contours for LSRR rotor passage - heat transfer, film cooling	190
110	Temperature coefficient distribution for 3-stator/4-rotor LSRR simulation with a heat flux	191
111	Static temperature contours for 3-stator/4-rotor LSRR simulation with a heat flux and film cooling	192
112	Pressure amplitude coefficient for mid-span stator section of LSRR - heat flux	193
113	Pressure amplitude coefficient for mid-span rotor section of LSRR - heat flux	193
114	Rotor mid-span time-averaged temperature distributions - heat flux	194
115	Time-averaged temperature contours for rotor surface - heat flux	194
116	Time-averaged velocity vectors in the vicinity of mid-span film cooling hole .	195
117	Time-averaged, minimum and maximum pressure coefficient distribution for LSRR rotor - 2 rows film cooling (f.c.)	196
118	Pressure amplitude coefficient for stator mid-span - 2 rows f.c.	197
119	Pressure amplitude coefficient for rotor mid-span - 2 rows f.c.	197
120	Mid-span rotor time-averaged temperature distribution - 2 rows f.c.	198
121	Time-averaged temperature contours for rotor surface - 2 rows f.c.	198
122	Rotor pressure surface time-averaged temperature contours - 2 rows f.c. . . .	199
123	Time-averaged velocity vectors in the vicinity of mid-span film cooling hole .	200
124	Time-averaged, minimum and maximum pressure coefficient distribution for LSRR rotor - 3 rows film cooling	201
125	Pressure amplitude coefficient for stator mid-span - 3 rows f.c.	202

126	Pressure amplitude coefficient for rotor mid-span - 3 rows f.c.	202
127	Mid-span time-averaged temperature distribution - 3 rows f.c.	203
128	Time-averaged temperature contours for rotor surface - 3 rows f.c.	203
129	Rotor pressure surface time-averaged temperature contours - 3 rows f.c. . . .	204
130	Static temperature contours for 2-D adiabatic hot streak simulation	205
131	Static pressure contours for 2-D adiabatic hot streak simulation	206
132	Perturbation pressure contours for 2-D adiabatic hot streak simulation . . .	207
133	Magnified perturbation pressure contours for 2-D adiabatic hot streak simulation	208
134	Surface pressure for 3-D adiabatic hot streak simulation (View - rotor suction side)	209
135	Surface pressure for 3-D adiabatic hot streak simulation (View - rotor pressure side)	210
136	Surface temperature for 3-D adiabatic hot streak simulation (View - rotor suction side)	211
137	Surface temperature for 3-D adiabatic hot streak simulation (View - rotor pressure side)	212
138	$T = 1.05T_{\infty}$ Isotherm for 3-D adiabatic hot streak simulation (View - rotor suction side)	213
139	$T = 1.05T_{\infty}$ Isotherm for 3-D adiabatic hot streak simulation (View - rotor pressure side)	214
140	Static temperature contours for 2-D hot streak with film cooling and heat flux	215
141	Surface temperature for 3-D hot streak with film cooling and heat flux (View - rotor suction side)	216

142	Surface temperature for 3-D hot streak with film cooling and heat flux (View - rotor pressure side)	217
143	$T = 0.99, 1.05T_{\infty}$ Isotherms for 3-D hot streak with film cooling and heat flux (View - rotor pressure side)	218

List of Tables

1	Discretizations for various values of ϕ	108
2	Grid refinement study for Langston cascade	108
3	Flow conditions for the CHS1 experiment	109
4	Flow conditions for the CHS2 experiment	109
5	Flow conditions for the PHS experiment	109

Acknowledgements

The authors would like to thank Man Mohan Rai, Nateri K. Madavan and Linda Haines of the NASA Ames Research Center for helpful discussions concerning computational aspects of this investigation. Computer time was provided by NASA Ames Research Center and the NAS facility. The authors appreciate the helpful discussions with James Carter, Robert Dring, Dick Roback, Dave Joslyn and Mike Blair of the United Technologies Research Center and Om Sharma and Ron Takahashi of Pratt & Whitney concerning interpretation of the experimental and numerical results. This work was supported by the Naval Air Systems Command under NAVAIR contract N00140-88-C-0677 from the office of George Derderian and Lewis Slotter, with Raymond Shreeve of the Naval Post Graduate School acting as technical monitor.

Nomenclature

- L - Reference length (0.254 m)
- M - Mach number
- P - Static pressure
- Pr - Prandtl number
- R - Universal gas constant
- Re - Free stream inlet reference Reynolds number
- T - Static temperature
- U - Rotor velocity
- V - Total velocity
- a - Speed of sound
- c_p - Specific heat at constant pressure
- c_v - Specific heat at constant volume
- e - Specific energy
- q - Heat flux
- u - x component of velocity
- v - y component of velocity
- w - z component of velocity
- Ω - Rotor rotational speed
- κ - Thermal conductivity
- λ - Second coefficient of viscosity
- μ - First coefficient of viscosity
- ρ - Density
- τ - Shear stress

Subscripts

<i>L</i>	- Laminar quantity
<i>T</i>	- Turbulent quantity
<i>amb</i>	- Ambient conditions
<i>fc</i>	- Film cooling
<i>hs</i>	- Hot streak
<i>i</i>	- Inviscid
<i>ms</i>	- Mid-span
<i>t</i>	- Stagnation quantity
<i>v</i>	- Viscous
<i>x, y, z</i>	- First derivative with respect to x, y or z
<i>xx, yy, zz</i>	- Second derivative with respect to x, y or z
<i>w</i>	- Wall
1	- Inlet quantity
2	- Exit quantity

Chapter 1

Introduction

This document presents the results of a computational study in which the primary focus has been to develop a diagnostic tool (or "Numerical Rotating Rig") for enhancing the understanding of complex three-dimensional flows in axial turbomachinery. The primary components of the Numerical Rotating Rig consist of a three-dimensional unsteady Navier-Stokes analysis and a scientific graphical visualization system. The three-dimensional Navier-Stokes analysis is based on the procedure developed by M. M. Rai [1], and is validated in this study by comparisons with experimental data obtained at the United Technologies Research Center for a linear cascade and a turbine stage. The scientific visualization system represents a combination of several state-of-the-art graphics software programs and provides innovative techniques for interrogating large data sets. In this investigation, the Numerical Rotating Rig has been used to perform numerical experiments to determine the effects of hot streak migration and film cooling on the heat transfer in a turbine stage.

The drive towards lower fuel consumption, maximum gas turbine efficiency, and increased aerodynamic performance for both military and commercial aircraft has led to increases in combustor exit temperature which in turn has had a direct impact on the durability of first-stage turbine airfoils. Experimental data taken from actual gas turbine combustors indicates that the flow exiting the combustor has both circumferential and radial temperature gradients. These temperature gradients arise from the combination of the combustor core flow with the combustor bypass and combustor surface cooling flows. It has been shown both experimentally and numerically [2, 3] that temperature gradients, in the absence of

total pressure non-uniformities, do not alter the flow within the first stage turbine stator but do have significant impact on the secondary flow and wall temperature of the first stage rotor. Combustor hot streaks, which can typically have temperatures twice the free stream stagnation temperature, increase the extent of the secondary flow in the first stage rotor and significantly alter the rotor surface temperature distribution. A combustor hot streak such as this has a greater streamwise velocity than the surrounding fluid and therefore a larger positive incidence angle to the rotor as compared to the free stream. Due to this rotor incidence variation through the hot streak and the slow convection speed on the pressure side of the rotor, the hot streak accumulates on the rotor pressure surface creating a "hot spot".

In order to keep turbine airfoil wall temperatures below critical levels, complex internal cooling schemes are designed to lay a film of relatively cool air adjacent to the blade. This film cooling air acts as a sealant to keep the high temperature combustor flow from coming in direct contact with turbine airfoil surfaces. During the design of the first stage turbine, flow field analyses which assume a uniform turbine inlet temperature profile are used to predict airfoil surface temperature distributions. These wall temperature distributions are subsequently used to guide the design of internal cooling schemes in terms of defining cooling mass flow requirements and its distribution. Both the secondary flow and wall temperature effects due to combustor hot streaks are important phenomena which should be accounted for by turbine designers to increase turbine aerodynamic performance and optimize turbine film cooling flow schemes. Without properly accounting for non-uniformities in turbine inlet temperature profiles such as those related to combustor hot streaks, first stage turbine performance and durability could suffer.

Computational fluid dynamic simulations of hot streak migration in turbine stage flows are useful for both increasing the understanding of this phenomena as well as to guide engineers for future experimental investigations. To gain insight into the influence of hot streak migration, secondary flow, heat transfer, and film cooling on the surface temperature distribution of a first stage rotor, numerical simulations of hot streak migration through a turbine stage have been performed. The main goals of these simulations have been to 1) understand the physical mechanisms which control the migration of hot streaks through a turbine stage and lead to "hot spots" on the rotor pressure surface, 2) demonstrate that numerical sim-

ulations can be used to predict when rotor surface heating will exceed allowable structural limits, 3) predict when the adverse effects of hot streaks on rotor surface temperature can be eliminated using film cooling, and 4) use advanced scientific visualization techniques to quickly identify and illustrate the pertinent aerodynamic and thermodynamic features of the flow fields.

This document is organized into eight chapters. Chapter 1 is the introduction and provides background information on the problem of hot streak migration. The three-dimensional numerical procedure, including the governing equations, the integration procedure, the turbulence/transition models, and the boundary conditions is discussed in Chapter 2. The grid generation procedure for the zonal grid topology is explained in Chapter 3. The fourth chapter reviews the visualization technology used in this investigation. Chapter 5 describes the test cases used to validate the numerical procedure. The results of numerous hot streak migration simulations are presented and analyzed in Chapter 6. A video, which was created from the animated results of the numerical simulations, is discussed in Chapter 7. Finally, Chapter 8 presents the conclusions and recommendations of this investigation.

The three-dimensional source code, users manual, and/or video resulting from this investigation may be obtained from

**Defense Logistics Agency
Defense Technical Information Center
Building No. 5, Cameron Station
Alexandria, Virginia 22304-6145
(final report AD-A250 688)
(user's manual AD-B164 302
(source code AD-M 200 104)
(video AD-M 200 105)**

Chapter 2

Numerical Procedure

The numerical analyses used in this study are the two- and three-dimensional rotor/stator interaction analyses developed by M. M. Rai. [1, 3, 4]. The two- and three-dimensional analyses can be used to simulate inviscid or viscous flow through a cascade passage or a single stage. In addition, both analyses can simulate hot streak migration with or without blade surface heat transfer and film cooling. The two-dimensional analysis can represent an arbitrary number of stator and rotor airfoils, while the three-dimensional analysis is restricted to one stator and one rotor. This section describes the governing equation set and the numerical solution procedure. In particular, the topics discussed in this chapter include

- Governing equations
- Integration procedure
- Turbulence/Transition models
- Boundary conditions

2.1 Governing Equations

The governing equations considered in this study are the time dependent, three-dimensional Reynolds averaged Navier-Stokes equations, which can be written in Cartesian coordinates

as:

$$Q_t + (F_i + F_v)_x + (G_i + G_v)_y + (H_i + H_v)_z = 0 \quad (2.1)$$

where

$$Q = \begin{bmatrix} \rho \\ \rho u \\ \rho v \\ \rho w \\ e_t \end{bmatrix} \quad (2.2)$$

$$F_i = \begin{bmatrix} \rho u \\ \rho u^2 + P \\ \rho uv \\ \rho uw \\ (e_t + P)u \end{bmatrix} \quad F_v = - \begin{bmatrix} 0 \\ \tau_{xx} \\ \tau_{xy} \\ \tau_{xz} \\ \tau_{hx} \end{bmatrix} \quad (2.3)$$

$$G_i = \begin{bmatrix} \rho v \\ \rho uv \\ \rho v^2 + P \\ \rho vw \\ (e_t + P)v \end{bmatrix} \quad G_v = - \begin{bmatrix} 0 \\ \tau_{yx} \\ \tau_{yy} \\ \tau_{yz} \\ \tau_{hy} \end{bmatrix} \quad (2.4)$$

$$H_i = \begin{bmatrix} \rho w \\ \rho uw \\ \rho vw \\ \rho w^2 + P \\ (e_t + P)w \end{bmatrix} \quad H_v = - \begin{bmatrix} 0 \\ \tau_{zx} \\ \tau_{zy} \\ \tau_{zz} \\ \tau_{hz} \end{bmatrix} \quad (2.5)$$

and

$$\tau_{xx} = 2\mu u_x + \lambda(u_x + v_y + w_z)$$

$$\tau_{xy} = \mu(u_y + v_x)$$

$$\tau_{xz} = \mu(u_z + w_x)$$

$$\tau_{yz} = \tau_{zy}$$

$$\tau_{yy} = 2\mu v_y + \lambda(u_x + v_y + w_z)$$

$$\begin{aligned}
\tau_{yz} &= \mu (v_z + w_y) \\
\tau_{zx} &= \tau_{xz} \\
\tau_{xy} &= \tau_{yx} \\
\tau_{zz} &= 2\mu w_z + \lambda (u_x + v_y + w_z) \\
\tau_{hx} &= u\tau_{xx} + v\tau_{xy} + w\tau_{xz} + \gamma\mu P_r^{-1} e_x \\
\tau_{hy} &= u\tau_{yx} + v\tau_{yy} + w\tau_{yz} + \gamma\mu P_r^{-1} e_y \\
\tau_{hz} &= u\tau_{zx} + v\tau_{zy} + w\tau_{zz} + \gamma\mu P_r^{-1} e_z \\
e &= \frac{P}{(\rho(\gamma - 1))} \\
e_t &= \rho e + \frac{\rho(u^2 + v^2 + w^2)}{2}
\end{aligned} \tag{2.6}$$

For the present application, the second coefficient of viscosity is calculated using Stokes' hypothesis, $\lambda = -2/3\mu$. The equations of motion are completed by the perfect gas law which takes the form

$$P = \rho RT \tag{2.7}$$

It is useful to non-dimensionalize the equations of motion so that certain parameters, such as the Reynolds and Mach numbers, can be varied independently. The non-dimensional variables chosen in this investigation are

$$\begin{aligned}
x^* &= \frac{x}{L} & y^* &= \frac{y}{L} & t^* &= \frac{t}{L/V_\infty} \\
u^* &= \frac{u}{V_\infty} & v^* &= \frac{v}{V_\infty} & w^* &= \frac{w}{V_\infty} \\
\rho^* &= \frac{\rho}{\rho_\infty} & P^* &= \frac{P}{\rho V_\infty^2} & T^* &= \frac{T}{T_\infty} \\
\mu^* &= \frac{\mu}{\mu_\infty}
\end{aligned} \tag{2.8}$$

In addition, for the analysis of arbitrary geometries the equations of motion can be generalized by using body-fitted coordinates. Using the independent variable transformations

$$\begin{aligned}
\tau &= t \\
\xi &= \xi(x, y, z, t)
\end{aligned} \tag{2.9}$$

$$\begin{aligned}\eta &= \eta(x, y, z, t) \\ \zeta &= \zeta(x, y, z, t)\end{aligned}$$

the body-fitted Cartesian coordinates in the physical domain become uniform coordinates in the computational domain. The transformation allows easier implementation of boundary conditions since the geometry surface lies along the boundaries of the computational domain. Upon applying the transformations and non-dimensionalizing, the three-dimensional Navier-Stokes equations can be written as (where the superscripts '*' have been omitted for clarity)

$$\tilde{Q}_\tau + (\tilde{F}_i + Re^{-1}\tilde{F}_v)_\xi + (\tilde{G}_i + Re^{-1}\tilde{G}_v)_\eta + (\tilde{H}_i + Re^{-1}\tilde{H}_v)_\zeta = 0 \quad (2.10)$$

where

$$\begin{aligned}\tilde{Q} &= J^{-1}Q \\ \tilde{F}_i(Q, \xi) &= J^{-1}(\xi_t Q + \xi_x F_i + \xi_y G_i + \xi_z H_i) \\ \tilde{G}_i(Q, \eta) &= J^{-1}(\eta_t Q + \eta_x F_i + \eta_y G_i + \eta_z H_i) \\ \tilde{H}_i(Q, \zeta) &= J^{-1}(\zeta_t Q + \zeta_x F_i + \zeta_y G_i + \zeta_z H_i)\end{aligned} \quad (2.11)$$

The viscous fluxes are simplified by incorporating the thin layer assumption [5]. The thin layer assumption states that for high Reynolds number flows that the diffusion terms normal to a solid surface will be greater than those parallel to the surface. In the current study, viscous terms are retained in the direction normal to the hub/shroud surfaces (ζ -direction) and in the direction normal to the blade surface (η -direction). Thus, the non-dimensionalized and transformed equations now become:

$$\tilde{Q}_\tau + (\tilde{F}_i)_\xi + (\tilde{G}_i + Re^{-1}\tilde{G}_v)_\eta + (\tilde{H}_i + Re^{-1}\tilde{H}_v)_\zeta = 0 \quad (2.12)$$

where

$$\tilde{G}_v = - \begin{bmatrix} 0 \\ K_1 u_\eta + K_2 \eta_x \\ K_1 v_\eta + K_2 \eta_y \\ K_1 w_\eta + K_2 \eta_z \\ K_1 \left(P_r^{-1} (\gamma - 1)^{-1} (a^2)_\eta + \left(\frac{q^2}{2} \right)_\eta \right) + K_2 K_3 \end{bmatrix} \quad (2.13)$$

$$\begin{aligned}
K_1 &= \mu (\eta_x^2 + \eta_y^2 + \eta_z^2) \\
K_2 &= \frac{\mu}{3} (\eta_x u_\eta + \eta_y v_\eta + \eta_z w_\eta) \\
K_3 &= u\eta_x + v\eta_y + w\eta_z \\
q^2 &= u^2 + v^2 + w^2
\end{aligned} \tag{2.14}$$

The vector \tilde{H}_v is obtained by replacing η with ζ in Eqs. (2.13) and (2.15). If all the viscous terms are neglected, then the equations become the inviscid (Euler) equations of motion. The Jacobian of the transformation and the other metric quantities are given by [6]

$$J^{-1} = x_\xi y_\eta z_\zeta + x_\zeta y_\xi z_\eta + x_\eta y_\zeta z_\xi - x_\xi y_\zeta z_\eta - x_\eta y_\xi z_\zeta - x_\zeta y_\eta z_\xi \tag{2.15}$$

$$\begin{aligned}
\xi_x &= J(y_\eta z_\zeta - y_\zeta z_\eta) & \eta_x &= J(z_\xi y_\zeta - y_\xi z_\zeta) \\
\xi_y &= J(z_\eta x_\zeta - z_\zeta x_\eta) & \eta_y &= J(x_\xi z_\zeta - z_\xi x_\zeta) \\
\xi_z &= J(x_\eta y_\zeta - y_\eta x_\zeta) & \eta_z &= J(y_\xi x_\zeta - x_\xi y_\zeta) \\
\zeta_x &= J(y_\xi z_\eta - z_\xi y_\eta) & \xi_t &= -x_\tau \xi_x - y_\tau \xi_y - z_\tau \xi_z \\
\zeta_y &= J(z_\xi x_\eta - x_\xi z_\eta) & \eta_t &= -x_\tau \eta_x - y_\tau \eta_y - z_\tau \eta_z \\
\zeta_z &= J(x_\xi y_\eta - y_\xi x_\eta) & \xi_t &= -x_\tau \zeta_x - y_\tau \zeta_y - z_\tau \zeta_z
\end{aligned} \tag{2.16}$$

The metric derivatives are evaluated using three point central differences in the interior of the computational domain and three point backward differences on the boundaries.

2.2 Integration Procedure

The governing equations of motion are integrated in time using the Approximate Factorization (AF) implicit technique developed by Beam and Warming [7]. Applying the AF technique for three-dimensional problems is accomplished by solving three one-dimensional operators, each requiring the inversion of a block tridiagonal matrix system with 5x5 blocks. Newton iterations are applied within each global time step to increase stability and eliminate the linearization errors caused by the factorization process. To apply Newton's method, one starts with an initial guess for the solution and iterates according to:

$$Q^{\tilde{p}+1} = \tilde{Q}^p - \frac{f(\tilde{Q})}{f'(\tilde{Q})} \tag{2.17}$$

This method can be applied to the unsteady Navier-Stokes equations by setting

$$f(\tilde{Q}) = \tilde{Q}_\tau + (\tilde{F}_i)_\xi + (\tilde{G}_i + Re^{-1}\tilde{G}_v)_\eta + (\tilde{H}_i + Re^{-1}\tilde{H}_v)_\zeta \quad (2.18)$$

and

$$f'(\tilde{Q}) = \frac{\partial}{\partial \tilde{Q}} [\tilde{Q}_\tau + (\tilde{F}_i)_\xi + (\tilde{G}_i + Re^{-1}\tilde{G}_v)_\eta + (\tilde{H}_i + Re^{-1}\tilde{H}_v)_\zeta] \quad (2.19)$$

Noting that, for example,

$$\frac{\partial}{\partial \tilde{Q}} \left(\frac{\partial \tilde{F}_i}{\partial \xi} \right) = \frac{\partial}{\partial \xi} \left(\frac{\partial \tilde{F}_i}{\partial \tilde{Q}} \right) = \frac{\partial \tilde{A}}{\partial \xi} \quad (2.20)$$

where \tilde{A} is a Jacobian matrix, the factored, iterative, implicit integration algorithm can be defined by [1, 4]

$$\begin{aligned} & [I + \frac{\Delta \tau}{\Delta \xi} (\nabla_\xi \tilde{A}_{i,j,k}^+ + \Delta_\xi \tilde{A}_{i,j,k}^-)]^p [I + \frac{\Delta \tau}{\Delta \eta} (\nabla_\eta \tilde{B}_{i,j,k}^+ + \Delta_\eta \tilde{B}_{i,j,k}^- - Re^{-1} \delta_\eta \tilde{M})]^p \\ & [I + \frac{\Delta \tau}{\Delta \zeta} (\nabla_\zeta \tilde{C}_{i,j,k}^+ + \Delta_\zeta \tilde{C}_{i,j,k}^- - Re^{-1} \delta_\zeta \tilde{N})]^p (\tilde{Q}_{i,j,k}^{p+1} - \tilde{Q}_{i,j,k}^p) \\ & = -\Delta \tau \left[\frac{\tilde{Q}_{i,j,k}^p - \tilde{Q}_{i,j,k}^n}{\Delta \tau} + \frac{(\hat{F}_i)^p_{i+1/2,j,k} - (\hat{F}_i)^p_{i-1/2,j,k}}{\Delta \xi} \right. \\ & + \frac{(\hat{G}_i)^p_{i,j+1/2,k} - (\hat{G}_i)^p_{i,j-1/2,k}}{\Delta \eta} - \frac{(\hat{G}_v)^p_{i,j+1/2,k} - (\hat{G}_v)^p_{i,j-1/2,k}}{Re \Delta \eta} \\ & \left. + \frac{(\hat{H}_i)^p_{i,j,k+1/2} - (\hat{H}_i)^p_{i,j,k-1/2}}{\Delta \zeta} - \frac{(\hat{H}_v)^p_{i,j,k+1/2} - (\hat{H}_v)^p_{i,j,k-1/2}}{Re \Delta \zeta} \right] \quad (2.21) \end{aligned}$$

where

$$\tilde{A}^\pm = \left(\frac{\partial \tilde{F}_i}{\partial \tilde{Q}} \right)^\pm \quad \tilde{B}^\pm = \left(\frac{\partial \tilde{G}_i}{\partial \tilde{Q}} \right)^\pm \quad \tilde{C}^\pm = \left(\frac{\partial \tilde{H}_i}{\partial \tilde{Q}} \right)^\pm \quad (2.22)$$

$$\tilde{M}^\pm = \left(\frac{\partial \tilde{G}_v}{\partial \tilde{Q}} \right)^\pm \quad \tilde{N}^\pm = \left(\frac{\partial \tilde{H}_v}{\partial \tilde{Q}} \right)^\pm \quad (2.23)$$

and Δ , ∇ , and δ represent forward, backward, and central difference operators. In equation (2.21), \tilde{Q}^p is an approximation to \tilde{Q}^{n+1} . The quantities \hat{F}_i , \hat{G}_i , \hat{H}_i , \hat{G}_v , and \hat{H}_v are numerical fluxes which are consistent with the physical fluxes \tilde{F}_i , \tilde{G}_i , \tilde{H}_i , \tilde{G}_v , and \tilde{H}_v . If $p = 0$ then $\tilde{Q}^p = \tilde{Q}^n$, and when the equation is iterated to convergence $\tilde{Q}^p = \tilde{Q}^{n+1}$. As the left hand side of equation (2.21) is driven to zero, the linearization and factorization errors associated with the AF technique are also driven to zero. If only one iteration is used then

the integration scheme reverts to the conventional AF type scheme [7]. Typically, unsteady calculations require two to three iterations per global time step to reduce the residual of the density by three orders of magnitude [1, 8, 9, 10].

The inviscid numerical fluxes \hat{F}_i , \hat{G}_i , and \hat{H}_i are discretized using Roe's scheme [11]. The numerical fluxes are then evaluated from a family of high accuracy representations of the fluxes developed in Ref. [12]. For example,

$$\begin{aligned} (\hat{F}_i)_{i+1/2,j,k} = & (\bar{F}_i)_{i+1/2,j,k} - \frac{(1-\phi)}{4} \Delta F^-_{i+3/2,j,k} - \frac{(1+\phi)}{4} \Delta F^-_{i+1/2,j,k} \\ & + \frac{(1+\phi)}{4} \Delta F^+_{i+1/2,j,k} + \frac{(1-\phi)}{4} \Delta F^+_{i-1/2,j,k} \end{aligned} \quad (2.24)$$

where $(\bar{F}_i)_{i+1/2,j,k}$ is the first order accurate upwind flux given by

$$(\bar{F}_i)_{i+1/2,j,k} = \frac{1}{2} [(\tilde{F}_i)_{i,j,k} + (\tilde{F}_i)_{i+1,j,k}] - \frac{1}{2} (\Delta F^+_{i-1/2,j,k} - \Delta F^-_{i+1/2,j,k}) \quad (2.25)$$

and the additional terms in Eq. (2.24) are used to increase the order of accuracy. Table 1 summarizes several difference schemes obtained by using different values for ϕ in Eq. (2.24). In the current study, the third order accurate upwind biased difference scheme is used for interior grid points and either first or second order accurate upwind differencing is used at boundary points.

The flux differences (ΔF^\pm) in Eqs. (2.24) and (2.25) are calculated using Roe's scheme and are given by

$$\Delta F^\pm_{i+1/2,j,k} = \tilde{A}^\pm_{i+1/2,j,k} \times (Q_{i+1,j,k} - Q_{i,j,k}) \quad (2.26)$$

The flow variables needed to determine \tilde{A}^\pm between grid points $(i+1/2, j, k)$ are calculated using Roe's averaging formulae:

$$\begin{aligned} u_{i+1/2,j,k} &= \frac{u_{i,j,k}\sqrt{\rho_{i,j,k}} + u_{i+1,j,k}\sqrt{\rho_{i+1,j,k}}}{\sqrt{\rho_{i,j,k}} + \sqrt{\rho_{i+1,j,k}}} \\ v_{i+1/2,j,k} &= \frac{v_{i,j,k}\sqrt{\rho_{i,j,k}} + v_{i+1,j,k}\sqrt{\rho_{i+1,j,k}}}{\sqrt{\rho_{i,j,k}} + \sqrt{\rho_{i+1,j,k}}} \\ w_{i+1/2,j,k} &= \frac{w_{i,j,k}\sqrt{\rho_{i,j,k}} + w_{i+1,j,k}\sqrt{\rho_{i+1,j,k}}}{\sqrt{\rho_{i,j,k}} + \sqrt{\rho_{i+1,j,k}}} \end{aligned} \quad (2.27)$$

$$(h_t)_{i+1/2,j,k} = \frac{(h_t)_{i,j,k}\sqrt{\rho_{i,j,k}} + (h_t)_{i+1,j,k}\sqrt{\rho_{i+1,j,k}}}{\sqrt{\rho_{i,j,k}} + \sqrt{\rho_{i+1,j,k}}}$$

where h_t is the total enthalpy and is defined as

$$h_t = \frac{e_t + P}{\rho} \quad (2.28)$$

The Jacobian matrix \tilde{A}^\pm can be rewritten as:

$$\tilde{A}^\pm = T_\xi^{-1} \Lambda_\xi^\pm T_\xi \quad (2.29)$$

where T_ξ and T_ξ^{-1} are eigenvectors and which can be expressed as [6]:

$$T_\xi = \begin{bmatrix} \tilde{\xi}_x & \tilde{\xi}_y \\ \tilde{\xi}_x u & \tilde{\xi}_y u - \tilde{\xi}_x \rho \\ \tilde{\xi}_x v + \tilde{\xi}_y \rho & \tilde{\xi}_y v \\ \tilde{\xi}_x w - \tilde{\xi}_y \rho & \tilde{\xi}_y w + \tilde{\xi}_x \rho \\ \tilde{\xi}_x R_1/(\gamma - 1) + \rho(\tilde{\xi}_x v - \tilde{\xi}_y w) & \tilde{\xi}_y R_1/(\gamma - 1) + \rho(\tilde{\xi}_x w - \tilde{\xi}_y u) \end{bmatrix}$$

$$\left[\begin{array}{ccc} \tilde{\xi}_x & R_2 & R_2 \\ \tilde{\xi}_x u + \tilde{\xi}_y \rho & R_2(u + \tilde{\xi}_x a) & R_2(u - \tilde{\xi}_x a) \\ \tilde{\xi}_x v - \tilde{\xi}_y \rho & R_2(v + \tilde{\xi}_y a) & R_2(v - \tilde{\xi}_y a) \\ \tilde{\xi}_x w & R_2(w + \tilde{\xi}_x a) & R_2(w - \tilde{\xi}_x a) \\ \tilde{\xi}_x R_1(\gamma - 1) + \rho(\tilde{\xi}_y u - \tilde{\xi}_x v) & R_2[(R_1 + a^2)/(\gamma - 1) + R_4 a] & R_2[(R_1 + a^2)/(\gamma - 1) - R_4 a] \end{array} \right] \quad (2.30)$$

$$T_\xi^{-1} = \begin{bmatrix} \tilde{\xi}_x(1 - R_1/a^2) - (\tilde{\xi}_x v - \tilde{\xi}_y w)/\rho & \tilde{\xi}_x(\gamma - 1)u/a^2 \\ \tilde{\xi}_y(1 - R_1/a^2) - (\tilde{\xi}_x w - \tilde{\xi}_y u)/\rho & \tilde{\xi}_y(\gamma - 1)u/a^2 - \tilde{\xi}_x/\rho \\ \tilde{\xi}_x(1 - R_1/a^2) - (\tilde{\xi}_y u - \tilde{\xi}_x v)/\rho & \tilde{\xi}_x(\gamma - 1)u/a^2 + \tilde{\xi}_y/\rho \\ R_3(R_1 - R_4 a) & -R_4[(\gamma - 1)u - \tilde{\xi}_x a] \\ R_3(R_1 + R_4 a) & -R_4[(\gamma - 1)u + \tilde{\xi}_x a] \end{bmatrix}$$

$$\left[\begin{array}{ccc} \tilde{\xi}_x(\gamma - 1)v/a^2 + \tilde{\xi}_z/\rho & \tilde{\xi}_x(\gamma - 1)w/a^2 - \tilde{\xi}_y/\rho & -\tilde{\xi}_x(\gamma - 1)/a^2 \\ \tilde{\xi}_y(\gamma - 1)v/a^2 & \tilde{\xi}_y(\gamma - 1)w/a^2 - \tilde{\xi}_x/\rho & -\tilde{\xi}_y(\gamma - 1)/a^2 \\ \tilde{\xi}_x(\gamma - 1)v/a^2 - \tilde{\xi}_z/\rho & \tilde{\xi}_x(\gamma - 1)w/a^2 & -\tilde{\xi}_x(\gamma - 1)/a^2 \\ -R_3[(\gamma - 1)v - \tilde{\xi}_y a] & -R_3[(\gamma - 1)w - \tilde{\xi}_x a] & R_3(\gamma - 1) \\ -R_3[(\gamma - 1)v + \tilde{\xi}_y a] & -R_3[(\gamma - 1)w + \tilde{\xi}_x a] & R_3(\gamma - 1) \end{array} \right] \quad (2.31)$$

$$\begin{aligned}
R_1 &= \frac{\gamma-1}{2}(u^2 + v^2 + w^2) & R_2 &= \rho/(a\sqrt{2}) & R_3 &= 1/(\rho a\sqrt{2}) & R_4 &= (\xi_x u + \xi_y v + \xi_z w)/\kappa \\
\tilde{\xi}_x &= \xi_x/\kappa & \tilde{\xi}_y &= \xi_y/\kappa & \tilde{\xi}_z &= \xi_z/\kappa & \kappa &= \sqrt{\xi_x^2 + \xi_y^2 + \xi_z^2}
\end{aligned} \tag{2.32}$$

The eigenvectors for the \tilde{B} and \tilde{C} matrices can be obtained by replacing ξ in Eqs. (2.30) and (2.31) with η and ζ . The matrix containing the eigenvalues of the Jacobian matrix is given by

$$\Lambda_{\xi}^{\pm} = \begin{bmatrix} \lambda_1^{\pm} & 0 & 0 & 0 & 0 \\ 0 & \lambda_2^{\pm} & 0 & 0 & 0 \\ 0 & 0 & \lambda_3^{\pm} & 0 & 0 \\ 0 & 0 & 0 & \lambda_4^{\pm} & 0 \\ 0 & 0 & 0 & 0 & \lambda_5^{\pm} \end{bmatrix} \tag{2.33}$$

where

$$\begin{aligned}
\lambda_{1,2,3} &= \xi_t + \xi_x u + \xi_y v + \xi_z w \\
\lambda_4 &= \lambda_1 + \kappa a \\
\lambda_5 &= \lambda_1 - \kappa a
\end{aligned} \tag{2.34}$$

The superscripts ' \pm ' in the previous equations refer to the contributions from the downstream and upstream running characteristic waves. To prevent expansion shocks, the eigenvalues in Eq. (2.34) are replaced by a nonvanishing, continuously differentiable approximation which can be written as [13]:

$$\tilde{\lambda}_n^{\pm} = \begin{cases} \frac{1}{2} [(\lambda_n^2/\delta) + \delta] & |\lambda_n| < \delta \\ |\lambda_n| & |\lambda_n| \geq \delta \end{cases} \tag{2.35}$$

where $n = 1, 5$ and in the present study

$$\delta = 0.05 a \kappa \tag{2.36}$$

The flow variables needed to determine the viscous fluxes, \tilde{G}_v and \tilde{H}_v , are evaluated using standard central differences. For example,

$$\begin{aligned}
(\tilde{G}_v)_{i,j+1/2,k} &= f(Q_{i,j+1/2,k}, (Q_{\eta})_{i,j+1/2,k}) \\
Q_{i,j+1/2,k} &= \frac{1}{2}(Q_{i,j,k} + Q_{i,j+1,k})
\end{aligned} \tag{2.37}$$

$$(Q_\eta)_{i,j+1/2,k} = Q_{i,j+1,k} - Q_{i,j,k}$$

The corresponding viscous flux Jacobian, \tilde{M} , can be written as [6]

$$\tilde{M} = J^{-1} \begin{bmatrix} 0 & 0 & 0 & 0 & 0 \\ m_{21} & S_1 \partial_\eta(\rho^{-1}) & S_2 \partial_\eta(\rho^{-1}) & S_3 \partial_\eta(\rho^{-1}) & 0 \\ m_{31} & S_2 \partial_\eta(\rho^{-1}) & S_4 \partial_\eta(\rho^{-1}) & S_5 \partial_\eta(\rho^{-1}) & 0 \\ m_{41} & S_3 \partial_\eta(\rho^{-1}) & S_5 \partial_\eta(\rho^{-1}) & S_6 \partial_\eta(\rho^{-1}) & 0 \\ m_{51} & m_{52} & m_{53} & m_{54} & S_0 \partial_\eta(\rho^{-1}) \end{bmatrix} \quad (2.38)$$

where

$$\begin{aligned} m_{21} &= -S_1 \partial_\eta(u/\rho) - S_2 \partial_\eta(v/\rho) - S_3 \partial_\eta(w/\rho) \\ m_{31} &= -S_2 \partial_\eta(u/\rho) - S_4 \partial_\eta(v/\rho) - S_5 \partial_\eta(w/\rho) \\ m_{41} &= -S_3 \partial_\eta(u/\rho) - S_5 \partial_\eta(v/\rho) - S_6 \partial_\eta(w/\rho) \\ m_{51} &= S_0 \partial_\eta[-(e_i/\rho^2) + (u^2 + v^2 + w^2)/\rho] \\ &\quad - S_1 \partial_\eta(u^2/\rho) - S_4 \partial_\eta(v^2/\rho) - S_6 \partial_\eta(w^2/\rho) \\ &\quad - 2S_2 \partial_\eta(uv/\rho) - 2S_3 \partial_\eta(uw/\rho) - 2S_5 \partial_\eta(vw/\rho) \\ m_{52} &= -S_0 \partial_\eta(u/\rho) - m_{21} \quad m_{53} = -S_0 \partial_\eta(v/\rho) - m_{31} \\ m_{54} &= -S_0 \partial_\eta(w/\rho) - m_{41} \\ S_0 &= \gamma \mu Pr^{-1}(\eta_x^2 + \eta_y^2 + \eta_z^2) \quad S_1 = \mu[(4/3)\eta_x^2 + \eta_y^2 + \eta_z^2] \\ S_2 &= (\mu/3)\eta_x \eta_y \quad S_3 = (\mu/3)\eta_x \eta_z \\ S_4 &= \mu[\eta_x^2 + (4/3)\eta_y^2 + \eta_z^2] \quad S_5 = (\mu/3)\eta_x \eta_z \\ S_6 &= \mu[\eta_x^2 + \eta_y^2 + (4/3)\eta_z^2] \end{aligned} \quad (2.39)$$

The viscous flux Jacobian, \tilde{N} can be obtained by replacing η in Eqs. (2.38) and (2.39) with ζ . The equations of motion and solution procedure used in the two-dimensional computational procedure are a direct subset of the equations developed above, except that the inviscid fluxes are calculated using Osher's [14, 15, 16, 17] approximate Riemann solver.

2.3 Turbulence/Transition Model

To extend the equations of motion to turbulent flows, an eddy viscosity formulation is used. Thus, the effective viscosity and effective thermal conductivity can be defined as:

$$\mu = \mu_L + \mu_T$$

$$\frac{\kappa}{C_p} = \frac{\mu_L}{Pr_L} + \frac{\mu_T}{Pr_T} \quad (2.40)$$

The Baldwin-Lomax [5] two-layer algebraic turbulence model is used to represent the turbulent eddy viscosity in the flow field. The Baldwin-Lomax (B-L) turbulence model is a two-layer model in which μ_T is described by

$$\mu_T = \begin{cases} \mu_{T_{inner}} & s \leq s_{crossover} \\ \mu_{T_{outer}} & s > s_{crossover} \end{cases} \quad (2.41)$$

where s is the distance normal to the solid surface and $s_{crossover}$ is the smallest value at which $\mu_{T_{inner}} = \mu_{T_{outer}}$. In the inner region, the eddy viscosity is calculated using the Prandtl-Van Driest formulation

$$\mu_{T_{inner}} = \rho l^2 |\omega^2| \quad (2.42)$$

where

$$l = ks(1 - \exp(-y^+/A^+)) \quad (2.43)$$

and the magnitude of the vorticity, $|\omega|$ can be written as:

$$|\omega| = \sqrt{(u_y - v_x)^2 + (v_z - w_y)^2 + (w_x - u_z)^2} \quad (2.44)$$

$$\begin{aligned} v_x &= v_\xi \xi_x + v_\eta \eta_x + v_\zeta \zeta_x \\ w_x &= w_\xi \xi_x + w_\eta \eta_x + w_\zeta \zeta_x \\ u_y &= u_\xi \xi_y + u_\eta \eta_y + u_\zeta \zeta_y \\ w_y &= w_\xi \xi_y + w_\eta \eta_y + w_\zeta \zeta_y \\ u_z &= u_\xi \xi_z + u_\eta \eta_z + u_\zeta \zeta_z \\ v_z &= v_\xi \xi_z + v_\eta \eta_z + v_\zeta \zeta_z \end{aligned}$$

and y^+ is the law-of-the-wall coordinate

$$y^+ = \frac{\sqrt{\rho_w \tau_w} s}{\mu_w} \quad (2.45)$$

In the outer region the eddy viscosity is calculated using

$$\mu_{T_{outer}} = KC_{cp} \rho F_{wake} F_{Kleb}(s) \quad (2.46)$$

where K is the Clauser constant, C_{cp} is an additional constant and F_{wake} is described by

$$F_{wake} = \min(s_{max} F_{max}, C_{wk} s_{max} q_{dis}^2 / F_{max}) \quad (2.47)$$

The term F_{max} is the maximum value of $F(s)$ along a given computational grid line normal to the surface and

$$F(s) = s|\omega|(1 - \exp(-y^+/A^+)) \quad (2.48)$$

The Klebanoff intermittency factor, $F_{Kleb}(s)$ is given by:

$$F_{Kleb}(s) = (1 + 5.5((sC_{Kleb})/s_{max})^6)^{-1} \quad (2.49)$$

and q_{diff} is the difference between the maximum and minimum velocity in the profile. It is important to note that the vorticity and velocity must be calculated in the appropriate reference frame (i.e. in the absolute reference frame for stationary surfaces and in the relative frame for moving surfaces). For film cooling applications, the eddy viscosity is set to zero at the film cooling injection holes. The constants used in the current implementation of the B-L turbulence model are:

$$\begin{aligned} A^+ &= 26 & C_{cp} &= 1.6 \\ C_{Kleb} &= 0.3 & C_{wk} &= 0.25 \\ k &= 0.4 & K &= .0168 \end{aligned} \quad (2.50)$$

For three-dimensional simulations, the transition from laminar to turbulent flow (given the location of transition) is assumed to be instantaneous. The onset of transition can be specified as a function of span, in accordance with the physics of the flow field. For two-dimensional simulations, transition can be specified to be instantaneous or to occur over a specified distance. In the latter case, the intermittency factor is controlled using the model of Dhawan and Narasimha [18]

$$\gamma = \begin{cases} 0 & x \leq x_{trb} \\ 1 - \exp(-4.64\bar{\xi}^2) & x_{trb} < x < x_{tre} \\ 1 & x \geq x_{tre} \end{cases} \quad (2.51)$$

where x_{trb} denotes the beginning of transition, x_{tre} denotes the end of transition and

$$\bar{\xi} = \frac{x - x_{trb}}{x_{tre} - x_{trb}} \quad (2.52)$$

The Baldwin-Lomax turbulence model is based upon two-dimensional boundary layer data and as such, is not well suited for corner flows such as those at the blade/endwall juncture.

Originally, the treatment used to implement this turbulence model in the corner regions [1, 4] was the technique proposed by Hung and Buning [19, 20]. In this technique, the turbulence model is computed separately for each endwall and the blade surface. The mixing length in the corner region is computed depending on the computational indices of a given node. For instance, consider the case when the $J=\text{constant}$ computational lines run normal to the blade and the $K=\text{constant}$ lines run normal to the endwall. For any computational node whose J -wise index is less than its K -wise index, the normal distance is defined as the distance from the blade surface to the grid point and the parallel distance is defined as the distance from the endwall to the grid point. The mixing length for the inner region of the boundary layer is then calculated as

$$l = 2sn / (s + n + \sqrt{(s^2 + n^2)}) \quad (2.53)$$

where s is the parallel distance and n is the normal distance. The eddy viscosity is then based on the flow variables along a computational grid line from the airfoil surface to the grid point under consideration. Likewise, for any computational node whose J -wise index is greater than its K -wise index, the parallel distance is measured from the blade surface to the grid point and the normal distance is measured from the endwall to the grid point. The eddy viscosity is then based on the flow variables along a computational grid line from endwall to the grid point. Two significant problems arise from this particular three-dimensional implementation of the Baldwin-Lomax turbulence model. First, the eddy viscosity distribution in the corner regions is discontinuous across the $J=K$ computational lines and can cause large gradients to occur in the velocity field. Secondly, this particular blending is dependent upon the computational grid density and stretching in both directions. It was found, based upon numerical simulations, that flow solutions in the blade/endwall region were extremely sensitive to changes in the computational grid structure.

In the present investigation, a blending function has been used to smoothly vary the eddy viscosity distribution between the blade and endwall. Separate eddy viscosity distributions are still computed for the blade and endwall surfaces along the computational lines which run normal to each surface, respectively. The eddy viscosity in the corner flow regions is then computed based upon the following blending function according to the work of Vatsa and Wedan [21]

$$\mu_T = \frac{l_{ew}^2 \mu_{T_b} + l_b^2 \mu_{T_{ew}}}{l_b^2 + l_{ew}^2} \quad (2.54)$$

where l_b is the distance from the blade surface to a given node, $l_e w$ is the distance from the endwall surface to the node, and μ_{T_b} and $\mu_{T_{ew}}$ are the eddy viscosities computed from the separate blade and endwall flows, respectively. This type of blending greatly reduces the computational grid dependence on the eddy viscosity distribution and creates a smooth eddy viscosity distribution in the corner regions.

2.4 Boundary Conditions

The theory of characteristics is used to determine the boundary conditions at the inlet and exit of the computational domain. For subsonic inlet flow, the total pressure, v and w velocity components and the downstream running Riemann invariant,

$$R_1 = u + \frac{2a}{\gamma - 1} \quad (2.55)$$

are specified, while the upstream running Riemann invariant

$$R_2 = u - \frac{2a}{\gamma - 1} \quad (2.56)$$

is extrapolated from the interior of the computational domain. In addition, for simulations containing incoming hot streaks, the boundary conditions at the upstream boundary of the hot streak must be modified. Within the hot streak the inlet flow variables used to define the specified the boundary conditions can be written as

$$\begin{aligned} u_{hs} &= u_{\infty} \sqrt{T_{hs}/T_{\infty}} & v_{hs} &= v_{\infty} \sqrt{T_{hs}/T_{\infty}} & w_{hs} &= w_{\infty} \sqrt{T_{hs}/T_{\infty}} \\ P_{hs} &= P_{\infty} & a_{hs} &= a_{\infty} \sqrt{T_{hs}/T_{\infty}} & \rho_{hs} &= \rho_{\infty} / (T_{hs}/T_{\infty}) \end{aligned} \quad (2.57)$$

where T_{hs} is the temperature within the hot streak and T_{∞} is the temperature of the undisturbed inlet flow. The static and total pressure within the hot streak are assumed to be equal to that of the undisturbed inlet flow, corresponding to the experimental conditions. For flow simulations without an inlet hot streak, the entropy may be prescribed in place of the total pressure. It was determined through numerical experimentation, however, that prescribing the entropy for cases with an inlet hot streak resulted in a distortion of the hot streak. This distortion may be caused by a trade-off between density and temperature within the hot streak. Since the theory of characteristics is derived from the inviscid flow

equations, the boundary conditions described above are not appropriate for the boundary layer flows associated with the hub and shroud endwalls. To alleviate this inconsistency, the no-slip condition along the hub and shroud is not imposed at the first few grid points inside the computational domain [1]. The inlet boundary conditions are implemented explicitly, following an implicit extrapolation of the flow variables from the computational grid points adjacent to the boundary.

For subsonic outflow, the v and w velocity components, entropy, and the downstream running Riemann invariant (Eq. (2.55)) are extrapolated from the interior of the computational domain. The pressure ratio, P_2/P_{t1} , is specified at mid-span of the computational exit and the pressure at all other radial locations at the exit are obtained by integrating the equation for radial equilibrium [1]

$$\frac{\partial P}{\partial r} = \frac{\rho v_t^2}{r} \quad (2.58)$$

where v_t is the tangential velocity and r is the radius measured from the center of the hub. Equation (2.58) assumes the flow is inviscid and that the radial velocity does not change with radius (i.e., $\frac{\partial v_r}{\partial r} \approx 0$) [22]. Therefore, this boundary condition assumes the computational exit is far downstream of the blade row and is not applicable to the interblade region between adjacent blade rows. Similar to the inlet boundary conditions, the exit boundary conditions are implemented explicitly, following an implicit extrapolation of the flow variables from the grid points adjacent to the boundary.

Periodic boundary conditions are enforced in the circumferential (θ) direction for the $n = 1$ and $n = nb$ blades in a given blade row, where nb is the number of blades used in the numerical simulation. For two-dimensional simulations, the maximum number of blades used in the current study is $nb = 4$, while in the three-dimensional simulations the maximum number of blades used is $nb = 1$. The periodicity condition is applied in the implicit portion of the solution procedure, then corrected with an explicit update to improve accuracy.

For viscous simulations, no-slip boundary conditions are enforced at the hub and shroud endwalls of the blade passage and along the surface of the stator and rotor airfoils. It is assumed that the normal derivative of the pressure is zero at solid wall surfaces. In addition, a specified heat flux or wall temperature distribution is held constant in time along the solid surfaces. The viscous wall boundary conditions are solved in the implicit portion of the

solution procedure, and then corrected explicitly to improve accuracy. The no-slip condition can easily be incorporated into the implicit portion of the computational procedure by noting that

$$\Delta(\rho u)_{j=1} = \Delta(\rho v)_{j=1} = \Delta(\rho w)_{j=1} = 0 \quad (2.59)$$

at the wall. The normal pressure derivative and heat flux/wall temperature conditions can be cast into the form needed for the implicit portion of the computational procedure with the help of the energy equation and the equation of state. The energy equation can be written as

$$e_t = \frac{P}{(\gamma - 1)} + \frac{1}{2}[(\rho u)^2 + (\rho v)^2 + (\rho w)^2]/\rho \quad (2.60)$$

Taking the normal derivative of Eq. (2.60) yields

$$\frac{\partial e_t}{\partial n} = \frac{1}{\gamma - 1} \frac{\partial P}{\partial n} + \frac{1}{2} \frac{\partial}{\partial n} [((\rho u)^2 + (\rho v)^2 + (\rho w)^2) / \rho] \quad (2.61)$$

Applying a zero normal pressure derivative and performing the differentiation of the velocity in terms of the conservation variables gives

$$\frac{\partial e_t}{\partial n} = u_w \frac{\partial(\rho u)}{\partial n} + v_w \frac{\partial(\rho v)}{\partial n} + w_w \frac{\partial(\rho w)}{\partial n} - \frac{1}{2}(u_w^2 + v_w^2 + w_w^2) \frac{\partial \rho}{\partial n} \quad (2.62)$$

Writing the resulting differential equation in difference form yields

$$\begin{aligned} \Delta(e_t)_2 - \Delta(e_t)_1 = & u_w [\Delta(\rho u)_2 - \Delta(\rho u)_1] + v_w [\Delta(\rho v)_2 - \Delta(\rho v)_1] + \\ & w_w [\Delta(\rho w)_2 - \Delta(\rho w)_1] - \frac{1}{2}(u_w^2 + v_w^2 + w_w^2) [\Delta(\rho)_2 - \Delta(\rho)_1] \end{aligned} \quad (2.63)$$

The equation of state can be written as

$$P = \rho RT \quad (2.64)$$

Taking the normal derivative of Eq. (2.64) yields

$$\frac{\partial P}{\partial n} = RT \frac{\partial \rho}{\partial n} + R\rho \frac{\partial T}{\partial n} \quad (2.65)$$

Applying a zero normal pressure derivative and simplifying results in

$$T \frac{\partial \rho}{\partial n} + \rho \frac{\partial T}{\partial n} = 0 \quad (2.66)$$

The specified heat flux can be described by

$$q_w = -\kappa \frac{\partial T}{\partial n} \quad (2.67)$$

Substituting Eq. (2.67) into Eq. (2.66) and writing the resulting equation in difference form yields

$$\Delta(\rho)_{j=2} - [1 + q_w/(T_w \kappa)] \Delta(\rho)_{j=1} = 0 \quad (2.68)$$

Equations (2.59, 2.63, 2.68) constitute the solid wall boundary conditions for no-slip, specified heat flux conditions. For no-slip, specified wall temperature conditions Eq. (2.68) is replaced by a new equation which is also based on the equation of state. If it is assumed that one set of computational grid lines is nearly orthogonal to a solid wall, then the zero normal pressure derivative condition implies

$$(P)_{j=2} - (P)_{j=1} = 0 \quad (2.69)$$

Substituting Eq. (2.64) into Eq. (2.69) yields

$$(\rho T)_{j=2} = (\rho T)_{j=1} \quad (2.70)$$

For a calorically perfect gas, Eq. (2.70) can be written as

$$\begin{aligned} (\rho T)_{j=2} &= (\rho T)_{j=2} (c_v / c_v) \\ &= \left[(e_t)_{j=2} - u_2 (\rho u)_{j=2} - v_2 (\rho v)_{j=2} - w_2 (\rho w)_{j=2} \right. \\ &\quad \left. + \frac{1}{2} (u_2^2 + v_2^2 + w_2^2) (\rho)_{j=2} \right] / c_v \\ &= (\rho T)_{j=1} \end{aligned} \quad (2.71)$$

where $e_t = c_v T$. Equation (2.71) can be rearranged and written as

$$\Delta(\rho)_{j=1} + \left[\Delta(e_t)_{j=2} - u_2 \Delta(\rho u)_{j=2} - v_2 \Delta(\rho v)_{j=2} - w_2 \Delta(\rho w)_{j=2} \right. \\ \left. + (u_2^2 + v_2^2 + w_2^2) \Delta(\rho)_{j=2} \right] / c_v T_{j=1} = 0 \quad (2.72)$$

Equations (2.59, 2.63, 2.72) constitute the solid wall boundary conditions for no-slip, specified wall temperature conditions. The boundary conditions detailed above are implemented into the implicit portion of the numerical procedure by replacing Eq. (2.21) with

$$B(\tilde{Q}_{i,1,k}^{p+1} - \tilde{Q}_{i,1,k}^p) + C(\tilde{Q}_{i,2,k}^{p+1} - \tilde{Q}_{i,2,k}^p) = 0 \quad (2.73)$$

where, considering the no-slip, specified heat flux conditions for example,

$$B = \begin{bmatrix} -[1 + q_w/(T_w \kappa)] \frac{J_2}{J_1} & -u_w \frac{J_2}{J_1} & -v_w \frac{J_2}{J_1} & -w_w \frac{J_2}{J_1} & \frac{J_2}{J_1} \\ 0 & \frac{J_2}{J_1} & 0 & 0 & 0 \\ 0 & 0 & \frac{J_2}{J_1} & 0 & 0 \\ 0 & 0 & 0 & \frac{J_2}{J_1} & 0 \\ \frac{1}{2}(u_w^2 + v_w^2 + w_w^2) \frac{J_2}{J_1} & -u_w \frac{J_2}{J_1} & -v_w \frac{J_2}{J_1} & -w_w \frac{J_2}{J_1} & \frac{J_2}{J_1} \end{bmatrix} \quad (2.74)$$

$$C = \begin{bmatrix} 1 & 0 & 0 & 0 & 0 \\ 0 & 0 & 0 & 0 & 0 \\ 0 & 0 & 0 & 0 & 0 \\ 0 & 0 & 0 & 0 & 0 \\ \frac{1}{2}(u_w^2 + v_w^2 + w_w^2) & -u_w & -v_w & -w_w & 1 \end{bmatrix} \quad (2.75)$$

The explicit correction of the boundary variables after each time step begins with the calculation of the velocity at the wall. The no-slip condition implies zero velocity for stationary surfaces. For moving surfaces, however, the no-slip condition implies that the fluid is moving at the speed of the surface. Thus, the wall velocities are given by

$$(u)_{j=1} = x_\tau \quad (v)_{j=1} = y_\tau \quad (w)_{j=1} = z_\tau \quad (2.76)$$

where x_τ , y_τ , and z_τ represent the velocity of the surface in the x , y , and z directions, respectively. Assuming a nearly orthogonal grid, the pressure at the surface is obtained by using Eq. (2.69). The wall temperature is either specified or obtained using Eq. (2.67), and the density at the wall is calculated from the equation of state.

For film cooling applications, the no-slip, constant wall temperature/specified heat flux boundary conditions are modified at discrete points corresponding to the film cooling injection holes. The surface transpiration is treated as a Dirichlet boundary condition in the implicit portion of the numerical procedure, then updated explicitly after each time step. The simulation of film cooling is accomplished by specifying

$$|V|, \theta_1, \theta_2, T_{fc}, \rho_{fc} \quad (2.77)$$

where $|V|$ is the magnitude of the film cooling injection velocity, θ_1 and θ_2 are the specified injection angles with respect to the axial and spanwise directions, respectively, T_{fc} is the

temperature of the film cooling fluid, and ρ_{fc} is the density of the film cooling fluid. The density of the film cooling fluid is usually chosen such that the static pressure at an injection location is equal to the time-averaged static pressure obtained in the absence of film cooling. The film cooling injection angles, θ_1 and θ_2 , are specified with respect to the local surface tangent, so that the fluid injection angles with respect to the Cartesian coordinate axes are given by

$$\begin{aligned}\psi_1 &= \theta_1 + \alpha_1 \\ \psi_2 &= \theta_2 + \alpha_2\end{aligned}\tag{2.78}$$

where

$$\begin{aligned}\alpha_1 &= \tan^{-1} \left(\frac{dy}{dx} \right) = \tan^{-1} \left(\frac{dy/d\xi}{dx/d\xi} \right) \\ \alpha_2 &= \tan^{-1} \left(\frac{dy}{dz} \right) = \tan^{-1} \left(\frac{dy/d\zeta}{dz/d\zeta} \right)\end{aligned}\tag{2.79}$$

are the local surface angles (see Fig. 1 for angle reference directions). The local velocity components at the film cooling hole are then calculated as

$$\begin{aligned}u_{fc} &= |V| \sin \psi_2 \cos \psi_1 \\ v_{fc} &= |V| \sin \psi_2 \sin \psi_1 \\ w_{fc} &= |V| \cos \psi_2\end{aligned}\tag{2.80}$$

For inviscid simulations, flow tangency boundary conditions are enforced at the hub and shroud endwalls of the blade passage and along the surface of the stator and rotor airfoils. The inviscid boundary conditions are approximated in the implicit portion of the numerical procedure, then corrected explicitly. For the implicit portion of the procedure, it is assumed that there is no mass flux normal to the surface, and the mass flux tangential to the surface is the same as that at the first computational grid point above the surface. For three-dimensional simulations, the tangential velocity at the surface will have two directional components. Assuming a nearly orthogonal grid, and an airfoil as the surface under consideration, the normal mass flux condition can be approximated by

$$\Delta(\rho V_n)_w \approx \Delta(\rho \tilde{V})_w = \eta_t \Delta(\rho)_w + \eta_x \Delta(\rho u)_w + \eta_y \Delta(\rho v)_w + \eta_z \Delta(\rho w)_w = 0\tag{2.81}$$

where V_n is the normal velocity and \tilde{V} is the contravariant velocity along the computational grid line intersecting the surface. The extrapolation of the tangential mass flux is approximated by the following two equations

$$\frac{\partial(\rho \tilde{U})}{\partial n} \approx \frac{\partial(\rho \tilde{U})}{\partial \eta} = 0$$

$$\frac{\partial(\rho\tilde{U})}{\partial n} \approx \frac{\partial(\rho\tilde{W})}{\partial \eta} = 0 \quad (2.82)$$

where \tilde{U} and \tilde{W} are the contravariant velocities in the ξ and ζ directions, respectively, and n represents the normal direction. Introducing the definition of the contravariant velocity, the first of Eqs. (2.82), for example, can be rewritten as

$$\begin{aligned} (\xi_x)_{j=2}\Delta(\rho u)_{j=2} - \tilde{J}(\xi_x)_{j=1}\Delta(\rho u)_{j=1} + (\xi_y)_{j=2}\Delta(\rho v)_{j=2} - \tilde{J}(\xi_y)_{j=1}\Delta(\rho v)_{j=1} + \\ (\xi_z)_{j=2}\Delta(\rho w)_{j=2} - \tilde{J}(\xi_z)_{j=1}\Delta(\rho w)_{j=1} = 0 \end{aligned} \quad (2.83)$$

where

$$\tilde{J} = (J)_{j=1}/(J)_{j=2} \quad (2.84)$$

For inviscid flows, the entropy is extrapolated to the surface from the grid point adjacent to the wall. The extrapolation of the entropy can be reduced to extrapolating the pressure and the density from the grid point adjacent to the surface. Thus, Eq. (2.72) is also used for inviscid flows, along with

$$\Delta(\rho)_{j=2} - \Delta(\rho)_{j=1} = 0 \quad (2.85)$$

The explicit correction of the boundary variables after each time step begins by calculating the velocity components in a manner similar to that done in the implicit portion of the integration step. The pressure is extrapolated to the surface and the density is obtained by either extrapolating the entropy or the total enthalpy. For two-dimensional simulations, the tangential velocity is extrapolated to the surface instead of the contravariant velocity, and the pressure is obtained from the normal momentum equation.

Dirichlet conditions, in which the time rate change in the vector Q of Eq. (2.2) is set to zero, are imposed at the overlaid zonal boundaries of the O- and H-grids. The flow variables of Q at zonal boundaries are explicitly updated after each time step by interpolating values from the adjacent grid. The interpolation is performed in a two-dimensional manner at each spanwise section of the three-dimensional grid. Because of the explicit application of the zonal boundary conditions, large time steps necessitate the use of more than one Newton iteration. The zonal boundary conditions are non-conservative, but for subsonic flow this should not affect the accuracy of the final flow solution. For flows containing complex discontinuities, however, the conservative zonal boundary conditions developed in Ref. [23] should be used.

Chapter 3

Grid Generation

The two- and three-dimensional Navier-Stokes analyses use zonal grids to discretize the blade row flow field. A combination of O- and H-grid sections are generated at constant radial spanwise locations in the blade-to-blade direction extending upstream of the airfoil leading edge to downstream of the airfoil trailing edge. Algebraically generated H-grids are used in the regions upstream of the leading edge, downstream of the trailing edge and in the inter-blade region. The O-grid, which is body-fitted to the surface of the airfoil and generated using an elliptic equation solution procedure, is used to properly resolve the viscous flow in the blade passages and to easily apply the algebraic turbulence model. Computational grid lines within the O-grid are stretched in the blade-normal direction with a fine grid spacing at the wall. The combined H- and O- overlaid grid sections are stretched in the spanwise direction away from the hub and shroud regions (by stacking two-dimensional grids) with a fine grid spacing located adjacent to the hub and tip. The numerical procedure used to generate the grid for the three-dimensional hot streak simulations was that developed by Rai [1]. A more flexible grid generation procedure was developed to generate grids for two-dimensional geometries and three-dimensional linear cascade geometries without tip clearance.

In the new grid generation procedure, the construction of the algebraically generated H-type grids begins with the calculation of the airfoil mean camberline. The mean camberline is extended upstream of the airfoil leading edge and downstream of the airfoil trailing edge, using decay functions to control the incremental changes in the axial and tangential distances (see Fig. 2). Half the blade pitch is added to and subtracted from every computational grid

point along the extended camberline to form the first and last grid lines in the tangential direction. Computational grid lines are then added at equal increments between the first and last grid lines in the tangential direction.

The generation of the O-type grids begins with the specification of four points on the H-grid which delineate the outer boundary of the O-grid. The "box" which forms the outer boundary of the O-grid (see Fig. 3) is then smoothed to eliminate the discontinuities in the slope at the corner points. The inner boundary of the O-grid is the surface of the airfoil. An initial grid with uniform spacing is generated between the inner and outer boundaries. An elliptic solution procedure, similar to that developed by Sorenson [24], is used to produce a nearly orthogonal grid. The elliptic equations can be written as

$$\alpha x_{\xi\xi} - 2\beta x_{\xi\eta} + \gamma x_{\eta\eta} = -J^2 (Px_{\xi} + Qx_{\eta}) \quad (3.1)$$

$$\alpha y_{\xi\xi} - 2\beta y_{\xi\eta} + \gamma y_{\eta\eta} = -J^2 (Py_{\xi} + Qy_{\eta}) \quad (3.2)$$

where

$$\alpha = x_{\eta}^2 + y_{\eta}^2 \quad (3.3)$$

$$\beta = x_{\xi}x_{\eta} + y_{\xi}y_{\eta} \quad (3.4)$$

$$\gamma = x_{\xi}^2 + y_{\xi}^2 \quad (3.5)$$

and P , Q are forcing functions used to control computational grid point clustering and orthogonality near solid walls. Equations (3.1 and 3.2) are solved using a successive line over-relaxation (SLOR) technique. Finally, the grid points are algebraically redistributed near the airfoil surface to resolve viscous layer quantities. Figure 3 shows the amount of overlap between the O- and H-grids typically used in unsteady calculations. Increasing the amount of grid overlap enhances the stability and accuracy of the flow solution, but also increases the number of redundant grid points in the calculation.

The grid generation procedure for two-dimensional simulations is similar to that for three-dimensional simulations, except that the O- and H-grids are patched instead of overlaid.

Chapter 4

Visualization Technology

Visualization has emerged in the 1990's as a key enabling technology of the computational sciences. As defined by the National Science Foundation [25], visualization encompasses and unifies the areas of computer graphics, image processing, computer vision, computer-aided design and human-computer interaction. It is a process of extracting meaningful information from voluminous data sets through the application of advanced computer graphics. Visualization provides procedures for probing scientific or engineering data to discover and identify important physical phenomena or to identify errors or limitations in the process used to create the data.

During the past decade, progress was made in developing visualization procedures to apply in the analysis of fluid dynamic data. The NASA Ames Workstation Application Office developed several visualization tools (PLOT3D [26], SURF [27], RIP [28], GAS [29]) to be used for examining three-dimensional steady and unsteady data. In addition, two commercial software companies, Intelligent Light and Wavefront, also developed animation systems that could be used to visualize engineering data [30, 31, 32]. These packages created three-dimensional images from the data, where these images could be recorded to videotape for animation. Several groups are currently developing visualization systems that attempt to address the limitations of the earlier systems. They include Stardent's Application Visualization System (AVS) [33], NASA Ames's FAST [34], MIT's VISUAL3 [35] and UTRC's VISA [36]

In this investigation, three visualization software tools have been used to examine the

results of the two-dimensional and three-dimensional hot streak migration simulations. They include

- NASA's PLOT3D
- UTRC's VISA
- Intelligent Light's 3DV animation system

A description of each software tool follows.

4.1 NASA's PLOT3D

The PLOT3D program (version 3.6) is initially used to locate and identify the interesting features of the hot streak migration. The PLOT3D program developed by Buning [26] (NASA-Ames) is a fluid dynamics graphics program which inputs x, y, z object data in the form of *grid files* and flow quantities (experimental or computational data) as *solution files* and displays a three-dimensional plot of the data which can be rotated, translated and scaled interactively using a mouse control box. The PLOT3D file format has become an industry accepted standard for fluid dynamic data. This fluid dynamics graphics package can produce many types of plots including particle path lines (directions particles move in flow) and two- and three-dimensional contours of various aerodynamic quantities (such as pressure, temperature and velocity) at various locations in the flow field. PLOT3D is a first generation graphics post-processing package that allows the user to select different plotting options using a menu. In the early stages of this investigation, PLOT3D was used to locate the *interesting* features of a data set. The features are converted to geometrical objects (contour surfaces, streamlines) which are used in the Intelligent Light animation process. The PLOT3D package was later replaced in this investigation with the visualization package VISA.

4.2 UTRC's VISA

An interactive post-processing graphics software, VISA, which has been developed in the Scientific Visualization Laboratory under the UTC corporate sponsored research program, can be utilized in examining the time-dependent two-dimensional and three-dimensional flow fields of the rotor-stator interaction. The objective in designing VISA was to provide a powerful software tool which could be used by the fluid dynamic engineer on a daily basis for analyzing scientific data. The system was designed to satisfy the following goals:

- **Highly Interactive User Interface** - The goal was to develop a user interface which was easy to learn and would provide the user with a significant amount of control when examining the data. The interactivity of user interfaces in previous systems was viewed as a major weakness in the success of those systems.
- **Advanced Visualization Techniques** - The goal was to apply advanced visualization techniques such as animation, light sources, transparency, and shading models in the display of three-dimensional scalar and vector fields.
- **Volumetric Data** - The goal was for this system to accept fluid dynamic data stored in the PLOT3D format, which has become the standard post-processing format for fluid dynamic data by the aerospace industry. This includes data that has structured multiple grids with blanking.
- **Portability** - A key goal in the design of this system was for it to be portable. The system was designed to run on UNIX workstations using the X-Window System and the Programmers Hierarchical Interactive Graphics Standard (PHIGS+) library.

VISA was developed on a Stardent GS2000 which has, on average, a sustained capability of 15 Mflops and 150,000 Gouraud-shaded triangles per second. The development of this system was broken up into two areas: 1) user interface; and 2) graphics.

4.2.1 User Interface

The user interface to this system is an event-driven graphical interface. An event is defined as an occurrence caused by user input through either mouse or keyboard. By using an interface of this type the user does not need to traverse through a series of different menus and can perform any action at any time. The user, not the visualization system, is in control.

Figure 4 shows a flow diagram of the operation of the user interface. An event is detected by the user interface, which then updates information in the data structures (variables in common blocks) and calls the appropriate procedure in the visualization library. The selected visualization procedure will then read the necessary information from the data structures and construct the visual object that is displayed in the three-dimensional graphics window.

In developing this system, procedures in the user interface were written in C and the procedures for visualization were written in FORTRAN. The two groups of procedures are combined into one system through the application of shared data structures. Data is shared between the FORTRAN and C procedures by declaring the data structures in the C code as C structures and declaring the same data structures in FORTRAN as common blocks.

The user interface is responsible for the coordination of the entire system. This coordination includes the management of user input from either a keyboard or mouse as well as system events necessary for window display. The user interface was built using the X-Window system [37] because of its windowing capability, as well as its portability to other computer platforms. In addition to the X-Window system, an X-toolkit consisting of the Xt Intrinsics Library and the Athena widget set [38] was used in the construction of the input/output panels, where a panel is a window consisting of a collection of widgets. A widget is a pre-built procedure that operates independently of the calling application except through prearranged interactions. A widget set is a library of widgets that provides commonly used interface components tied together with a consistent appearance and user interface (also called "look and feel"). The use of widgets separates application procedures from user interface procedures and provides ready-to-use components such as buttons and slide bars. The MIT Athena widget set was used in this effort due to its availability at the time. (Another widget set that was considered was the Open Software Foundation's

MOTIF [38], however, this set is not currently available from Stardent.)

The X-toolkit also allows for the user interface event handling to be managed through the use of translation tables associated with each widget. Translation tables allow the specification of a mapping between a user action and a function associated with a widget. Common user actions are made using the mouse (button press, button release, screen cursor movement) or keyboard (key press). The functions that are triggered by these actions are procedures that carry out specific tasks. The VISA system operates in a main loop that continually checks for events. When an event occurs in a specific widget, the translation table is checked to determine which procedure is required, and that procedure is then called. When the procedure is finished, control returns to the main loop. The event handling is transparent to the user.

In designing the layout for VISA's graphical interface, a review was made of Stardent's AVS [33] and NASA's FAST [34], two of the first visualization systems with event-driven graphical user interfaces. While these systems are very powerful tools, it was our opinion that the layout of the windows in these systems tended to overlap too much, resulting in a cluttered screen and an awkward-to-use system. The primary focus in the physical layout of VISA's graphical interface was to make efficient use of all available screen space. An objective was to design a graphical interface that eliminated overlapping windows and have a three-dimensional graphics window as large as possible. The latter half of this objective was deemed necessary since the visual image is the most important output to the user. The layout of VISA's graphical interface is shown in Fig. 5. The main panel across the top of the screen consists of a series of pull-down menus that open various panels for:

- **File Input** - used to specify names for the PLOT3D type grid (x,y,z) and solution files to be read by the system.
- **Function Selection** - used to specify the current scalar, vector, iso-surface and thresholding functions. The functions are selected from a set of built-in CFD scalar and vector variables such as pressure and vorticity. The uses of these four functions types are discussed in the visualization subsection.
- **Object Creation** - used to specify the procedure (Computation Surface, Iso-Surface,

or Streamline) to be used in analysis of data field. These procedures are described in the visualization subsection.

- **Read/Save Options** - used to read/save information about each of the panels in this system. This allows for a complete restart capability.
- **Interactive Help** - used to provide information about the purpose and operation of each of the panels in this system.
- **System Exit** - used to leave the visualization system.

In Fig. 5 the large center window is the three-dimensional graphics window where the objects created by the system are displayed. The panel to the right of the three-dimensional graphics window is one of the object creation panels which control the creation of visual objects that are displayed in the three-dimensional graphics window. All of the object creation panels are positioned along the right edge of the three-dimensional graphics window. The object creation panels not only have the same location but also have a similar layout and function. The panel in the lower left of the screen is used to control the viewing position (translation, rotation, and scaling) of the objects being displayed in the three-dimensional graphics window. The panel in the lower right of the screen is used to control color specifications (background color, color maps of scalar functions) in the three-dimensional graphics window. These make up the primary panels of the VISA system. In addition to these primary panels, there are secondary panels that are designed to be temporary. These panels are opened, selections are made, and the panels are then closed. Since these panels are temporary, they may overlap other panels.

From Fig. 5, it can be seen that the graphical controls in each of the panels of this system consist of buttons, slide bars, and text input. The system was designed such that the majority of user input could be specified using a mouse. However, the system will accept text input from the keyboard as required.

4.2.2 Graphics

The procedures used for the visualization of three-dimensional fluid dynamic data are described. In the design phase, it was decided that the volumetric data to be analyzed by this system would be restricted to be on multiple structured grids with blanking (specification of non-fluid regions). Visualization procedures were developed that could be applied as a set of tools to interactively probe or examine a volumetric scalar or vector field to identify the "interesting" features contained within the field. The end result was the creation of visual objects that would be displayed in the three-dimensional graphics window. The following visualization procedures were developed:

- Computation surface
- Iso-surface
- Streamlines

Each of these procedures was written in FORTRAN using the PHIGS+ library to provide portability to other platforms. Application of a high level graphics standard did not result in a significant loss of graphical performance, as has been suggested by others [35]. A discussion of each of these procedures follows.

Computation Surface

This procedure is used for examining data on a computational grid. Surfaces consisting of computational planes can be created. A variety of options exists for displaying the surface. The surface can be displayed as either a mesh line or solid surface, where the user specifies the surface color. A scalar function (specified by the user) can be mapped onto the surface and displayed as either a color-mapped mesh line, contour line, or contour surface. Also, a vector function (either a total vector or components of it, again specified by the user) can be mapped onto the surface as vector lines, where the magnitude of the vector determines the vector line length. In creating the surface, a threshold function can be applied, which acts

as a discriminator. Only those parts of the surface which are in the range of the threshold function will be displayed. Other options that are available when defining the surface include the specification of transparency, on/off visibility, and on/off light source.

In addition to the functionality described above, this tool was designed to provide animation capability by allowing the current surface to sweep through a specified computational direction. By displaying a three-dimensional flow field in an animated form, the engineer can quickly understand the data being examined.

Iso-Surface

An iso-surface is constructed after defining an iso-surface function and selecting a specific value. The technique to create the iso-surface consists of two parts. The first part is to determine the computational cells where the iso-surface is located. An efficient sorting/searching algorithm recently developed by Giles and Haines [35] is used to accomplish this. The second part is to construct surfaces in each of the identified cells. This is accomplished using the marching cubes procedure developed by Lorensen and Cline [39]. Once the iso-surface has been created, it may be displayed in a similar fashion to that described in the Computational Surface Procedure. The iso-surface procedure is also used to display cutting planes of user-specified orientation, and allows for animation by sweeping through a specified range of values of the iso-surface function.

Streamlines

This procedure is used to construct streamlines after the user has selected an initial starting position or "seed" point and is similar to the technique used in PLOT3D [26] and by others [35, 40]. Since the velocity field $\vec{u}(\vec{x})$ is known, the streamline can be determined by the integration of

$$\frac{\partial \vec{x}}{\partial t} = \vec{u}(\vec{x}) \quad (4.1)$$

A second order Runge-Kutta technique is used to perform the integration and requires finding \vec{u} at arbitrary points in space. This is accomplished by recognizing that each hexahedral cell

in the data has a trilinear mapping from a unit cube ($0 < \xi_1 < 1, 0 < \xi_2 < 1, 0 < \xi_3 < 1$) in mathematical space to the hexahedron in physical space. This can be represented as

$$\vec{x} = \sum_{j=1}^8 f_j(\xi_1, \xi_2, \xi_3) \vec{x}_j \quad (4.2)$$

where the sum is over the eight corner nodes, \vec{x} is the coordinate vector of the j^{th} node, and f_j is a trilinear function which is equal to 1 at node j and 0 at all other nodes. The velocity field can also be expressed as

$$\vec{u} = \sum_{j=1}^8 f_j(\xi_1, \xi_2, \xi_3) \vec{u}_j \quad (4.3)$$

This problem then becomes one of finding the cell where the arbitrary point \vec{x} is located and then determining the corresponding value of $\vec{\xi}$ and hence \vec{u} .

Streamlines can be integrated either forward or backward in time. Restrictions can be placed on them to confine them to computational grid surfaces. After the streamline is determined, it can be displayed in the three-dimensional graphics window in several different ways using combinations of lines, line filaments and spheres. A scalar function can also be mapped onto the streamline. The procedure also allows for the streamlines to be animated.

4.3 Intelligent Light's 3DV

The primary animation capability is achieved through the use of the Intelligent Light 3DV software [41]. This software can be used to construct arbitrary animated sequences, such as those required for time-dependent (unsteady) data sets or for parameter studies of time-average (steady) data sets. This software is a complete commercial software package for the creation, visualization and animation of three-dimensional objects. At each step of the object building process, objects may be examined in wireframe or shaded form. Once objects are created they may be placed in simulated scenes, with various lighting and surface traits assigned to each object. The objects may be choreographed through time and space on a frame by frame basis. Animation software allows for the time variance of all geometrical and surface trait parameters. The user of this system need only specify object traits at *key* frames or points in time. The animation software creates all the intermediate values for the

intervening frames. Interpolation between the frames may be linear, eased, or controlled by an external, user supplied data file. The software contains a raster image generator which produces images that can be computed at user selectable resolutions of up to 8192 by 8192 pixels, with up to 24 bits of color resolution per pixel. These images may then be "averaged down" to a lesser resolution to display on a terminal or to record on video or film.

The animation is generated in a network of Apollo workstations using distributed parallel processing where frames of animation are created simultaneously on multiple workstations. Animation is recorded frame by frame to videotape. The images produced by the visualization software are converted to a RS170 RGB format that can be encoded by a Lyon/Lamb encoder into the single National Television Standards Committee (NTSC) signal used by standard American video recorders and players. A Mini-Vas animation controller controls the rewind and preroll on the tape recorder required for placing a single frame on the tape. The controller itself is controlled from the workstation using the RS232 hardware connection and the animation software. The videotape recorder is a Sony 5850 which has the single frame recording option. Each frame of animation requires 20 seconds to record to videotape. A minute of animation, at 15 frames per second, require 5 hours to record to videotape on a frame by frame basis.

4.4 Data Compression

The advances in scientific computing that have taken place during the 1980's, and now in the 1990's, have resulted in computer simulations that create massive amounts of information. For example, at each time step of the analysis of the three-dimensional rotor/stator interaction 410,677 grid points were used in the computer simulation. Eight pieces of information ($x, y, z, \rho, \rho_u, \rho_v, \rho_w, e$) were stored at each point in space. The simulation consisted of 2000 time steps per cycle. This requires approximately 26 gigabytes of information to store the entire data set. This created a set of problems including, 1) how to transfer the data from the remote supercomputer to the local workstation network, 2) where to store the information in the local network, and 3) how to interrogate (analyze and visualize) the information. For the final animation, a complete cycle of the three-dimensional rotor/stator simulation consists of 80 separate time segments (where a time segment is a snapshot of the flow field

at a particular instant in time). This resulted in reducing the amount of information to approximately 1 gigabyte of data. It is worth noting that eliminating data through this process introduces the possibility of smearing high frequency phenomena associated with the flow field. In the future, the complete data set should be interrogated to determine the number of time steps which should be saved for the post-processing of the numerical results. Similar sampling procedures were applied to the data for the two-dimensional simulations.

For the animation sequences, additional data compression was used to reduce the number of polygons used to represent surfaces in the image rendered. The procedure involved reducing the number of redundant data points defining each planar surface in the animation, as suggested by Dannenhoffer [42]. In this work, a data point was defined to be redundant when its quantity being displayed in the animation was within some user-specified tolerance of its neighbor's values. This resulted in the elimination of data points in regions where there were gradual changes in the animated quantity, and a concentration of data points in regions containing large gradients. This resulted in fewer polygons being used in the image and resulted in a reduction of the time required to render the images using the Intelligent Light 3DV software. Figure 6 shows an example of data compression for the two-dimensional hotstreak, where the static temperature field is shown. In this figure tolerances of 0, .01, .05 and .10 were used to remove points from the surface. As the tolerance was increased, data points in regions of gradual change were removed. However, it can be seen that the temperature contours do not exhibit major differences until around a tolerance of approximately .10 is used. For all the animations shown in the video-tape, a tolerance of .01 was used.

Chapter 5

Validation Test Cases

A series of validation test cases have been performed to determine the accuracy and limitations of the two- and three-dimensional Navier-Stokes procedures described in the previous sections. The predicted results for the validation test cases are compared with solutions of another Navier-Stokes procedure, a boundary layer analysis, and experimental data. The Validation Test Cases chapter is divided into three sections. These sections include

- The first section describes the validation of the two-dimensional numerical procedure for boundary layer and heat transfer quantities by simulating flow through a turbine stator passage.
- The second section demonstrates the ability of the two-dimensional computational procedure to predict performance quantities over a wide range of operating conditions for a modern turbine blade.
- The third section describes the validation of the three-dimensional procedure for heat transfer and performance quantities by simulating flow through a linear cascade.

5.1 LSRR Stator

In the first test case, the current two-dimensional Navier-Stokes procedure, called TOMCAT2, was used to simulate steady viscous flow through the mid-span section of the

United Technologies Large Scale Rotating Rig [43, 44] (LSRR) stator passage, with and without heat transfer. The predicted results were compared with the corresponding results of the ALESEP [45] 2-D boundary layer procedure and the VISCAS [46] Navier-Stokes code developed at the United Technologies Research Center (UTRC).

The computational grid topology used in the current simulations is shown in Fig. 7. The inner O-grid contains 101 grid points around the blade and 31 grid points normal to the blade surface, while the outer H-grid contains 41 grid points in the streamwise direction and 21 grid points in the blade-to-blade direction.

In the initial calculation, the blade surface temperature was specified to be equal to the free stream stagnation temperature. A comparison of the predicted steady-state pressure distribution for viscous flow through the stator passage predicted by the TOMCAT2 procedure and the VISCAS analysis is shown in Fig. 8. In this validation study, the pressure coefficient is defined as

$$C_p = \frac{2(P - P_{t1})}{\rho_1 U_{ms}^2} \quad (5.1)$$

where P_{t1} is the inlet total pressure, ρ_1 is the inlet density, and U_{ms} is the mid-span velocity of the rotor in the LSRR. The inlet and free stream conditions for this case are also shown in the figure. Agreement between the two Navier-Stokes solutions is good in general. Small differences exist between the two predicted pressure distributions, especially on the suction surface of the blade. These differences are due to the fact that the TOMCAT2 procedure converged to a slightly higher inlet Mach number than the VISCAS analysis. The blockage due to the boundary layer in the VISCAS code is slightly greater than that predicted by the TOMCAT2 analysis and can be attributed to a different implementation of the algebraic turbulence model within each code. The VISCAS code does not predict the strong spike in the pressure distribution at the trailing edge that results from the current procedure. The spike predicted by the TOMCAT2 analysis is linked to inadequate grid resolution and a breakdown of the thin layer assumption in the blunt trailing edge region.

Predicted results from the current analysis for skin friction and displacement thickness were compared to the corresponding results of the ALESEP 2-D boundary layer procedure. A direct boundary layer calculation was performed using the velocity computed from the predicted pressure distribution shown in Fig. 8 as edge boundary conditions. The edge of

the boundary layer predicted by the current Navier-Stokes procedure was determined using the numerical technique described in Ref. [46].

Figure 9 shows a comparison of the predicted skin friction coefficient between the TOMCAT2 analysis and the ALESEP boundary layer calculation. As Fig. 9 illustrates, the skin friction distribution predicted by the current procedure agrees well with the results of ALESEP, except for some discrepancies at approximately 40% axial chord on the suction side of the airfoil. The differences in this region are probably the result of insufficient grid resolution in the boundary layer for the Navier-Stokes analysis. The predicted displacement thickness using the present Navier-Stokes code shows very good agreement with the boundary layer calculation as shown in Fig. 10.

Predicted velocity profiles obtained using the current Navier-Stokes procedure and the ALESEP code at 25, 50, and 75% axial chord locations along the pressure and suction surfaces are presented in Figs. 11 and 12. Excellent agreement exists between the two predictions for both surfaces of the airfoil. Overall, the agreement between the predicted results of the TOMCAT2 Navier-Stokes procedure and those of the boundary layer analysis are quite good for this test case in which heat transfer effects were negligible.

The mass averaged total pressure loss, $\Delta P_t/P_{t1}$, and the exit flow angle predicted by the TOMCAT2 code for this case was 0.0016 and 22.12°. The VISCAS Navier-Stokes code predicted values of 0.0011 and 21.85° for the mass averaged total pressure loss and exit flow angle, which are in fairly good agreement with TOMCAT2. A wake mixing analysis [47] was performed using the average Mach number, pressure, and angle at the trailing edge plane, and the displacement and momentum thicknesses at the trailing edge tangency points predicted by the TOMCAT2 code. The wake mixing analysis, a control volume calculation which mixes the effects of the trailing edge boundary layers to uniform conditions located an infinite distance downstream, predicted a mixed out total pressure loss coefficient of 0.00021 and a far-field exit air angle of 20.18°. The predicted total pressure loss of the TOMCAT2 code is high compared to the wake mixing analysis, probably due to both inadequate grid resolution in the numerical procedure and assumptions made in the wake mixing analysis. The exit angle predicted by the TOMCAT2 code is also high relative to the mixed out exit angle.

To verify the robustness of the specified wall temperature boundary conditions in the TOMCAT2 code, a viscous steady-state calculation was performed for the stator passage in which the airfoil surface temperature was specified to be equal to 1.5 times the free stream stagnation temperature. For this simulation, the outer H-grid contained 41 points in the streamwise direction and 21 grid points in the blade-to-blade direction, while the inner O-grid contained 101 grid points around the blade and 71 grid points in the direction normal to the blade surface.

The steady-state pressure distribution for viscous flow through the stator with specified wall temperature as predicted by TOMCAT2 is shown in Fig. 13. The inlet and exit free stream conditions for this case are also shown in this figure. Predicted results of the TOMCAT2 code for skin friction and displacement thickness were again compared to the corresponding results of the ALESEP boundary layer analysis.

Figure 14 shows a comparison of the predicted skin friction coefficient distribution from the TOMCAT2 code and the ALESEP boundary layer calculation. As Fig. 14 illustrates, the skin friction distribution predicted by the TOMCAT2 code agrees well with the results of ALESEP on the pressure surface, but discrepancies exist on the suction surface. These differences are believed to be caused by the mesh density of the inner O-grid. A grid refinement study was performed to determine the mesh density required to adequately resolve the heat transfer effects. Figure 15 shows the effect of inner O-grid mesh density and wall spacing on the predicted suction side skin friction distribution. This figure illustrates that nearly four times the number of grid points and a wall spacing which is ten times finer than that used for adiabatic flow calculations is required to obtain good agreement with boundary layer theory for this strong heat transfer case.

Fig. 16 presents the Stanton number distributions calculated from the TOMCAT2 and ALESEP procedures. The Stanton number is defined as:

$$St = \left(\frac{\partial h}{\partial n} \right) / (RePr(h_{aw} - h_w)) \quad (5.2)$$

and n is the normal distance from the wall, h_{aw} is the adiabatic enthalpy at the wall, and h_w is the enthalpy at the wall. The Stanton number distributions are considerably different on the suction surface, but like the skin friction distribution the Stanton number distribution improves as the grid is refined. The predicted displacement thicknesses calculated from the

TOMCAT2 code and the boundary layer analysis are shown in Fig. 17. The predicted results show fair agreement on both the pressure and suction surfaces.

The predicted velocity profiles obtained from the TOMCAT2 and ALESEP codes at 25, 50, and 75 percent axial chord locations along the pressure and suction surfaces are presented in Figs. 18 and 19. Good agreement exists between the two predictions, on both the pressure surface and the suction surface, in the inner part of the boundary layer. However, small differences are observed in the outer portion of the boundary layer. It is believed that packing the grid points so tightly near the wall has left the grid too coarse in the outer portion of the boundary layer.

The predicted temperature profiles obtained from the TOMCAT2 and ALESEP codes at 25, 50, and 75 percent axial chord locations along the pressure and suction surfaces are presented in Figs. 20- 25. Good agreement exists between the two predictions in the inner part of the boundary layer, but again differences are observed where the grid coarsens in the outer portion of the boundary layer. It is apparent from Figs. 16 - 25 that the accurate determination of boundary layer quantities for cases involving heat transfer requires an extremely fine mesh.

The mass averaged total pressure loss, $\Delta P_t/P_{t1}$, and the exit flow angle predicted by the TOMCAT2 code for this case was 0.00138 and 22.60°. The wake mixing analysis [47] predicted a mixed out total pressure loss coefficient of 0.00048 and a far-field exit air angle of 21.34°. While the total pressure loss and exit angle predicted by the TOMCAT2 code are high relative to the mixed out results, they exhibit closer agreement with the mixing analysis than the adiabatic test case. It is believed the improved results are due to the use of a much finer grid than in the adiabatic test case.

The specified wall heat flux boundary conditions were also validated using the LSRR stator mid-span section. For this calculation, the wall heat flux was specified to yield a wall temperature equal to 1.5 times the free stream stagnation temperature, the heat flux distribution being obtained from the specified wall temperature test case. A comparison of predicted steady-state pressure distributions for the specified heat flux case and the case with the wall temperature specified as 1.5 times the free stream stagnation temperature is presented in Fig. 26. The predicted results are nearly identical, as would be expected for

this test case. The final wall temperature obtained from the specified heat flux is illustrated in Fig. 27. The calculated wall temperature is everywhere within 3 percent of the expected wall temperature of 1.5 times the free stream stagnation temperature. The slight differences may be caused by the use of the algebraic turbulence model.

5.2 Energy Efficient Engine (E^3) Turbine Blade

To verify the ability of the TOMCAT2 analysis to predict blade loading and total pressure losses at off-design operating conditions, viscous steady-state cascade calculations were performed for the Energy Efficient Engine (E^3) lightweight turbine blade section [48] at various incidence angles. The incidence angle was varied from 10 degrees below to 15 degrees above the design point incidence angle of 49.5 degrees.

The inner and outer grids used in these calculations are shown in Fig. 28. The outer grid contains 41 grid points in the streamwise direction and 21 grid points in the blade-to-blade direction. The inner grid contains 101 grid points around the blade and 71 points in the direction normal to the blade surface.

Comparisons of steady-state pressure distributions for viscous flow through the E^3 blade passage predicted by the TOMCAT2 analysis, the VISCAS [46] Navier-Stokes procedure, and experimental data [48] are illustrated in Figs. 29-34. In general, the agreement between the predicted and experimental results is excellent. At positive incidence angles, the TOMCAT2 and VISCAS procedures indicate a slightly larger overspeed region near the suction surface leading edge than the experimental data. The TOMCAT2 code predicts a leading edge separation bubble at the positive incidence angles (see Fig. 35) which was also observed in the experiments [48]. The mass averaged total pressure loss at the exit plane of the blade passage predicted by the TOMCAT2 analysis is compared to the results of the VISCAS procedure and experimental data in Fig. 36. At positive incidence angles the predicted results from the TOMCAT2 analysis are in fair agreement with the experimental data, while the predicted VISCAS results show somewhat better agreement with the experimental data. At negative incidence angles, the predicted total pressure loss levels from both the TOMCAT2 and VISCAS procedures become almost constant with decreasing incidence,

while the experimental data indicates decreasing total pressure losses. These discrepancies are probably due to the fact that the leading edge separation bubble disappears at negative incidence angles, resulting in the transition point moving downstream along the airfoil. In this investigation, however, the flow in both Navier-Stokes simulations was assumed to be fully turbulent.

5.3 Langston Cascade

A set of viscous three-dimensional numerical simulations of flow through the Langston low speed turbine cascade with a thin inlet boundary layer (0.41 cm), including heat transfer and transition, have been performed using the TOMCAT3 numerical procedure and the predicted performance and heat transfer quantities compared to experimental data [49, 50]. The heat flux values at the endwall and airfoil surfaces were specified to be the same as in Ref. [50]. The inlet Mach number was set to $M_1 = 0.0917$ and the inlet flow angle was specified to be $\beta_1 = 44.7$ degrees. The inlet Reynolds number was set to $Re_1 = 2.56 \times 10^6$ per meter and the ratio of the exit static pressure to the inlet total pressure was fixed at $P_2/P_{t1} = 0.9847$ based on the experimental data. Transition was prescribed to be a function of the span, with the endwalls assumed to be fully turbulent, and mid-span transition beginning at the 25% axial chord location on the suction surface according to the experimental data.

A computational grid refinement study has been performed to establish the grid density required to produce essentially grid-independent solutions in both the blade-to-blade and spanwise directions. A combination of two- and three-dimensional simulations were performed to establish the required grid density and wall spacing in the blade-to-blade direction to accurately predict turbine blade heat transfer. As a result of the two-dimensional simulations, it was determined that a computational grid consisting of 70×21 grid points in the H-grid and 131×61 grid points in the O-grid with an average wall spacing of .00002 ($y^+ = .059$) produced grid-independent solutions. Once this was established, a similar grid topology and density were used in the blade-to-blade direction for the three-dimensional simulations. The wall spacing adjacent to the airfoil surface was then refined during a series of three-dimensional simulations to insure the accuracy of the three-dimensional blade-to-blade solution. Finally, the spanwise computational grid was refined both in terms of endwall spac-

ing and density until the exit total pressure loss and exit flow angle distributions remained unchanged and exhibited close agreement with the experimental data.

A summary of the cases executed during this investigation are given in Table 2. The columns labelled 'Total' in Table 2 indicate area-averaged values in the spanwise direction, while the columns labelled 'Profile' refer to mid-span values. The area-averaged values were calculated using trapezoidal integration and only the computational grid points at the experimental data locations were included in the integration (a total of 13 locations for the half-span) in order to be consistent with the experimental area-averaged exit loss and flow angle values. The column labelled 'Trns' indicates whether or not transition was modelled. Since the geometry was symmetric about the mid-span, the numerical simulations were performed for only the half-span and a symmetry boundary condition was used along the symmetry plane. The spanwise grid densities given in Table 2 are for the half-span geometry. Figure 37, which illustrates the 'Total' exit flow angle and total pressure loss (see Eq. 5.4) values as a function of grid point density, demonstrates that a half-span grid-independent solution was obtained with approximately 450,000 grid points. Except where noted, the predicted results shown below are for this fine grid (Case 6) solution.

Figure 38 illustrates an example of the blade-to-blade computational grid used in the numerical simulations. Planes of blade-to-blade computational grids such as shown in Figure 38 are stacked in the spanwise direction to create the discretized geometry. Computational grid lines are clustered adjacent to the airfoil surface and endwall to properly resolve the viscous flow.

Figure 39 illustrates the predicted fine grid (Case 6) and experimentally measured pressure coefficient distributions along the surface of the airfoil at the 2.9, 12.5, 25.0, and 50.0% span locations, where the pressure coefficient is now defined as

$$C_p = \frac{2(P - P_1)}{\rho V_1^2} \quad (5.3)$$

and V_1 is the total inlet velocity. Experimental data was taken on two separate blades in the cascade and both sets of data are presented for each spanwise location. There is close agreement between the predicted results and the experimental data for the entire span of the cascade. In both the predicted results (Cases 4-6 in Table 2) and the experimental data the

effects of the endwall secondary flow on the pressure distribution are visible on the suction surface of the airfoil near the trailing edge at 12.5% span. This phenomenon was not present in the coarser grid calculations (Cases 1-3).

The predicted and experimental [50] endwall static pressure coefficient contours are illustrated in Figures 40 and 41, respectively. Comparison of the two figures show that the predicted results and experimental data agree very well. Both figures show a pressure "island", corresponding to the minimum pressure point, located on the suction surface at approximately 60% axial chord. The predicted results also exhibit the characteristic "footprint" of the endwall secondary flow on the suction side of the passage, similar to that observed in computational studies for a thick inlet boundary layer [51, 52]. This suggests that the boundary layer in the numerical procedure grows slightly faster than that observed experimentally. In the leading edge plane, the boundary layer thickness predicted by the current numerical procedure is approximately 4% greater than that observed experimentally.

The predicted static pressure coefficient contours for the suction and pressure surfaces of the airfoil are shown in Figs. 42 and 43, while the experimental contours for both surfaces are shown in Figs. 44 and 45, respectively. It is important to note that Figs. 42 and 43 are three-dimensional renderings of the airfoil surface, while Figs. 44 and 45 are two-dimensional projections of the airfoil surface. There is good agreement between the predicted results and experimental data on both surfaces of the airfoil. The static pressure island associated with the minimum pressure point, located at 38% axial chord on the suction surface, is shown in both the predicted and experimental results. The effects of the endwall boundary layer are visible in Figs. 42 and 44 just downstream of the mid-axial chord location. In both the predicted results and the experimental data, the static pressure changes very little for the first 50% axial chord of the pressure surface (see Figs. 43 and 45), then decreases very rapidly as the flow accelerates near the trailing edge.

The predicted limiting streamlines for the suction surface of the airfoil are shown in Fig. 46. Limiting streamlines obtained experimentally using surface flow visualization techniques are included for comparison in Fig. 47. The predicted limiting streamlines (Fig. 46) show close agreement with the experimental data. The flow in the mid-span region of the suction surface is two-dimensional, while the flow in the endwall region is highly three-

dimensional. A separation streamline forms at the airfoil leading edge in the endwall region and extends spanwise to approximately the 25% span position at the trailing edge. As the flow moves towards the exit of the blade passage, it is forced towards mid-span by the endwall secondary flow. The predicted pressure surface limiting streamlines are shown in Fig. 48. The corresponding experimental pressure surface limiting streamlines are presented in Fig. 49. The leading edge stagnation line is well illustrated in Fig. 48 and it is evident from both the predicted and experimental limiting streamlines that the flow on the pressure surface is predominantly two-dimensional in nature.

The predicted endwall limiting streamlines from the fine grid simulation are shown in Fig. 50, while the experimental endwall limiting streamlines are shown in Fig. 51. In both Figs. 50 and 51, a saddle point is evident near the pressure surface leading edge of the airfoil. In the numerical simulation, the saddle point location is predicted somewhat further upstream than that observed in the experiment. This again indicates that the predicted endwall boundary layer is slightly too thick. In Ref. [50], it was demonstrated that the location of the saddle point moves upstream as the endwall boundary layer is thickened. In both Figs. 50 and 51, the flow in the leading edge region moves onto the suction side of the passage and intersects the suction surface near the minimum pressure point. The flow on the pressure side of the passage migrates towards the suction surface, intersecting it in the region downstream of the minimum pressure point.

To assess the ability of the TOMCAT3 analysis to predict heat transfer, the Stanton number was calculated along the surface of the airfoil and compared with the experimental data of Graziani *et al* [50]. Figure 52 compares the predicted suction surface mid-span Stanton number distributions obtained with and without transition, the predicted results from the two-dimensional simulation, and the experimental data. The fully turbulent calculation overpredicts the Stanton number in the first 25% of the axial chord, demonstrating the importance of modelling transition. As discussed earlier, mid-span transition was prescribed, according to the experimental data, to be instantaneous at the 25% axial chord position. The effects of transition are evident from the rapid increase in the Stanton number at the 25% axial chord location. The Stanton number is predicted very well ahead of transition but is slightly underpredicted aft of the transition point. It has been found, based upon a number of two-dimensional simulations, that this small discrepancy is due to the instantaneous tran-

sition model currently used in the three-dimensional procedure. Very good agreement was found to exist between the predicted Stanton number distribution and the experimental data in the two-dimensional simulations when transition was modelled over a region extending between 25 – 60% axial chord (see Fig. 52).

A comparison of the predicted three-dimensional mid-span pressure surface Stanton number distribution with the experimental data is presented in Fig. 53. The three-dimensional predicted results demonstrate only fair agreement with the experimental data. A series of two-dimensional simulations were performed to determine if the differences between the predicted Stanton number and the experimental data near the 25% axial chord location was due to transition, similar to the suction surface. The results from these two-dimensional simulations showed that transition had little effect on the pressure side Stanton number distribution in this region of the flow. The differences may be due to limitations inherent to the algebraic turbulence model.

The predicted three-dimensional fine grid suction surface Stanton number contours are shown in Fig. 54. The experimental suction surface Stanton number contours are illustrated in Fig. 55. The predicted results demonstrate good quantitative agreement with the experimental data, except along the hub endwall downstream of the separation streamline, where the experimental data indicates increased amounts of heat transfer. In Fig. 54, the variation of the transition location with span is apparent in the leading edge endwall regions. Both the predicted results and the experimental data indicate enhanced heat transfer at the airfoil leading edge in the endwall regions and large heat transfer gradients associated with the endwall separation line.

Figures 56 and 57 illustrate the predicted fine grid and experimental Stanton number contours for the pressure surface. The predicted Stanton number distribution shows good agreement with the experimental data. Both the predicted results and the experimental data reveal much less heat transfer taking place on the pressure surface, as indicated by smaller values of the Stanton number.

Figures 58 and 59 present the predicted fine grid and experimental Stanton number contours for the endwall. In both the predicted results and the experimental data, the lowest values of the endwall Stanton number are located on the pressure surface, beginning

just downstream of the saddle point and extending to the trailing edge. In both figures, a region of increased heat transfer is located near the suction surface leading edge and in the vicinity of the minimum pressure point on the suction surface. In the wake region, discrepancies exist between the predicted results and the experimental data. The predicted results indicate a small amount of heat transfer in the wake region, while the experimental data indicates larger amounts of heat transfer. These discrepancies may be partially due to the use of O-grids to discretize around the airfoil surface. In the wake region, the gradients used in the turbulence model are parallel, rather than normal, to the wake. A previous numerical study for a multi-stage compressor, however, has shown that this technique can be used to obtain accurate wake profile predictions [53]. Other than in the wake region, the predicted results show good agreement with the experimental data.

The predicted spanwise distributions of the total pressure loss coefficient downstream of the trailing edge for all of the cases given in Table 2 are compared with the experimental data in Fig. 60. The total pressure loss coefficient is defined as:

$$C_{Pt} = \frac{2(P_t - P_{t1})}{\rho V_1^2} \quad (5.4)$$

The mid-span profile loss is accurately predicted using the fine grid, but overpredicted using the coarser grids. The predicted fine grid spanwise loss distribution shows features similar to the experimental data. The profile loss at mid-span is predicted very well by the current procedure, but the peak loss region near the 25% span location is not being accurately predicted. The predicted loss in this region associated with the secondary flow is predicted to be lower and more towards mid-span. The small rise in the predicted loss distribution in the endwall region (Cases 5-6) agrees well with the experimental data.

Table 2 provides the area-averaged total pressure loss for each of the curves shown in Fig. 60. These values of area-averaged loss were computed using C_{Pt} values at the experimental data locations in order to be consistent. Table 2 shows that for the finest grid solution, a 2% error exists between the predicted and experimental area-averaged losses. The primary source of this error is the underprediction of the secondary flow loss near the 25% span location as shown in Fig. 60. Since an essentially grid-independent solution was achieved using the finest grid (see Fig. 37), this error can be mainly attributed to the algebraic turbulence model and the transition model.

Figures 61 and 62 illustrate the predicted and experimental total pressure loss contours at the exit plane of the turbine passage. The effects of the passage vortex and endwall secondary flow on the total pressure loss distribution are accurately predicted by the numerical analysis. Both the predicted and the experimental total pressure loss contours indicate the existence of three peak loss regions. These peak loss regions may be associated with three separate vortices which form a triangle bounded by the airfoil suction surface and the hub endwall. The largest vortex, associated with the secondary flow, is located at the apex of the triangle [50]. By examining the vorticity field, it was determined that the secondary flow vortex rotates in the clockwise direction (see Fig. 61). A slightly smaller vortex, which may be associated with the suction side leg of the horseshoe vortex, rotates in the counter-clockwise direction and is located more towards the mid-span region than the secondary flow vortex [50]. The smallest vortex, which is probably associated with the suction side corner vortex, also rotates in the counter-clockwise direction and is located closer to the hub endwall than the other two vortices.

The predicted spanwise distribution of the gap-averaged flow angle (in the pitch-wise direction) downstream of the trailing edge for the cases given in Table 2 are compared with the experimental data in Fig. 63. The shape of the predicted three-dimensional flow angle distribution demonstrates good qualitative agreement with the experimental data, but the numerical values are uniformly larger than the experimentally measured flow angles by approximately 1 degree. It should be noted that the experimentally measured flow angles are generally accurate to within approximately 0.5 degree. As shown in Table 2, the exit flow angle changed very little with increasing grid density, indicating that grid dependence is not the cause of the discrepancy between the predicted and experimental flow angles. The 3.5% difference between the predicted area-averaged exit flow angle and the experimental data could possibly be due to inadequacies in the modelling of transition and turbulence, and/or it could be due to a breakdown of the thin layer assumption in the secondary flow regions.

Chapter 6

Numerical Experiments

A series of numerical experiments have been performed using the TOMCAT2 and TOMCAT3 analyses to simulate hot streak migration through the LSRR turbine stage, including the effects of a surface heat flux and film cooling. The two-dimensional numerical hot streak simulations include the use of 3-stator/4-rotor/1-hot streak and 1-stator/1-rotor/1-hot streak configurations to study the effects of blade count ratio, a rotor surface heat flux, rotor surface film cooling, and stator base cooling on the time-averaged rotor surface temperature. The three-dimensional numerical simulations were all performed for a 1-stator/1-rotor/1-hot streak configuration and include the effects of a rotor surface heat flux and film cooling. The Numerical Experiments chapter is divided into three sections,

- The first section describes the experimental apparatus.
- The second section describes the two-dimensional and three-dimensional adiabatic hot streak simulations.
- The third section describes the two-dimensional and three-dimensional hot streak simulations which include the effects of a surface heat flux and film cooling.

6.1 Experimental Apparatus

The turbine used in the experimental tests was the first stage of the LSRR [2, 43, 44], which includes 22 stator airfoils and 28 rotor airfoils. The LSRR is a large scale, low speed,

rotating wind tunnel facility designed to simulate the flow field in axial flow turbomachines. For the hot streak experiments, the LSRR was configured to resemble the first stage of a high-pressure turbine, typical of those used in aircraft gas turbine designs.

In the first experimental study [2], one hot streak was introduced through a 5.08 cm diameter circular pipe at 40% span, and midway between, two stator airfoils of the LSRR. The temperature of the hot streak was twice that of the surrounding inlet flow, whereas the static and stagnation pressures were identical to the free stream. The hot streak was seeded with CO_2 and the path of the hot streak was determined by measuring CO_2 concentrations at various locations within the turbine stage. The flow conditions used in the first experiment are shown in Table 3. In the following sections, the first experimental test will be referred to as the "circular hot streak # 1 (CHS1) " experiment.

A second experimental study [54] was conducted using the same configuration as in the CHS1 experiment, except that the temperature of the hot streak was only 1.2 times that of the surrounding inlet flow and the flow coefficient was slightly increased (see Table 4). In the following sections, this experimental test will be referred to as the "circular hot streak # 2 (CHS2) " experiment.

In a third experimental study [55, 56], one hot streak was introduced in the form of a two-dimensional jet from the hub to the tip between two stator airfoils of the LSRR. In this experiment, the stator vanes were rotated down 7 degrees with respect to the tangential direction relative to the design point operating conditions. The flow conditions used in the third experimental test are presented in Table 5. In the following sections, this experimental configuration will be referred to as the "planar hot streak (PHS)" experiment.

6.2 Adiabatic Simulations

6.2.1 Two-Dimensional Simulations

A two-dimensional 3-stator/4-rotor/1-hot streak and a 1-stator/1-rotor/1-hot streak simulation have been performed as part of a numerical investigation into the effects of stator-to-rotor blade count ratio on hot streak migration and time-averaged wall temperature distributions.

In these two simulations, adiabatic wall conditions were enforced on both the stator and rotor surfaces. For both adiabatic two-dimensional simulations, approximately six cycles at 3000 time steps per global cycle on a four processor Alliant FX-80 mini-supercomputer were needed to obtain a time-periodic solution. A global cycle corresponds to the rotor blade rotating through an angle of $2\pi/N$ where N is the number of stator blades (i.e. $N=3$ and $N=1$). Typical calculations required 0.00191 seconds per grid point per time step computation time.

A 15% axial gap between the stator and rotor was used in both the two-dimensional adiabatic simulations, while the experimental configurations had a 65% axial gap. A 15% axial gap was chosen for the current numerical study since: 1) previous numerical simulations [1, 3, 4] for the same geometry and similar flow conditions used this axial gap, and 2) a large experimental data base [43] exists for the 15% axial gap test case. It has been demonstrated [44] that the axial gap has no significant impact on either the time-averaged pressure distributions or time-averaged heat transfer coefficients on the stator or rotor. Secondary flow and other viscous mechanisms, however, can be affected by the stator/rotor axial gap. The inlet Mach number to the stator was 0.07 and the inlet flow was assumed to be axial. The rotor rotational speed was 468 rpm and the flow coefficient was $\phi = u/U = .78$. The free stream Reynolds number was 3.939×10^6 per meter. A pressure ratio of $P_2/P_{t1} = .963$ was determined from the inlet total pressure and the static pressure measured in the rotor trailing-edge plane.

An accurate representation of the LSRR configuration requires at least 11 stator and 14 rotor airfoils. For the 1-stator/1-rotor simulation, the rescaling strategy of Madavan *et al.* [57] was used to reduce the number of airfoils to one stator and one rotor. The stator was scaled down by a factor of (22/28) and it was assumed that there were 28 stator airfoils. The pitch to chord ratio of the stator was not changed. This is different than the scaling strategy used by Rai and Dring [3] in which the rotor was scaled by a factor of (28/22) and it was assumed there were 22 rotor airfoils. Since the unsteady and hot streak effects are much more pronounced in the rotor passage, the stator airfoil was rescaled in the current study in order to maintain similitude with the experimental rotor configuration. For the two-dimensional 3-stator/4-rotor simulation, a rescaling strategy was used to reduce the number of airfoils to 3 stators and 4 rotors. In this case, it was assumed that there were 21 stator airfoils and 28 rotor airfoils and the stators were enlarged by the factor (22/21).

For the 1-stator/1-rotor simulation, one hot streak was introduced to the inlet of each stator passage over one quarter of the stator pitch and centered at mid-gap. For the 3-stator/4-rotor simulation, one hot streak was introduced to the inlet of every third stator passage. Introducing one hot streak every third passage more closely models the experiment, where only one hot streak was introduced for the entire turbine stage. For the 3-stator/4-rotor simulation, the hot streak was introduced over a distance equal to one quarter of a stator pitch and centered at the mid-gap position between the second and third stator. In the two-dimensional calculations, the temperature profile used at the stator inlet to simulate the combustor hot streak consisted of a hyperbolic tangent (step-like) distribution. The temperature of the hot streak in the current investigation is 1.2 times the temperature of the surrounding inlet flow. Shear layer instabilities, caused by the step-like temperature profile, developed in the numerical simulations when the hot streak temperature was increased beyond 1.2 times that of the surrounding flow.

For the 3-stator/4-rotor simulation, each of the three stator grids was constructed with 101×31 (streamwise \times tangential) grid points in the O-grid and 71×51 grid points in the H-grid. Each of the four rotor grids was constructed with 101×31 grid points in the O-grid and 75×51 grid points in the H-grid. A total of 48,080 grid points and an average blade wall spacing of 5.08×10^{-6} meters ($y^+ \approx 1.70$) were used in this simulation. For the 1-stator/1-rotor simulation, the stator zone was constructed with 101×31 grid points in the O-grid and 75×31 grid points in the H-grid. The rotor zone was constructed with 101×31 grid points in the O-grid and 71×31 grid points in the H-grid. A total of 10,788 grid points and an average wall spacing of 5.08×10^{-6} meters ($y^+ \approx 1.50$) were used in this calculation. The grid topology used in the 1-stator/1-rotor simulation is shown in Fig. 64.

To ascertain the time periodicity of the solutions, unsteady pressure and temperature data was obtained at selected points along the stator and rotor surfaces over two global time cycles. Figures 65 and 66 show the unsteady pressure histories obtained from the 3-stator/4-rotor simulation at the mid-axial chord location of the stator and rotor, respectively. These two figures demonstrate that the simulation has achieved time-periodicity. In Fig. 65, the periodic changes in the pressure on the stator surface are related to the rotor blade passing frequency. In Figure 66, the predominant contributions to the periodic changes in the pressure on the rotor surface are from the passing stator blades and associated stator

wakes. However, a slight variation in the pressure at the passing frequency of the hot streak is also visible.

The influence of the hot streak on the surface temperature at the mid-axial chord position of the stator and rotor as a function of time is shown in Figs. 67 and 68. The magnitude of the temperature variations on the rotor is large due to the rotor passing through the hot streak, while only small temperature variations are observed on the stator. The temperature variations on the stator are mainly due to the interaction effects of the rotor blade, since the hot streak passes between adjacent stator blades without contacting the blade surfaces. Figures 67 and 68 would suggest that there is at most a weak coupling between the pressure field and temperature fields.

Results of the two-dimensional adiabatic simulations have been compared with the time-averaged experimental data of Refs. [2] and [43]. Figure 69 shows a comparison of the time-averaged stator surface pressure distribution predicted by the numerical analysis for the 3-stator/4-rotor and 1-stator/1-rotor configurations with experimental data reported by Dring *et al.* [43]. The time-averaged pressure coefficient is defined as:

$$C_p = \frac{P_{avg} - P_{t1}}{\frac{1}{2}\rho_1 U_{ms}^2} \quad (6.1)$$

where P_{avg} is the local time-averaged pressure and U_{ms} is the mid-span rotor velocity. The predicted results for the 3-stator/4-rotor and 1-stator/1-rotor configurations exhibit good agreement with the experimental data. Figure 70 presents a comparison of the predicted results of the two simulations with the experimental time-averaged surface pressure data for the rotor. Excellent agreement exists between the numerical predictions and the data. The predicted results shown in Figs. 69 and 70 are also in good agreement with those reported by Rai *et al.* [3, 4] for a similar 1-stator/1-rotor configuration with and without a hot streak. These figures substantiate the supposition that the hot streak has negligible effects on the time-averaged pressure fields of the stator and rotor passages.

A measure of the unsteadiness of the flow can be obtained by evaluating the size of the surface pressure fluctuations on the stator and rotor. The pressure fluctuations can be quantified through the use of an unsteady pressure amplitude coefficient defined by:

$$\tilde{C}_p = \frac{P_{max} - P_{min}}{\frac{1}{2}\rho_1 U_{ms}^2} \quad (6.2)$$

Figure 71 illustrates the predicted and experimental values of the unsteady pressure amplitude coefficient for the surface of the stator. Good agreement exists between the predicted 3-stator/4-rotor results and the experimental data. This figure shows that the amplitude of the pressure variations is small on the stator, except near the trailing edge. The predicted results for the 1-stator/1-rotor configuration show larger pressure fluctuations than both the 3-stator/4-rotor configuration and the experimental data. The larger fluctuations are due to pressure signals which do not decay for even blade count configurations [4] and the reflective exit boundary conditions used in the numerical procedure. Figure 72 illustrates the predicted and experimental values of the unsteady pressure amplitude coefficient for the rotor. Good agreement exists between the predicted 3-stator/4-rotor results and the experimental data except near the pressure surface trailing edge, where the pressure variations are greater than those observed experimentally. Again, the predicted pressure fluctuations for the 1-stator/1-rotor configuration are larger than those predicted in the 3-stator/4-rotor configuration, as well as the experimental data. Figures 69-72 illustrate that the stator/rotor blade count ratio has little effect on the time-averaged pressure field, but has considerable impact on the unsteady pressure field.

To quantify the effects of the hot streak on the rotor surface time-averaged temperatures, a temperature coefficient is introduced. The temperature coefficient, \bar{C}_T , is defined as [3, 55]:

$$\bar{C}_T = \frac{T - T_1}{T_{avg_{rle}} - T_1} \approx \frac{CO_2 - CO_{2amb}}{CO_{2avg_{rle}} - CO_{2amb}} \quad (6.3)$$

where T is the local time-averaged temperature, $T_{avg_{rle}}$ is the mid-span time-averaged temperature at the rotor leading edge, CO_2 is the local time-averaged CO_2 concentration, and $CO_{2avg_{rle}}$ is the mid-span time-averaged CO_2 concentration at the rotor leading edge. This definition of \bar{C}_T inherently includes a number of assumptions regarding the equivalence between the CO_2 concentration and the temperature distribution. In particular, this definition assumes the relationship between CO_2 concentration and temperature distribution is governed by only one variable, the ratio of hot streak temperature to the free stream temperature,

$$\bar{C}_T = f(T_{hs}/T_\infty) \quad (6.4)$$

Previous experimental [2] and numerical [3] investigations give valuable insight towards determining the validity of Eq.(6.3). These investigations showed that the hot streak fluid

impacts the rotor blades near the leading edge and is quickly convected onto the pressure surface of the airfoil. This suggests that the average temperature near the leading edge is relatively insensitive to the number of hot streaks in the turbine. The flow on the suction surface of the rotor should also be approximately independent of the number of hot streaks in the turbine because, 1) the hot gases have a natural tendency to migrate towards the pressure surface of the rotor, and 2) the hot fluid which does move onto the suction surface is rapidly convected downstream. Thus, Eq.(6.3) is probably adequate for correlating the experimental CO_2 concentrations and the numerically determined time-averaged temperatures near the leading edge and on the suction surface of the rotor.

The nature of the flow on the pressure surface of the rotor, however, requires that the time-averaged temperature coefficient be a function of several variables. The hot fluid will linger on the pressure surface of the blade for a considerable amount of time because the convection speeds are significantly lower than on the suction surface. As the number of hot streaks introduced at the stator inlet is increased, a critical point is reached where a second (or possibly third) hot streak impacts the pressure surface before the hot fluid from the first hot streak has been convected downstream of the trailing edge. Therefore, the temperature coefficient should include a dependence on the number of hot streaks in the turbine, their physical extent relative to the cascade pitch (i.e., the hot streak solidity), and the residence time of the hot fluid on the pressure surface,

$$\bar{C}_T = f(T_{hs}/T_\infty, \sigma, t_r) \quad (6.5)$$

where $\sigma = N_{HS}/N_s$, N_{HS} is the number of hot streaks, N_s is the number of stator passages, and t_r is the residence time of the hot fluid on the pressure surface. In two-dimensional simulations, the residence time is a function of the instantaneous axial convection speed

$$(t_r)_{2D} = f(c_x) \quad (6.6)$$

In three-dimensional simulations the residence time is a function of both the instantaneous axial and radial convection speeds

$$(t_r)_{3D} = f(c_x, c_r) \quad (6.7)$$

It should be noted that the instantaneous convection speed is in fact a function of the hot streak to free stream temperature ratio. Previous studies [2, 3] have concluded that the

velocity increase within the hot streak, relative to the free stream, is a contributing factor to the accumulation of hot gases on the pressure surface of the rotor due to the resulting incidence variation on the rotor. This suggests that for a constant hot streak temperature ratio, changes in the free stream flow velocity (or flow coefficient) will affect the migration patterns of the hot fluid. Thus,

$$\bar{C}_T = f(T_{hs}/T_{\infty}, \sigma, t_r, \phi) \quad (6.8)$$

where ϕ is the flow coefficient. In addition, the temperature coefficient should also include a shape factor which accounts for the geometry of the hot streak,

$$\bar{C}_T = f(T_{hs}/T_{\infty}, \sigma, t_r, \phi, S) \quad (6.9)$$

where S is some shape factor. Finally, the temperature coefficient should account for any differences between the experimental and numerical data sampling techniques. In the numerical simulations, the temperature at the surface is known directly. In the experimental simulations, the CO_2 concentrations are determined by drawing gas samples through the airfoil surface static pressure taps. The suction force used to sample the CO_2 is not regulated, and may be large enough to cause CO_2 from well above the surface to be included in the sample. Thus, the experimental CO_2 concentration data may actually be representative of the flow conditions some distance δ above the airfoil surface. If the experimental values of δ , which are probably a function of location on the airfoil surface and boundary layer thickness, are known then the predicted temperature field from the numerical simulations can be interrogated at these locations. Therefore, the definition of the temperature coefficient given in Eq.(6.3) should be expected to reveal trends, but not necessarily provide a direct correlation, between the experimental data and numerical results.

Figure 73 compares the predicted 3-stator/4-rotor and 1-stator/1-rotor time-averaged temperature coefficient distributions with the CHS1 and CHS2 experimental data [2, 54]. Also included in Fig. 73 are the two-dimensional numerical results of Rai and Dring (1-stator/1-rotor) [3] and Krouthen and Giles (1-stator/1-rotor, data rescaled) [58]. The time-averaged temperature coefficient distribution for the current 1-stator/1-rotor hot streak calculation is essentially the same as that reported by Rai and Dring [3], except for a small difference on the pressure surface. The predicted time-averaged temperature coefficient distribution for the pressure surface of the 3-stator/4-rotor simulation is similar to that of

the 1-stator/1-rotor calculation, but the suction surface temperature coefficient distribution shows lower time-averaged temperatures than that predicted in the 1-stator/1-rotor calculation. The lower suction surface temperatures predicted in the 3-stator/4-rotor simulation may be the result of introducing one hot streak every third stator passage, instead of one hot streak in each stator passage. The temperature coefficient distribution obtained by Krouthen and Giles [58] is similar to the present 3-stator/4-rotor prediction. All of the two-dimensional numerical simulations shown in Fig. 73 predict nearly equal time-averaged temperatures on the pressure and suction surfaces, and exhibit only fair agreement with the experimental data for a hot streak temperature ratio of 1.2 (CHS2). The experimental data for a hot streak temperature ratio of 2.0 (CHS1) shows a much higher pressure surface temperature than all of the the two-dimensional numerical predictions and the CHS2 experimental data.

The segregation of the hot gases to the pressure side of the rotor passage has been, until this time, believed to be caused solely by the relative inlet angle difference between the hot streak and the surrounding fluid at the inlet to the rotor passage [2]. Results of the two-dimensional simulations confirm experimental observations which indicate that the static pressure, total pressure, and absolute flow angle are the same in the hot streak as in the surrounding fluid at the stator exit. The difference in the total temperature between the hot streak and the surrounding fluid results in an absolute velocity difference equal to the square root of the ratio of the hot streak and surrounding fluid temperatures. In the relative frame, a difference in the rotor relative inlet angle and velocity results. As a result, the hot streak fluid moves towards the pressure surface at a higher relative velocity compared to the surrounding fluid [2]. Time-averaged static temperature contours for the rotor passage of the two-dimensional 3-stator/4-rotor configuration are shown in Fig. 74. Although the hot streak fluid accumulates near the pressure side of the rotor, the hot fluid does *not* penetrate the boundary layer to the surface of the rotor blade. The thin layer of cooler fluid which exists between the hot fluid and rotor pressure surface helps explain the relatively flat temperature coefficient profiles shown in Fig. 73 for the two-dimensional solutions.

To gain better insight into the unsteady phenomena within the turbine stage, animated sequences of the flow field were created using procedures described in Ref. [30]. Figure 75 shows the temperature field at one instant in time during the animated sequence. The hot streak is undisturbed as it migrates through the stator passage, except that the width of

the hot streak decreases due to flow acceleration. The geometry of the turbine rotor blades is such that the hot streak impinges first on the pressure surface, then wraps around the leading edge and moves along the suction surface. As a result of this movement, the rotor pressure surface temperature does not peak until some time after the rotor blade interacts with the hot streak. The hot streak assumes a 'V' shape as it continues to convect through the rotor passage.

To determine the role of hot streak shape on the hot fluid migration patterns, a 1-stator/1-rotor/1-hot streak simulation was performed and compared to the experimental planar hot streak (PHS) data [55, 56]. In this hot streak simulation, the stator grid system was constructed with 101×31 grid points in the O-grid and 85×51 grid points in the H-grid. The rotor grid system was constructed with 101×31 grid points in the O-grid and 78×51 grid points in the H-grid. A total of 14,575 grid points were used in this simulation. The stator airfoils had an average y^+ value of 0.84, while the rotor airfoils had an average y^+ value of 0.70. Figure 76 illustrates the grid topology used in the numerical simulations, where every other grid point in the O-grid has been omitted for clarity.

The flow conditions used in the numerical simulation of the planar hot streak are shown in Table 5, with the exception that in the numerical simulation a flow coefficient of $\phi = .385$ was used. The flow coefficient used in the numerical simulation was chosen to alleviate a pressure surface separation bubble which occurred at a flow coefficient of $\phi = .35$. The difference in the numerical and experimental flow coefficients equates to the numerical simulation being performed at approximately 3 degrees more positive incidence at the rotor inlet than in the experiment. This increase in incidence corresponds to only a 10% shift in the spanwise location (towards the tip) at which the numerical simulation was performed, to a position located at 60% span. A pressure ratio of $P_2/P_{t1} = .9630$ was determined from the inlet total pressure and the static pressure measured in the rotor trailing-edge plane.

Figure 77 illustrates the predicted stator surface time-averaged pressure coefficient distribution. Unfortunately, no experimental time-averaged pressure data was available for the stator airfoils. Figure 78 shows the predicted and experimental [43] rotor surface time-averaged pressure coefficient distributions. Excellent agreement exists between the predicted results and the experimental data for the rotor, except near the suction surface leading edge

where the numerical simulation predicts a strong overspeed. This discrepancy is probably due to the difference (3 deg) in the time-averaged incidence to the rotor between the numerical simulation and the experiment [43].

Figure 79 illustrates the experimental time-averaged CO_2 concentration contours for the rotor surface. The movement of the hot streak fluid from leading edge to the trailing edge of the pressure surface at approximately constant spanwise locations indicates the two-dimensional nature of the hot streak. Conspicuously absent is the radial migration of the hot streak on the pressure surface observed both experimentally [2], and in previous numerical simulations [9, 59] for a circular hot streak. Figure 80 compares the predicted time-averaged temperature coefficient (Eq.(6.3)) distribution along the surface of the rotor to the experimental data taken at mid-span. The predicted numerical results exhibit fair agreement with the experimental data. The numerical simulation underpredicts the temperature near the pressure surface leading edge, and also predicts a rapid temperature fall-off on the suction surface which is not observed in the experimental data. In an attempt to discover the source of the discrepancies between the numerical and experimental temperature distributions, the time-averaged temperature profiles were plotted at three locations along the pressure surface of the rotor (see Fig. 81). Time-averaged boundary layer edge locations are also included in Figure 81. At 25% axial chord the maximum temperature in the boundary layer occurs off the surface, approximately one-third the distance to the boundary layer edge. Similarly, at 50% axial chord the maximum temperature in the boundary layer occurs well above the rotor surface. At 75% axial chord, however, the time-averaged boundary layer is noticeably thinner and the maximum time-averaged temperature occurs at the rotor surface. A general observation drawn from this investigation is that as the boundary layer becomes thinner, the maximum temperature in a given boundary layer profile moves closer to the airfoil surface.

Using Fig. 81 as a guide, and expanding upon the earlier discussion of the temperature coefficient, it is believed that one factor which may contribute to the discrepancies between the experimental data and the two-dimensional simulation is the method of experimental data acquisition at the rotor surface. In the experiment, the CO_2 concentrations along the surface of the rotor were determined by drawing samples of the gas in through static pressure taps. The suction force may cause CO_2 gas from well above the airfoil surface to be included in the sample. To test this hypothesis, the time-averaged temperature coefficient

was redefined as:

$$\hat{C}_T = \frac{T_{bl} - T_1}{T_{avg_{rle}} - T_1} \quad (6.10)$$

where T_{bl} is the time-averaged temperature, area-averaged over a given boundary layer profile. Figure 82 compares the predicted results using the modified temperature coefficient definition with the experimental data. Excellent agreement now exists between the predicted and experimental results. A comparison of Figures 80 and 82 reveals that the predicted surface temperature is approximately equal to the area-averaged temperature in the boundary layer, except in the leading edge region. Figure 82 shows that two-dimensional simulations can be used to provide guidance as to when and where rotor surface temperatures will exceed allowable limits. This is an important finding which shows that under certain conditions costly and time consuming three-dimensional simulations of hot streak migration may not need to be executed to determine if rotor pressure surface burning is likely. This simulation also underscores the need for including the additional dependencies discussed earlier in the relationship between the experimental CO_2 and numerical temperature distributions.

6.2.2 Three-Dimensional Simulations

An adiabatic three-dimensional 1-stator/1-rotor/1-hot streak simulation with a hot streak temperature 20 percent greater than the free stream temperature has been performed to establish the effects of combustor hot streak migration on the time-averaged rotor surface temperature distribution. In this numerical simulation, one hot streak was introduced through a 5.08 cm circular region at the inlet of each stator passage, corresponding to the 5.08 cm diameter pipe used in the CHS1 and CHS2 experiments [2, 54]. The center of the hot streak was located at the mid-gap, 40% span location. Figure 83 illustrates a perspective view of the hot streak at various axial locations within the stator passage. The circular nature and intensity of the hot streak are maintained as the hot streak is convected through the stator passage. A 15% axial gap was used between the rotor and stator airfoils. The inlet Mach number and rotor rotation speed are given in Table 3. The flow coefficient in the numerical simulations was $\phi = 0.78$ and a pressure ratio of $P_2/P_{t1} = .9630$ was determined from the inlet total pressure and the static pressure measured in the rotor trailing edge plane.

For this three-dimensional simulation, the stator grid system was constructed with $101 \times$

21 grid points in each spanwise O-grid and 58×31 grid points in each spanwise H-grid. The rotor grid system was constructed with 101×21 grid points in each spanwise O-grid and 60×31 grid points in each spanwise H-grid. A total of 51 O-H grid planes were distributed in the spanwise direction. The rotor region had a tip clearance grid system that contained 101×11 grid points in each of 7 spanwise locations. A total of 410,677 grid points were used in the three-dimensional simulation. A wall spacing of 1.27×10^{-5} meters ($y^+ \approx 4$) was used in the blade-to-blade direction, while a wall spacing of 7.62×10^{-4} meters ($y^+ \approx 20$) was used in the spanwise direction. The experimental rotor has a tip gap equal to 1% of the rotor span, while the tip clearance in the three-dimensional simulation was equal to 3.9% of the rotor span. A larger tip clearance was used in the numerical simulation than in the experiment because the grid required to resolve the circular nature of the hot streak in the mid-span region forced the relaxation of the grid line spacing in the spanwise direction at the hub endwall and in the tip clearance region. Unlike the two-dimensional simulations, the rotor geometry was scaled in the three-dimensional simulations to be consistent with previous three-dimensional simulations [1, 9]. A spanwise section of the three-dimensional computational grid topology is shown in Fig. 84.

The three-dimensional calculation was performed on the NAS Cray 2 and Cray YMP supercomputers located at the NASA Ames Research Center. Seven cycles at 2000 time steps per cycle were needed to obtain time-periodic solutions. This calculation required approximately 0.000263 seconds per grid point per time step computation time on the Cray 2.

In this three-dimensional simulation, adiabatic boundary conditions were enforced along the surface of the rotor. To be certain of the time periodicity of the three-dimensional temperature field, unsteady temperature data was obtained at the the mid-axial chord location on the pressure and suction surfaces of the rotor at the 2, 25, 50, 75 and 98% span locations (see Figs. 85-89). These figures confirm that the temperature field is periodic. It is worth noting that the temperature field did not become periodic until two global cycles *after* the pressure field became periodic.

As part of the numerical investigation, the predicted unsteady pressures and temperatures have been time-averaged and compared to experimental data [43]. Figure 90 illustrates the

predicted and experimental time-averaged pressure coefficient distributions on the stator at 2, 12.5, 25, 50, 75, 87.5 and 98% span locations. In general, there is good agreement between the predicted results and the experimental data. The predicted results also agree well with those presented by Rai [1] and Madavan *et al.* [57].

Predicted and experimental time-averaged pressure coefficient distributions for the rotor at the 2, 12.5, 25, 50, 75, 87.5 and 98% span locations are shown in Fig. 91. Good agreement between the predicted results and the experimental data is observed from the hub to the mid-span location of the rotor. Some discrepancies between the predicted and the experimental pressure distributions are evident on the suction surface of the rotor, however, from the mid-span location out to the tip. These discrepancies are probably caused by the stronger secondary flows which arose in the calculation due to the relatively large tip clearance.

Figure 92 shows the predicted and experimental values of the unsteady pressure amplitude coefficient for the mid-span section of the stator. The predicted suction surface pressure fluctuations near the trailing edge are smaller than those of the experimental data and the two-dimensional results shown in Fig. 71. In addition, the pressure amplitude coefficient on the pressure surface does not rise near the trailing edge compared to the experimental data and predicted two-dimensional results (see Fig. 71). Figure 93 illustrates the predicted and experimental values of the unsteady pressure amplitude coefficient for the mid-span section of the rotor. Fair agreement exists between the predicted results and experimental data, as the predicted results show larger pressure fluctuations than those observed experimentally and predicted two-dimensionally (see Fig. 72). The stator and rotor pressure amplitude results shown in Figs. 92 and 93 are similar to the coarse grid predictions of Rai [1]. Madavan *et al.* [57] showed that the pressure amplitudes on both the stator and rotor are sensitive to the computational grid density. The results shown in Figs. 92 and 93 are predicted using the same fine computational grid density as Madavan *et al.* [57]. However, the wall spacing used in the current calculation was increased in order to yield a nearly uniform grid near mid-span/mid-gap, which was necessary to maintain a circular hot streak. Comparison between the current results and those of Rai [1] and Madavan *et al.* [57] show that the predicted pressure amplitude is not only sensitive to computational grid density, but also to the spanwise distribution of grid points. Figures 90-93 again suggest that the hot streak does not affect the pressure field.

Figure 94 illustrates the predicted time-averaged temperature coefficient (Eq.(6.3)) distribution from the three-dimensional adiabatic hot streak simulation and the experimental data [2, 55] for the mid-span section of the rotor. Also included in Fig. 94 are the three-dimensional 3-stator/4-rotor/1-hot streak inviscid (with viscous modelling) results of Takahashi *et. al.* [55, 59]. The three-dimensional Navier-Stokes simulation predicts time-averaged pressure surface temperatures which are significantly higher than either the CHS1 or CHS2 experimental data indicates, while the three-dimensional inviscid calculation exhibits fair agreement with the experimental data. It is believed that the magnitude of the time-averaged temperatures in the Navier-Stokes simulation is large due to long hot streak residence times (see Section 5.2.1) on the rotor pressure surface. In this numerical 1-stator/1-rotor/1-hot streak simulation, the hot fluid from two additional hot streaks impacts the pressure surface before the first hot streak has been convected downstream. The predicted results of the current Navier-Stokes simulation do indicate that pressure surface heating could become significantly more severe when the turbine contains multiple hot streaks. The hot streak residence time on the rotor pressure surface is not as large in the inviscid 3-stator/4-rotor/1-hot streak calculation of Takahashi as in the viscous simulation because the hot streak solidity, σ is much lower and the inviscid flow assumption results in higher near-surface convection speeds.

On the suction surface of the rotor, the current Navier-Stokes simulation correctly predicts the rapid fall-off of the time-averaged temperature, while the inviscid solution of Takahashi exhibits a nearly constant temperature. As discussed in Section 5.2.1, the definition of the time-averaged temperature coefficient given by Eq.(6.3) should be approximately independent of the number of hot streaks and the hot streak residence time. The fact that the Navier-Stokes solution shows closer agreement with the experimental data than the inviscid solution on the suction surface of the rotor suggests that the secondary and wall layer flows play an important role in determining the rotor surface temperature distributions.

The rotor surface temperature coefficient contours predicted in the three-dimensional adiabatic simulation are illustrated in Fig. 95, while the CHS1 experimental [2] contours are shown in Fig. 96. The predicted contour patterns are similar to the experimental contours, except near the pressure surface trailing edge where the numerical contours do not close as the experimental data indicates. The differences between the prediction and the experiment

coincide with those shown in Fig. 94 for the mid-span pressure surface, near the trailing edge. Both the numerical and experimental results indicate that the hot fluid spreads over the entire pressure surface of the rotor, while on the suction surface, the hot fluid is generally confined to the mid-span region by the strong endwall and secondary flows. Figure 97 shows a three-dimensional perspective of the predicted time-averaged temperature contours on the pressure surface of the rotor to give a better understanding of where the high temperature regions are located.

A series of flow field animations were created from the predicted results of the three-dimensional adiabatic simulation [30]. A sequence from the animation of the $T = 1.05T_\infty$ temperature isotherm at four instants in time during a global cycle are shown in Figs. 98 and 99. These four instants in time correspond to 0, 25, 50 and 75% of the global cycle. Figure 98 shows the isotherm from a viewing position that displays the pressure surface of the stator blades and the suction surface of the rotor blades. Figure 99 shows the isotherm from a viewing position that displays the suction surface of the stator blades and the pressure surface of the rotor blades. This sequence of pictures illustrates the migration of the hot streak through the stator passage and how it is broken into discrete spherical eddies as it interacts with the passing rotor blades. The hot fluid remains on the pressure surface of the rotor for a long period of time after it encounters the hot streak (due to the low convection speeds), eventually migrating towards the pressure surface tip, where it leaks over onto the suction surface. Figure 99 shows that the residence time of the hot streak fluid on the rotor pressure surface is large enough to allow two additional hot streaks to impact the surface before the hot gases of the initial hot streak are convected downstream. On the suction surface, the endwall secondary flow forces the hot fluid towards the mid-span region of the blade, where it is rapidly convected downstream.

6.3 Heat Transfer and Film Cooling Simulations

6.3.1 Two-Dimensional Simulations

Thermal fatigue due to combustor hot streaks can greatly reduce the life of a turbine rotor blade. One technique for alleviating the adverse effects of combustor hot streaks is to film

cool the surface of the rotor blade. Therefore, a series of two-dimensional 1-stator/1-rotor/1-hot streak simulations with film cooling and a specified heat flux have been performed. In this investigation, the number and location of the film cooling holes, the fluid injection velocity, and the level of the surface heat flux were all varied to obtain both the qualitative and quantitative characteristics of different film cooling schemes. The flow conditions used in the film cooling simulations are representative of the circular hot streak (CHS2) and are shown in Table 4.

The computational grid topology used in the two-dimensional film cooling simulations is similar to that used in previous adiabatic simulations. The stator grid was constructed with 101×31 grid points in the inner O-grid and 75×31 points in the outer H-grid. The rotor grid was constructed with 101×31 grid points in the O-grid and 71×31 points in the H-grid. The average wall value of y^+ was approximately 0.80 for stator and 0.75 for the rotor.

In the first portion of the film cooling investigation, the impact of film cooling injection hole location was studied. Since the current goal of film cooling is to alleviate the excessive temperatures and thermal gradients which are observed on the pressure surface of first stage turbine rotor blades in the presence of hot streaks, a film cooling injection hole (consisting of two adjacent streamwise computational grid points) was located at approximately 27% of the axial chord on the pressure surface of the rotor airfoil. The fluid was injected at a velocity equal to 0.2 times that of the inlet free stream velocity and at an angle of 10 degrees with respect to the local surface tangent. The temperature of the injected fluid was specified to be 520° Rankine (compared to 530° Rankine for the free stream and 636° within the hot streak) and the density ratio was chosen such that the static pressure at the injection location was equal to the time-averaged static pressure obtained in the absence of film cooling. These film cooling parameters were chosen to be representative of those used in actual turbines [60]. It is important that the injected fluid does not initiate boundary layer separation, reducing the turbine efficiency. Figure 100, which illustrates time-averaged velocity vectors in the vicinity of the film cooling injection hole, indicates that the specified film cooling conditions do not cause boundary layer separation in the time-averaged flow field.

The time-averaged pressure coefficient distributions for the surface of the rotor, with and without the influence of film cooling, are shown in Fig. 101. Also included in Fig. 101 are

the maximum and minimum pressure coefficient distributions for the film cooling simulation. The equations for the maximum and minimum pressure coefficients are obtained by replacing P_{avg} in Eq.(6.1) with P_{max} and P_{min} , respectively. As Fig. 101 illustrates, the time-averaged pressure coefficient distributions for the simulations with and without film cooling are nearly identical. The maximum and minimum pressure coefficient distributions for the two cases exhibit similar agreement, except in the vicinity of the film cooling injection hole, where the specified film cooling conditions force the local pressure to match the time-averaged pressure.

Figure 102 illustrates the time-averaged rotor surface temperature coefficient distribution for this simulation, where the temperature coefficient definition is the same as in Eq. (6.3). Equation (6.3) is similar to the definition of the film cooling *effectiveness* parameter, which is obtained if the time-averaged temperature at the rotor leading edge ($T_{avg,le}$) in Eq. (6.3) is replaced by the film cooling temperature. Also included in Fig. 102 is the temperature coefficient distribution for the two-dimensional 1-stator/1-rotor hot streak simulation without film cooling. A substantial reduction of the time-averaged temperature on the rotor pressure surface is observed in the vicinity of the film cooling hole. As the cooling fluid is convected downstream and away from the airfoil surface, the time-averaged surface temperature increases due to the influence of the hot streak. The time-averaged temperature on the suction surface of the rotor is basically unaffected by the pressure surface film cooling.

In an effort to further reduce the time-averaged temperature along the rotor pressure surface, a second film cooling hole (again modelled with two computational grid points) was added at approximately 47% axial chord on the pressure surface. Shown in Fig. 103 are the time-averaged temperature coefficient distributions from the simulation without film cooling, from the film cooling simulation using one injection hole, and from the film cooling simulation using two injection holes. The insertion of the second injection hole further reduces the time-averaged temperature along the aft portion of the rotor pressure surface, and again has little effect on the suction surface. The slope of the temperature gradient downstream of the second film cooling injection hole in Fig. 103 appears to be similar to the temperature gradient downstream of the first injection hole, suggesting that for the current injection conditions a linear relationship exists between the number of film cooling holes and the reduction of the time-averaged temperature. While the specified film cooling conditions have the desired effect of reducing the time-averaged temperature on the rotor pressure

surface, they also create a large time-averaged temperature spike immediately upstream of the first injection hole. Noting that the film cooling fluid temperature was more than 20% less than the maximum temperature of the hot streak, the temperature spike can be reduced by nominally increasing the film cooling fluid temperature and/or applying film cooling to both surfaces of the airfoil, including the leading edge region.

A different approach to reducing the time-averaged temperatures along the pressure surface of the rotor is to inject cooling fluid through the trailing edge (base) of the stator airfoil. This has the effect of introducing a *cold streak* into the flow. In the current study, cooling air was injected through a slot in the stator trailing edge (consisting of three computational grid points) in the direction of the main stream flow. The temperature of the cooling fluid was specified to 424° Rankine and the density was chosen to have the static pressure match that of the time-averaged solution without film cooling. The temperature of the cooling fluid was specified to be 20% less than the free stream temperature because the maximum temperature of the hot streak was 20% greater than the free stream temperature. The cooling fluid was injected with velocities equal to 0.50, 1.00, and 1.50 times that of the inlet free stream velocity.

Figure 104 illustrates the rotor surface time-averaged temperature coefficient distributions for these simulations, along with the temperature distribution for the case without film cooling. For the specified conditions, the use of stator base cooling has much less of an impact on the rotor surface temperatures than film cooling the rotor airfoil. For all three injection velocities the time-averaged temperature on the suction surface of the rotor is reduced, the amount of the temperature reduction increasing linearly with the injection velocity. On the rotor pressure surface, however, the time-averaged temperature *increases* for the injection velocity less than free stream, stays approximately *constant* for the injection velocity equal to the free stream, and *decreases* for the injection velocity greater than the free stream.

Additional factors must also be considered in estimating the impact of the current cold streak (base cooling) on the rotor surface time-averaged temperatures. The current model uses only three computational grid points to model the trailing edge slot. Actual trailing edge slots are somewhat larger, and the effectiveness of the current base cooling scheme can probably be improved by using more computational grid points to model a larger injection

slot. In addition, the cold streak is being injected directly into a viscous wake, while the migration of the hot streak is basically convected in the inviscid portion of the flow until it reaches the rotor airfoil. Thus, the cold streak is more likely to mix with the surrounding fluid in the wake, thus reducing its temperature deficit.

The impact of the film cooling injection velocity was also studied. Two film cooling injection holes, located at 27% and 47% axial chord on the rotor pressure surface (each modelled with two adjacent streamwise computational grid points), were used in this portion of the study. The film cooling fluid temperature and injection angle were 520° Rankine and 10 degrees with respect to the local surface tangent, respectively. The injection velocities used were 0.05, 0.10, 0.20, and 0.40 of the inlet free stream velocity.

Figure 105 illustrates the rotor surface time-averaged temperature coefficient distributions for these simulations, along with the temperature distribution for the case without film cooling. Increasing the film cooling injection velocity is seen to increase the effectiveness of the film cooling, eventually ($V/V_\infty = 0.40$) eliminating the effects of the hot streak completely. Increasing the injection velocity also reduces the thermal gradients between adjacent film cooling holes, which is very important to structural designers. While increasing the injection velocity is beneficial in terms of reducing the time-averaged temperature, there are practical limits on the mass flow rate of the injected fluid since it is usually bled from the compressor. A more efficient overall approach may be to use numerous film cooling holes with low mass flow injection, rather than a few film cooling holes with large mass flow injection.

The addition of a specified heat flux at the rotor surface and the combination of a specified heat flux and film cooling was also studied. The initial simulation in this portion of the investigation was performed with the addition of a mild negative heat flux ($\dot{q} = -0.2$), which for a simulation without a hot streak would correspond to a surface temperature approximately 5° Rankine below the free stream temperature. A second simulation was performed with the addition of both a specified heat flux and film cooling. Cooling air was injected from both the stator trailing edge and the rotor pressure surface. At the stator trailing edge, the cooling air was injected in the main stream flow direction with a velocity equal to the inlet free stream velocity. The temperature of the cooling air was 424° Rankine,

and the density was specified to yield the time-averaged static pressure in the absence of film cooling. Along the rotor pressure surface, injection holes (each modelled with two computational grid points) were positioned at 27% and 47% of the axial chord. The fluid was injected at 0.20 of the free stream velocity at an angle of 10 degrees with respect to the local surface tangent. The temperature of the cooling fluid was specified to be 520° and the density was chosen to yield the time-averaged static pressure in the absence of film cooling.

Figure 106 illustrates the rotor surface time-averaged temperature coefficient distributions for these simulations, along with the temperature distribution for the case without film cooling or a heat flux. The specified heat flux alone is seen to have only a minimal effect on rotor time-averaged temperatures, slightly reducing the pressure surface temperature. The minor changes incurred with a specified heat flux make it difficult to analyze the combined effects of heat transfer and film cooling.

Static temperature contours at one instant in time for the simulation including a specified heat flux and film cooling are presented in Fig. 107. The contours levels in Fig. 107 have been adjusted to highlight both the hot streak and the cold streak. The hot streak is characterized by the red and yellow contours, the cold streak by the blue contours, and the free stream temperature by the green contours. Figure 108 illustrates a close up of the stator trailing edge/rotor leading edge region, where the contour levels have been adjusted to highlight the rotor surface film cooling, as well as the hot streak and cold streak. The manner by which the rotor pressure surface film cooling *seals off* the hot streak from the surface is evident. Figure 109 shows time-averaged temperature contours for the rotor passage with film cooling and heat transfer. Figures 107 and 109 reveal that the cold fluid tends to migrate towards the suction side of the rotor passage, while the hot fluid migrates towards the pressure side of the passage. This phenomena, which may be due to the difference in the relative rotor passage inlet angles between the hot and cold gases, has been explained by Butler *et al.* [2] and Kerrebrock and Mikolajczak [61] and is consistent with recent experimental data obtained by Roback and Dring [54]. On the pressure surface of the rotor, the hot streak fluid is isolated from the surface by the thin layer of cooling fluid. In general, reducing the time-averaged surface temperature decreases the thermal fatigue and increases the lifetime of the blade.

A 3-stator/4-rotor/1-hot streak simulation was performed using the same heat flux as that used in the 1-stator/1-rotor simulations. This simulation was performed to determine if the application of a specified heat flux becomes more effective at alleviating the adverse effects of a hot streak as the stator-to-hot streak ratio of the numerical simulation (3 to 1) approaches that of the experiment (22 to 1). Figure 110 illustrates the time-averaged temperature coefficient distribution for this simulation, along with the results of the adiabatic 3-stator/4-rotor simulation. The specified heat flux in the current simulation appears to be slightly more effective at reducing the time-averaged surface temperature than in the 1-stator/1-rotor simulation. The specified heat flux, however, is still not as effective as film cooling at decreasing the rotor surface temperature.

A 3-stator/4-rotor/1-hot streak simulation with a specified rotor surface heat flux, stator trailing edge injection, and rotor pressure surface film cooling was performed to yield a better understanding of the interaction between the hot and cold fluids as they migrate through the turbine stage. Figure 111 illustrates static temperature contours at one instant in time for this simulation. Similar to the 1-stator/1-rotor simulation, the hot fluid migrates towards the pressure side of the rotor passage, while the cold fluid migrates towards the suction side of the passage. The hot fluid is inhibited from increasing the pressure surface temperature due to the pressure surface film cooling. In addition, the hot streak is prevented from contacting the suction surface by the stator base cooling fluid, which acts as a buffer between the hot streak and the rotor surface. The fluid injected from the base of the stator is rapidly convected off the suction surface of the rotor in a vortex-like shedding behavior. Thus, the relative ineffectiveness of the stator base cooling at reducing the rotor pressure surface temperature in the 1-stator/1-rotor simulations is a consequence of the cooling fluid migrating primarily towards the suction surface of the airfoil. This also suggests that the application of stator base cooling with a higher injection velocity or a fluid injection temperature slightly higher than the local free stream temperature, but less than that of the hot streak, may be more effective at reducing the rotor pressure surface temperature.

6.3.2 Three-Dimensional Simulations

In an effort to further understand how to alleviate the rotor pressure surface time-averaged temperature increase due to the hot streaks, a series of three-dimensional numerical simulations were performed with both a heat transfer and film cooling at the rotor surface. The computational grid topology used in the heat transfer/film cooling simulations was the same as that used in the adiabatic simulation. The flow conditions used in the film cooling and heat flux simulations are representative of the circular hot streak (CHS2) and are shown in Table 4. In the first of these simulations, a heat flux was applied to the rotor surface *without* film cooling. The heat flux was specified to yield a surface temperature approximately 5 degrees less than the local adiabatic surface temperature. The addition of a heat flux did not alter the stator and rotor time-averaged pressure distributions, but there was a noticeable effect on the unsteady pressure amplitude coefficient distributions (see Figs. 112 and 113). There is closer agreement between the predicted unsteady pressure amplitude distributions and the experimental data than was observed in the adiabatic simulation. It is unclear if the improved agreement is a result of the addition of heat transfer, or a consequence of the unsteady pressure amplitude requiring more global cycles than either the temperature or static pressure fields to become periodic.

Figure 114 illustrates the rotor surface mid-span time-averaged temperature coefficient distributions for the adiabatic simulation and the simulation with a specified rotor surface heat flux. The addition of a heat flux is seen to have little effect on the time-averaged rotor surface temperature distribution. This is expected considering the relatively small specified heat flux and the high local time-averaged surface temperatures due to the hot streak. A more negative heat flux value may reduce the influence of the hot streak on the surface temperature, but may also have adverse effects on the stability of the computational procedure. Figure 115 shows time-averaged temperature contours for the rotor surface with a specified heat flux. Comparing Figs. 95 and 115 confirms that the current heat flux does little to alleviate the high time-averaged temperatures associated with the hot streak.

In the second of the heat flux/film cooling simulations, cooling fluid was injected through holes in the rotor pressure surface at a velocity equal to 0.2 times that of the free stream velocity and at an angle of 25 degrees with respect to the local axial direction surface tangent.

The temperature of the injected fluid was specified to be 520° Rankine (2% lower than the free stream and 22% lower than the hot streak) and the density ratio was chosen such that the static pressures at the injection locations were equal to the time-averaged static pressures in the absence of film cooling. The injection holes were located at 20% and 40% of the axial chord and extended from 20% of the span to 80% of the span, at approximately 5% spanwise intervals. Similar to the two-dimensional simulations, two-adjacent grid points were used to model an injection hole. A total of 22 injection holes were used in the first portion of the simulation. The surface heat flux was again specified to yield a surface temperature approximately 5 degrees less than the local adiabatic surface temperature. Figure 116, which illustrates time-averaged velocity vectors in the vicinity of a film cooling injection hole near mid-span, indicates that the specified film cooling conditions do not cause boundary layer separation in the time-averaged flow field.

Figure 117 shows the predicted time-averaged, minimum, and maximum pressure coefficient distributions, along with the experimental data [43], for the rotor at the 25, 50, and 75% span locations. The effects of film cooling on the unsteady pressure envelope of the rotor are most evident at the 50% and the 75% span locations. Figure 118 and 119 illustrate the predicted unsteady pressure amplitude coefficient distributions for the stator and the rotor, respectively, along with the experimental data [43]. The predicted results exhibit good agreement with the experimental data, except near the film cooling holes, where the value of the pressure is constant in time.

Figure 120 illustrates the rotor surface mid-span time-averaged temperature coefficient distributions for the adiabatic simulation, the simulation with a rotor surface heat flux only, and the simulation with two film cooling rows and a surface heat flux. A substantial reduction of the time-averaged temperature on the rotor pressure surface is observed in the vicinity of the film cooling injection holes. As the cooling fluid convects downstream and away from the airfoil surface, the time-averaged surface temperature increases due to the influence of the hot streak. In this three-dimensional simulation, the time-averaged surface temperature in the region between film cooling injection holes and downstream of the last film cooling hole increases much more rapidly than in the two-dimensional simulations. This may be partially due to the interaction between the secondary and wall layer flows in the rotor passage, which cause the cooler injected fluid to mix very rapidly with the hot streak fluid. Another cause

of the temperature increase may be that the current injection angle (25 degrees) is greater than that used in the two-dimensional simulations (10 degrees). While it appears to be beneficial to reduce the injection angle, structural and manufacturing considerations limit the actual range of possible injection angles. The current injection angle was chosen to be commensurate with those found in actual gas turbines. In spite of placing film cooling injection holes at 20% and 40% axial chord locations, the rapid mixing between the cooling fluid and the hot streak causes an increase in the temperature of the pressure surface near the trailing edge region. The time-averaged temperature on the rotor suction surface is unaffected, since the film cooling holes were placed only on the pressure surface.

Figure 121 shows the time-averaged temperature contours for the surface of the rotor with 2 rows of film cooling holes and heat transfer. The film cooling locations are characterized by the dark blue (low temperature) contours. While discrete film cooling jets can be seen inboard of approximately 35% span and outboard of about 65% span, the cooling fluid near mid-span appears to be contained within one continuous jet. As noted above, the film cooling injection holes were located at approximately 5% span increments. In the mid-span region, the computational grid lines were also spaced approximately 5% of the span apart, resulting in 6 film cooling holes being placed at six consecutive grid points. Figure 122, which illustrates a three-dimensional perspective of the time-averaged temperature contours on the pressure surface of the rotor, shows that the combination of cooling fluid injection angle and secondary/boundary layer flow causes rapid mixing of the cooling fluid and allows the hot streak to increase the rotor pressure surface temperature aft of mid-chord region.

In an effort to eliminate the high time-averaged temperatures aft of mid-chord, a third row of film cooling holes was added at approximately 60% axial chord. Thus, in this simulation a total of 33 film cooling holes (each consisting of two adjacent grid points) were used. In addition, the injection velocity was increased to 0.4 times that of the free stream velocity. The heat flux was held at the same value as in the previous three-dimensional film cooling simulation. Figure 123, which illustrates time-averaged velocity vectors in the vicinity of a film cooling injection hole near mid-span, indicates that the specified film cooling conditions do not cause boundary layer separation in the time-averaged flow field.

Figure 124 shows the predicted time-averaged, minimum, and maximum pressure coef-

ficient distributions, along with the experimental data [43], for the rotor at the 25, 50, and 75% span locations. Again, the effects of film cooling on the unsteady pressure envelope of the rotor are most evident at the 50% and the 75% span locations. Figure 125 and 126 illustrate the predicted unsteady pressure amplitude coefficient distributions for the stator and the rotor surfaces, respectively, along with the experimental data [43]. The predicted results exhibit good agreement with the experimental data, except near the film cooling holes, where the value of the pressure is constant in time.

Figure 127 illustrates the rotor surface mid-span time-averaged temperature coefficient distributions for the adiabatic simulation, the simulation with a rotor surface heat flux only, and the simulation with three film cooling rows and a surface heat flux. In this simulation, the combination of a greater injection velocity and a third row of film cooling injection holes has eliminated most of the high temperature regions on the rotor pressure surface. The high temperature region aft of mid-chord has been reduced, as have the high temperature regions between the film cooling injection holes. A small spike in the time-averaged temperature distribution is noticeable just upstream of the first row of film cooling holes, and just downstream of the first and second rows of film cooling holes. These spikes may be due to the sudden change from a no-slip to a transpiration boundary condition, resulting in sudden changes in the density and velocity. One possible technique for avoiding these spikes is to gradually increase and decrease the film cooling parameters of adjacent computational nodes (i.e. inject the cooling fluid at different rates through different film cooling holes).

Figure 128 shows time-averaged temperature contours for the surface of the rotor with 3 rows of film cooling holes and heat transfer. The film cooling locations are again characterized by the dark blue (low temperature) contours. Comparing Figs. 127 and 128 shows that increasing the injection velocity extends the range of effectiveness of the cooling fluid. Figure 128 also illustrates that the addition of a third row of film cooling holes has significantly decreased the time-averaged rotor pressure surface temperature aft of the mid-chord point. Figure 129, which illustrates a three-dimensional perspective of the time-averaged temperature contours on the pressure surface of the rotor, suggests that a fourth row of film cooling holes placed at approximately 5% axial chord would probably eliminate the lingering remnants of the hot streak in the leading edge region.

Chapter 7

Scientific Visualization Results

A video tape has been created showing the animated results of the following computer simulations:

- 2-D Adiabatic Hot Streak Migration
- 3-D Adiabatic Hot Streak Migration
- 2-D Hot Streak Migration with Film Cooling
- 3-D Hot Streak Migration with Film Cooling

Details of each of the animations are in the following subsections. Copies of the videotape can be obtained from

Defense Logistics Agency
Defense Technical Information Center
Building No. 5, Cameron Station
Alexandria, Virginia 22304-6145
(NAVAIR video AD-M200038)

7.1 2-D Adiabatic Hot Streak Simulation

An animation containing the predicted results of the two-dimensional 3-stator/4-rotor/1-hot streak simulation with an inlet hot streak temperature 20 percent greater than the free stream temperature has been created. In each of the animated sequences, a rainbow color map (blue, green, yellow, red) was used to display color contour surfaces of a scalar quantity, where the lowest scalar value is indicated by a blue color and the highest scalar value is indicated by a red color. In the video, a complete cycle of the hot streak simulation consists of 50 separate time segments (where a time segment is a snapshot of the flow field at a particular instant in time). The 50 time segments were determined from the 3000 time steps per cycle used in the numerical simulation. After carefully reviewing the results from the two-dimensional numerical hot streak simulation, the following flow features were chosen for animation:

- Static temperature
- Static pressure
- Perturbation pressure

Figure 130 shows the temperature field at four instants in time during the animated cycle. The four instants in time correspond to 25, 50, 75 and 100% of a global cycle, where a global cycle is equal to a rotor blade moving through an angle of $2\pi/N$, where N is the number of stator blades. The surface temperature of a rotor airfoil (the shaded airfoil in the figure) is also presented in the form of line plots. Line plots of the surface temperature were included so that the video would yield both qualitative and quantitative information about the numerical simulation. The video illustrates the hot streak migrating through the stator passage and being distorted by the passing rotor blades.

Figure 131 shows the static pressure field at the four instants in time during the animated cycle. The skin friction distribution of a rotor airfoil (the shaded airfoil in the figure) is also shown in the form of line plots. From Figs. 130 and 131, it is apparent that the temperature field is approximately independent of the pressure field. However, the interaction effects between the rotor and stator are present in the animation of the pressure field.

Since static pressure exhibits only slight variations during the cycle, it was decided to animate the perturbation pressure field. The pressure perturbation is defined as

$$\tilde{p} = p - p_{avg} \quad (7.1)$$

where \tilde{p} is the perturbation pressure, p is the local instantaneous static pressure, and p_{avg} is the local time-averaged static pressure. Figure 132 shows the perturbation static pressure field at the four instants in time during the cycle. The displacement thickness and pressure coefficient C_p (see Eq.(5.1)) distribution on a rotor airfoil (the shaded airfoil in the figure) are also illustrated in the form of line plots. The perturbation pressure is discontinuous between the stator and rotor blade rows because the time-averaged pressure, p_{avg} , in Eq.(7.1) is frame-dependent. The pressure waves, created by the interaction of the stationary stator row and the moving rotor row, can be seen propagating between the rotor and stator rows and through the rotor passages. The zonal boundary between the inner and outer grids of the rotor can be detected in this visualization (see Fig. 133), indicating possible deficiencies in the zonal boundary conditions.

7.2 3-D Adiabatic Hot Streak Simulation

A video tape showing the results of an adiabatic three-dimensional 1-stator/1-rotor/1-hot streak simulation with an inlet hot streak temperature which is 20 percent greater than the free stream temperature has been created.

For this animation, a complete cycle of the hot streak simulation consists of 40 separate time segments. The computational solution is shown from the fifth cycle of the computation, unless otherwise specified. The 40 time segments were determined from the 2000 time steps per cycle used in the numerical simulation. After reviewing the results of the three-dimensional numerical hot streak simulation, the following features were chosen for animation:

- Surface static pressure
- Surface static temperature

- Temperature isotherms

The surface static pressure at four instants in time during the animated cycle is shown in Figs. 134 and 135. The four instants in time correspond to 0., 37.5, 75, and 100% of a global cycle. Figure 134 shows static pressure contours from a viewing position that displays the suction surface of the rotor blades and the pressure surface of the stator blades, while Fig. 135 illustrates the static pressure contours on the pressure surface of the rotor blades and the suction surface of the stator blades. Line plots of the static pressure along the surface of the rotor blade at the 25%, 50% and 75% spanwise locations are also shown in these two figures. From the animated sequence of static pressure contours, it appears that the pressure field is time-periodic.

The surface static temperature at four instants in time during the animated cycle is shown in Figs. 136 and 137. The four instances in time correspond to 0., 37.5, 75 and 100% of a global cycle. The viewing positions in Figs. 136 and 137 are the same as those in Figs 134 and 135, respectively. Line plots of the static temperature along the surface of the rotor blade at 25%, 50% and 75% spanwise locations are also included in these two figures. The line plots of the surface static temperature were included so that the animated sequence would yield both qualitative and quantitative information about the numerical simulation. This animated sequence shows that, unlike the pressure field, the temperature field is not yet periodic in time. Specifically, there is a difference in the rotor surface static temperature (notably on the pressure surface, see Fig. 137) at the first and last time segments in the cycle. Although this cycle of the temperature field is not yet time-periodic, the visualization from this cycle does show qualitative trends. As a results of this video sequence, additional cycles were run in the numerical simulation and a time-periodic temperature field was obtained.

The temperature field off the surface was also examined in turns of isotherms. An animation of the $T = 1.05T_{\infty}$ isotherm during this cycle was created. Four segments from this animation are shown in Figs. 138 and 139. The viewing positions in Figs. 138 and 139 are the same as those in Figs 134 and 135, respectively. This animated sequence also suggests that the static temperature field is not yet time-periodic. The video sequence illustrates how the hot streak migrates from the stator passage to the rotor passage, where the isotherm is sliced, distorted and broken up by the passing rotor blades.

Two additional computational cycles were performed to achieve a time-periodic static temperature field. New animations were created for the time-periodic solution which consisted of 80 separate time segments. The 80 time segments were determined from the 2000 time steps per cycle used in the computational simulation. It was decided to animate the following flow features:

- Temperature isotherms
- Surface static temperature

The first animated sequence in the video shows the $T = 1.05T_\infty$ isotherm for one cycle of the rotor motion. Visualization of a single isotherm is used to highlight the path of the hot streak as it migrates through the turbine stage. This animation further illustrates how the hot streak migrates through the stator passage into the rotor passage, where it is broken up into discrete temperature eddies by the passing rotor blades.

The next animation in the video shows the surface static temperature. This sequence shows that the hot fluid remains on the pressure surface of the rotor for a long period after it encounters the hot streak, eventually migrating towards the tip of the blade where it washes over to the suction surface.

7.3 2-D Hot Streak Simulation with Film Cooling

Video animations showing the results of the two-dimensional 3-stator/4-rotor/1-hot streak simulation with film cooling and a specified heat flux have also been created. In this video, a complete cycle of the hot streak simulation consists of 80 separate time segments (where a time segment is a snapshot of the flow field at a particular instant in time). The 80 time segments were determined from the 3000 time steps per cycle used in the numerical simulation.

Figure 140 shows the static temperature field at four instants in time during the animated cycle. The four instants in time correspond to 25, 50, 75 and 100% of a global cycle. The surface static temperature of a rotor airfoil (the shaded airfoil in the figure) is also included in the form of line plots. The video illustrates the migration of the cooling fluid which is

injected from both the trailing edge of the stator blades and the pressure surface of the rotor blades.

7.4 3-D Hot Streak Simulation with Film Cooling

Animations showing the results of a three-dimensional 1-stator/1-rotor/1-hot streak simulation with film cooling and a specified heat flux have been created.

In this video, a complete cycle of the simulation consists of 80 separate time segments. The computational solution is shown from the tenth cycle of the computation unless otherwise specified. The 80 time segments were determined from the 2000 time steps per cycle used in the numerical simulation. After reviewing the results of the three-dimensional numerical hot streak simulations which included film cooling and a specified heat flux, it was decided to animate the following:

- Surface static temperature
- Temperature isotherms

The surface static temperature at four instants in time during the animated cycle is shown in Figs. 141 and 142. The four instants in time correspond to 25, 50, 75 and 100% of a global cycle. The viewing positions in Figs. 141 and 142 are the same as those in Figs 134 and 135, respectively. The surface temperature of a rotor blade at 25%, 50% and 75% spanwise locations is also displayed as line plots in these two figures. This video sequence suggests that the simulation is not quite time-periodic in terms of the film cooling patterns on the rotor pressure surface. Additional computing cycles were performed a completely time-periodic temperature field was attained.

The temperature field off the surface was also examined in terms of isotherms. An animation of the $T = 0.99T_\infty$ and the $T = 1.05T_\infty$ isotherms were created for this cycle of motion. In the animation, the $T = 1.05T_\infty$ isotherm is represented as a red surface, and the $T = 0.99T_\infty$ isotherm is represented as a blue surface. The $T = 0.99T_\infty$ isotherm was used to represent the boundary of the film cooling region on the rotor surface. The $T = 0.99T_\infty$ isotherm was calculated only on the pressure side of the rotor using information from the

inner O-grid. The isotherm was confined to this region because the temperature of the film cooling fluid was very close to the free stream temperature. Four time segments of this animation are shown in Fig. 143. Figure 143 shows the isotherms from a viewing position that displays the pressure surface of the rotor blades and the suction surface of the stator blades. This figure illustrates the interaction between the two isotherms as the hot streak migrates through the rotor passage and encounters the cooling fluid. Thus, the visualization shows both qualitative and quantitative trends on how hot streaks and film cooling effect the temperature of turbine rotor blades.

Chapter 8

Conclusions

This document has presented the results of a computational study in which the primary focus was to develop a Numerical Rotating Rig for enhancing the understanding of complex three-dimensional flows in axial turbomachinery. The primary components of the Numerical Rotating Rig developed in this study consist of a three-dimensional unsteady Navier-Stokes analysis and a scientific graphical visualization system. The Numerical Rotating Rig was extensively validated and then used to perform numerical experiments to determine the effects of hot streak migration and film cooling on the heat transfer in a turbine stage.

To gain insight into the influence of hot streak migration, secondary flow, heat transfer, and film cooling on the surface temperature distribution of a first stage rotor, numerical simulations of hot streak migration through a turbine stage have been performed. The main goals of these simulations have been to 1) understand the physical mechanisms which control the migration of hot streaks through a turbine stage and lead to "hot spots" on the rotor pressure surface, 2) demonstrate that numerical simulations can be used to predict when rotor surface heating will exceed allowable structural limits, 3) eliminate the adverse effects of hot streaks using heat transfer and film cooling, and 4) use advanced scientific visualization techniques to identify the pertinent aerodynamic and thermodynamic features of the flow fields.

A set of rigorous validation cases were performed to assess the ability of the Navier-Stokes procedure to accurately predict aerodynamic performance, boundary layer, and heat transfer quantities. The predicted results were compared with results of another Navier-Stokes

procedure, results of a boundary layer analysis, and experimental data. The current Navier-Stokes procedure provided accurate results for all the validation cases, provided adequate grid computational grid density was used.

Several two- and three-dimensional hot streak migration simulations with a hot streak temperature 20 percent greater than the free stream temperature have been performed and the predicted results compared with experimental data. The predicted results from the two-dimensional adiabatic simulations indicate that blade count ratio has little effect on predicted time-averaged surface pressure and temperature distributions, but a substantial effect on the unsteady flow characteristics. It was demonstrated that two-dimensional simulations can be used to provide reliable warnings as to when and where rotor surface temperatures exceed allowable limits. Results of the three-dimensional adiabatic hot streak simulation confirm the experimental observations that high temperature hot streak fluid accumulates on the pressure surface of the rotor blades, resulting in a high time-averaged surface temperature "hot spot". The influence of secondary flows on the predicted three-dimensional migration pattern of the hot streak has been shown to be consistent with experimental data. In addition, it was determined that the time-averaged rotor pressure surface temperature is a function of several inter-related variables, all of which control the "residence time" of the hot streak in the vicinity of the rotor pressure surface. Much more research is necessary to develop a non-dimensional parameter which adequately describes the complex interaction between hot streaks and a three-dimensional viscous flow field.

Results of numerous two- and three-dimensional hot streak simulations indicate that the addition of a rotor surface heat flux is an ineffective means of reducing the high time-averaged temperatures on the pressure surface of the rotor. The addition of film cooling holes on the rotor pressure surface, however, was found to be highly effective in eliminating the adverse effects of the hot streak on the rotor surface. The cooling hole location, fluid injection angle, and fluid injection velocity were all varied to determine a reasonable and practical film cooling scheme.

Animated sequences have been created showing the temperature and pressure fields for rotor/stator interacting flows. The effects of hot streaks migration, with and without film cooling and a heat transfer flux, have been displayed using scientific visualization techniques.

In this video, the temperature field was displayed as contours on the airfoil surfaces and isotherms away from the surfaces. For each of the cases examined in this investigation, the animations were used to verify the time periodicity of both the pressure and temperature fields. The numerical simulations, coupled with the animations, have given new insights into the physics of the rotor/stator interaction and the effect of hot streak migration and heat transfer.

The successful demonstration of three-dimensional 1-stator/1-rotor/1-hot streak numerical simulations, with and without the effects of film cooling, warrants the application of this technology to the design environment. Using a three-dimensional Numerical Rotating Rig, advanced turbine blade designs could be optimized by reducing secondary flows and surface heat transfer through re-contouring of the three-dimensional blade shape and refinement of film cooling schemes. In the future, visualization research should be focused on developing data compression techniques and automated feature detection procedures which locate critical physical phenomena using the smallest possible data set. In addition, research is needed to develop and apply advanced user-interfaces, such as virtual reality, which will help engineers more efficiently analyze large scientific data sets.

Bibliography

- [1] Rai, M. M., "Three-Dimensional Navier-Stokes Simulations of Turbine Rotor-Stator Interaction," *AIAA Journal of Propulsion and Power*, Vol. 5, May-June, 1989 pp. 307-319.
- [2] Butler, T. L., Sharma, O. P., Joslyn, H. D., and Dring, R. P., "Redistribution of an Inlet Temperature Distortion in an Axial Flow Turbine Stage," *AIAA Journal of Propulsion and Power*, Vol. 5, January-February, 1989, pp. 64-71.
- [3] Rai, M. M. and Dring, R. P., "Navier-Stokes Analyses of the Redistribution of Inlet Temperature Distortions in a Turbine," *AIAA Journal of Propulsion and Power*, Vol. 6, May-June 1990, pp. 276-282.
- [4] Rai, M. M. and Madavan, N. K., "Multi-Airfoil Navier-Stokes Simulations of Turbine Rotor-Stator Interaction," AIAA Paper 88-0361, 1988.
- [5] Baldwin, B. S. and Lomax, H., "Thin-Layer Approximation and Algebraic Model for Separated Turbulent Flows," AIAA Paper 78-257, January, 1978.
- [6] Pulliam, T. H. and Steger, J. K., "Recent Improvements in Efficiency, Accuracy, and Convergence for Implicit Approximate Factorization Algorithms," AIAA Paper 85-0360, 1985.
- [7] Beam, R. M. and Warming, R. F., "An Implicit Factored Scheme for the Compressible Navier-Stokes Equations," AIAA Paper 77-645, 1977.
- [8] Rai, M. M., "Navier-Stokes Simulations of Rotor/Stator Interaction Using Patched and Overlaid Grids," *AIAA Journal of Propulsion and Power*, Vol. 3, No. 5, September-October 1987, pp. 387-396.

- [9] Dorney, D. J., Davis, R. L., Edwards, D. E. and Madavan, N. K., "Unsteady Analysis of Hot Streak Migration in a Turbine Stage," AIAA Paper 90-2354, July 1990, also to appear in the AIAA *Journal of Propulsion and Power*.
- [10] Dorney, D. J. and Davis, R. L., "Centrifugal Compressor Impeller Aerodynamics (A Numerical Investigation)," ASME Paper 90-GT-213, June 1990.
- [11] Roe, P. L., "Approximate Riemann Solvers, Parameter Vectors, and Difference Schemes," *Journal of Computational Physics*, Vol. 43, 1981, pp. 357-372.
- [12] Chakravarthy, S. R. and Osher, S., "A New Class of High Accuracy TVD Schemes for Hyperbolic Conservation Laws," AIAA Paper 85-0363, 1985.
- [13] Yee, H. C., Warming, R. F., and Harten, A., "Implicit Total Variation Diminishing (TVD) Schemes for Steady-State Calculations," *Journal of Computational Physics*, Vol. 57, No. 3, 1985, pp. 327-360.
- [14] Osher, S., "Numerical Solution of Singular Perturbation Problems and Hyperbolic Systems of Conservation Laws," *North Holland Mathematical Studies No. 47*, 1981, pp. 179-205.
- [15] Chakravarthy, S. and Osher, S., "Numerical Experiments with the Osher Upwind Scheme for the Euler Equations," AIAA Paper 82-0975, 1982.
- [16] Chakravarthy, S. and Osher, S., "High Resolution Applications of the Osher Upwind Scheme for the Euler Equations," AIAA Paper 83-1943.
- [17] Rai, M. M. and Chakravarthy, S., "An Implicit Form for the Osher Upwind Scheme," AIAA Paper 84-0088, January, 1984.
- [18] Dhawan, S. and Narasimha, R., "Some Properties of Boundary Flow During Transition from Laminar to Turbulent Motion," *Journal of Fluid Mechanics*, Vol. 3, 1958 pp.418-436.
- [19] Hung, C. M. and Buning, P. G., "Simulation of Blunt-Fin Induced Shock Wave and Turbulent Boundary Layer Interaction," AIAA Paper 84-0457, January, 1984.

- [20] Hung, C. M. and MacCormack, R. W., "Numerical Solution of Three-Dimensional Wave and Turbulent Boundary Layer Interaction," AIAA Paper 78-161, January, 1978.
- [21] Vatsa, V. N. and Wedan, B. W., "Navier-Stokes Solutions for Transonic Flow Over a Wing Mounted in a Wind Tunnel," AIAA Paper 88-0102, January, 1988.
- [22] Hill, P. G. and Peterson, C. R., *Mechanics and Thermodynamics of Propulsion*, Addison-Wesley Publishing, Reading, MA, 1970.
- [23] Rai, M. M., "An Implicit, Conservative, Zonal-Boundary Scheme for Euler Equation Calculations," AIAA Paper 85-0488, 1985.
- [24] Sorenson, R. L., "A Computer Program to Generate Two-Dimensional Grids about Airfoils and Other Shapes by the Use of Poisson's Equation," NASA TM-81198, May, 1980.
- [25] McCormick, B.H., DeFanti, T.A., and Brown, M.D., "Visualization in Scientific Computing," NSF workshop on Graphics, Image Processing, and Workstations, July, 1987.
- [26] Buning, P. G. and Steger, J. L., "Graphics and Flow Visualization in Computational Fluid Dynamics," AIAA Paper 85-1507, 1985.
- [27] Plessel, T., *SURF Users Manual*, NASA Ames Research Center, Code RFW, 1988.
- [28] Rogers, S., "Distributed Interactive Graphics Applications in Computational Fluid Dynamics," *International Journal of Supercomputing Applications*, Vol. 1, No. 4, Winter 1987.
- [29] Plessel, T., *GAS Users Manual*, NASA Ames Research Center, Code RFW, 1988.
- [30] Edwards, D. E., "Three-Dimensional Visualization of Fluid Dynamics Problems," AIAA Paper 89-0136, 1989.
- [31] Edwards, D. E., "Application of Scientific Visualization to Fluid Dynamics Problems," AIAA paper 88-3351, 1988.

- [32] Haber, R.B., "Visualization in Engineering Mechanics: Techniques, Systems and Issues," Presented at Visualization Techniques in the Physical Sciences, SIGGRAPH, 1988.
- [33] Upson, C., et al., "The Application Visualization System (AVS): A Computational Environment for Scientific Visualization," *IEEE Computer and Graphics Applications*, July, 1989.
- [34] Bancroft, G. V., et al., "FAST: A Multi-Processed Environment for Visualization of Computational Fluid Dynamics," *Proceedings of IEEE Visualization 90*, 1990.
- [35] Giles, M. and Haimes, R., "Advanced Interaction Visualization for CFD," *Computing Systems in Engineering*, Vol. 1, No. 1, pp. 51-62, 1990.
- [36] Miller, S. L., and D. E. Edwards, "VISA: An Interactive Graphics System for Scientific Visualization," AIAA Paper 91-0795, 1991.
- [37] Jones, Oliver, *Introduction to the X Window System*, Prentice-Hall, 1989.
- [38] Nye, Adrian and O'Reilly, Tim, *X Toolkit Intrinsics Programming Manual*, O'Reilly & Associates, 1990.
- [39] Lorenson, W. E., and Cline, H. E., "Marching Cubes in a High Resolution 3D Surface Construction Algorithm", *ACM Computer Graphics*, Vol. 21, No. 4, pp. 163-169, July, 1987.
- [40] Hultquist, J., "Interactive Numerical Flow Visualization Using Stream Surfaces", NASA RNR-90-009, April, 1990.
- [41] Intelligent Light, "Intelligent Light Users Manual, Volume I — Modeling", 1987.
- [42] Dannenhoffer, J. F., Haimes, R., and Giles, M. B., "Data Compression Through the User of grid Adaptation Techniques", Presented at AIAA 17th Computational Fluid Dynamics Conference, Honolulu, Hawaii, July, 1991.
- [43] Dring, R. P., Joslyn, H. D., Hardin, L. W., and Wagner, J. H., "Turbine Rotor-Stator Interaction," *ASME Journal of Engineering for Power*, Vol. 104, October, 1982, pp. 729-742.

- [44] Joslyn, H. D. and Dring, R. P., "Three Dimensional Flow and Temperature Profile Attenuation in an Axial Flow Turbine," UTRC Report R89-957334-1, March, 1989.
- [45] Carter, J. E., "Inverse Boundary Layer Theory and Comparison with Experiment," NASA TP-1208, September, 1978.
- [46] Davis, R. L., Hobbs, D. E., and Weingold, H. D., "Prediction of Compressor Cascade Performance Using a Navier-Stokes Technique", *ASME Journal of Turbomachinery*, Vol. 110, No. 4, October, 1988, pp. 520-531.
- [47] Stewart, W. L., "Analysis of Two-Dimensional Compressible-Flow Loss Characteristics Downstream of Turbomachine Blade Rows in Terms of Basic Boundary-Layer Characteristics", NACA TN-3515, July, 1955.
- [48] Sharma, O. P., Kopper, F. C., Knudsen, L. K., and Yustinich, J. B., "Energy Efficient Engine Low-Pressure Turbine Subsonic Cascade Component Development and Integration Program", NASA CR-165592, January, 1982.
- [49] Langston, L. S., Nice, M. L., and Hooper, R. M., "Three-Dimensional Flow Within a Turbine Cascade Passage," *ASME Journal of Engineering for Power*, Vol. 99, 1977, pp. 21-28.
- [50] Graziani, R. A., Blair, M. F., Taylor, J. R., and Mayle, R. E., "An Experimental Study of Endwall and Airfoil Surface Heat Transfer in a Large Scale Turbine Blade Cascade," *ASME Journal of Engineering for Power*, Vol. 102, No. 2, April, 1980, pp. 257-267.
- [51] Hah, C., "Numerical Study of Three-Dimensional Flow and Heat Transfer Near the Endwall of a Turbine Blade Row," AIAA Paper 89-1689, June, 1989.
- [52] Hah, C., "A Navier-Stokes Analysis of Three-Dimensional Turbulent Flows Inside Turbine Blade Rows at Design and Off-Design Conditions," *ASME Journal of Engineering for Gas Turbines and Power*, Vol. 106, April, 1984, pp. 421-429.
- [53] Gundy-Burlet, K. L., Rai, M. M., Stauter, R. C., and Dring, R. P., "Temporally and Spatially Resolved Flow in a Two-Stage Axial Compressor, Part2 - Computational Assessment," NASA TM-102273, 1990.

- [54] Roback, R., Private Communication, United Technologies Research Center, April, 1991.
- [55] Sharma, O. P., Pickett, G. F., and Ni, R., H., "Assessment of Unsteady Flows in Turbomachines," ASME Paper 90-GT-150.
- [56] Dorney, D. J., Davis, R. L., and Sharma, O. P., "Two-Dimensional Inlet Temperature Profile Attenuation in a Turbine Stage," ASME Paper 91-GT-406.
- [57] Madavan, N. K., Rai, M. M., and Gavali, S., "Grid Refinement Studies of Turbine Rotor-Stator Interaction," AIAA Paper 89-0325, 1989.
- [58] Krouthen, B., and Giles, M., "Numerical Investigation of Hot Streaks in Turbines," AIAA Paper 88-3015, July, 1988.
- [59] Takahashi, R. and Ni, R. H., "Unsteady Euler Analysis of the Redistribution of an Inlet Temperature Distortion in a Turbine," AIAA Paper 90-2262, 1990.
- [60] Dring, R. P., Blair, M. F. and Joslyn, H. D., "An Investigation of Film Cooling on a Turbine Rotor Blade," ASME *Journal of Engineering for Power*, Vol. 102, No. 1, January, 1980, pp. 81-87.
- [61] Kerrebrock, J. L., and Mikolajczak, A. A., "Intra-Stator Transport of Rotor Wakes and Its Effect on Compressor Performance," ASME *Journal of Engineering for Power*, Vol. 92, Oct. 1970, pp. 359-369.

ϕ	Difference Scheme
-1	Second order fully upwind
0	Second order Fromm's
1/3	Third order upwind biased
1/2	Second order low truncation error
1	Second order central

Table 1: Discretizations for various values of ϕ

Case	Grid Density stream \times tang \times span	Δy_{blade} (y^+)	$\Delta y_{endwall}$ (y^+)	Profile $\Delta P_i/P_{t1}$	Total $\Delta P_i/P_{t1}$	Profile β_2	Total β_2	Trns
1	H-70 \times 31 \times 25	0.00100	0.00300	0.20846	0.19065	27.96	27.34	yes
	O-101 \times 31 \times 25	(4.260)	(7.430)					
2	H-70 \times 31 \times 25	0.00010	0.00100	0.16102	0.18373	27.49	27.36	no
	O-101 \times 31 \times 25	(0.384)	(2.920)					
3	H-70 \times 31 \times 25	0.00010	0.00100	0.16100	0.18372	27.49	27.58	yes
	O-101 \times 31 \times 25	(0.379)	(2.781)					
4	H-70 \times 31 \times 51	0.00010	0.00010	0.14575	0.17271	27.67	27.38	yes
	O-101 \times 31 \times 51	(0.360)	(0.266)					
5	H-70 \times 31 \times 71	0.00010	0.00010	0.13898	0.17075	27.73	27.26	yes
	O-101 \times 31 \times 71	(0.351)	(0.266)					
6	H-70 \times 31 \times 91	0.00010	0.00010	0.13051	0.17064	27.75	27.25	yes
	O-101 \times 31 \times 91							
2-D	O-131 \times 61	0.00002	—	0.12030	—	26.58		yes
	H-71 \times 21	(0.059)	—					
EXPT	—	—	—	0.13000	0.17437	26.80	26.32	—

Table 2: Grid refinement study for Langston cascade

Flow coefficient, ϕ	0.68
Inlet Mach number, M_1	0.07
Rotor rotation speed, Ω	470 RPM
Reynolds number, Re	$3.937 \times 10^6/\text{meter}$
Axial gap, g	65%
Free stream temperature, T_1	530° Rankine
Hot streak temperature, T_{hs}	1060° Rankine

Table 3: Flow conditions for the CHS1 experiment

Flow coefficient, ϕ	0.78
Inlet Mach number, M_1	0.07
Rotor rotation speed, Ω	410 RPM
Reynolds number, Re	$3.937 \times 10^6/\text{meter}$
Axial gap, g	65%
Free stream temperature, T_1	530° Rankine
Hot streak temperature, T_{hs}	636° Rankine

Table 4: Flow conditions for the CHS2 experiment

Flow coefficient, ϕ	0.35
Inlet Mach number, M_1	0.051
Rotor rotation speed, Ω	710 RPM
Reynolds number, Re	$3.937 \times 10^6/\text{meter}$
Axial gap, g	65%
Free stream temperature, T_1	530° Rankine
Hot streak temperature, T_{hs}	1060° Rankine

Table 5: Flow conditions for the PHS experiment

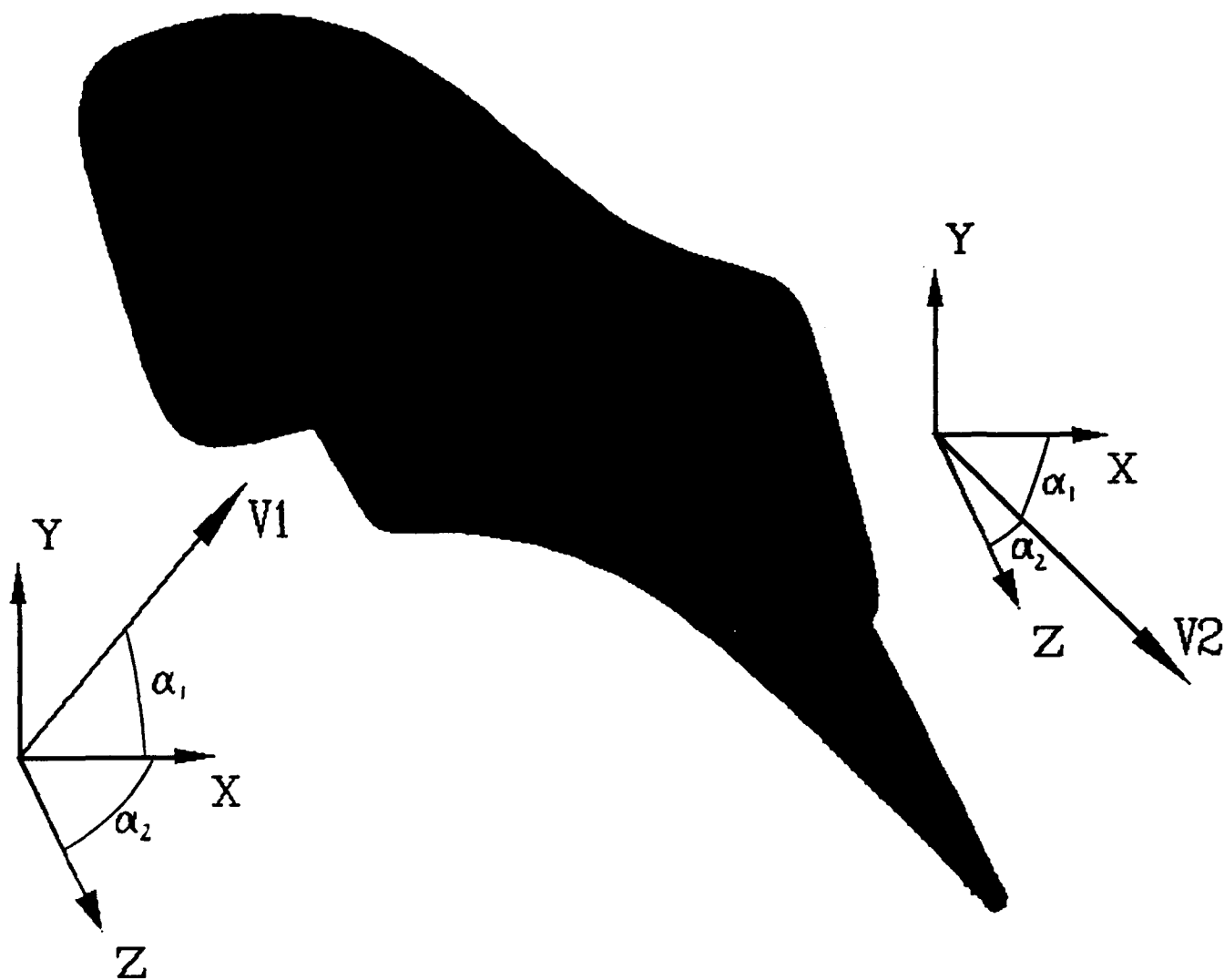


Figure 1: Angle definitions for film cooling applications

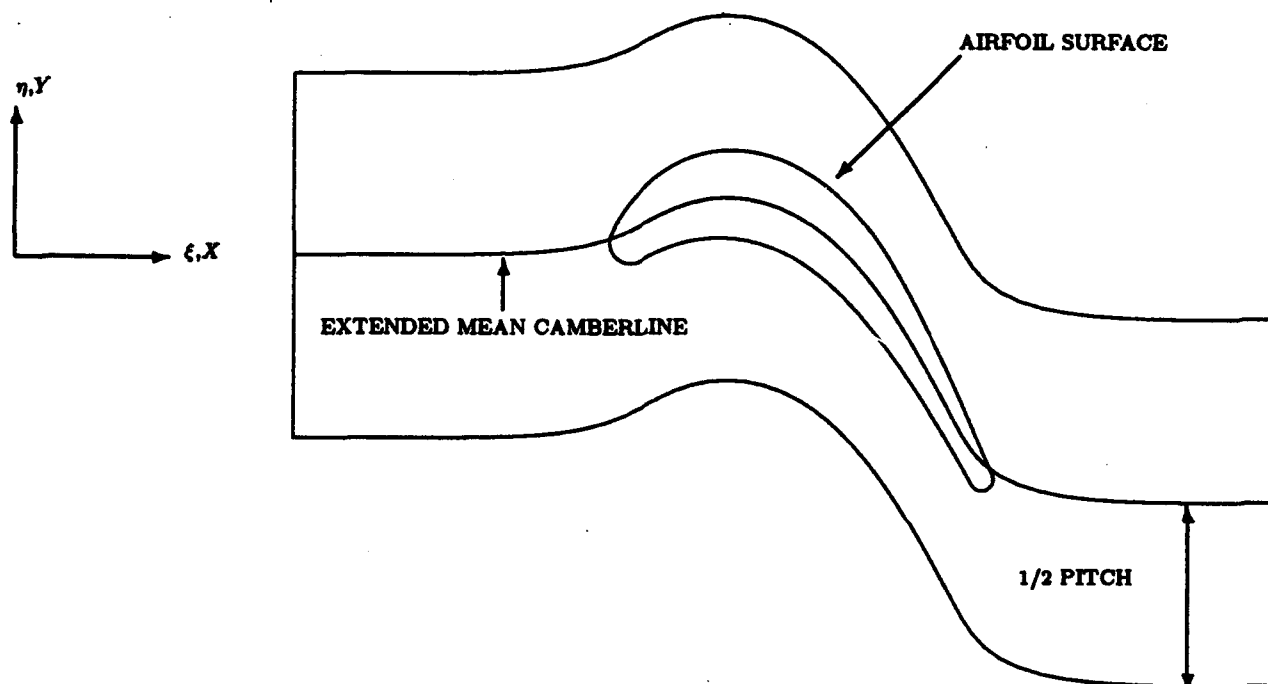


Figure 2: H-grid development

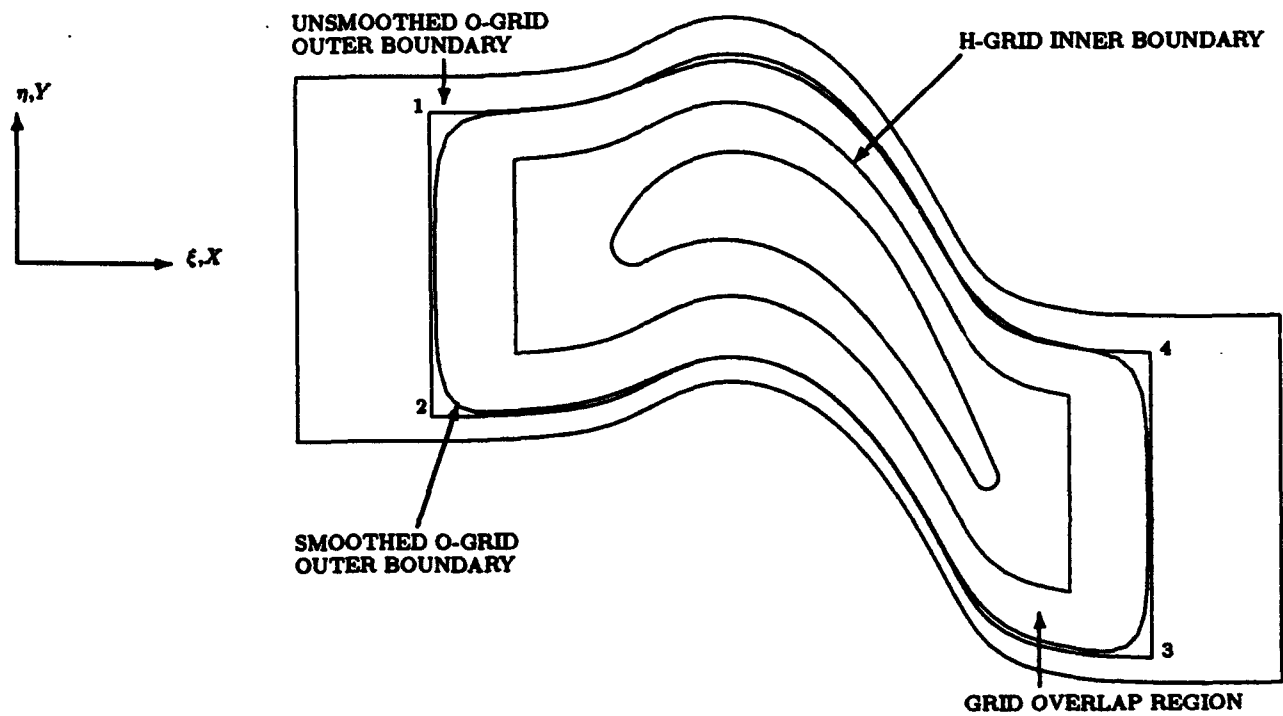


Figure 3: O-grid development

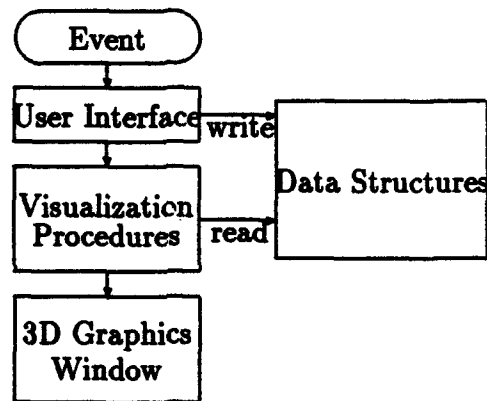


Figure 4: Flow diagram of user interface operation

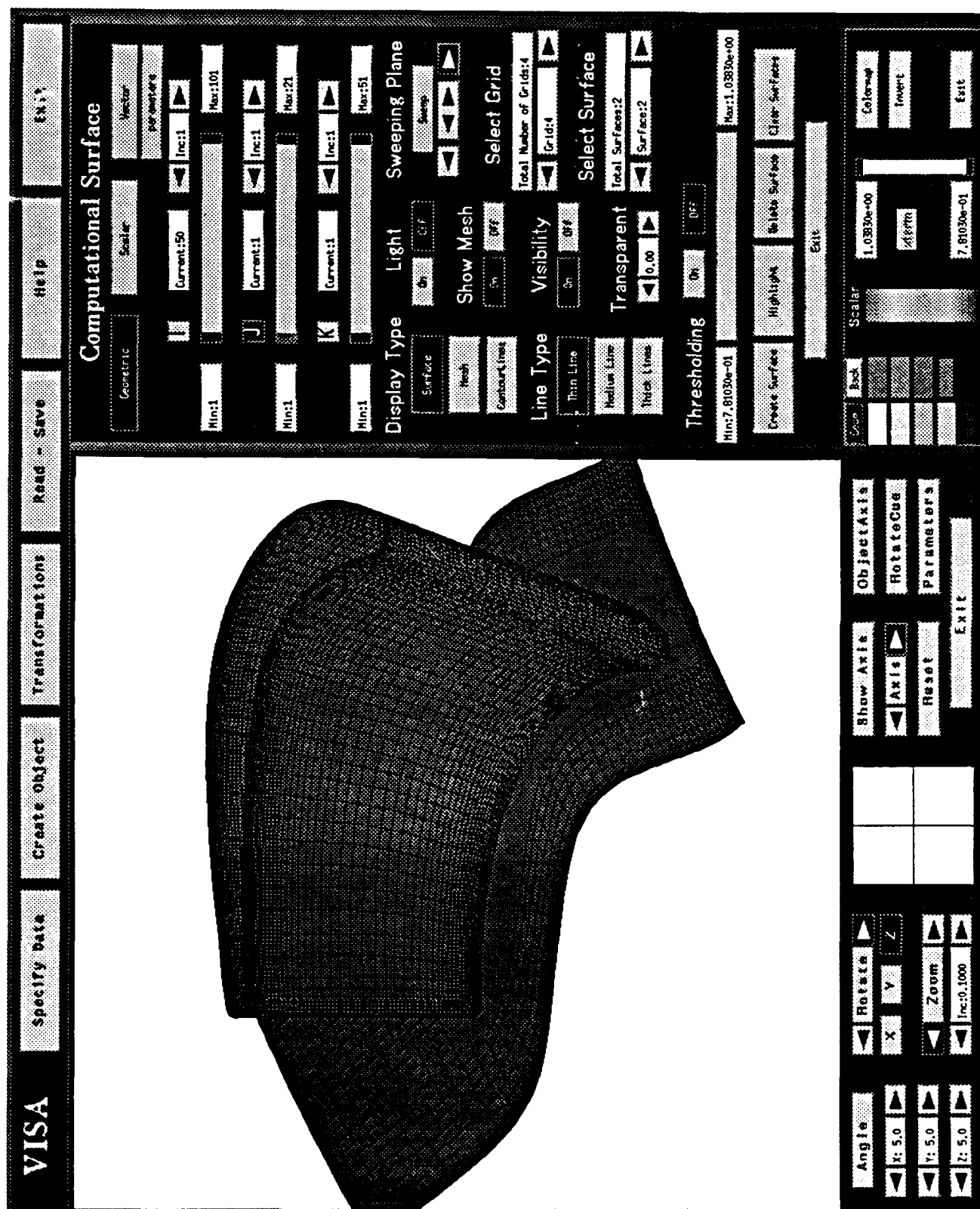


Figure 5: System layout of VISA

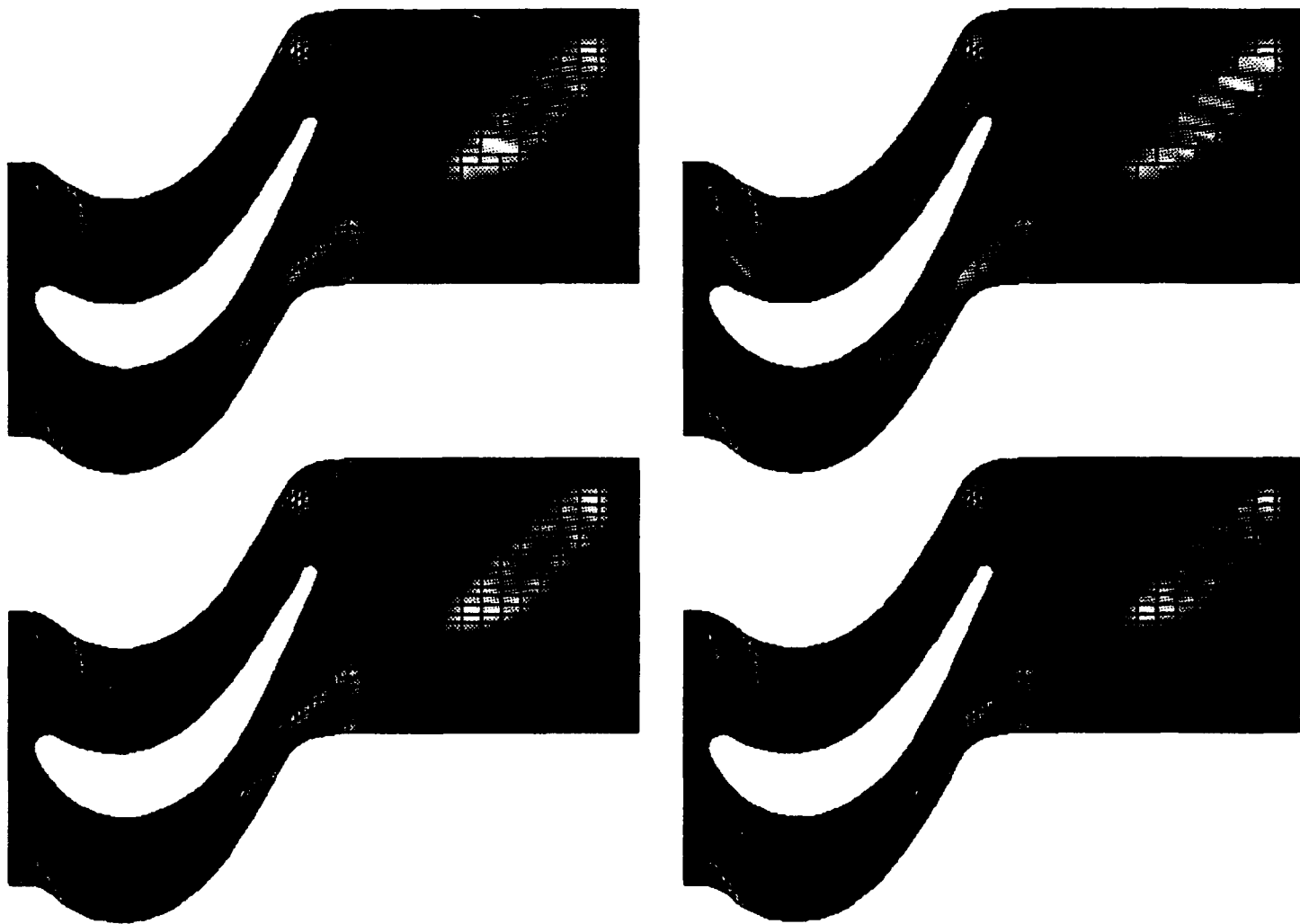
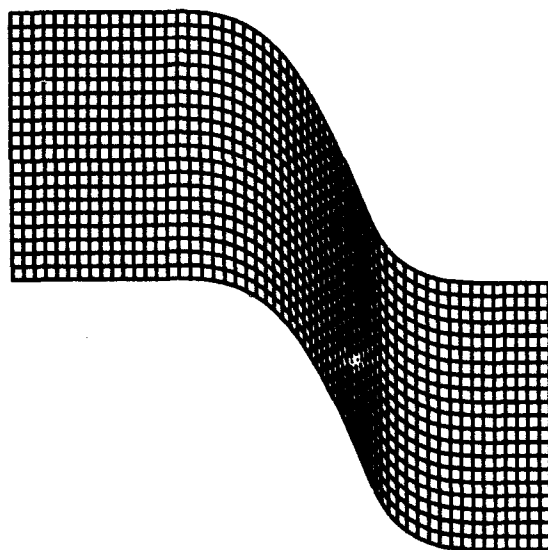
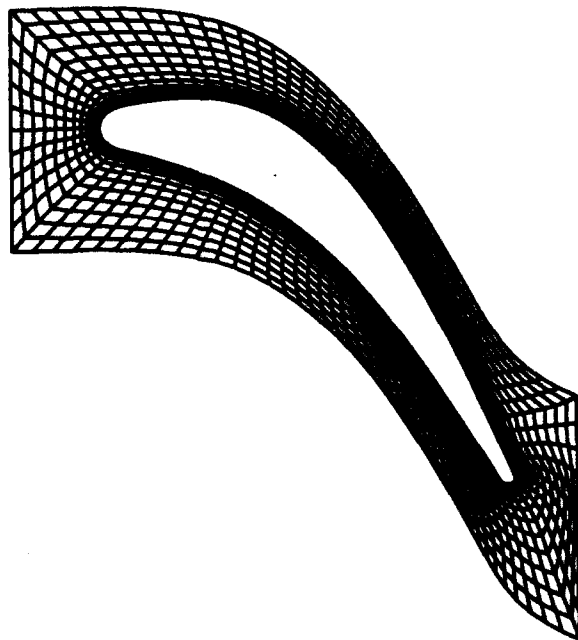


Figure 6: Data compression of static temperature contours for a two-dimensional hot streak simulation



a: Outer H-grid



a: Inner O-grid

Figure 7: Computational grid for LSRR stator

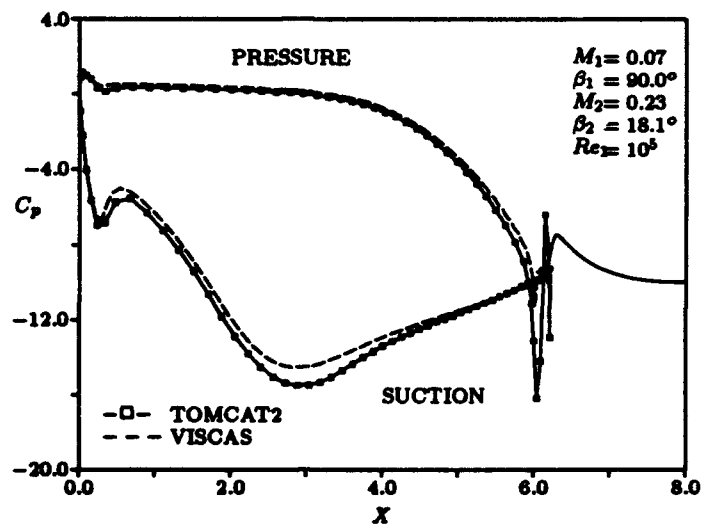


Figure 8: Predicted pressure distributions for LSRR stator

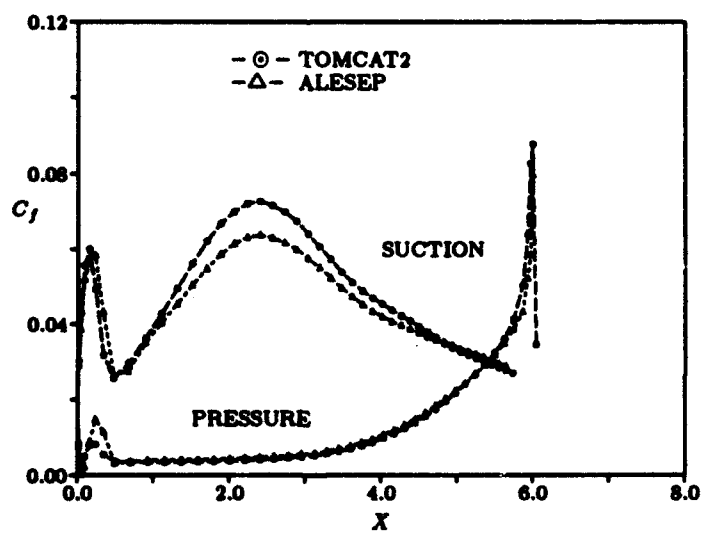


Figure 9: Predicted skin friction distribution for LSRR stator

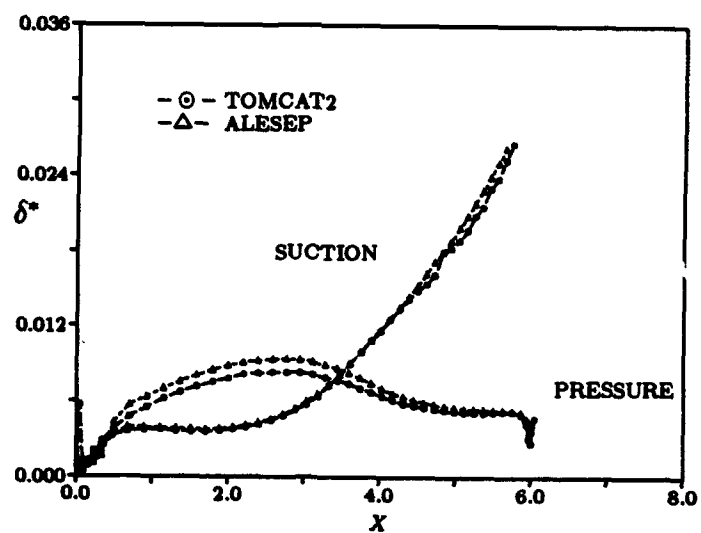


Figure 10: Predicted displacement thickness distribution for LSRR stator

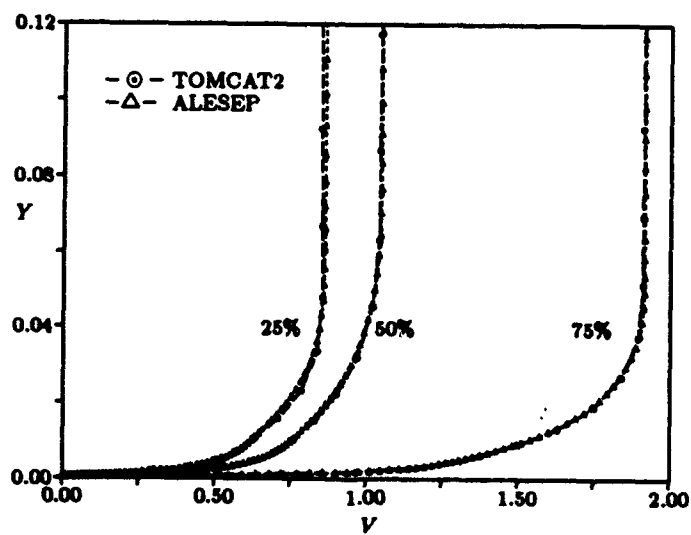


Figure 11: Velocity profiles on pressure side of LSRR stator

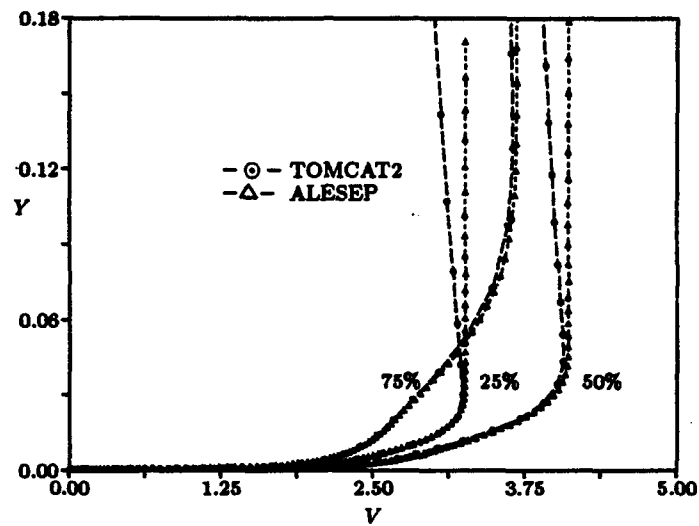


Figure 12: Velocity profiles on suction side of LSRR stator

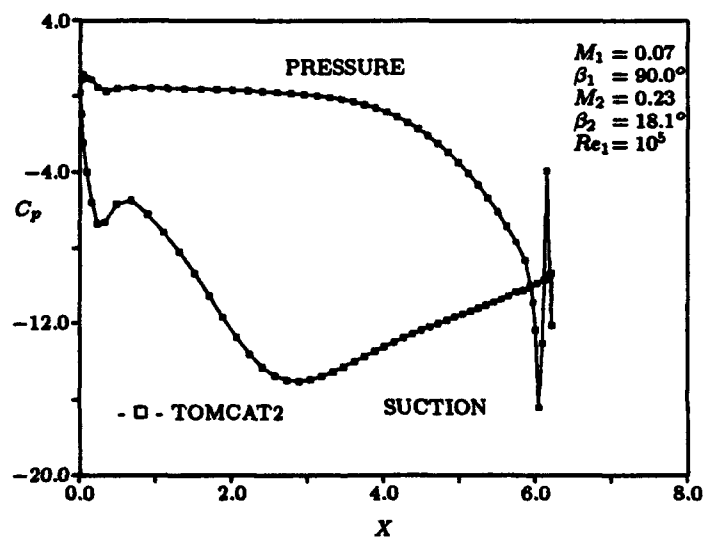


Figure 13: Predicted pressure distribution for LSRR stator with specified wall temperature

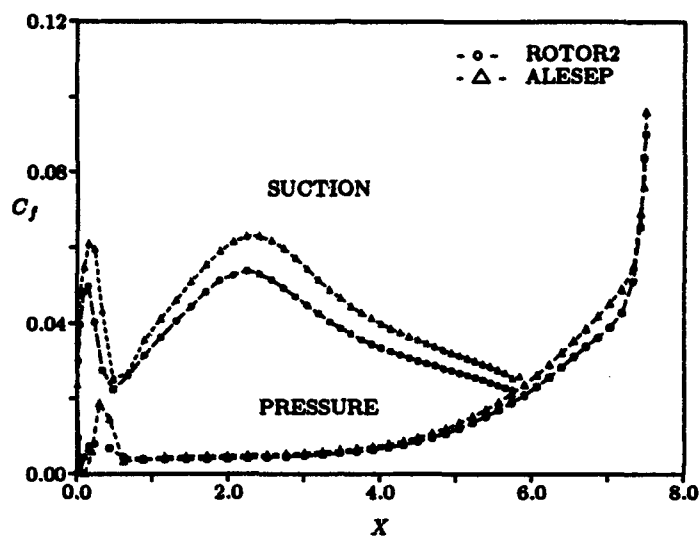


Figure 14: Predicted skin friction distribution for LSRR stator with specified wall temperature

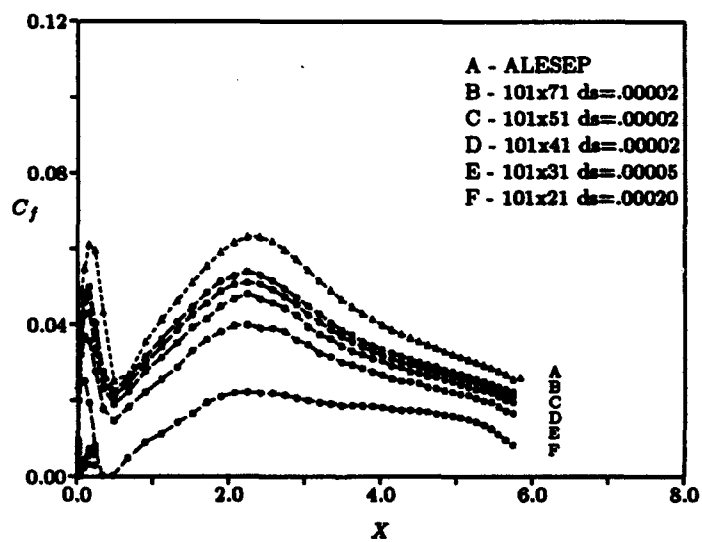


Figure 15: Suction side skin friction distributions for LSRR stator with specified wall temperature

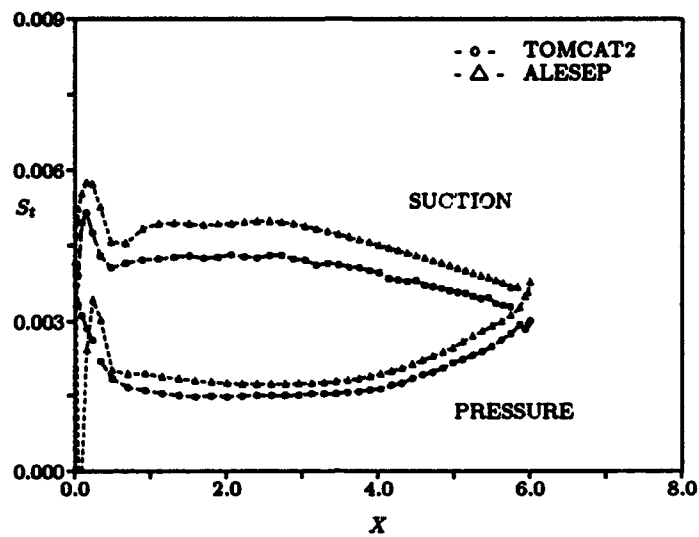


Figure 16: Predicted Stanton number distribution for LSRR stator

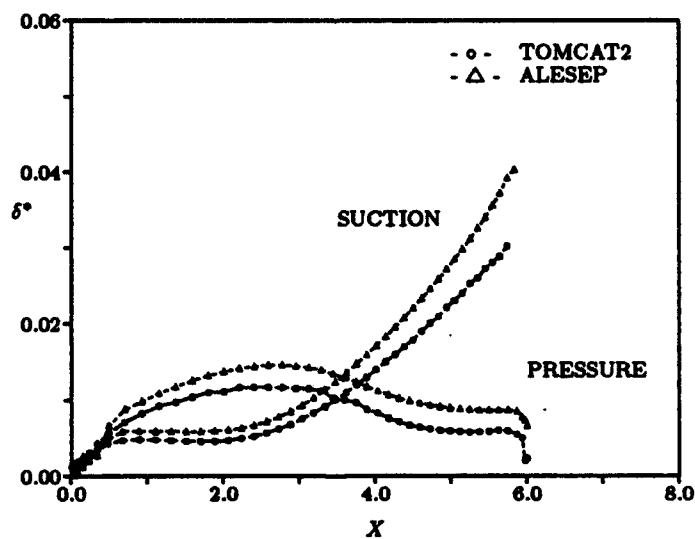


Figure 17: Predicted displacement thickness distribution for LSRR stator

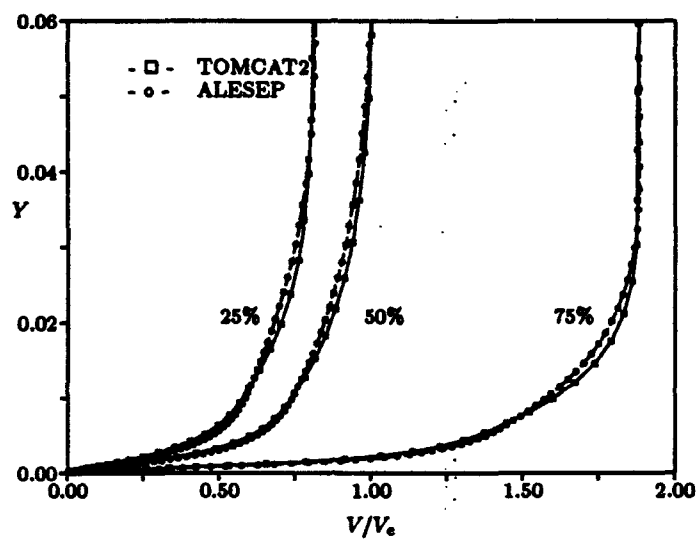


Figure 18: Pressure surface velocity profiles for LSRR stator with specified wall temperature

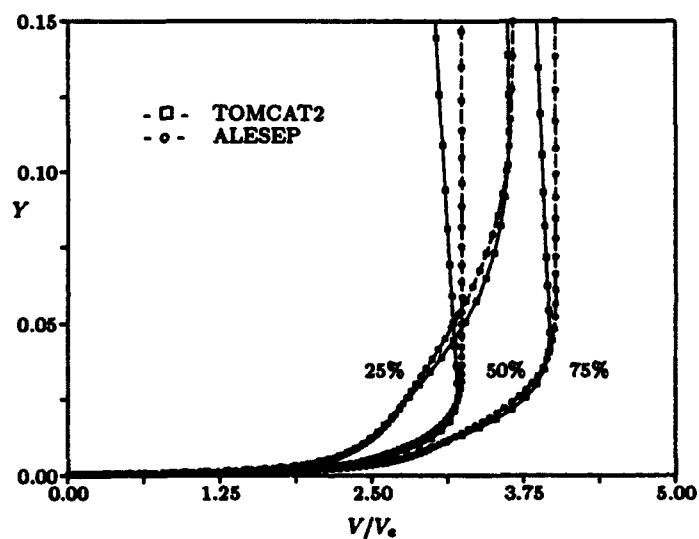


Figure 19: Suction surface velocity profiles for LSRR stator with specified wall temperature

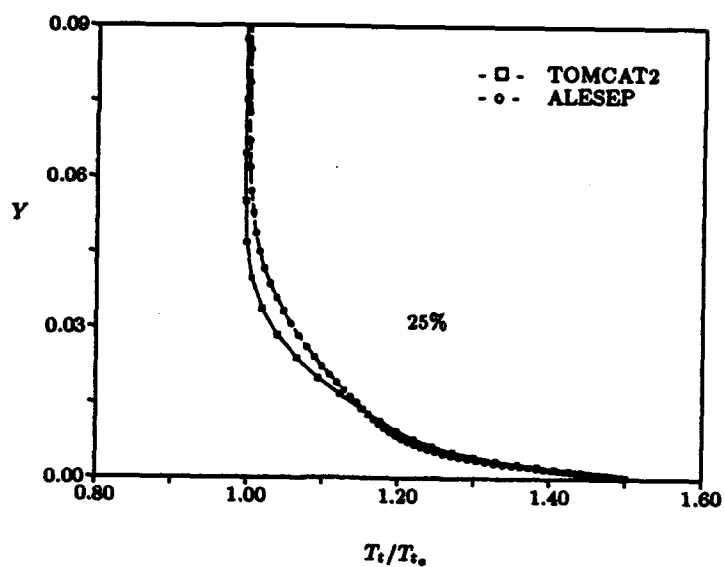


Figure 20: Pressure surface temperature profiles for 25% axial chord of LSRR stator

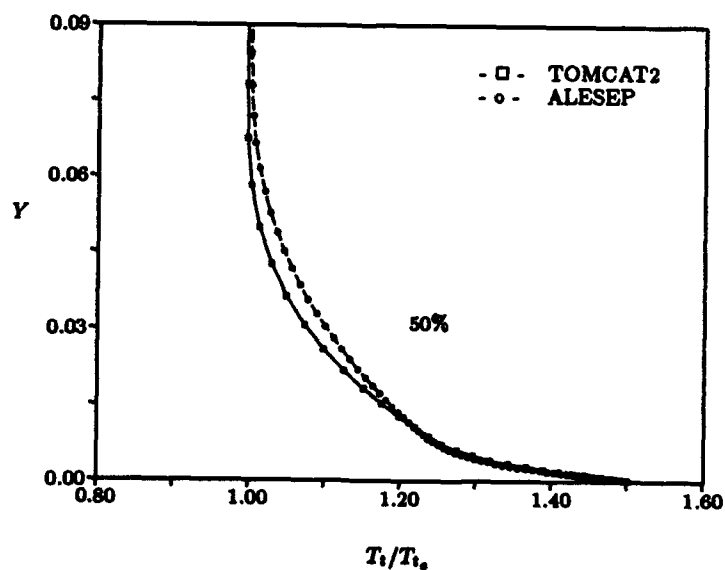


Figure 21: Pressure surface temperature profiles for 50% axial chord of LSRR stator

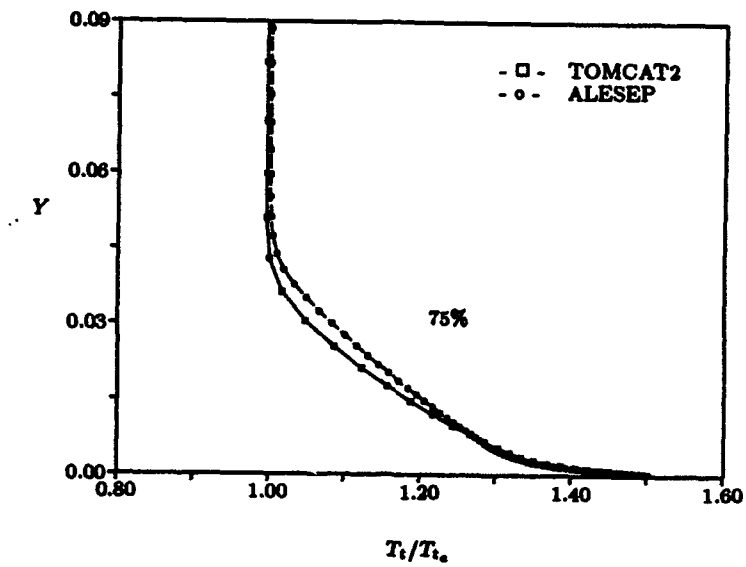


Figure 22: Pressure surface temperature profiles for 75% axial chord of LSRR stator

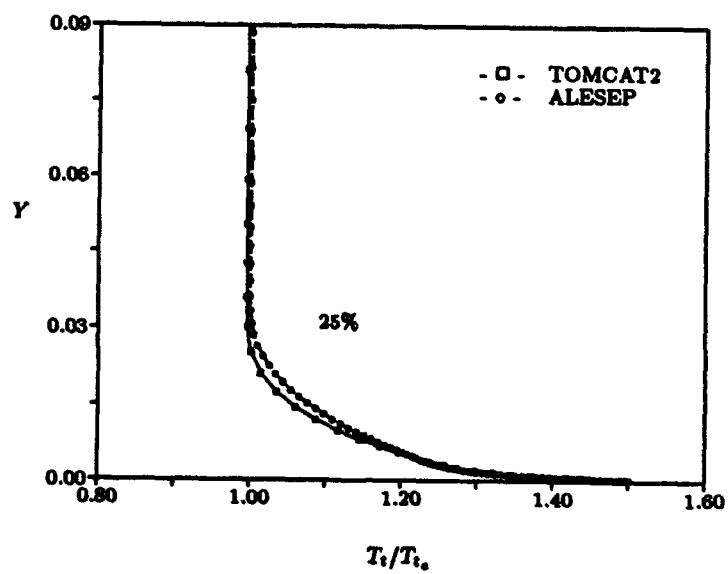


Figure 23: Suction surface temperature profiles for 25% axial chord of LSRR stator

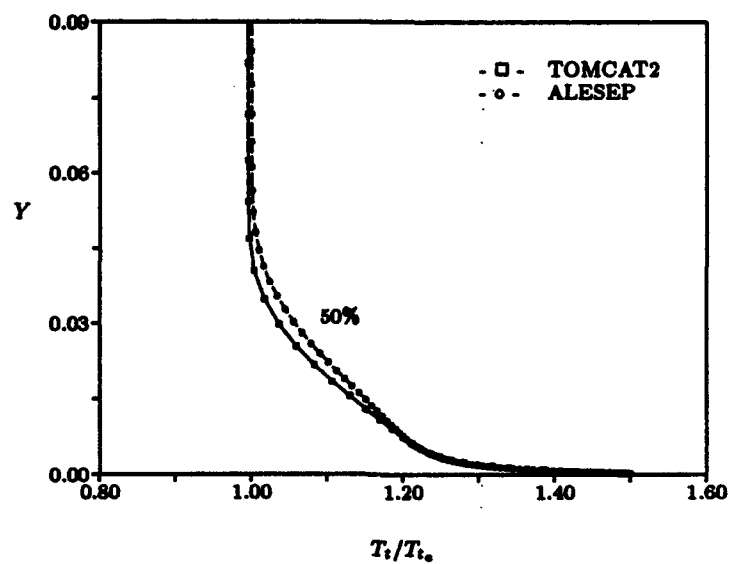


Figure 24: Suction surface temperature profiles for 50% axial chord of LSRR stator

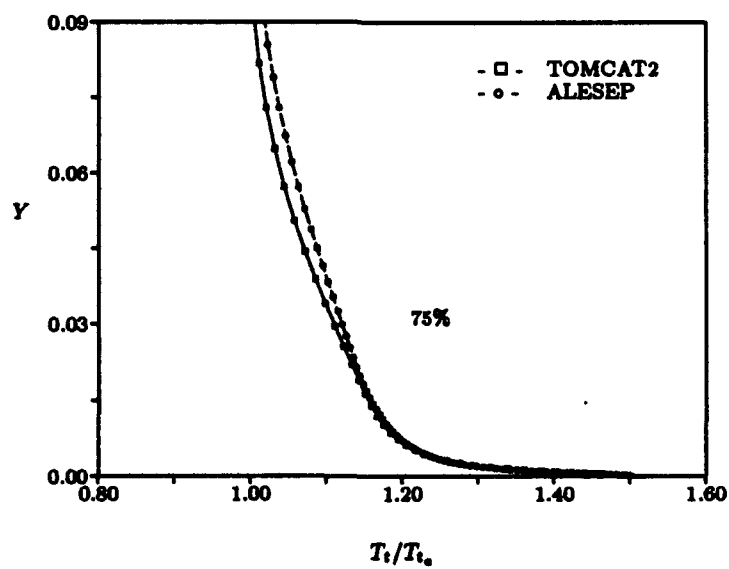


Figure 25: Suction surface temperature profiles for 75% axial chord of LSRR stator

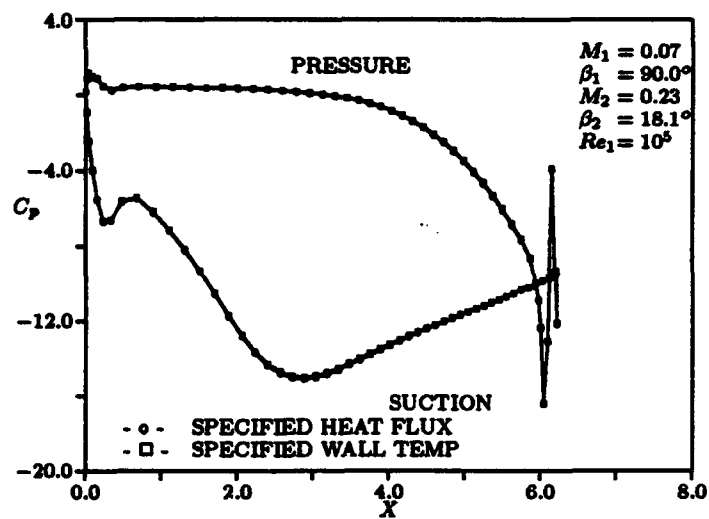


Figure 26: Predicted pressure distribution for LSRR stator with specified heat flux

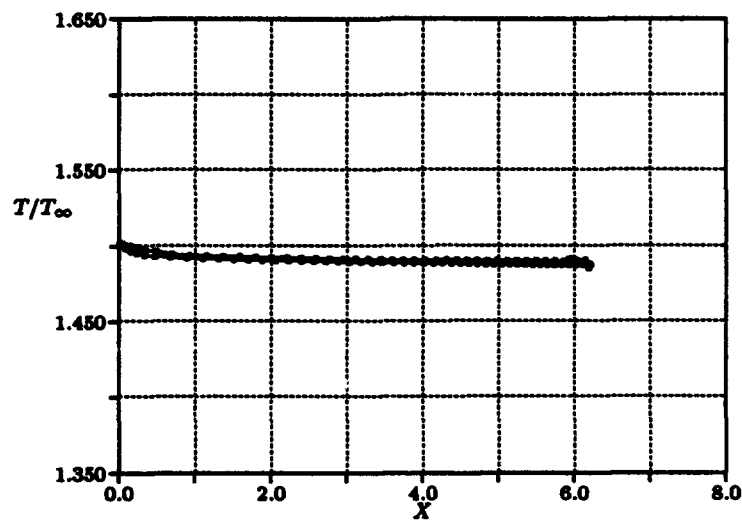
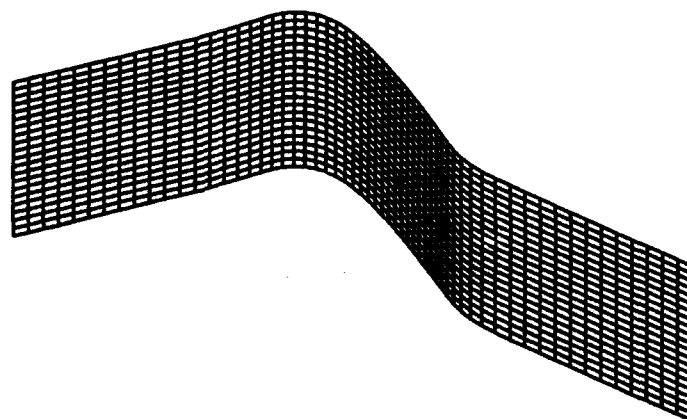
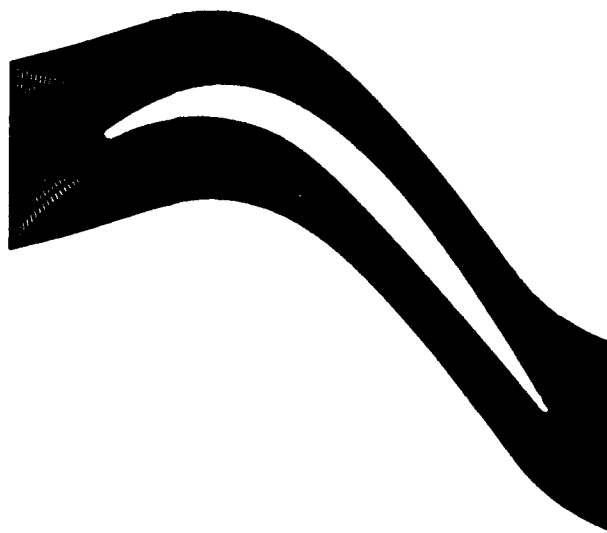


Figure 27: Wall temperature distribution for LSRR stator with specified heat flux



a: Outer H-grid



a: Inner O-grid

Figure 28: Viscous computational grid for E^3 lightweight turbine blade

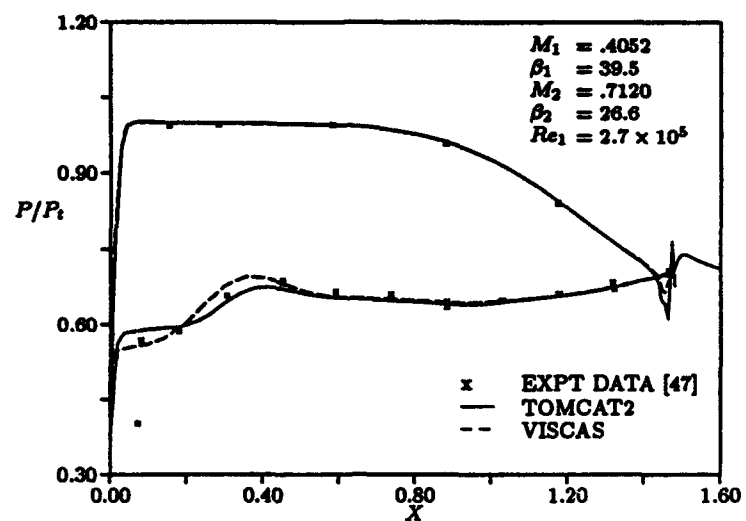


Figure 29: Pressure distribution for E^3 turbine blade, 10° incidence

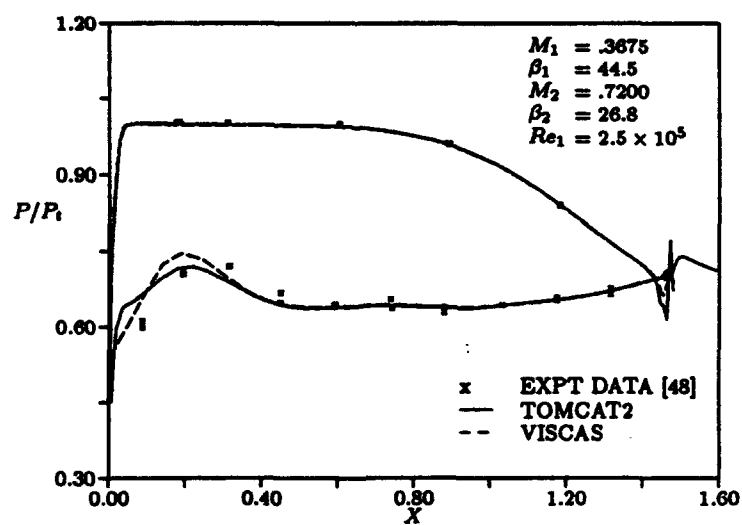


Figure 30: Pressure distribution for E^3 turbine blade, 5° incidence

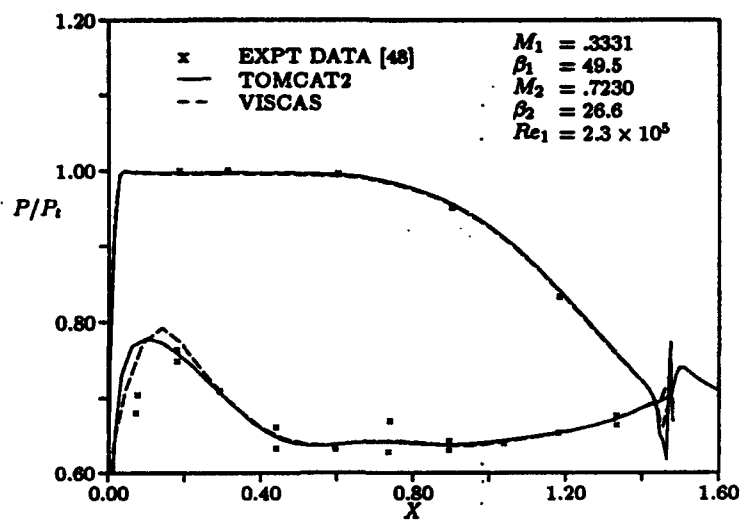


Figure 31: Pressure distribution for E^3 turbine blade, 0° incidence

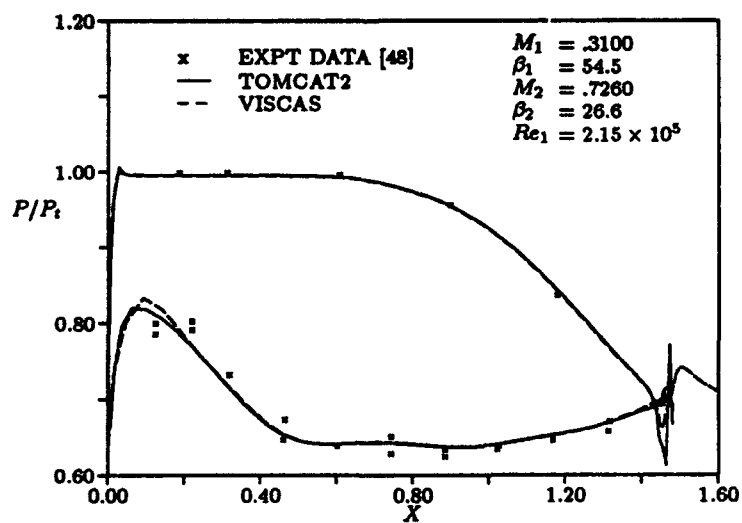


Figure 32: Pressure distribution for E^3 turbine blade, -5° incidence

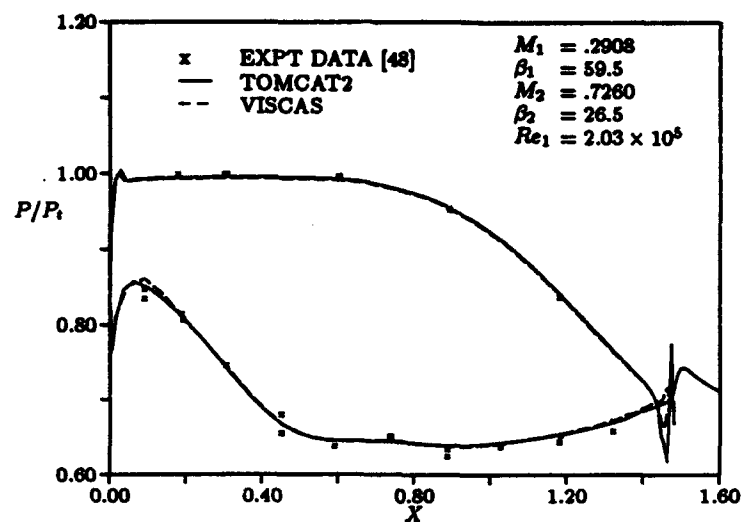


Figure 33: Pressure distribution for E^3 turbine blade, -10° incidence

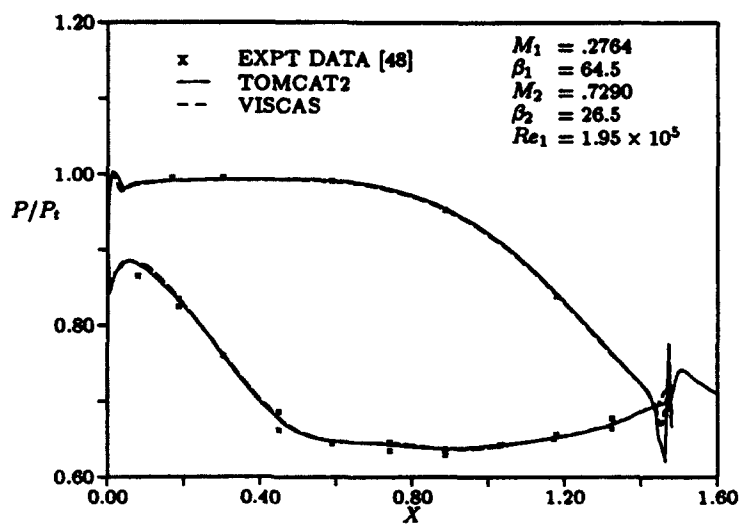


Figure 34: Pressure distribution for E^3 turbine blade, -15° incidence

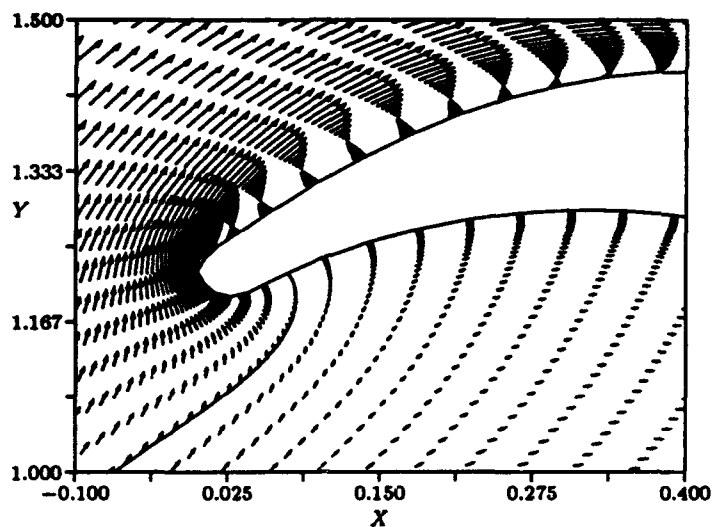


Figure 35: Velocity vectors for E^3 turbine blade at 10° positive incidence

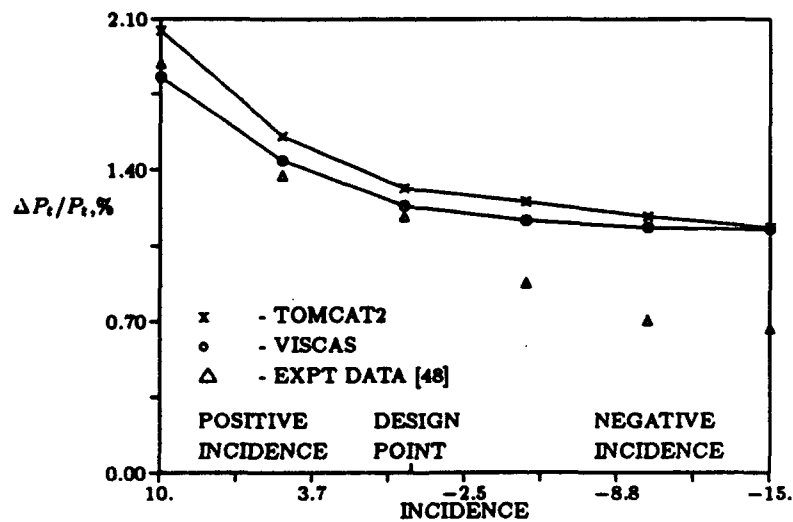


Figure 36: Total pressure loss map for E^3 lightweight turbine blade

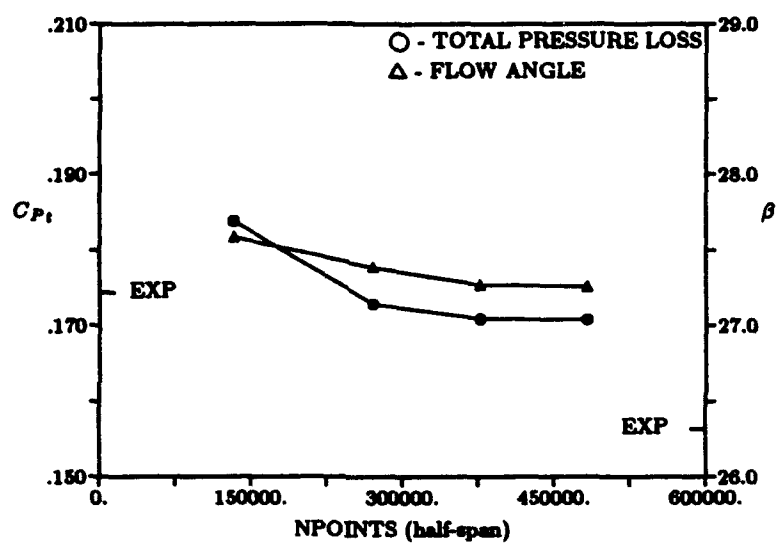


Figure 37: Exit flow angle and total pressure loss as a function of grid point density for Langston cascade

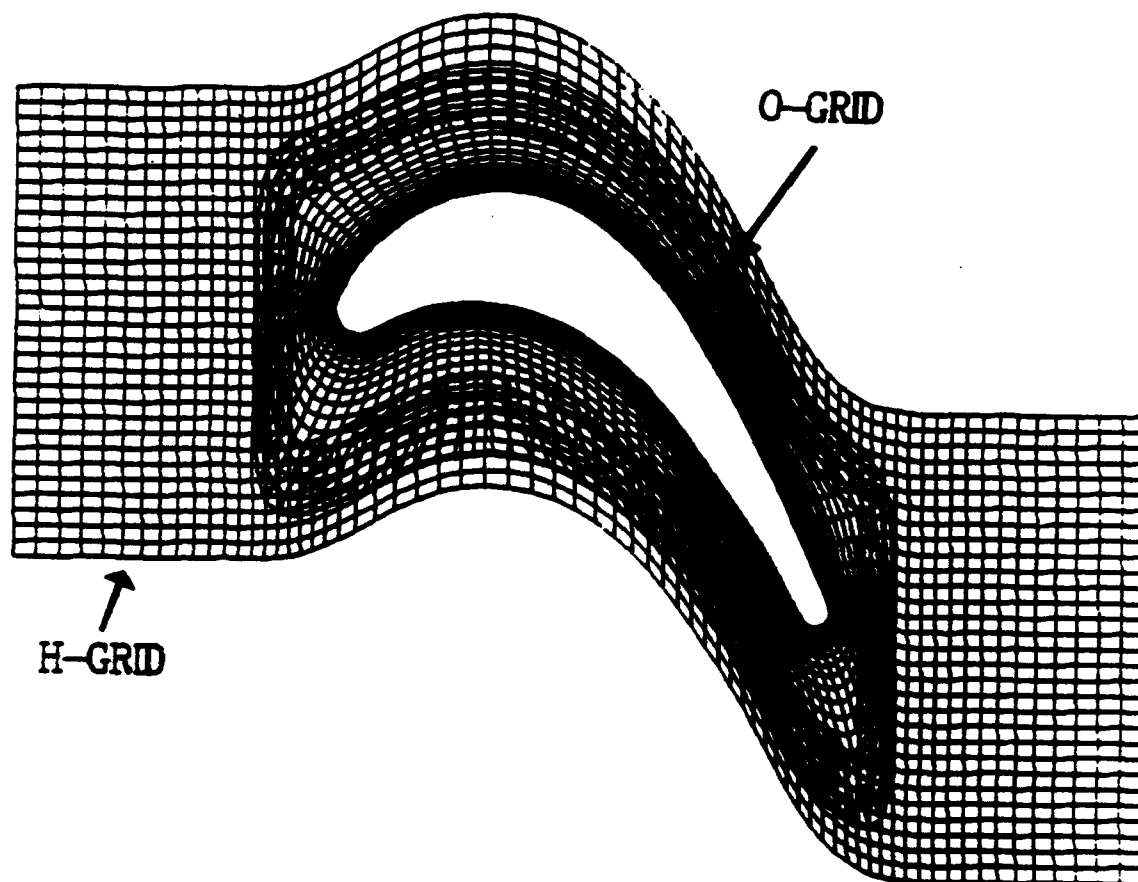


Figure 38: Blade-to-blade computational grid for Langston cascade

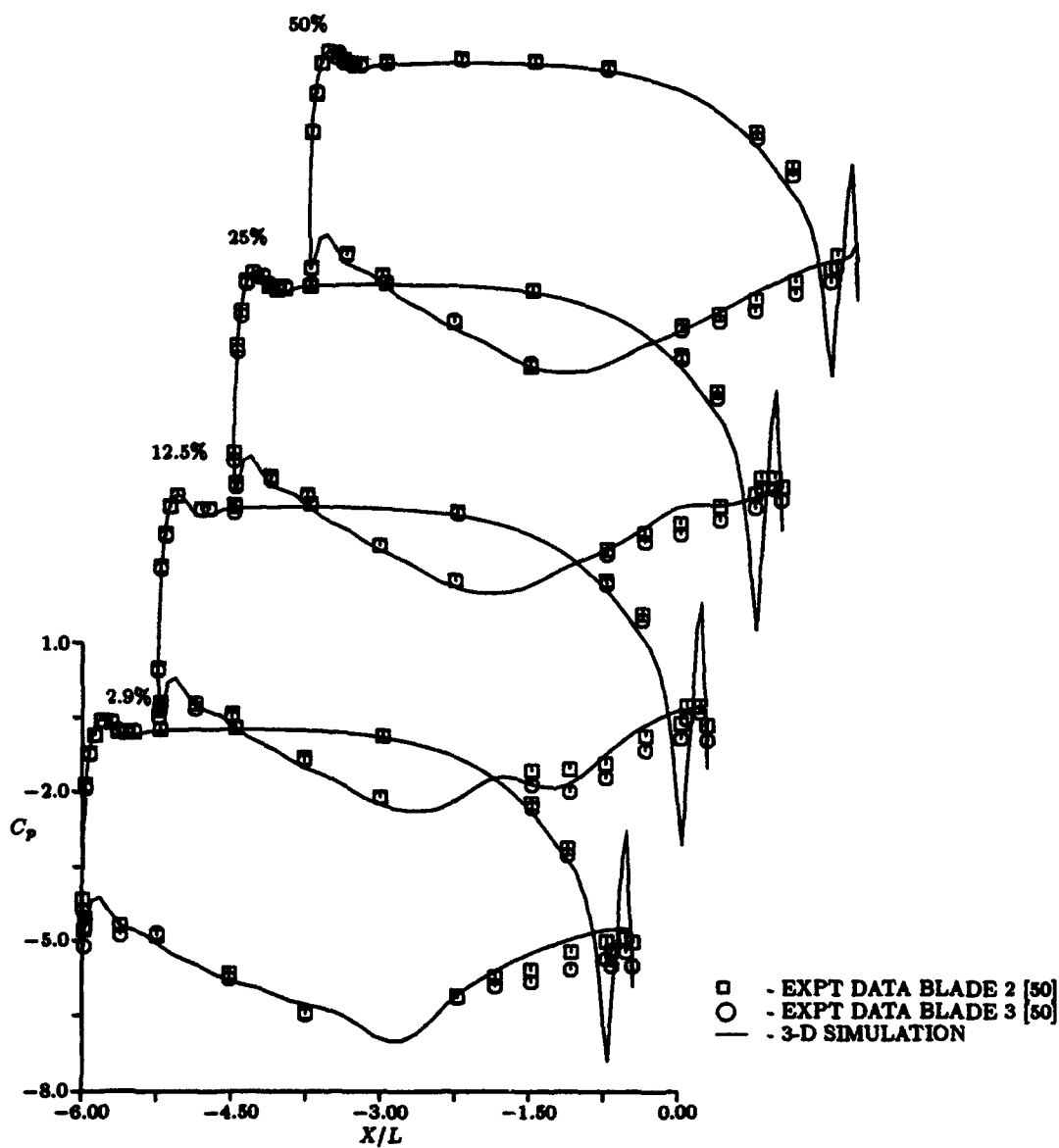


Figure 39: Static pressure coefficient distributions for Langston cascade

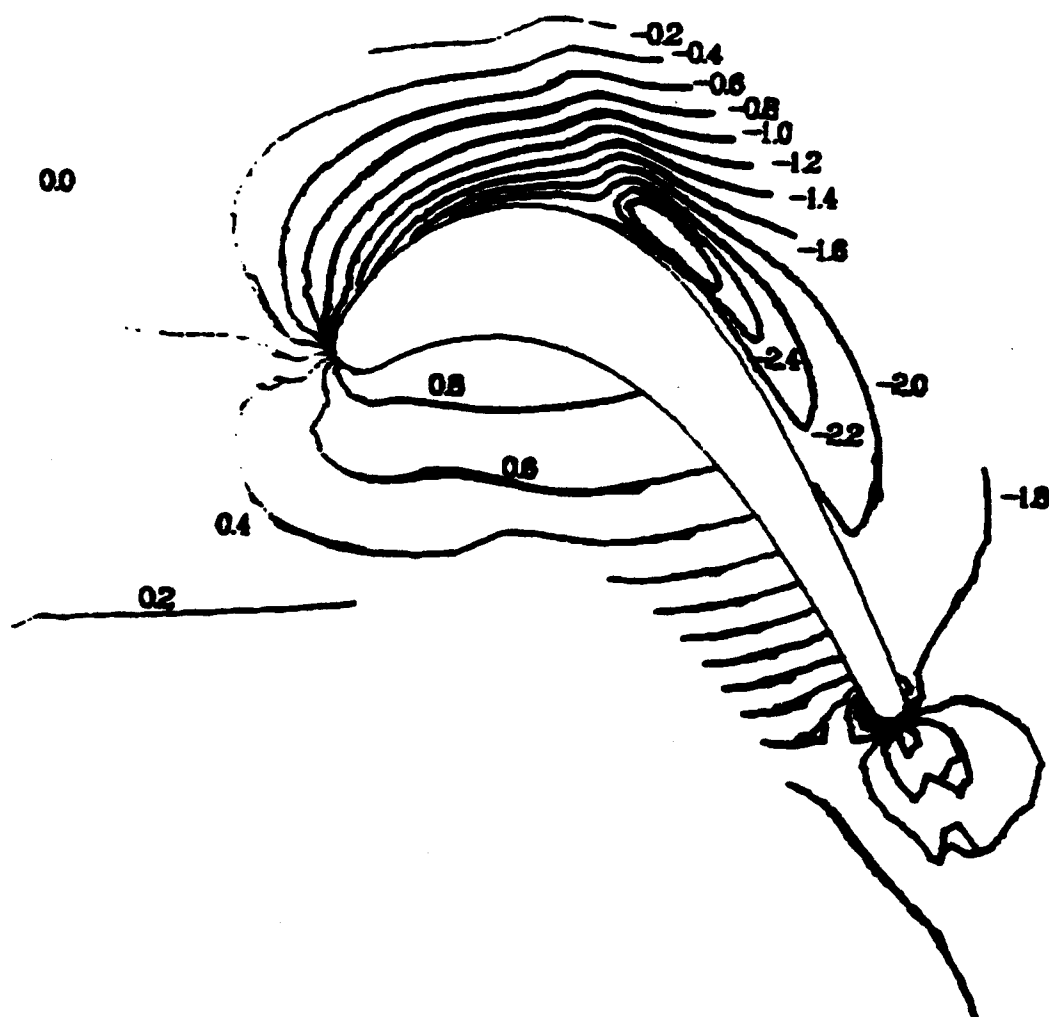


Figure 40: Predicted endwall static pressure coefficient contours for Langston cascade

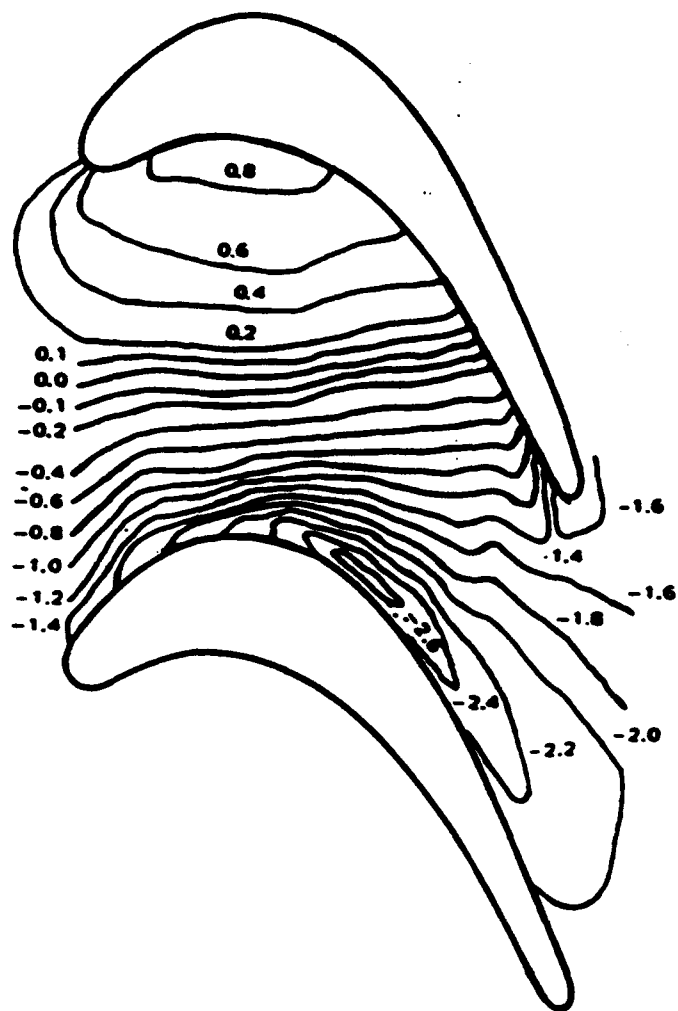


Figure 41: Experimental endwall static pressure coefficient contours for Langston cascade

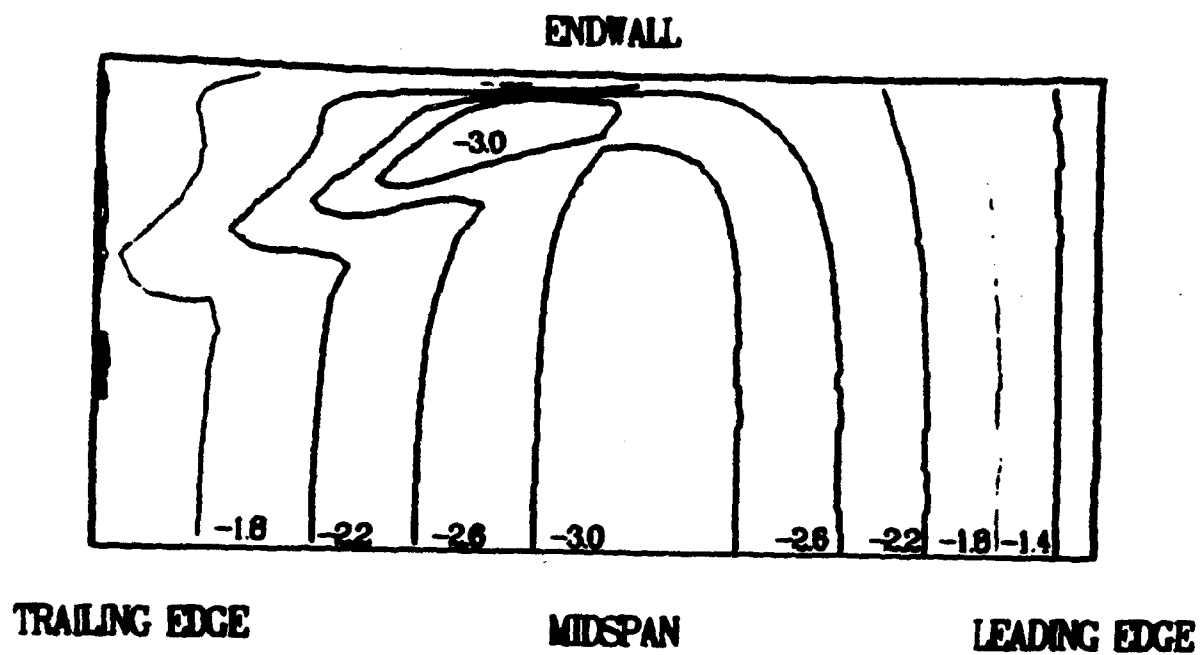


Figure 42: Predicted suction surface static pressure coefficient contours for Langston cascade

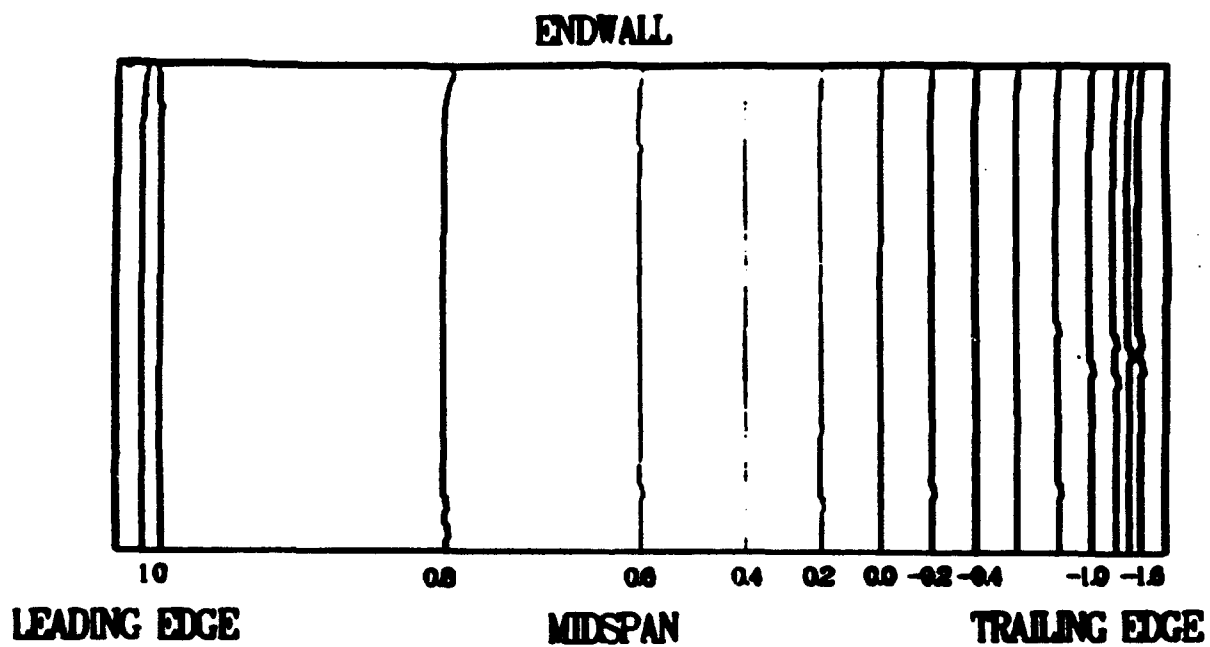


Figure 43: Predicted pressure surface static pressure coefficient contours for Langston cascade

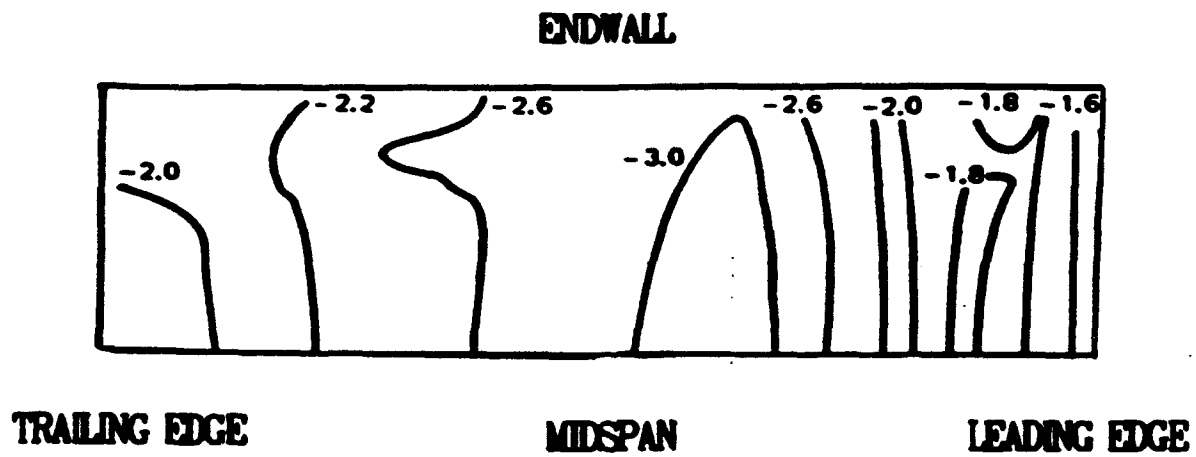


Figure 44: Experimental suction surface static pressure coefficient contours for Langston cascade

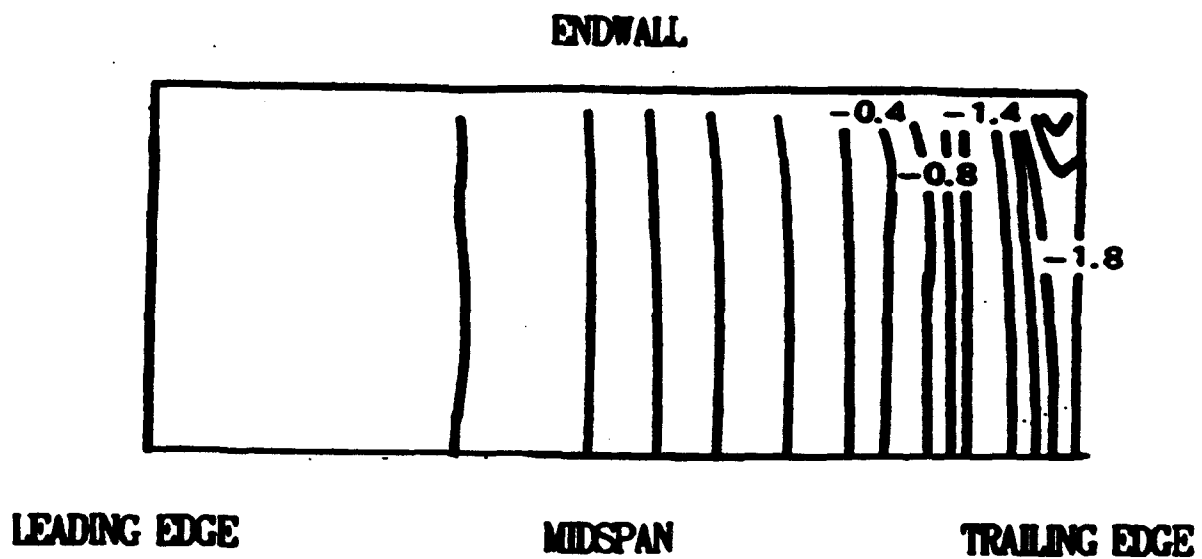


Figure 45: Experimental pressure surface static pressure coefficient contours for Langston cascade

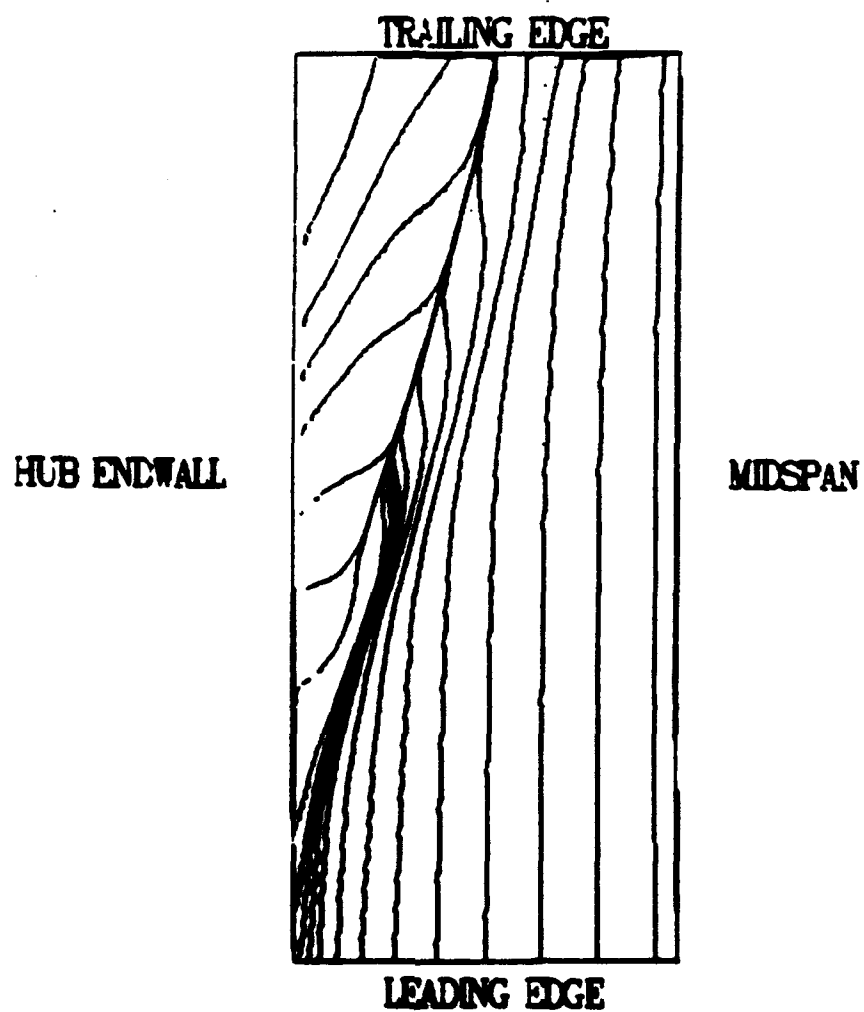


Figure 46: Predicted suction surface limiting streamlines for Langston cascade

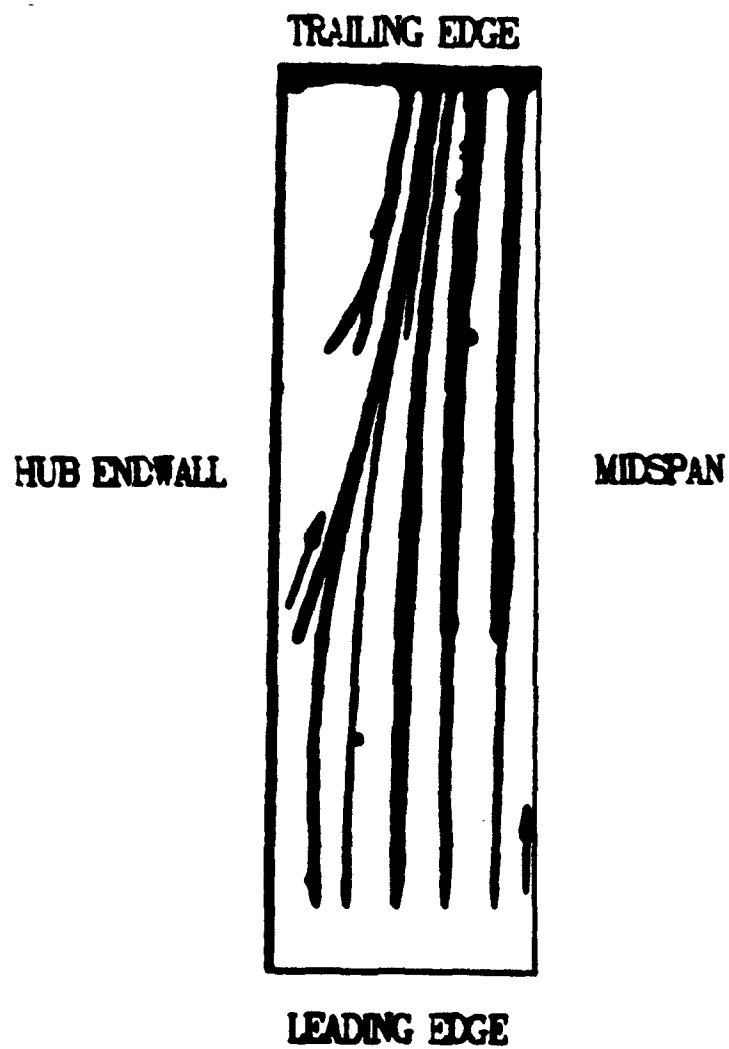


Figure 47: Experimental suction surface limiting streamlines for Langston cascade

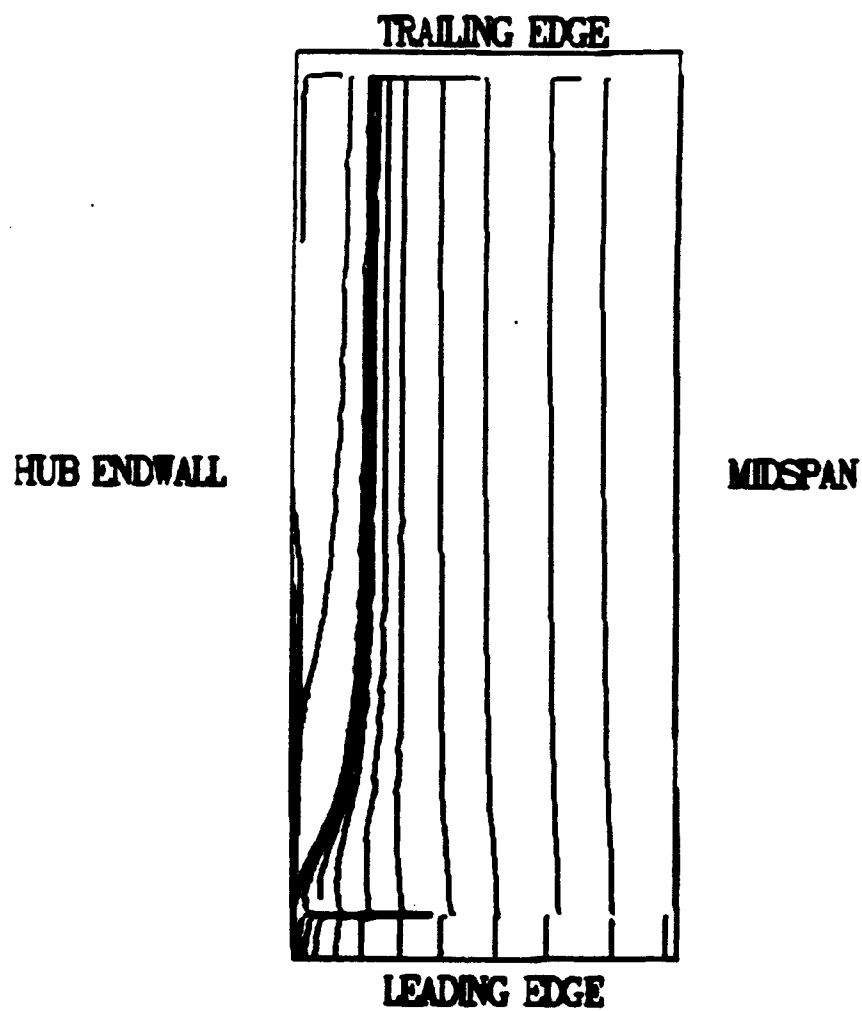


Figure 48: Predicted pressure surface limiting streamlines for Langston cascade

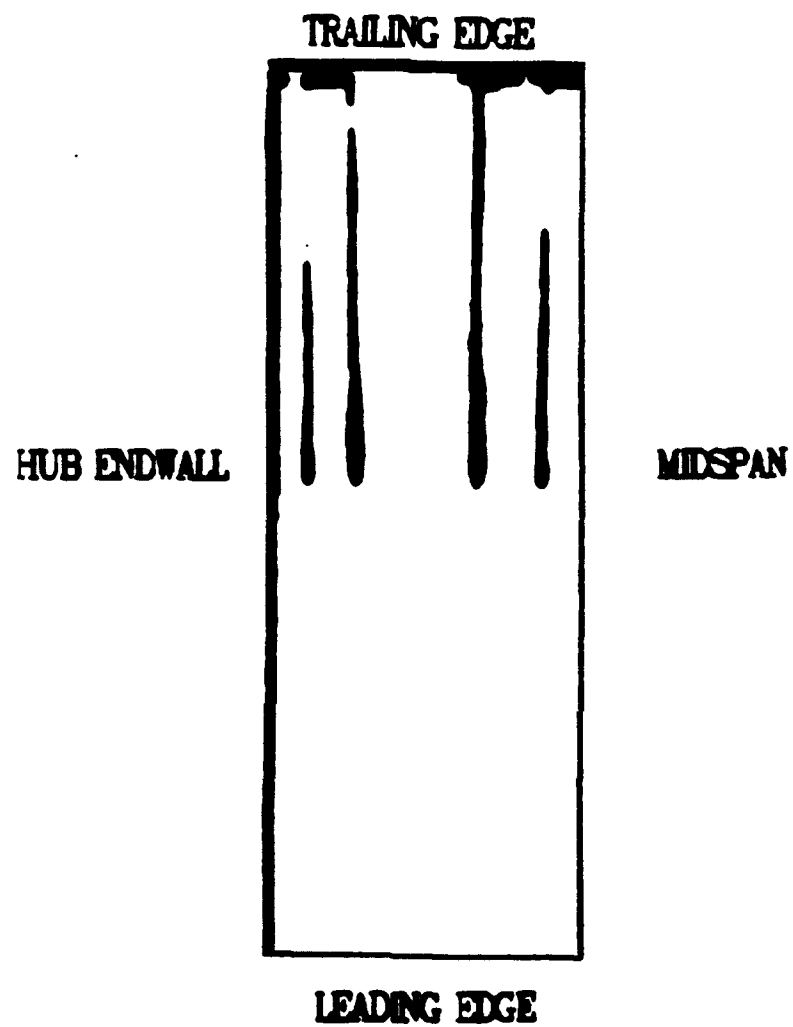


Figure 49: Experimental pressure surface experimental limiting streamlines for Langston cascade

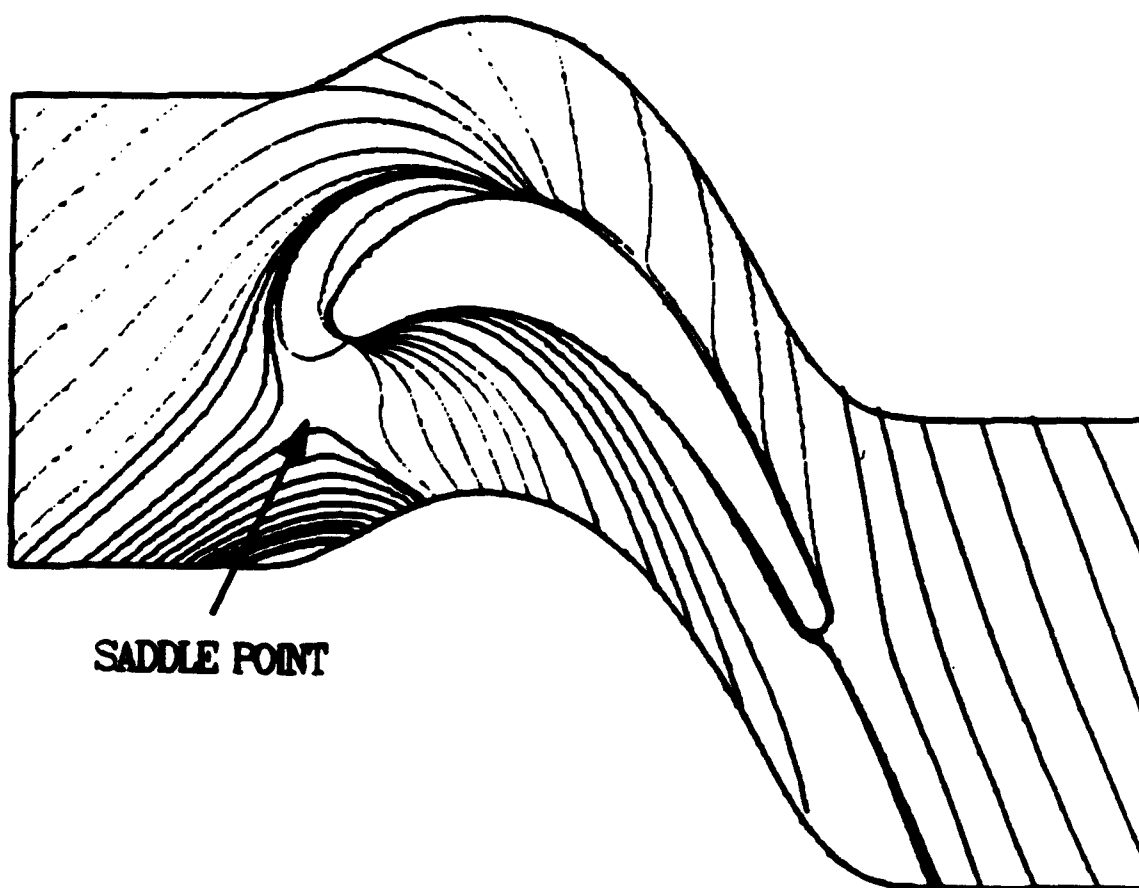


Figure 50: Predicted endwall limiting streamlines for Langston cascade

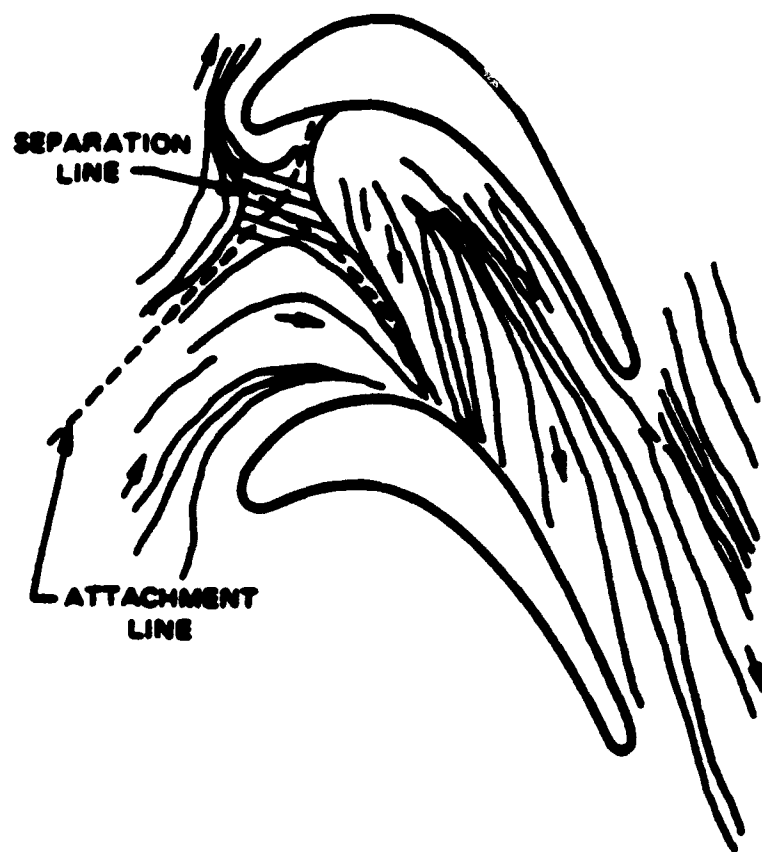


Figure 51: Experimental endwall limiting streamlines for Langston cascade

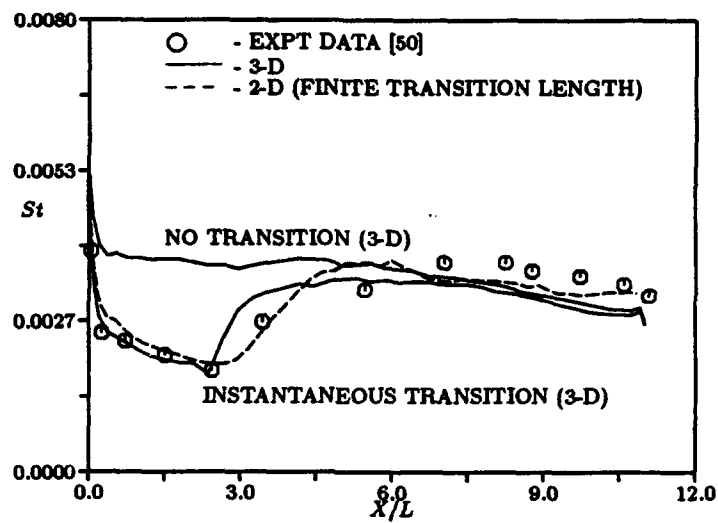


Figure 52: Mid-span suction surface Stanton number distributions for Langston cascade

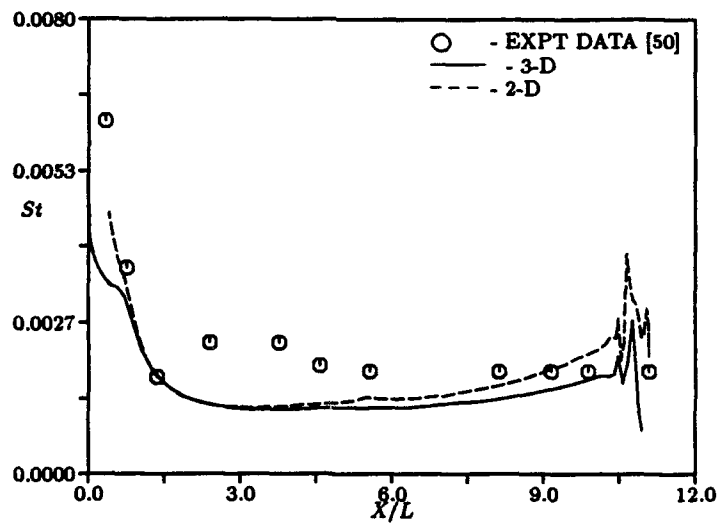


Figure 53: Mid-span pressure surface Stanton number distributions for Langston cascade

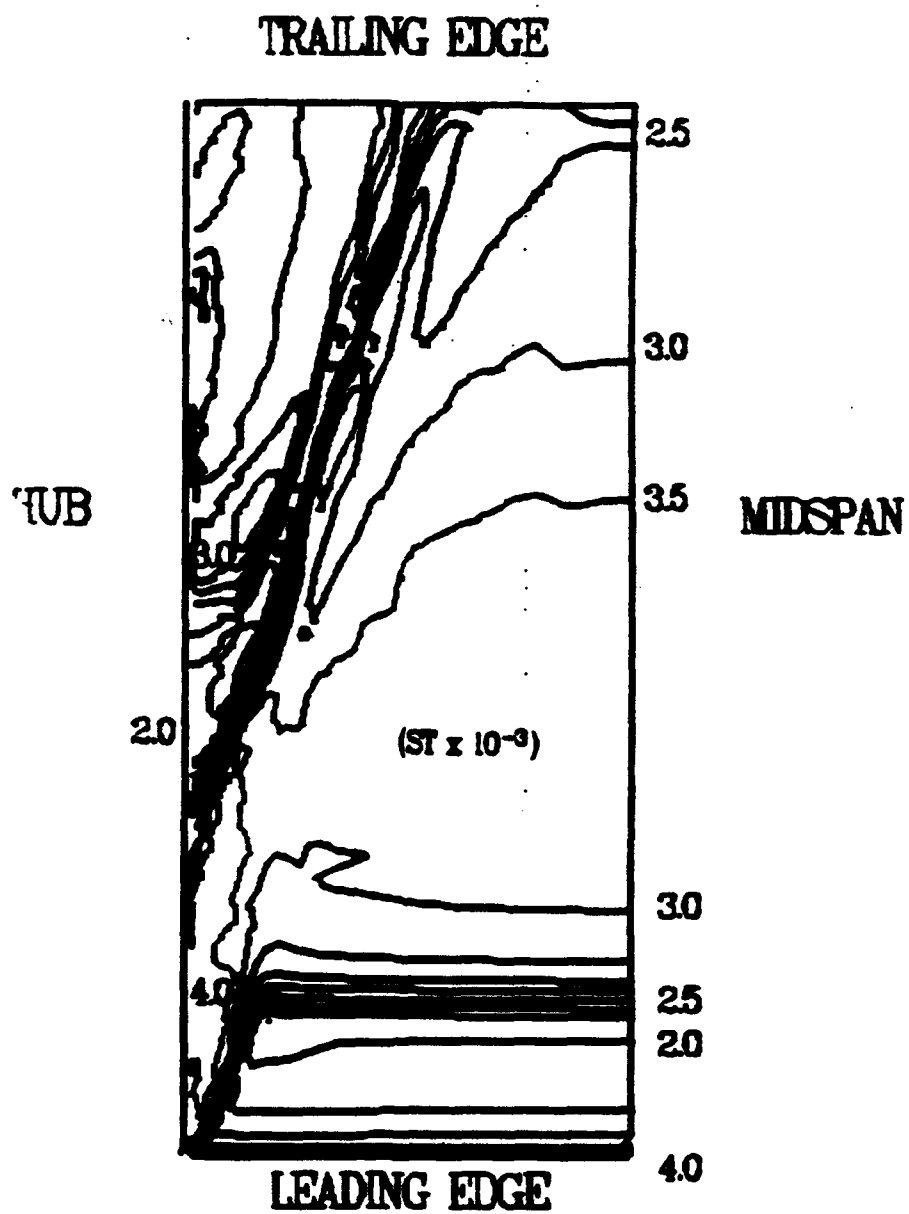


Figure 54: Predicted suction surface Stanton number contours for Langston cascade

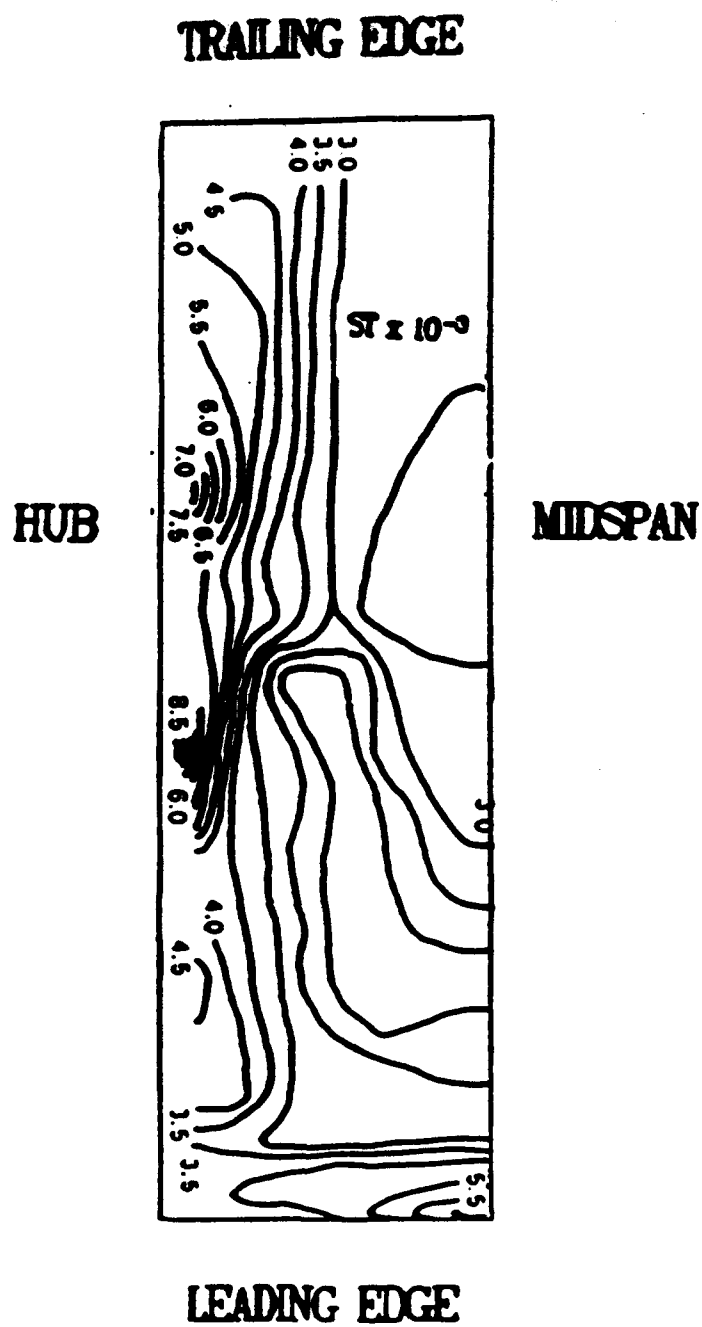


Figure 55: Experimental suction surface Stanton number contours for Langston cascade

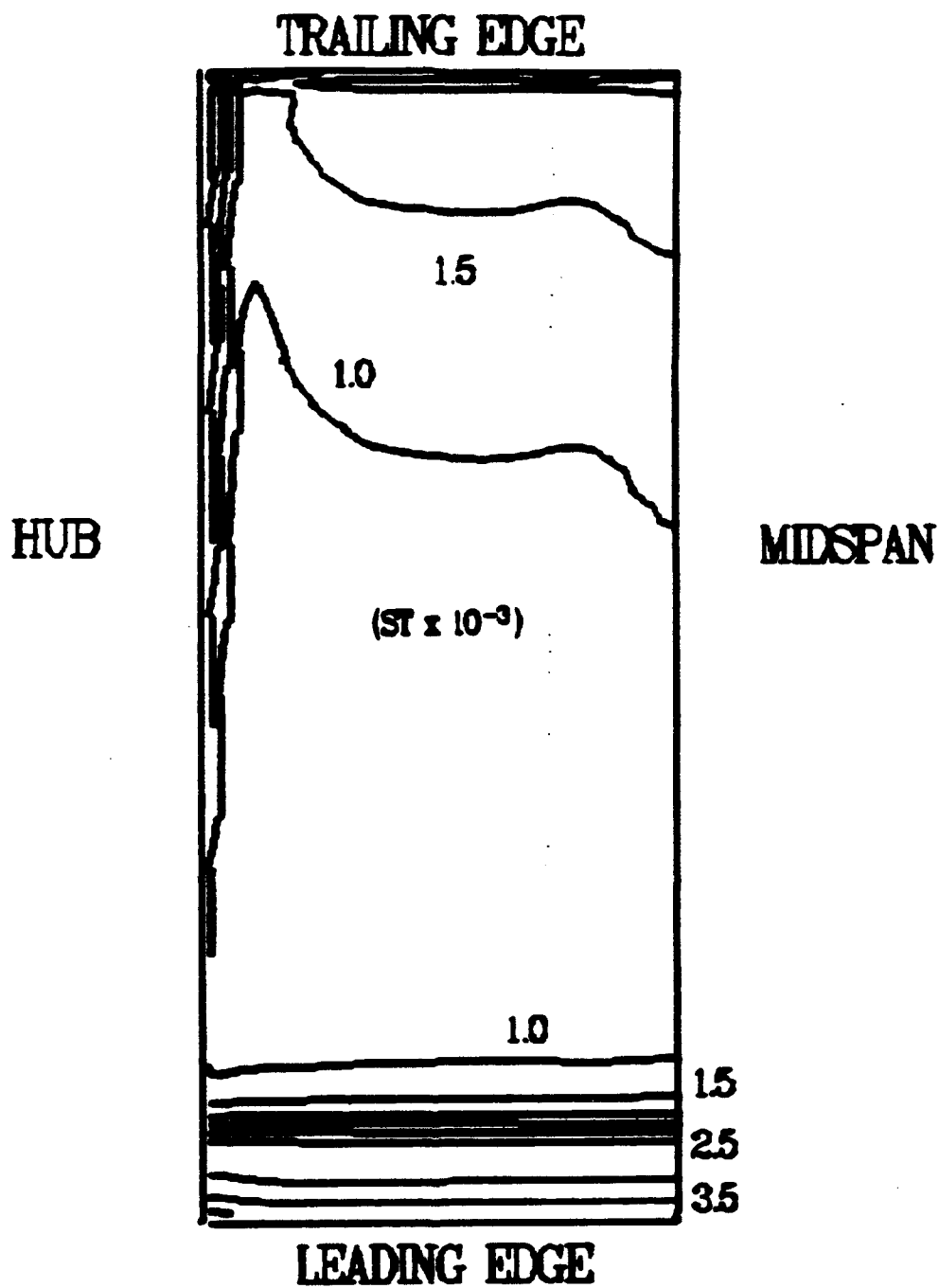


Figure 56: Predicted pressure surface Stanton number contours for Langston cascade

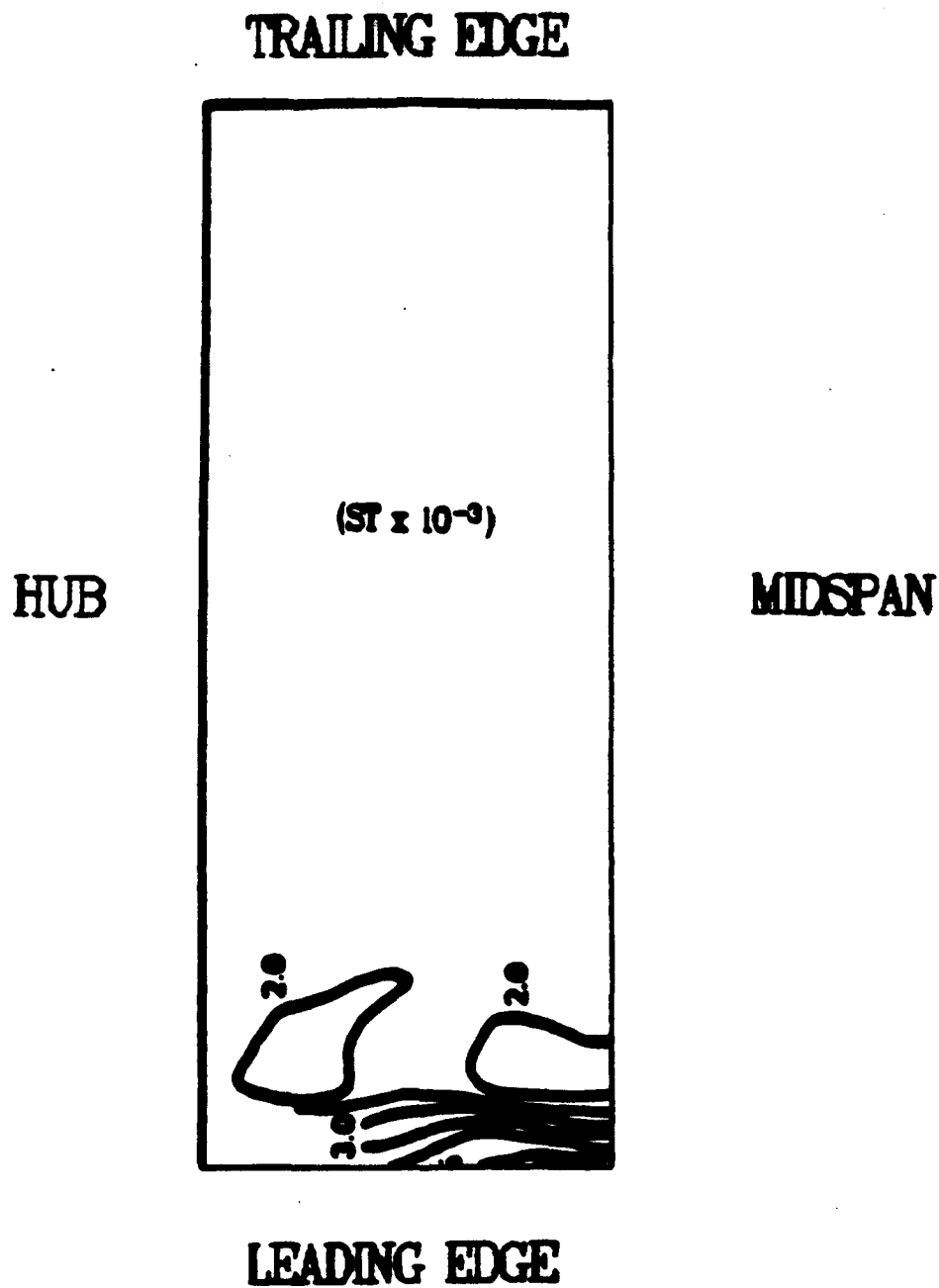


Figure 57: Experimental pressure surface Stanton number contours for Langston cascade

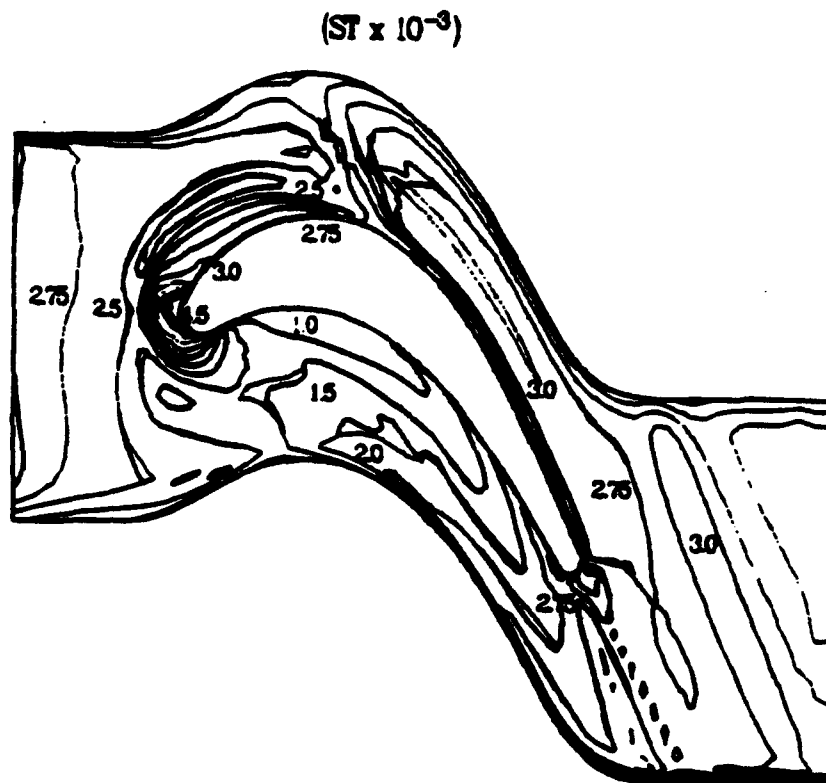


Figure 58: Predicted endwall Stanton number contours for Langston cascade

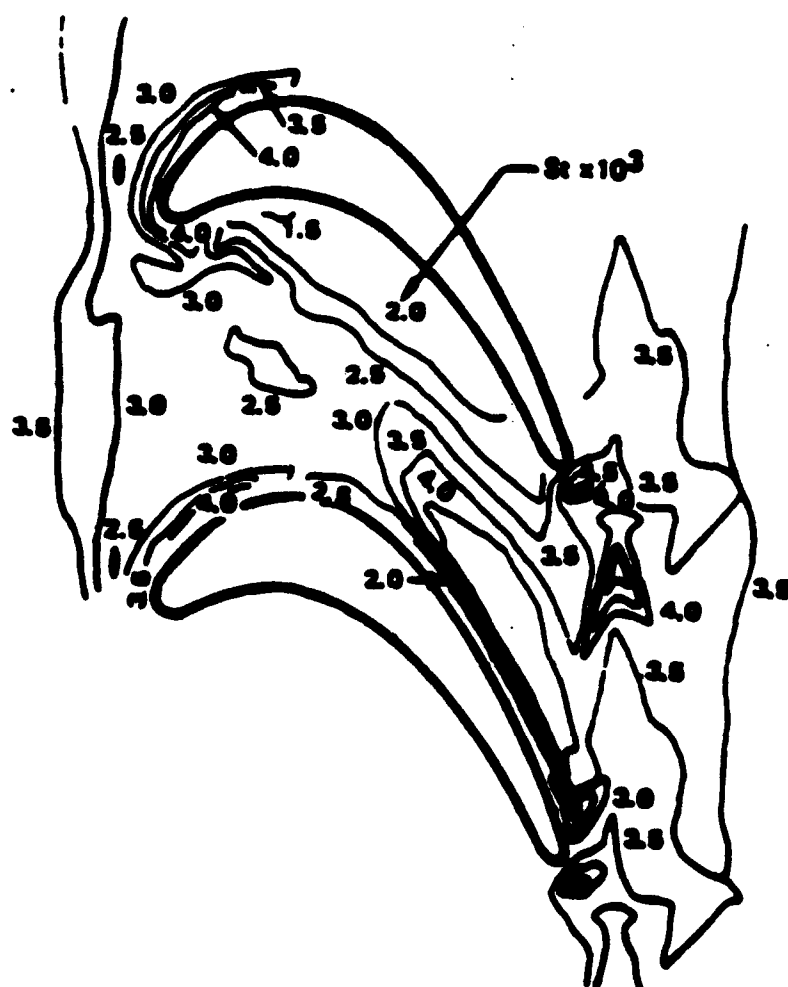


Figure 59: Experimental endwall Stanton number contours for Langston cascade

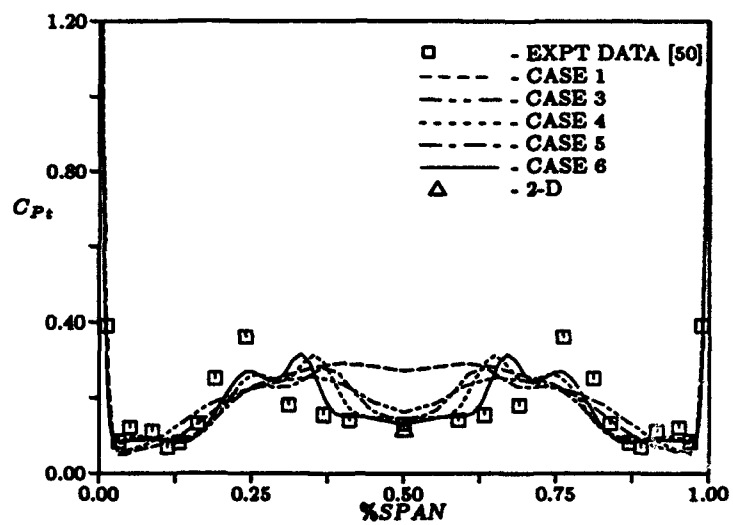


Figure 60: Gap-averaged total pressure coefficient distributions for Langston cascade

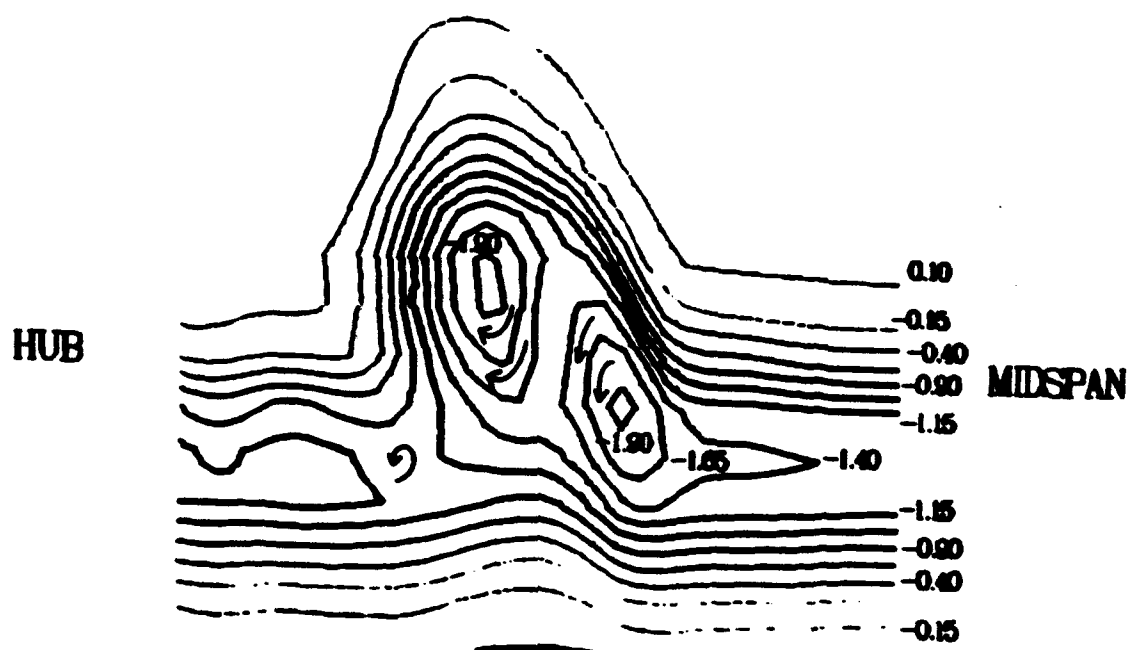
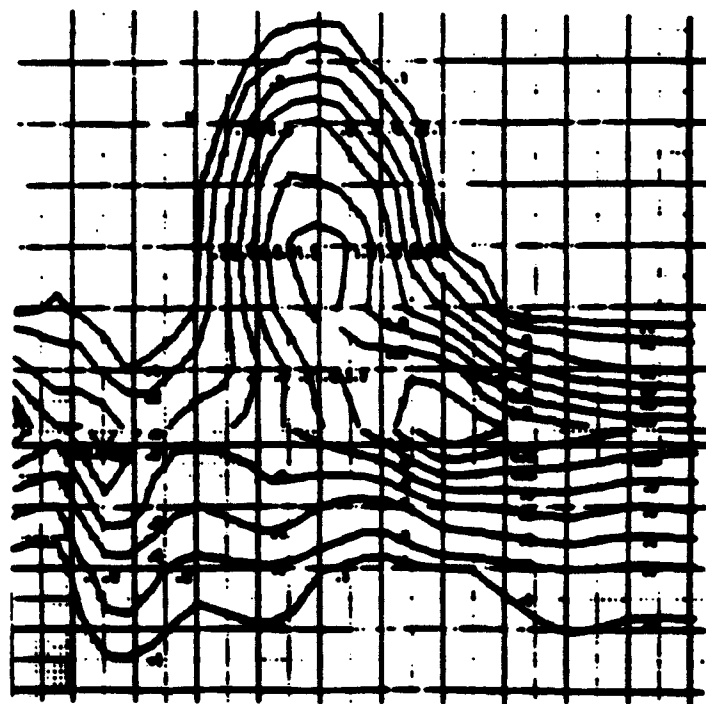


Figure 61: Predicted total pressure loss coefficient contours at exit of turbine passage

HUB



MIDSPAN

Figure 62: Experimental total pressure loss coefficient contours at exit of turbine passage

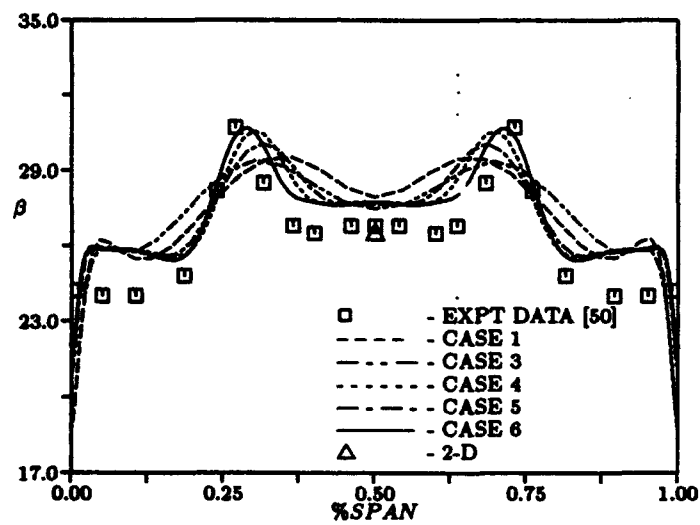


Figure 63: Gap-averaged flow angle distributions for Langston cascade

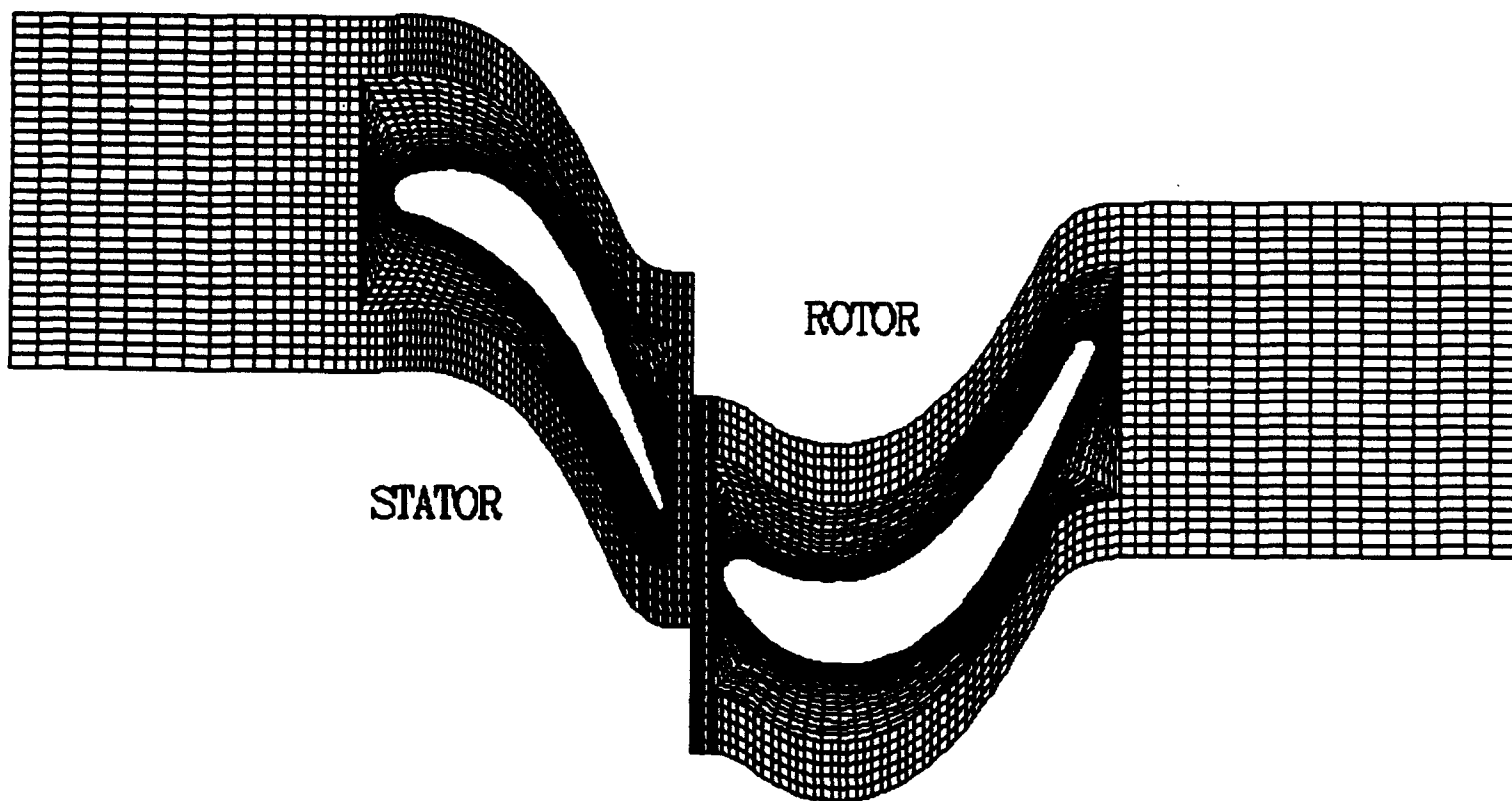


Figure 64: Computational grid topology for 1-stator/1-rotor hot streak simulation

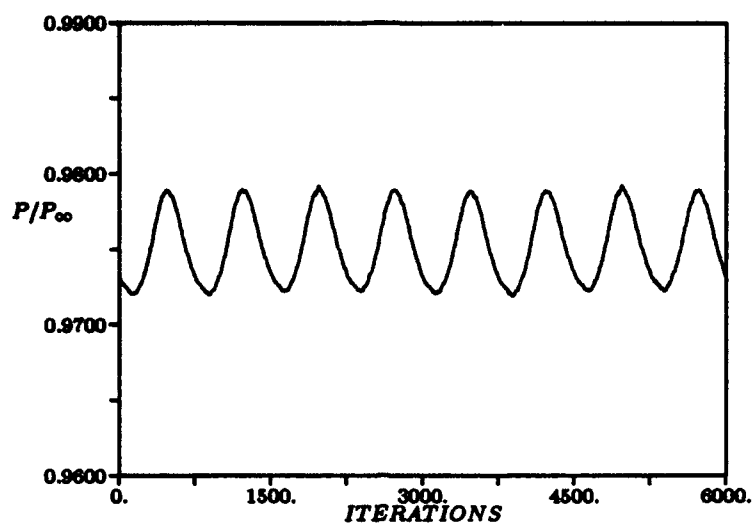


Figure 65: Pressure history for midchord of LSRR stator

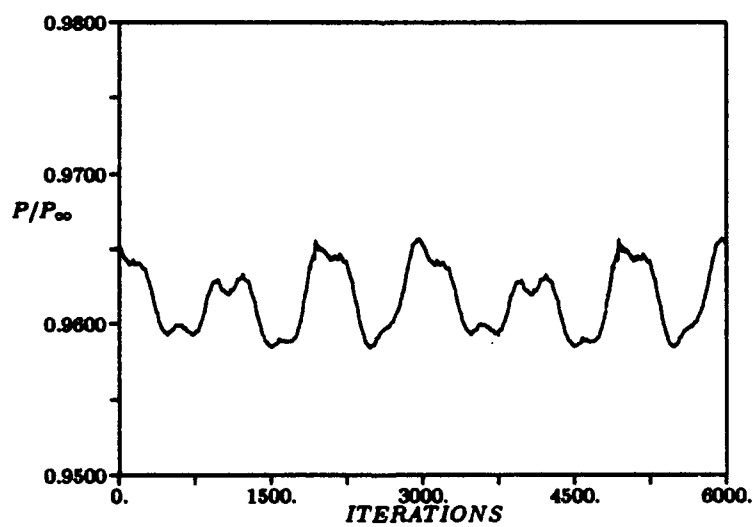


Figure 66: Pressure history for midchord of LSRR rotor

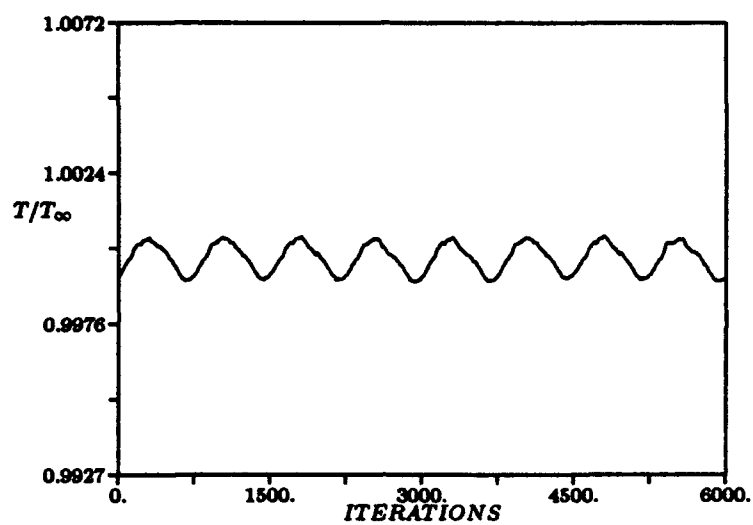


Figure 67: Temperature history for midchord of LSRR stator

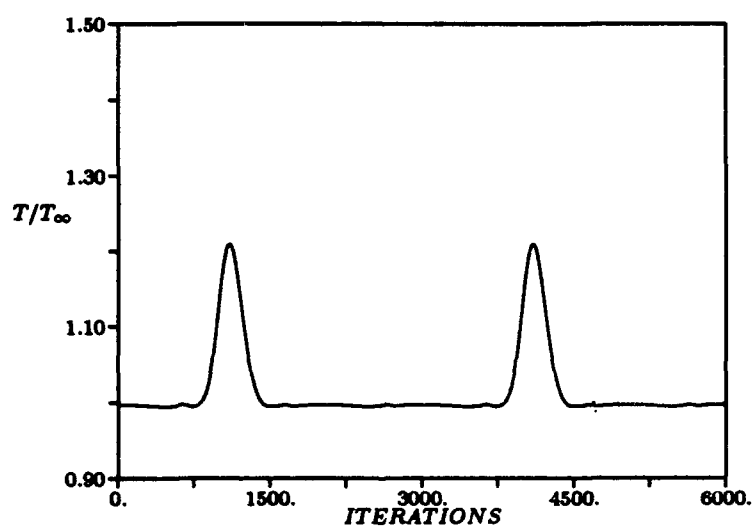


Figure 68: Temperature history for midchord of LSRR rotor

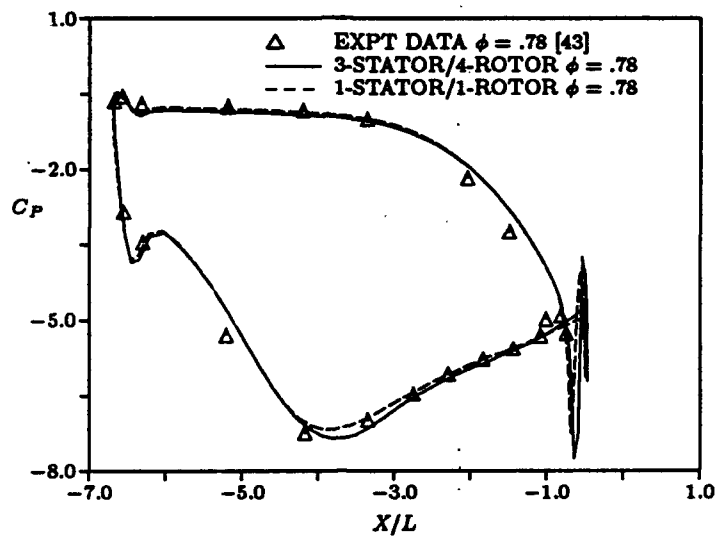


Figure 69: Predicted and experimental blade loading for the LSRR stator

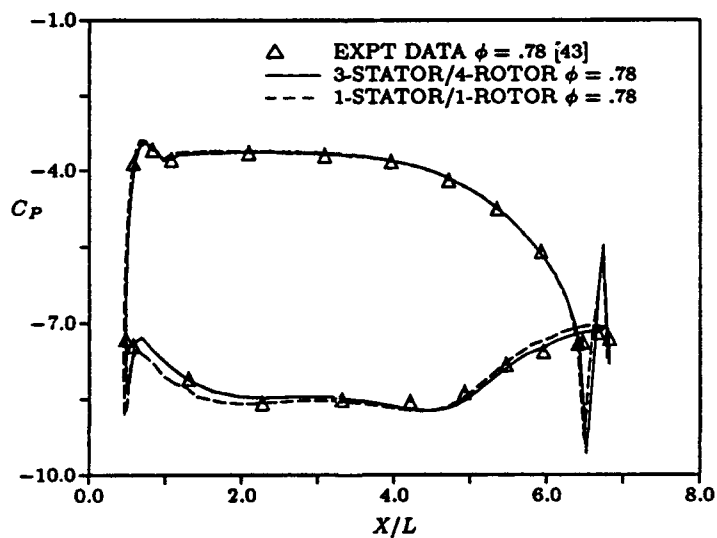


Figure 70: Predicted and experimental blade loading for the LSRR rotor

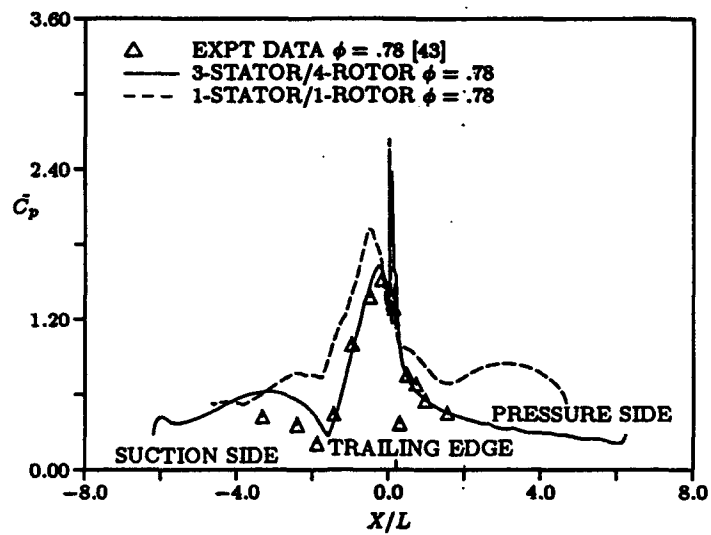


Figure 71: Pressure amplitude coefficient distribution for LSRR stator

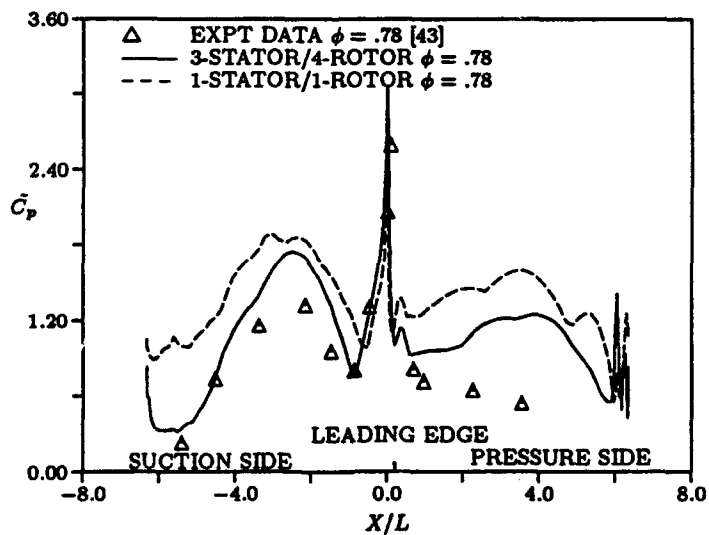


Figure 72: Pressure amplitude coefficient distribution for LSRR rotor

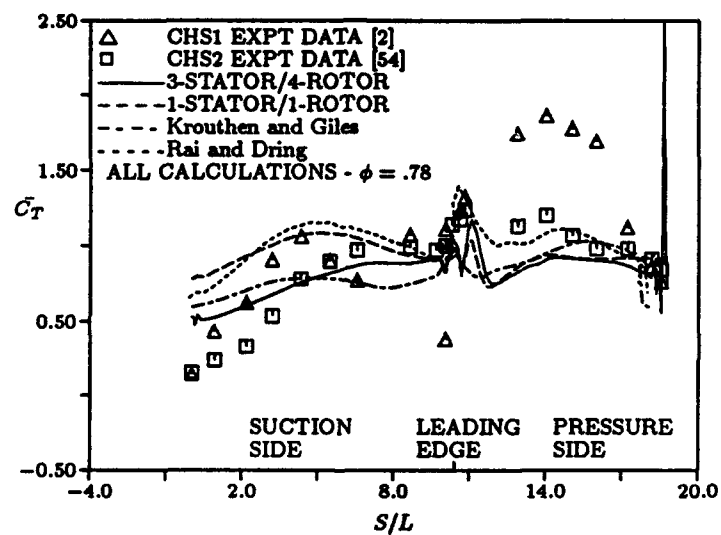


Figure 73: Predicted and experimental time-averaged surface temperature for rotor



Figure 74: Time-averaged static temperature contours for 3-stator/4-rotor hot streak simulation



Figure 75: Static temperature contours for 3-stator/4-rotor hot streak simulation

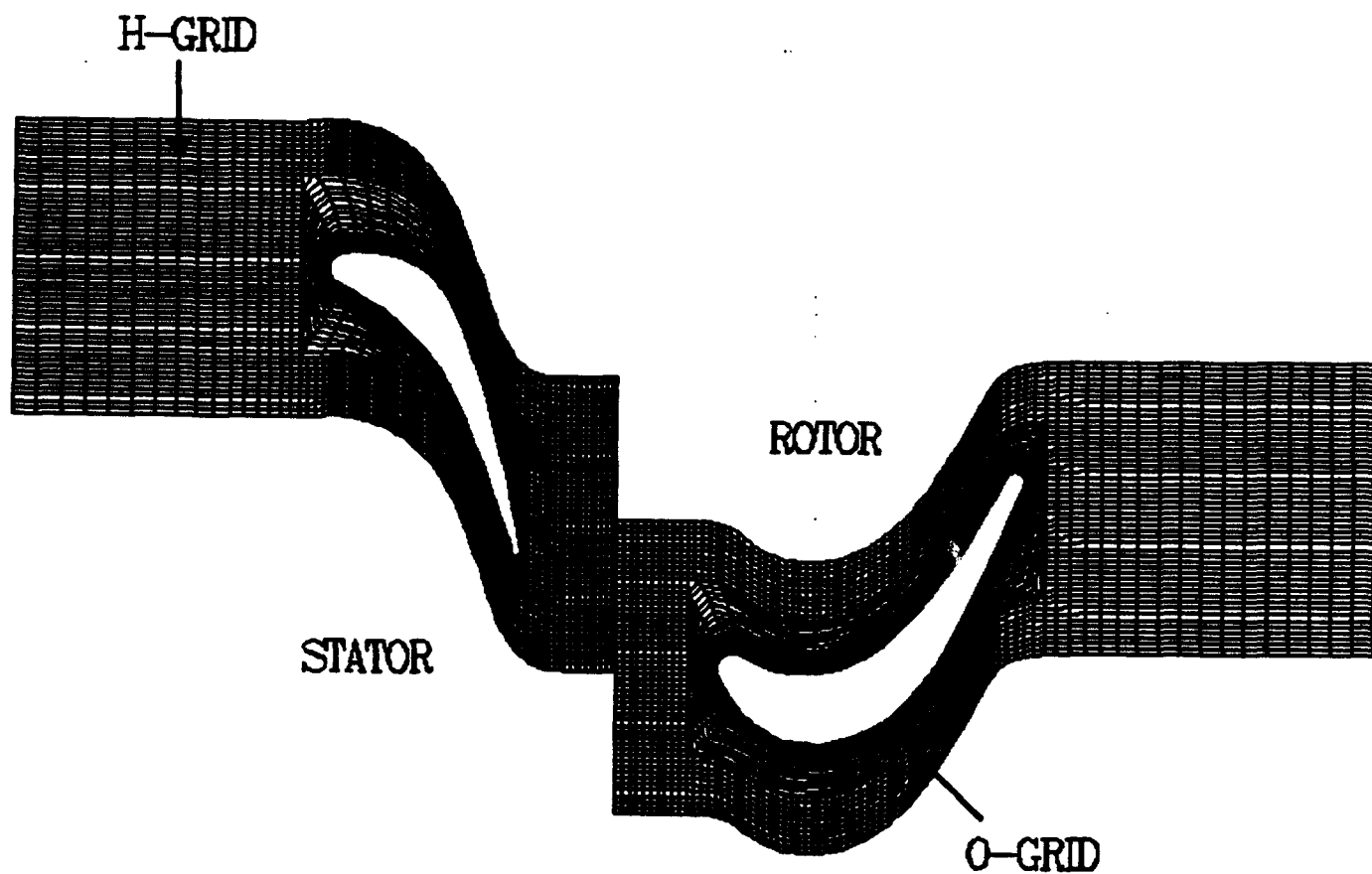


Figure 76: Computational grid for planar hot streak simulation

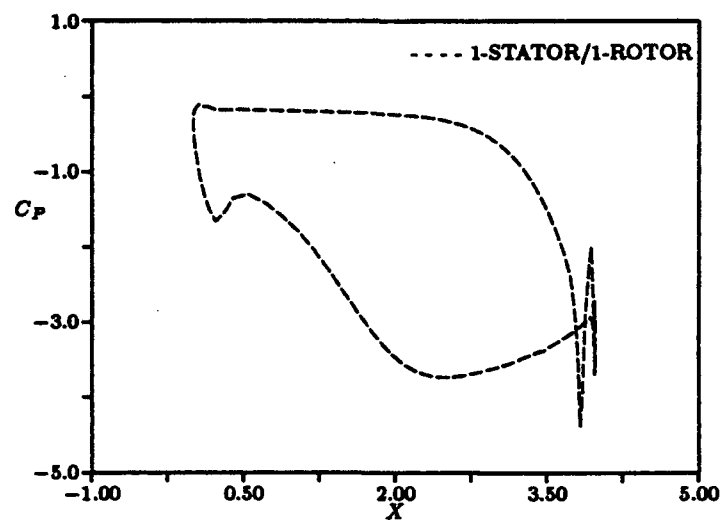


Figure 77: Predicted pressure coefficient distribution for the LSRR stator

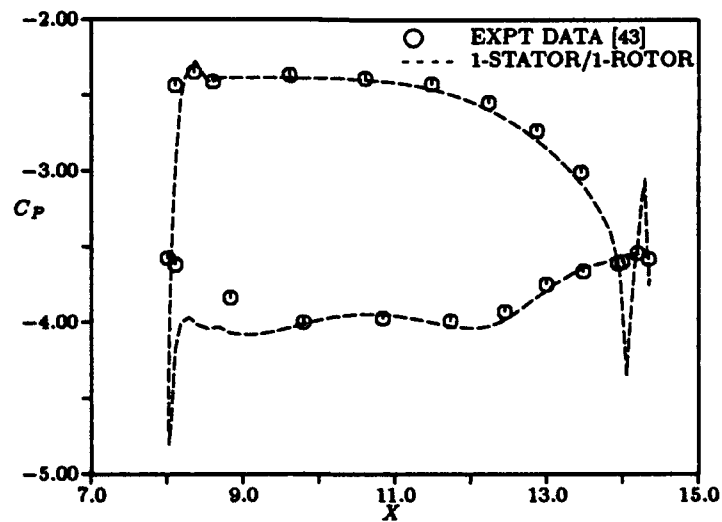


Figure 78: Predicted and experimental pressure coefficient distributions for the LSRR rotor

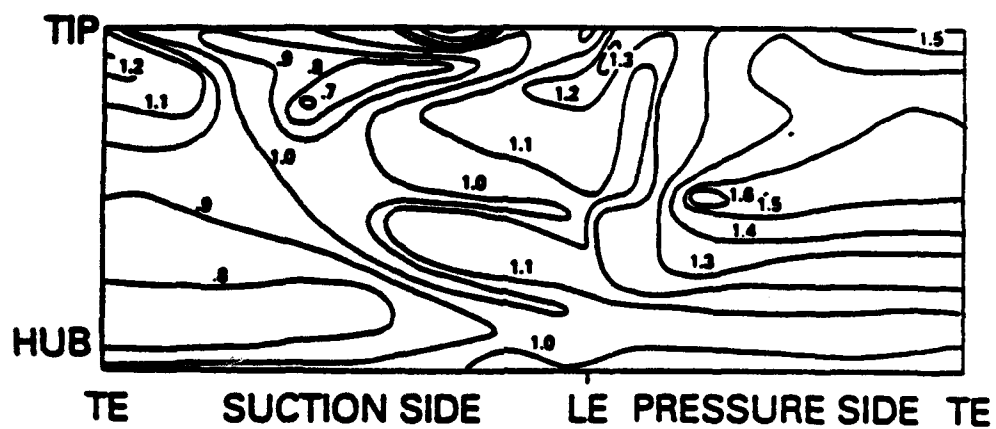


Figure 79: Experimental time-averaged CO_2 contours for the LSRR rotor - planar hot streak

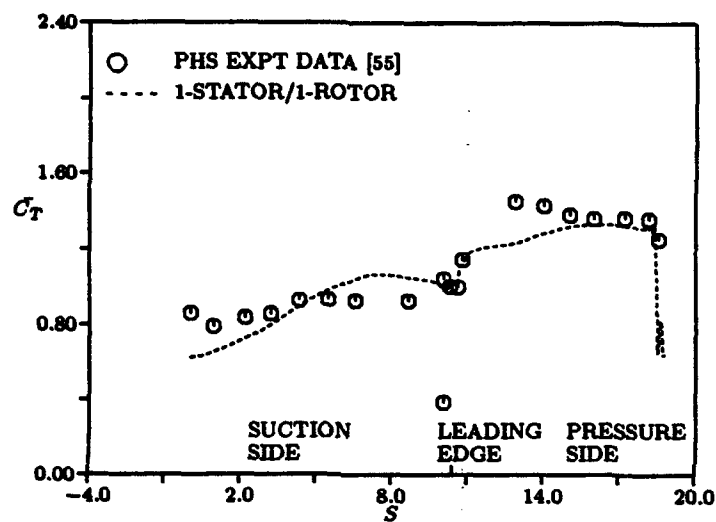


Figure 80: Predicted and experimental rotor surface temperatures for a planar hot streak

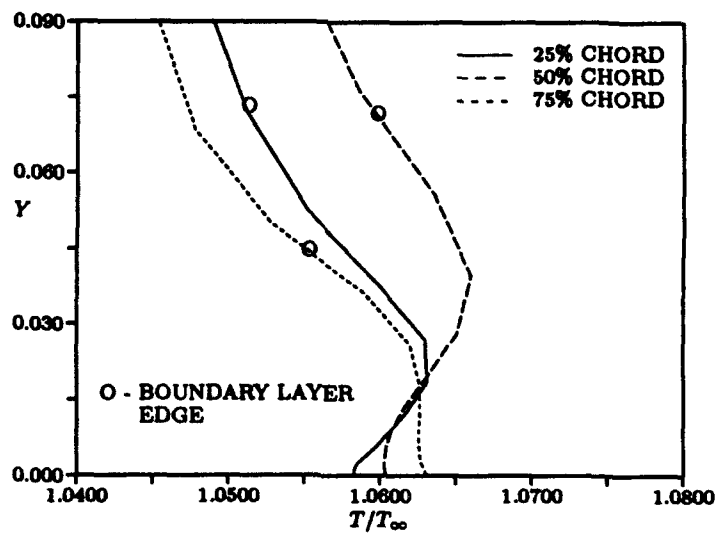


Figure 81: Predicted time-averaged temperature profiles for LSRR rotor - planar hot streak

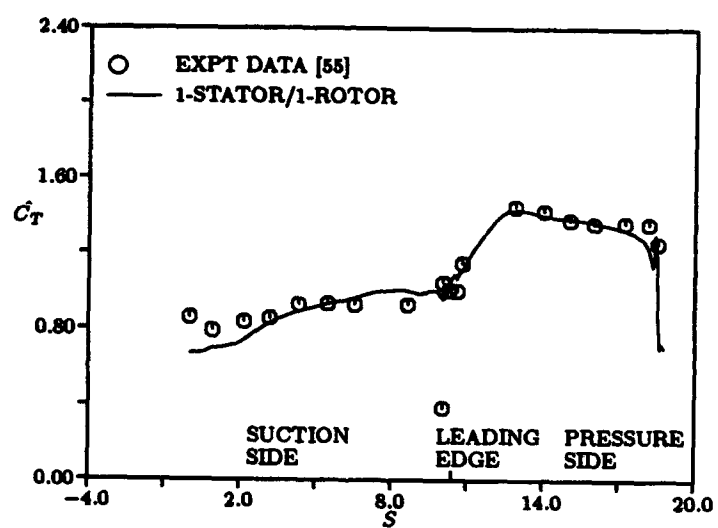


Figure 82: Predicted and experimental rotor surface temperatures for a planar hot streak using new correlation

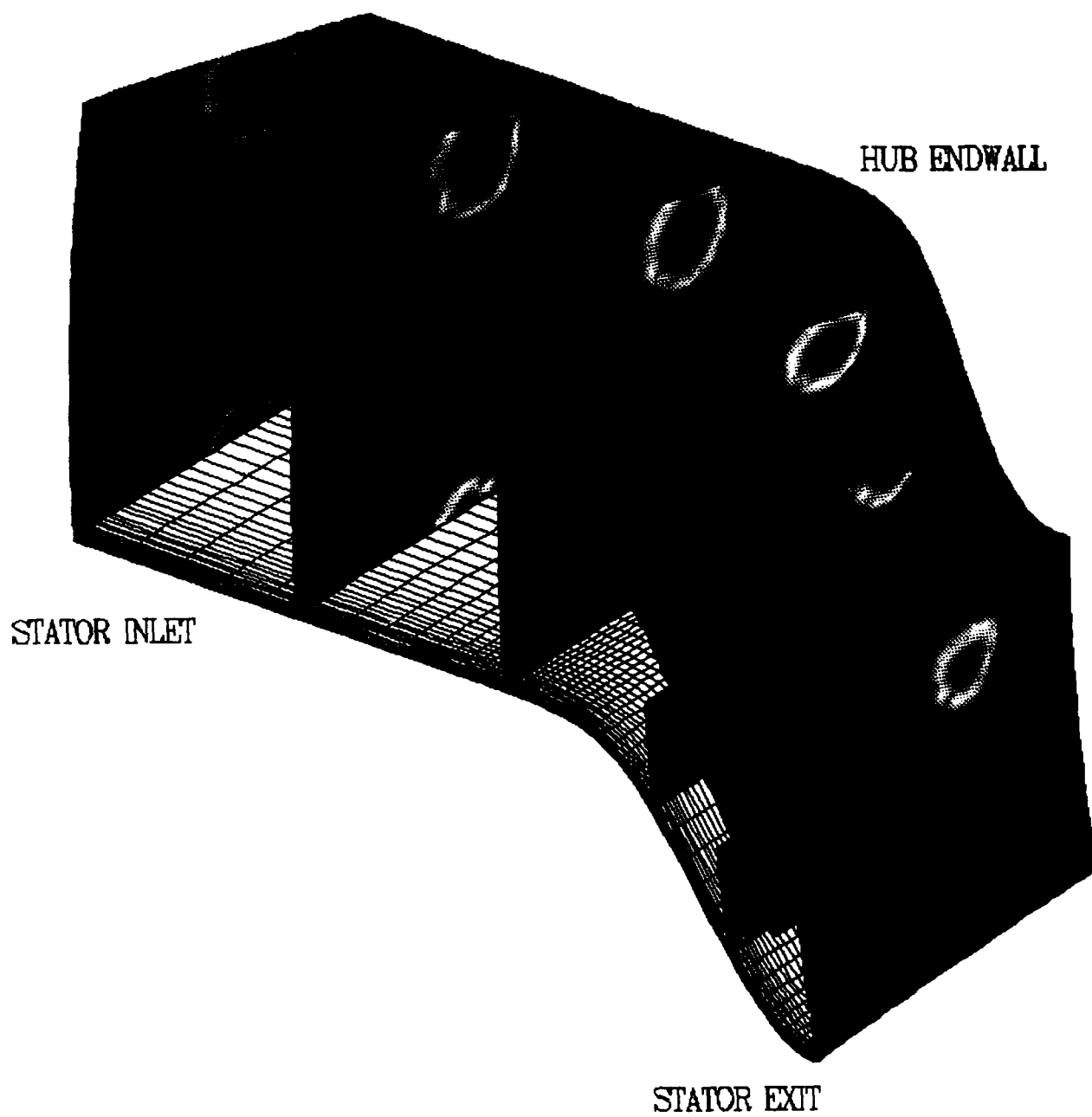


Figure 83: Static temperature contours in stator passage for three-dimensional hot streak simulations

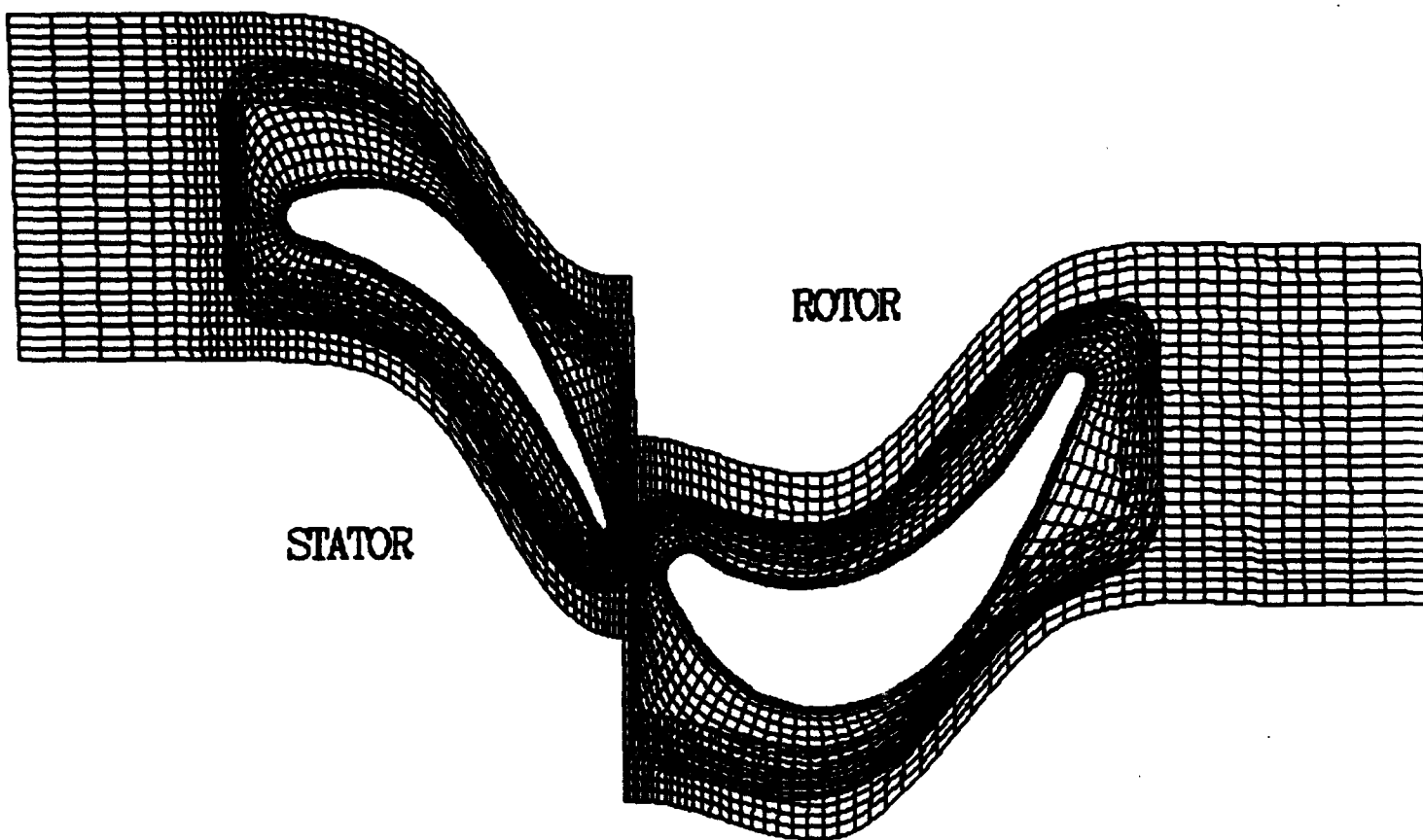


Figure 84: Blade-to-blade computational grid for LSRR turbine

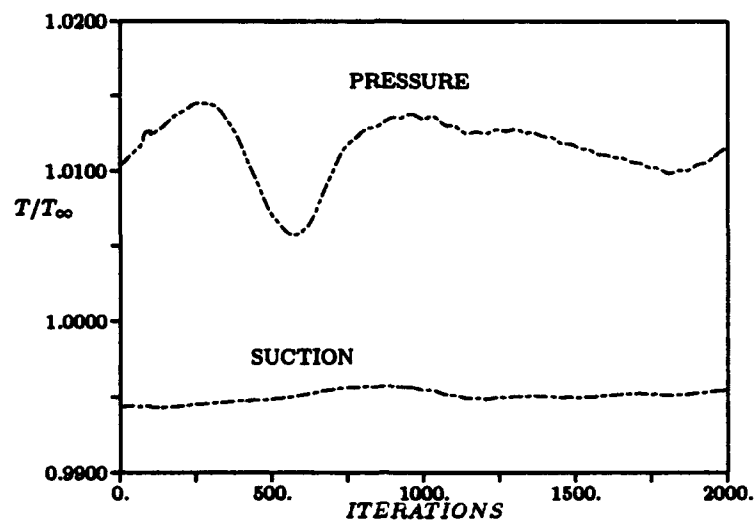


Figure 85: Temperature history at mid-span LSRR rotor surface - 2% span

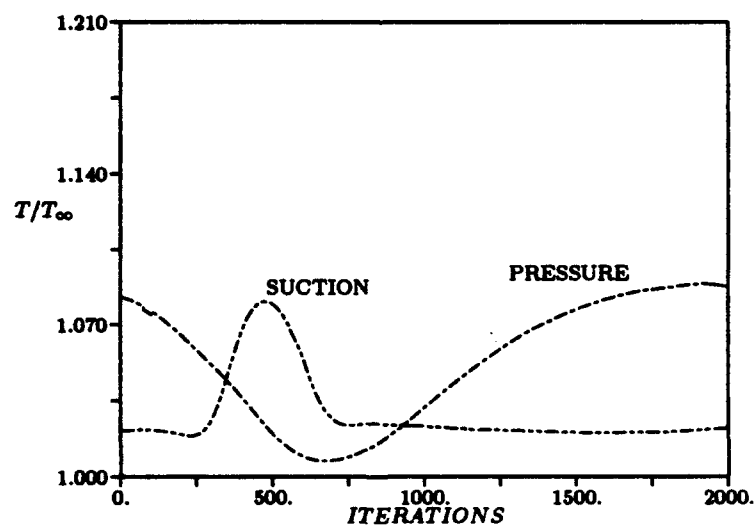


Figure 86: Temperature history at mid-span LSRR rotor surface - 25% span

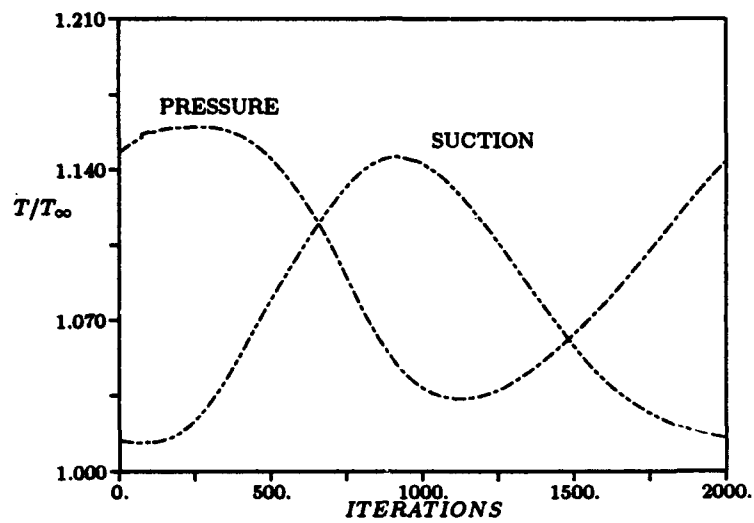


Figure 87: Temperature history at mid-span LSRR rotor surface - 50% span

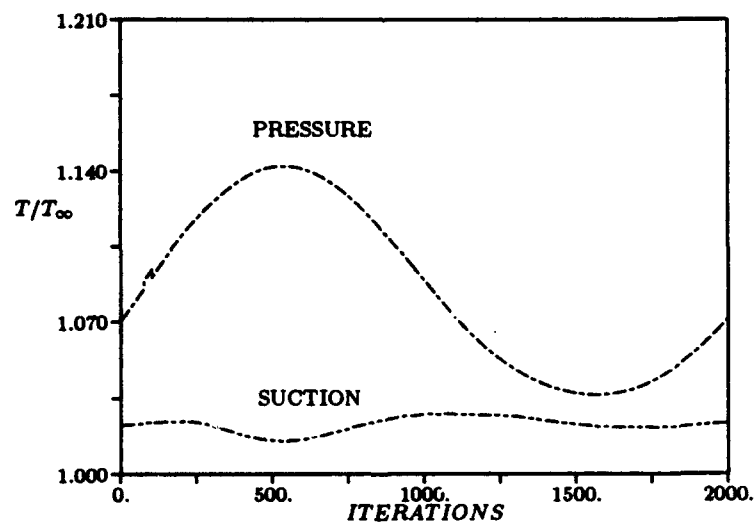


Figure 88: Temperature history at mid-span LSRR rotor surface - 75% span

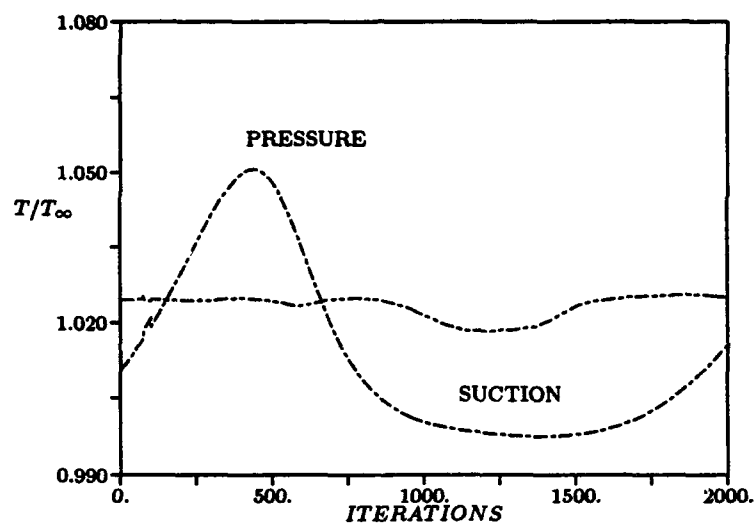


Figure 89: Temperature history at mid-span LSRR rotor surface - 98% span

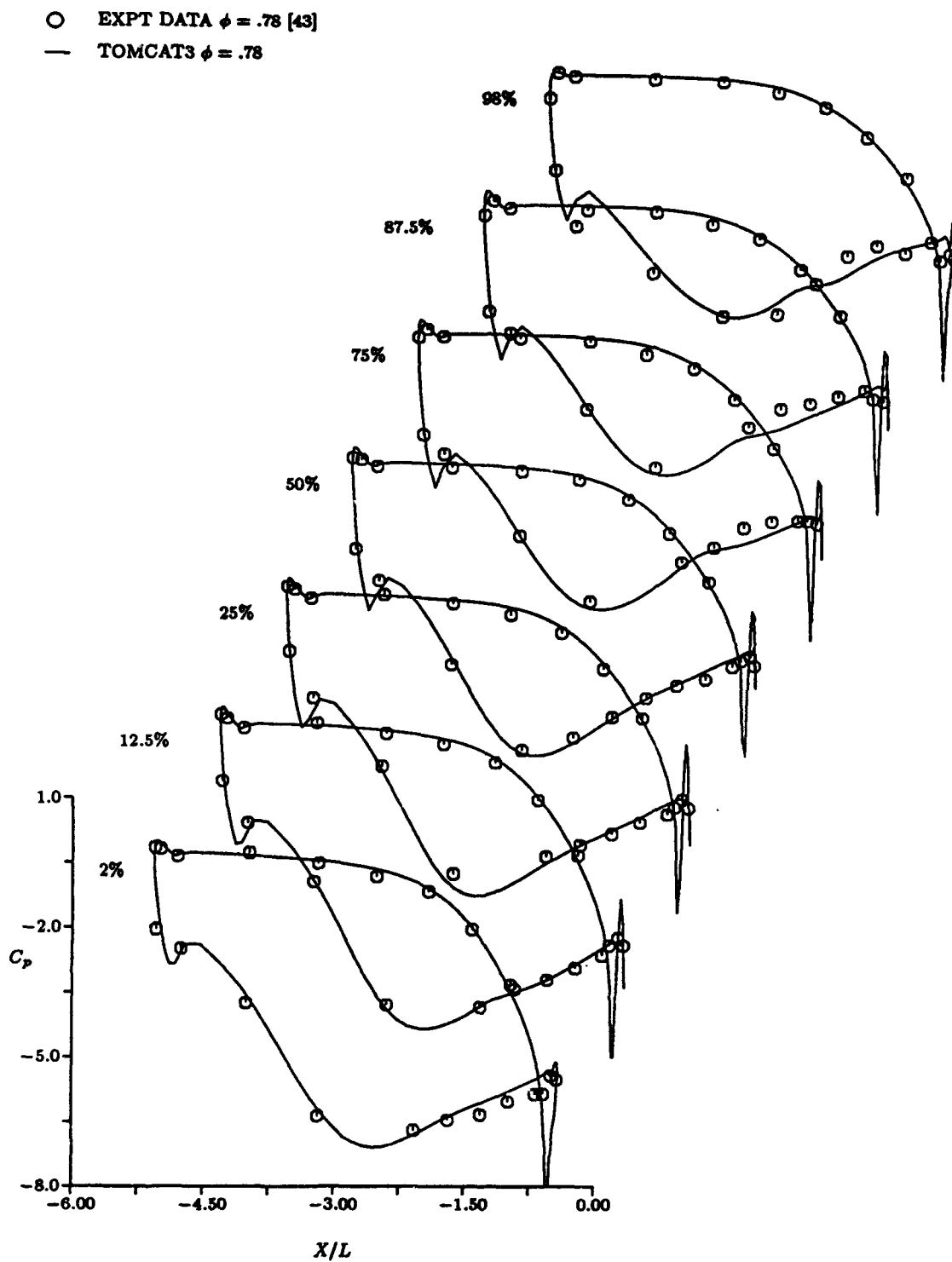


Figure 90: Time-averaged pressure coefficient distribution for LSRR stator

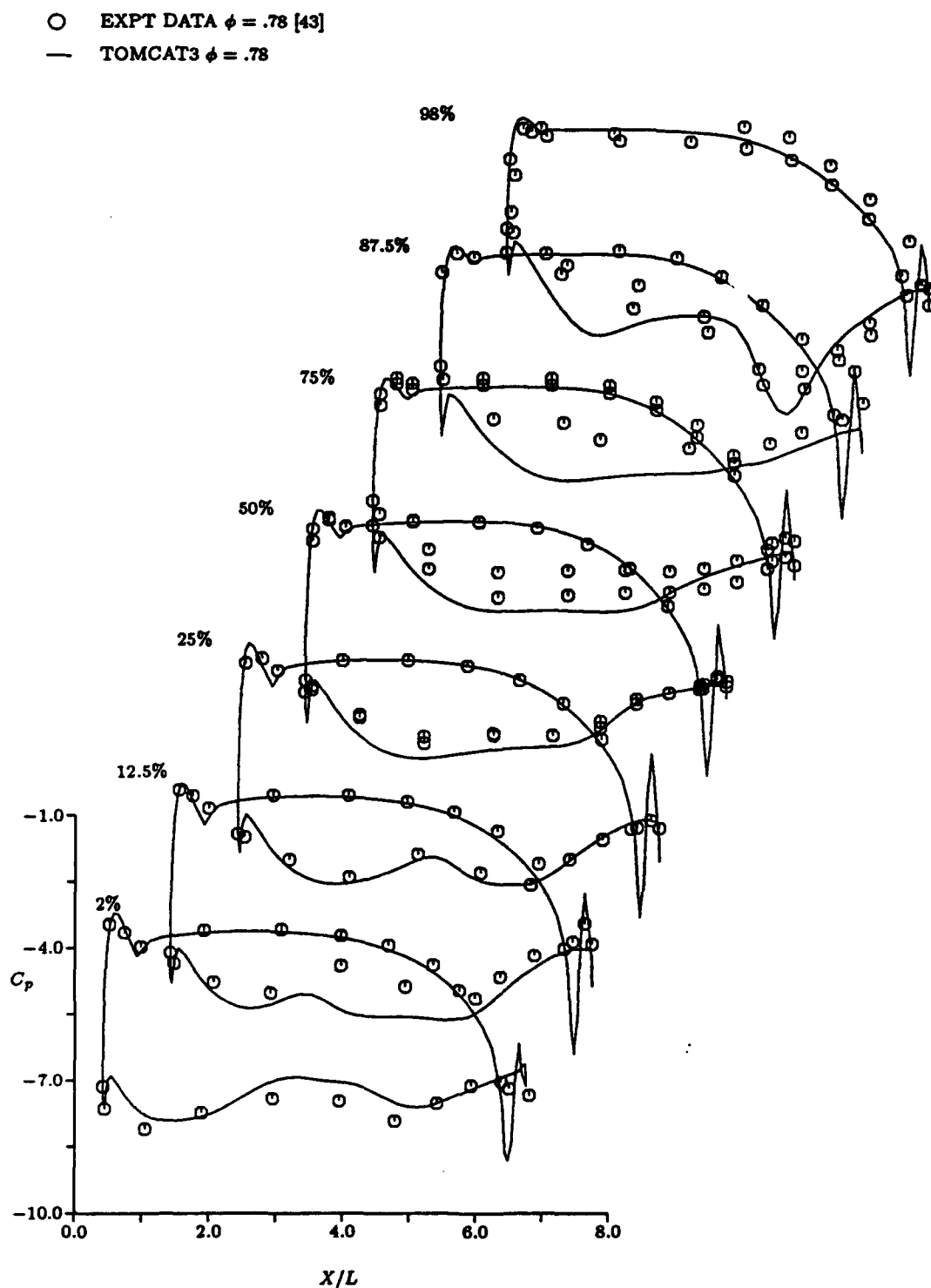


Figure 91: Time-averaged pressure coefficient distribution for LSRR rotor

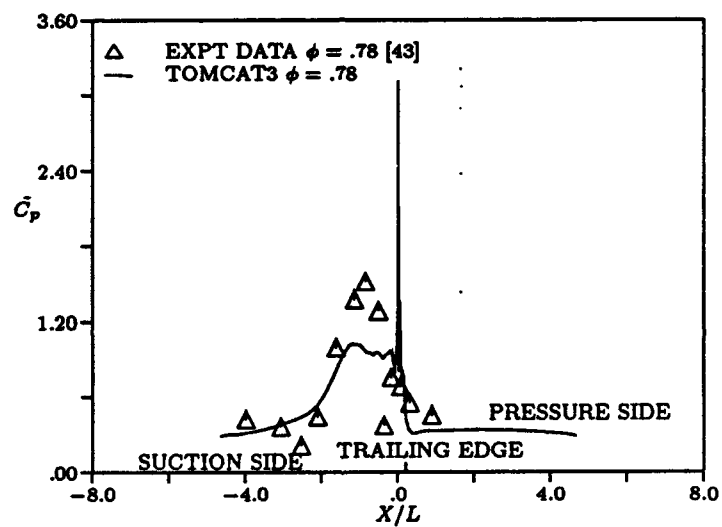


Figure 92: Pressure amplitude coefficient for mid-span stator section of LSRR

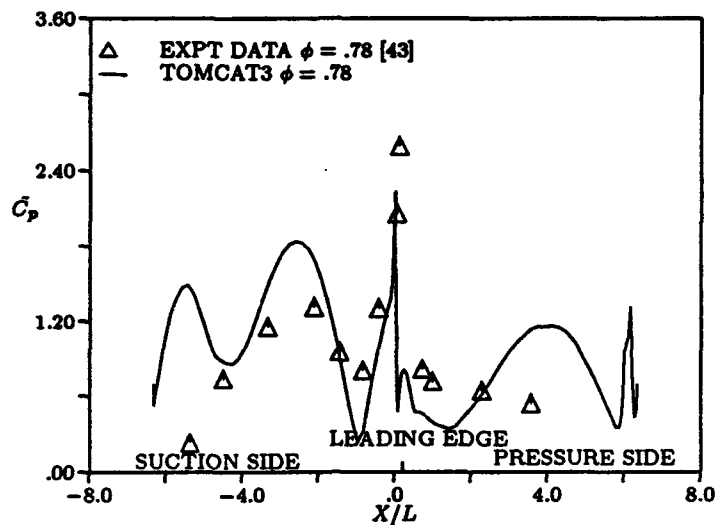


Figure 93: Pressure amplitude coefficient for mid-span rotor section of LSRR

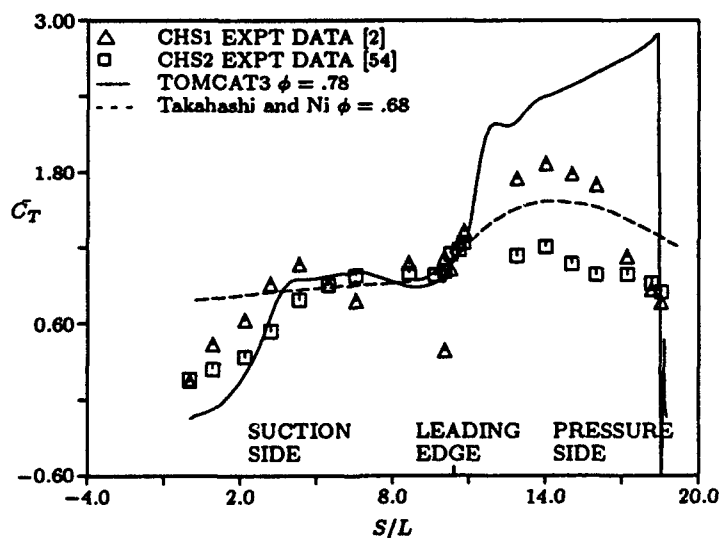


Figure 94: Predicted and experimental time-averaged surface temperature for LSRR rotor mid-span section

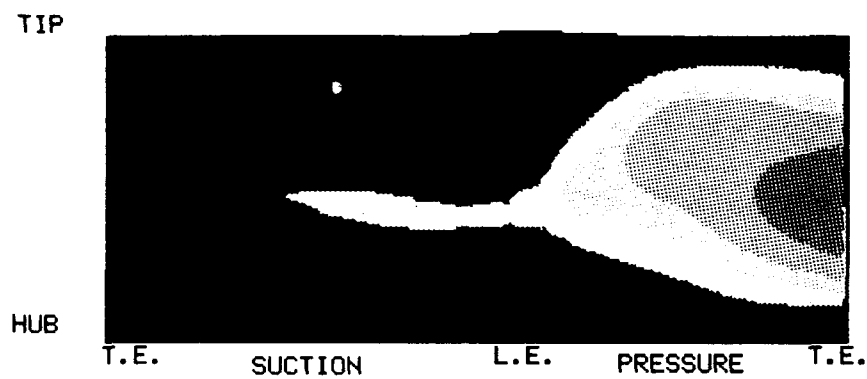


Figure 95: Predicted time-averaged surface temperature contours for LSRR rotor

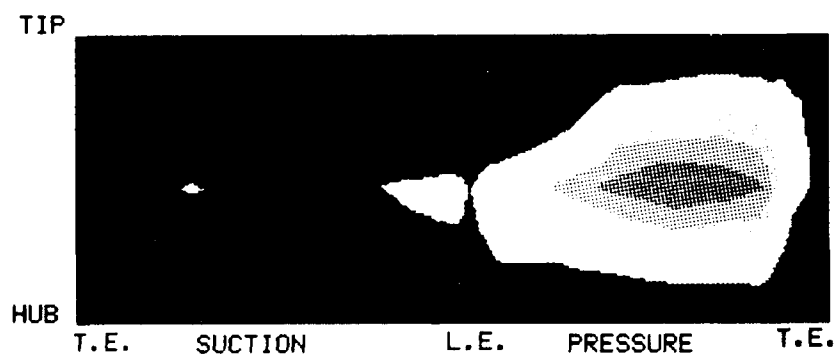


Figure 96: Experimental time-averaged surface temperature contours for LSRR rotor

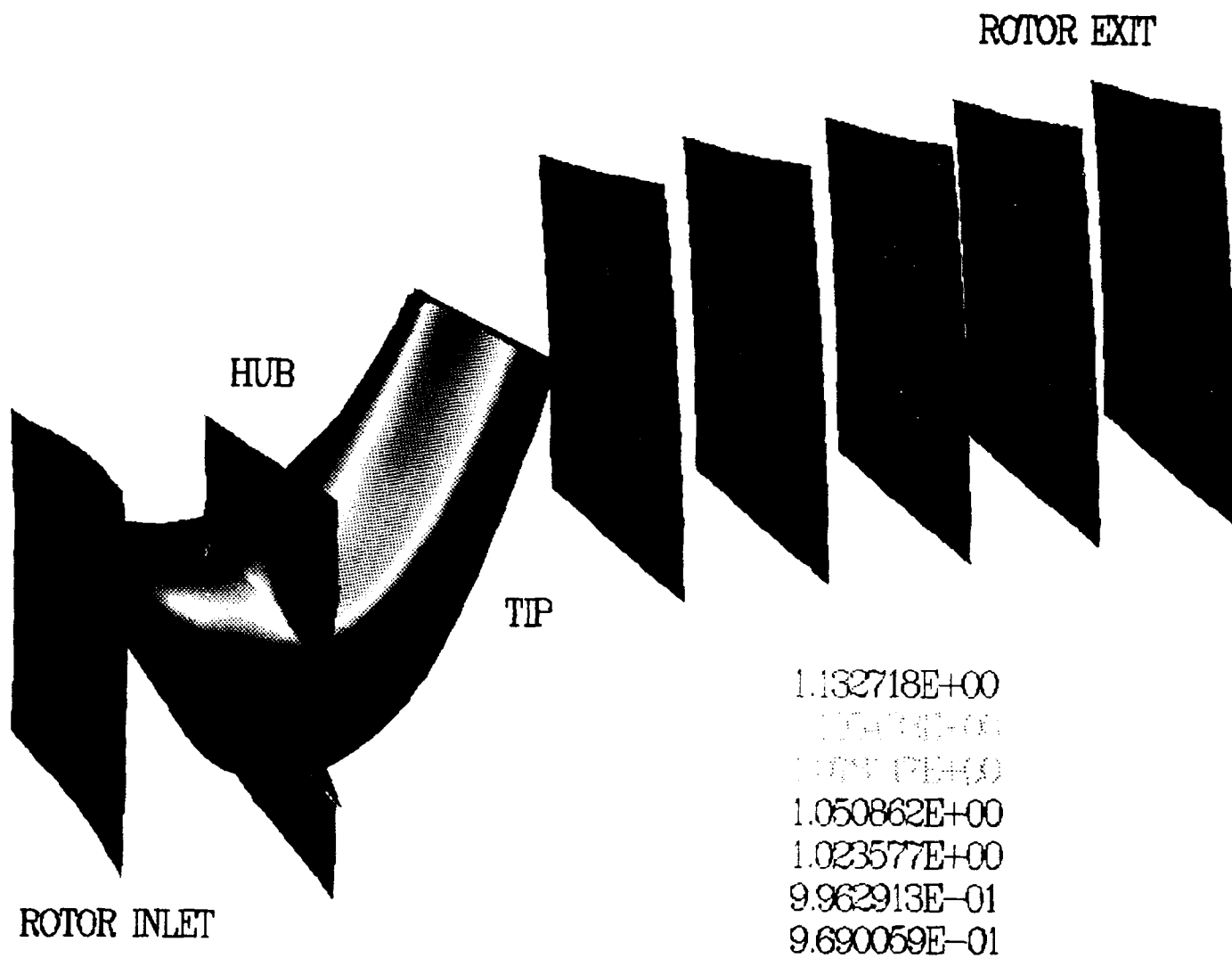


Figure 97: Rotor pressure surface time-averaged temperature contours - adiabatic simulation



0%



50%



25%



75%

Figure 98: $T = 1.05$ Isotherm for adiabatic 3-D hot streak simulation (rotor suction side)



0%



50%



25%



75%

Figure 99: $T = 1.05$ Isotherm for adiabatic 3-D hot streak simulation (rotor pressure side)

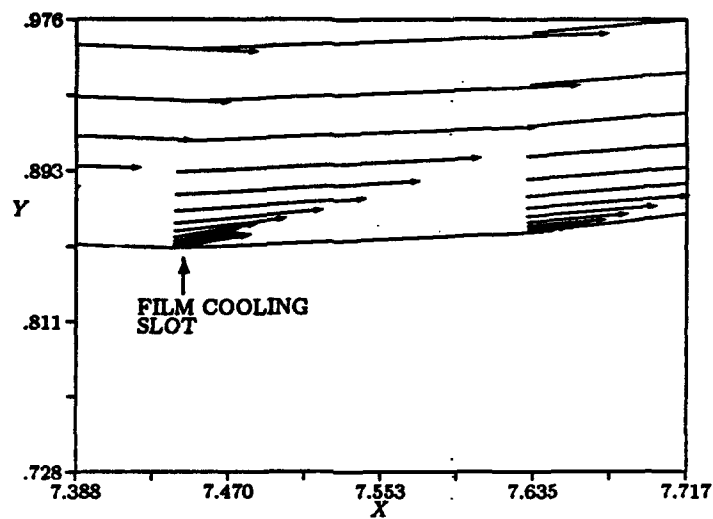


Figure 100: Time-averaged velocity vectors in the vicinity of the film cooling hole

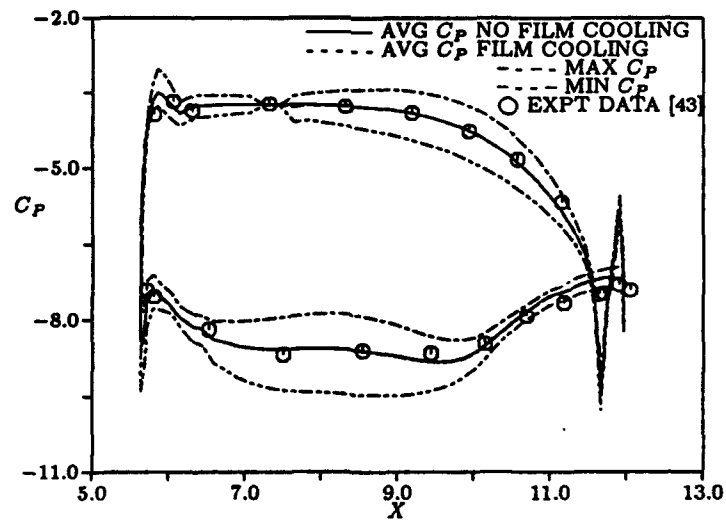


Figure 101: Rotor pressure surface time-averaged, maximum, and minimum coefficient distributions

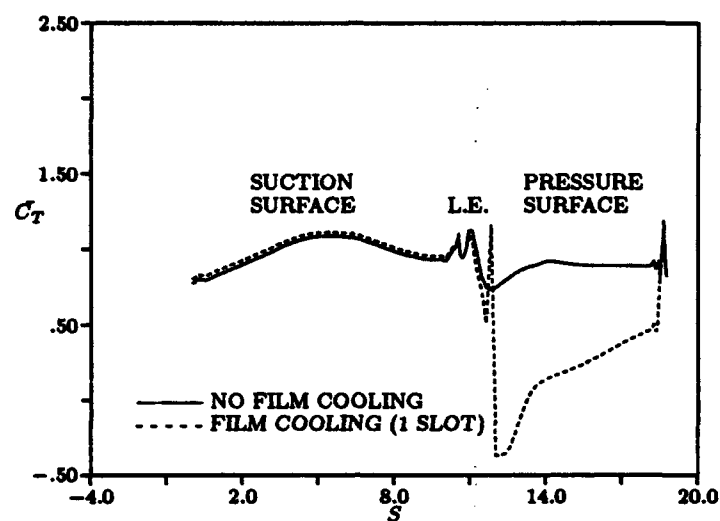


Figure 102: Temperature coefficient distributions for film cooling simulation

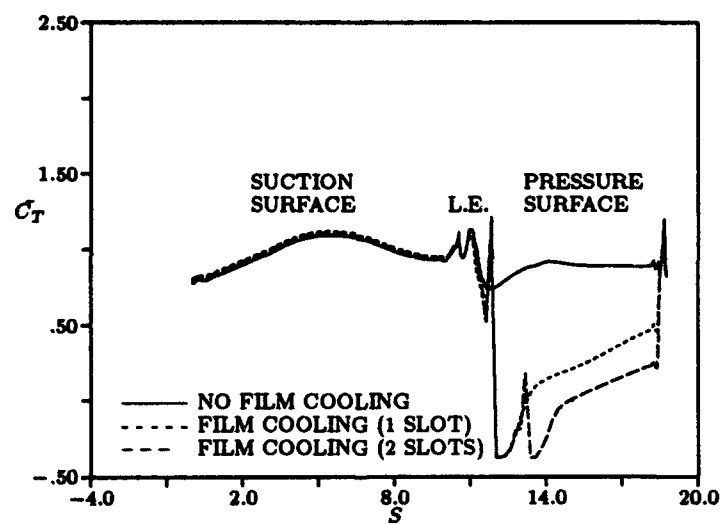


Figure 103: Temperature coefficient distributions for film cooling simulations

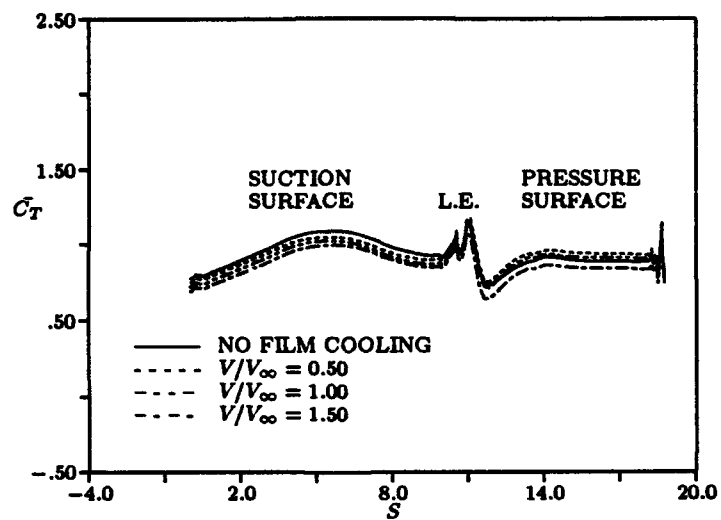


Figure 104: Temperature coefficient distributions for film cooling simulations

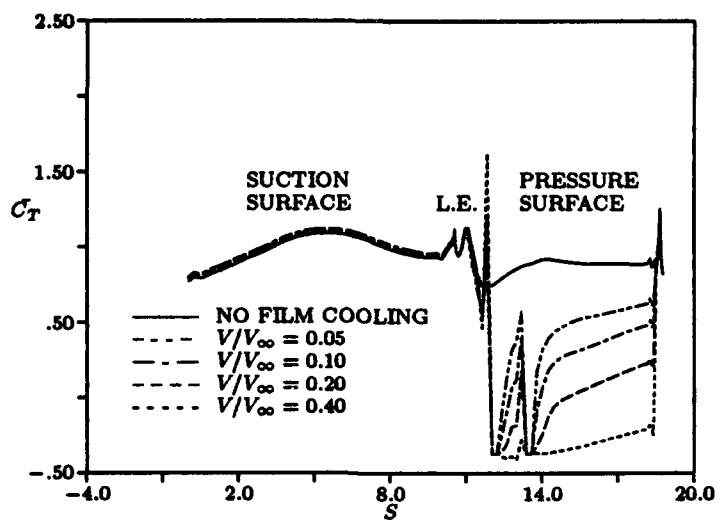


Figure 105: Temperature coefficient distributions for film cooling simulations

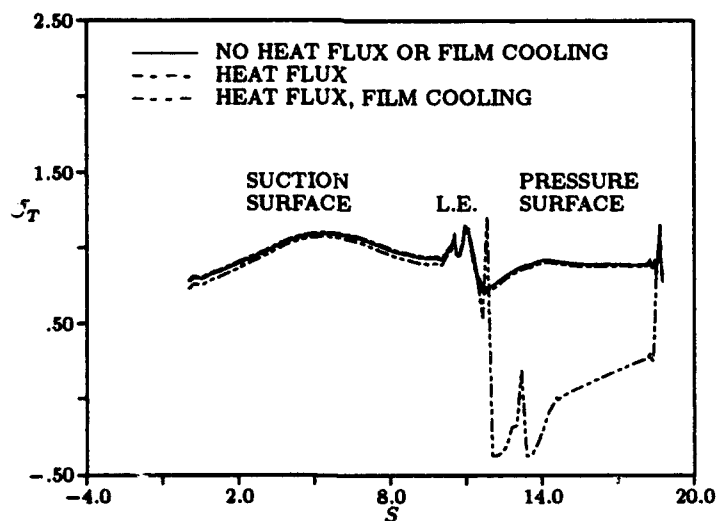


Figure 106: Temperature coefficient distributions for film cooling simulations

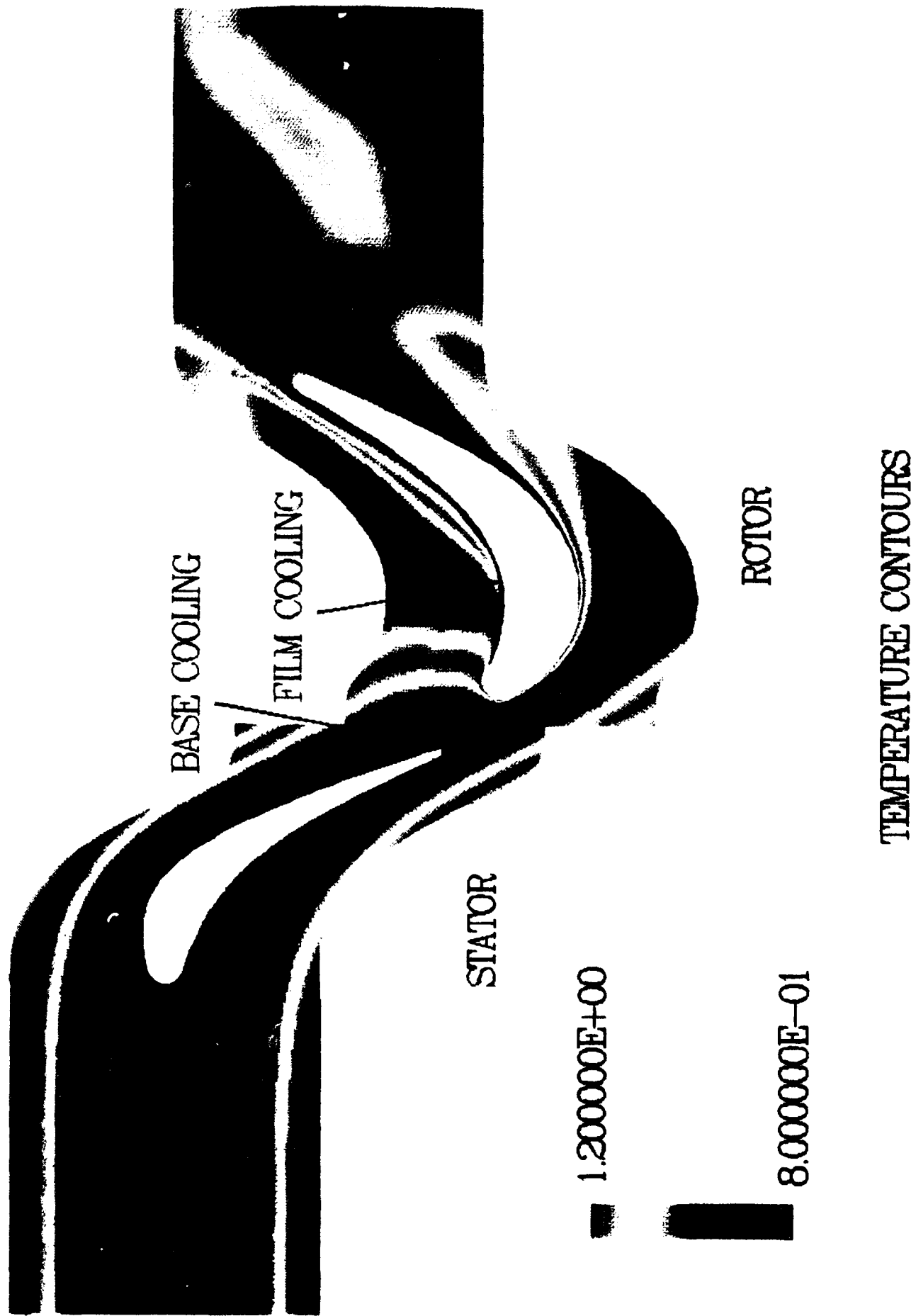


Figure 107: Static temperature contours for LSRR turbine stage - heat flux, film cooling

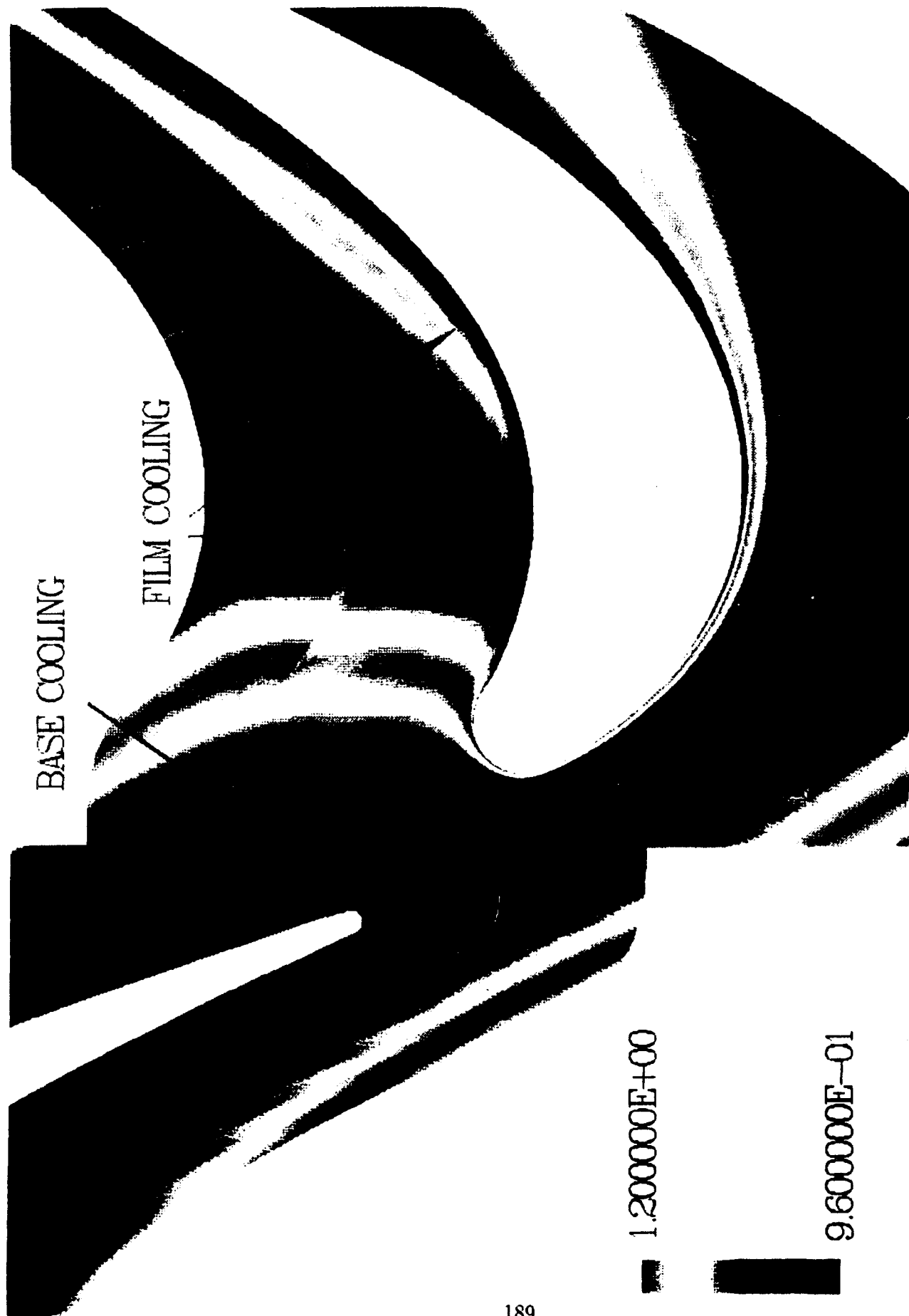


Figure 108: Static temperature contours for LSRR turbine stage - heat flux, film cooling

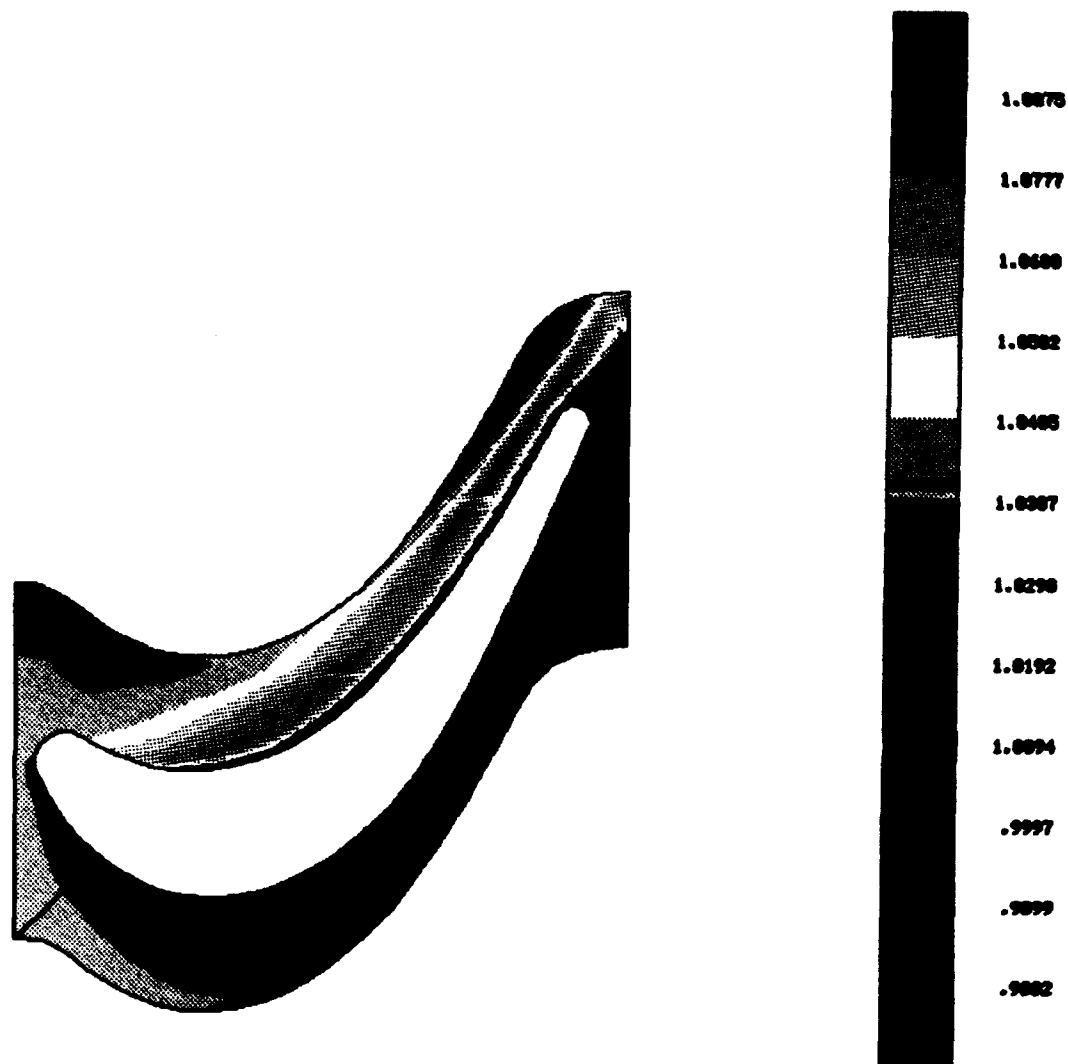


Figure 109: Time-averaged temperature contours for LSRR rotor passage - heat transfer, film cooling

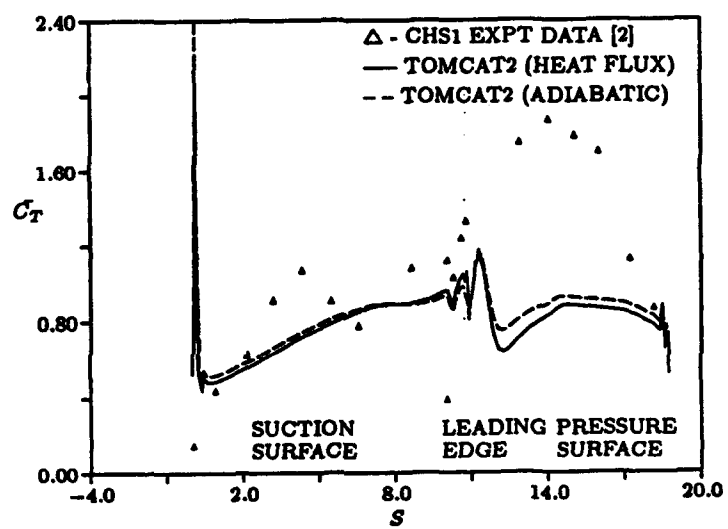


Figure 110: Temperature coefficient distribution for 3-stator/4-rotor LSRR simulation with a heat flux



Figure 111: Static temperature contours for 3-stator/4-rotor LSRR simulation with a heat flux and film cooling

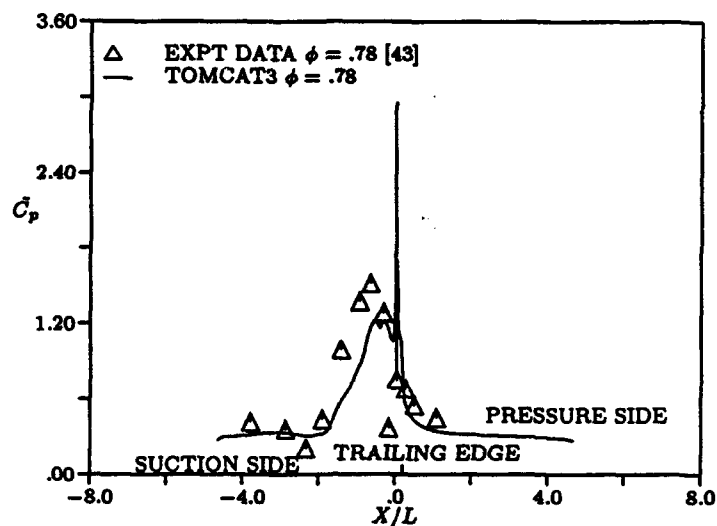


Figure 112: Pressure amplitude coefficient for mid-span stator section of LSRR - heat flux

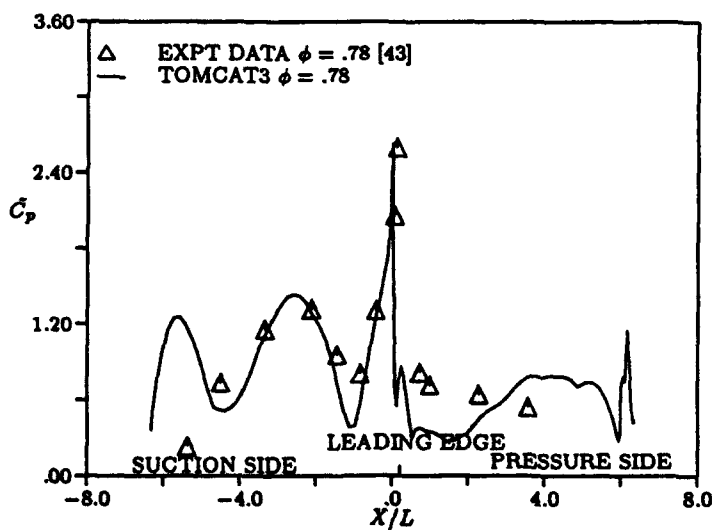


Figure 113: Pressure amplitude coefficient for mid-span rotor section of LSRR - heat flux

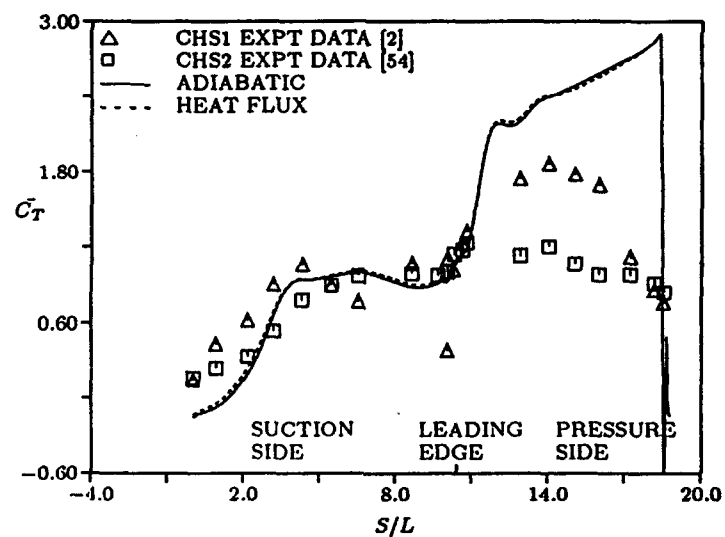


Figure 114: Rotor mid-span time-averaged temperature distributions - heat flux

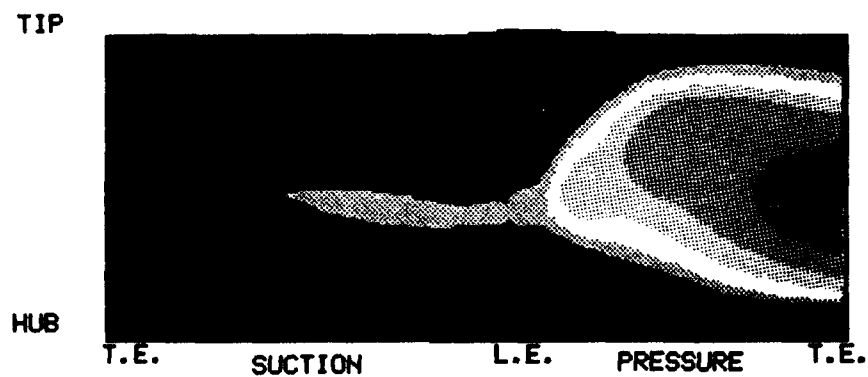


Figure 115: Time-averaged temperature contours for rotor surface - heat flux

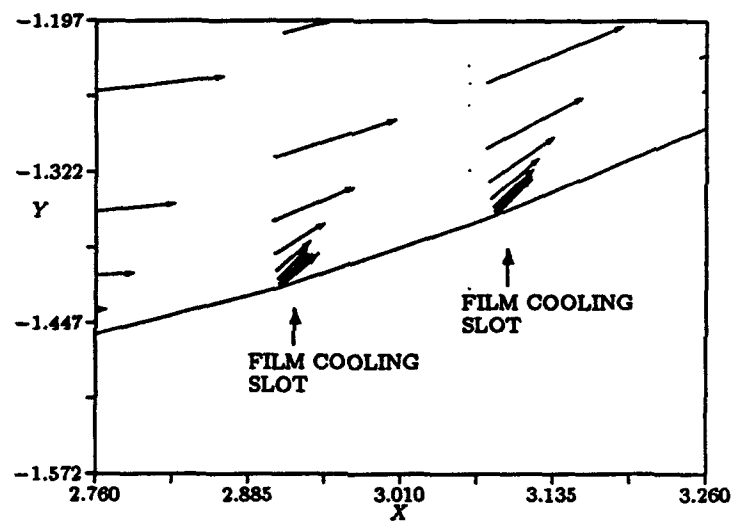


Figure 116: Time-averaged velocity vectors in the vicinity of mid-span film cooling hole

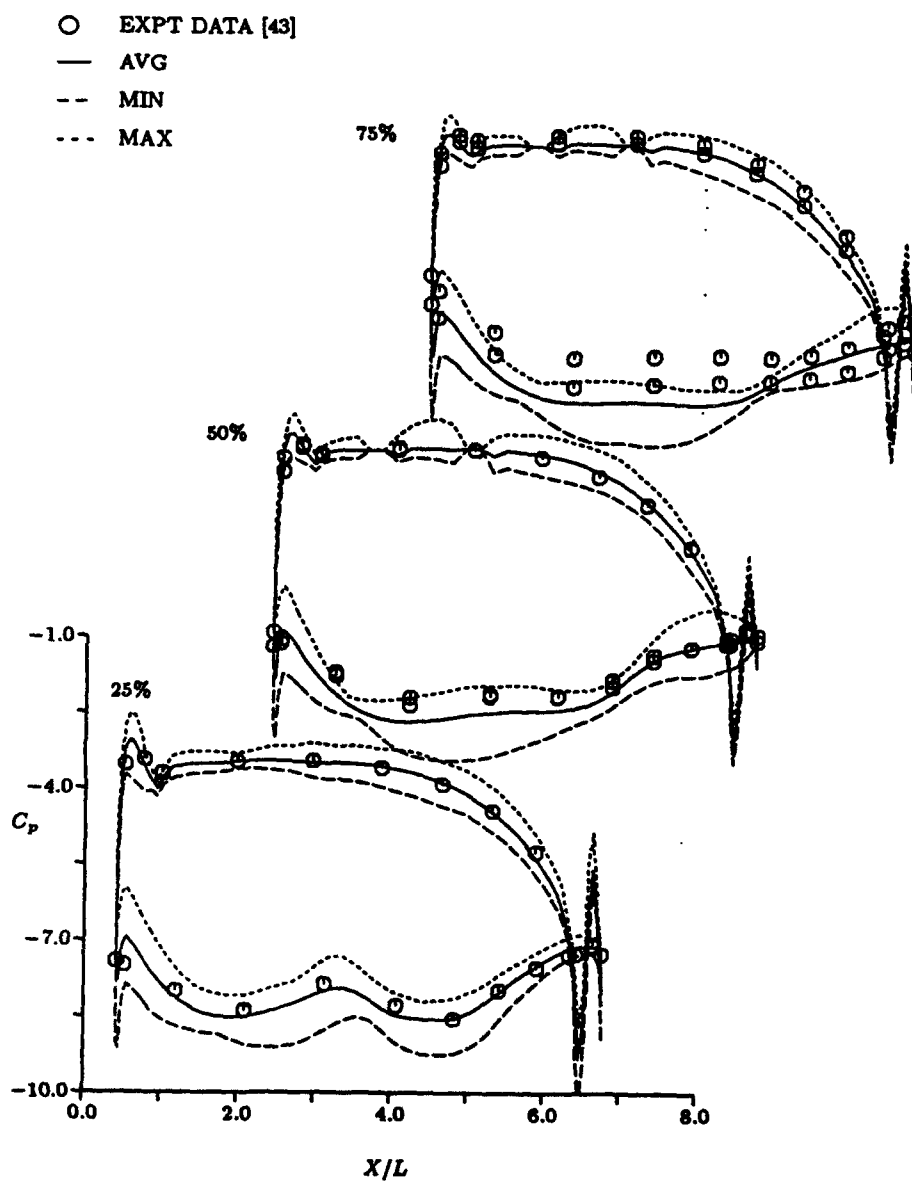


Figure 117: Time-averaged, minimum and maximum pressure coefficient distribution for LSRR rotor - 2 rows film cooling (f.c.)

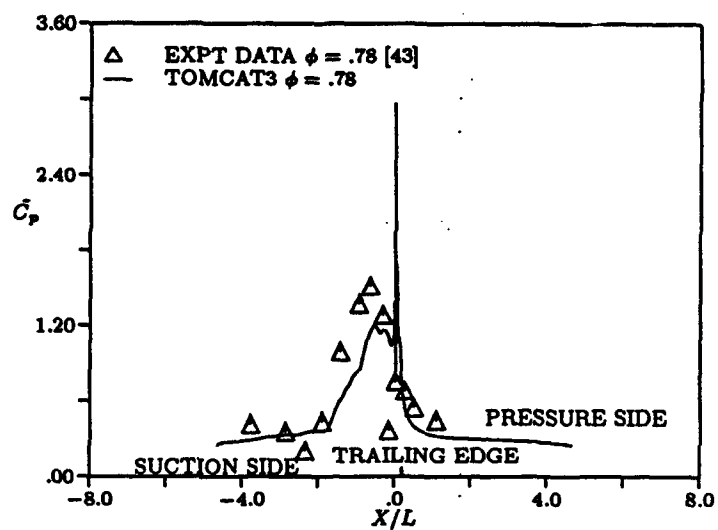


Figure 118: Pressure amplitude coefficient for stator mid-span - 2 rows f.c.

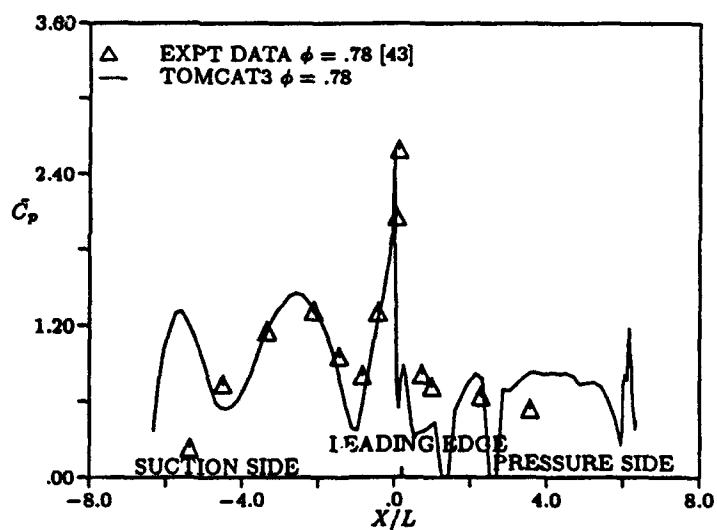


Figure 119: Pressure amplitude coefficient for rotor mid-span - 2 rows f.c.

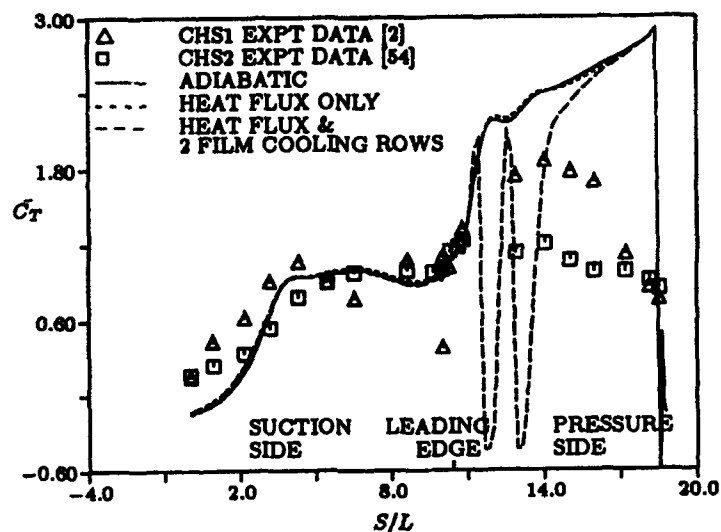


Figure 120: Mid-span rotor time-averaged temperature distribution - 2 rows f.c.

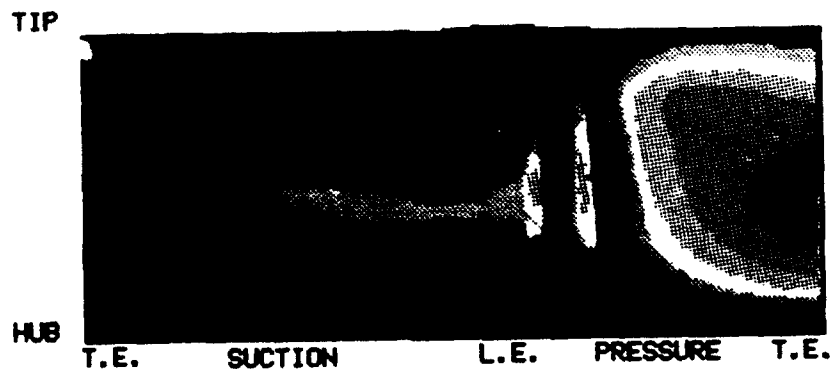


Figure 121: Time-averaged temperature contours for rotor surface - 2 rows f.c.

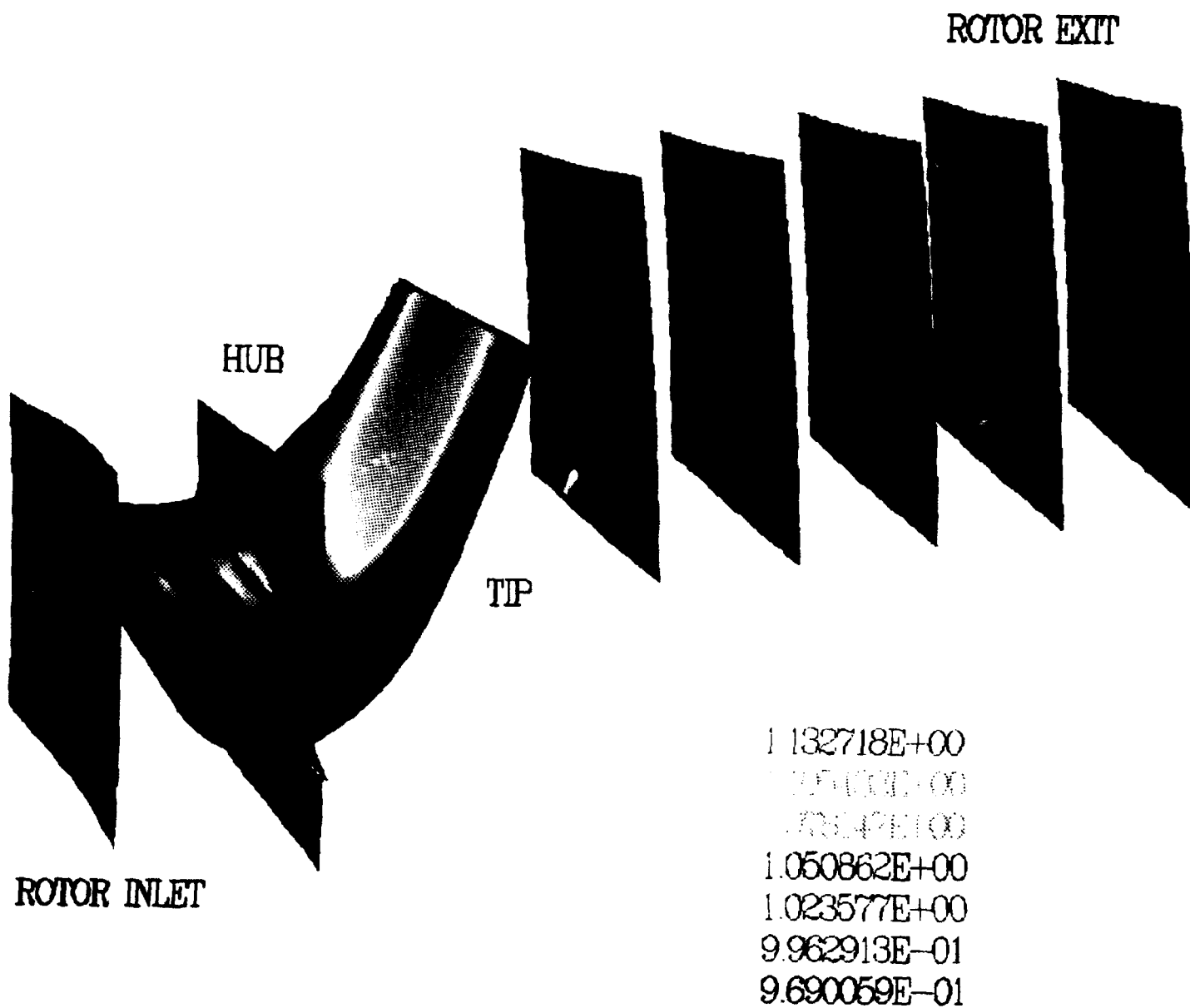


Figure 122: Rotor pressure surface time-averaged temperature contours - 2 rows f.c.

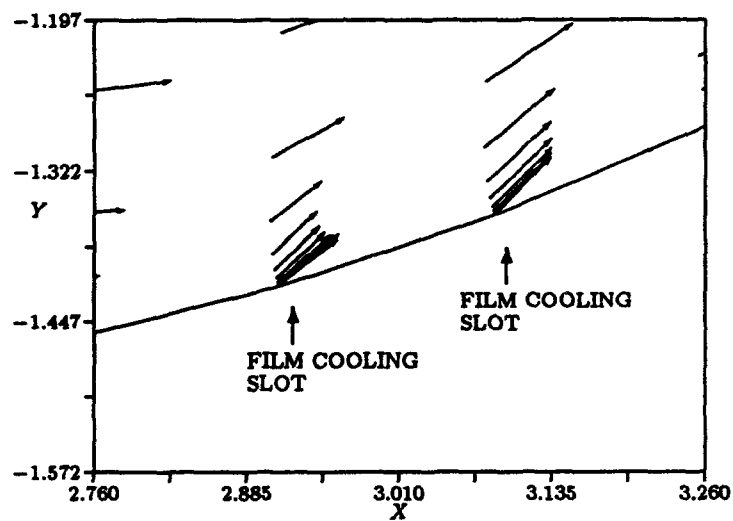


Figure 123: Time-averaged velocity vectors in the vicinity of mid-span film cooling hole

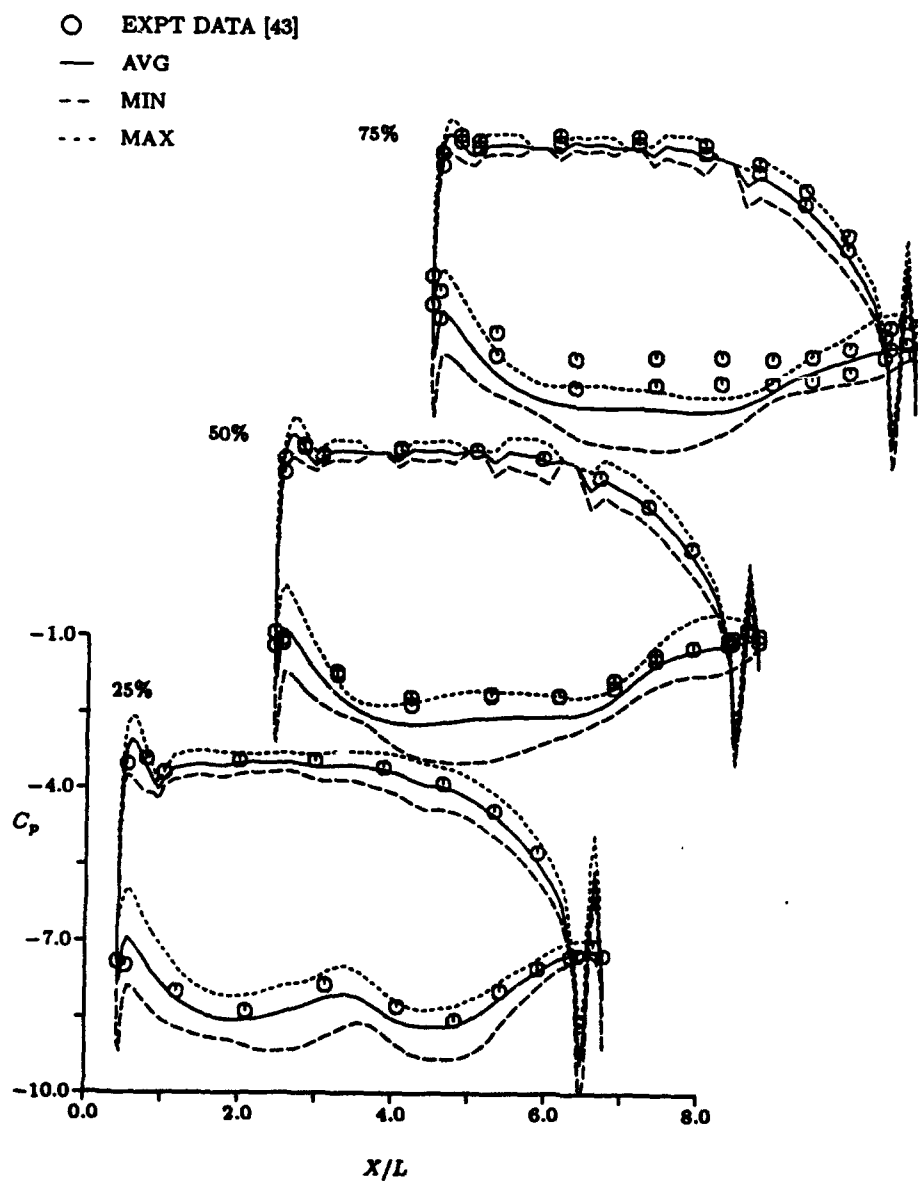


Figure 124: Time-averaged, minimum and maximum pressure coefficient distribution for LSRR rotor - 3 rows film cooling

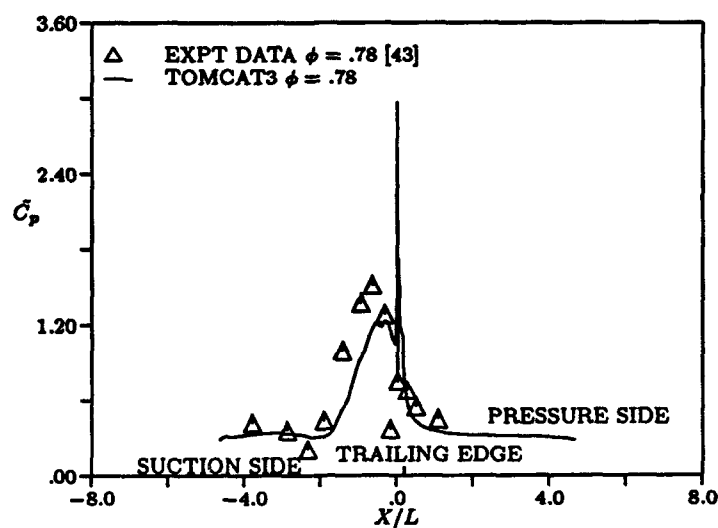


Figure 125: Pressure amplitude coefficient for stator mid-span - 3 rows f.c.

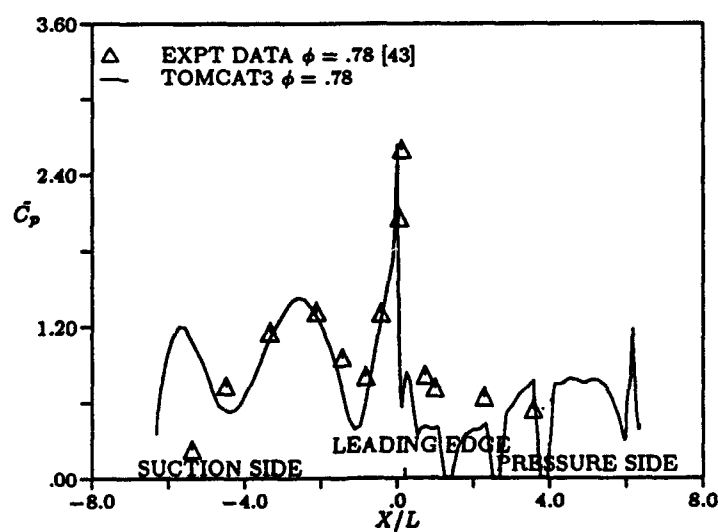


Figure 126: Pressure amplitude coefficient for rotor mid-span - 3 rows f.c.

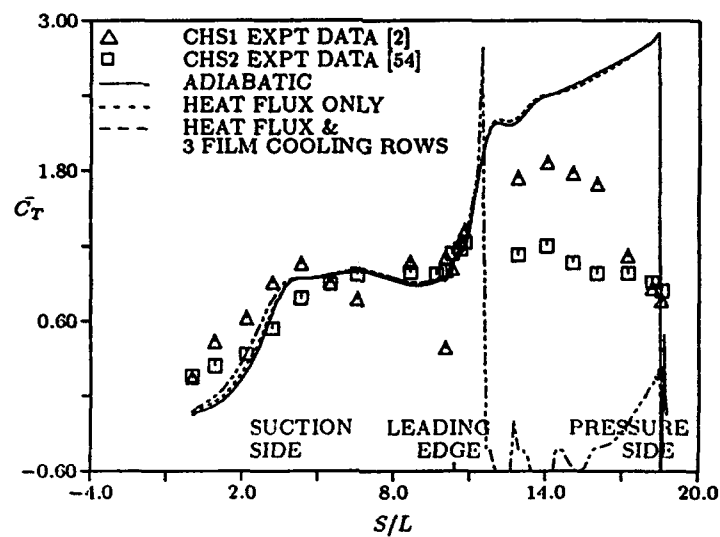


Figure 127: Mid-span time-averaged temperature distribution - 3 rows f.c.

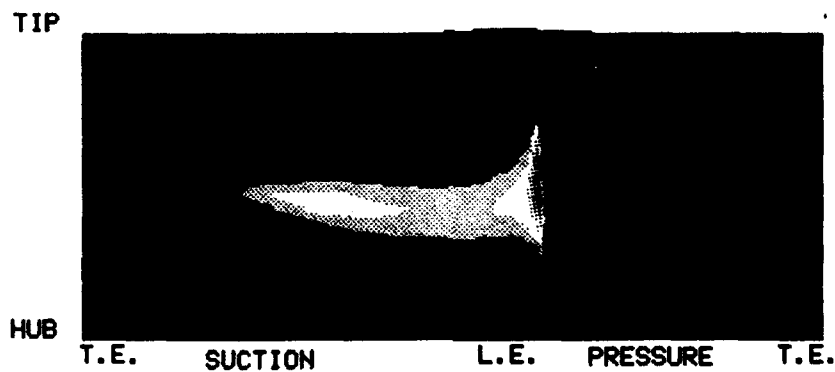


Figure 128: Time-averaged temperature contours for rotor surface - 3 rows f.c.

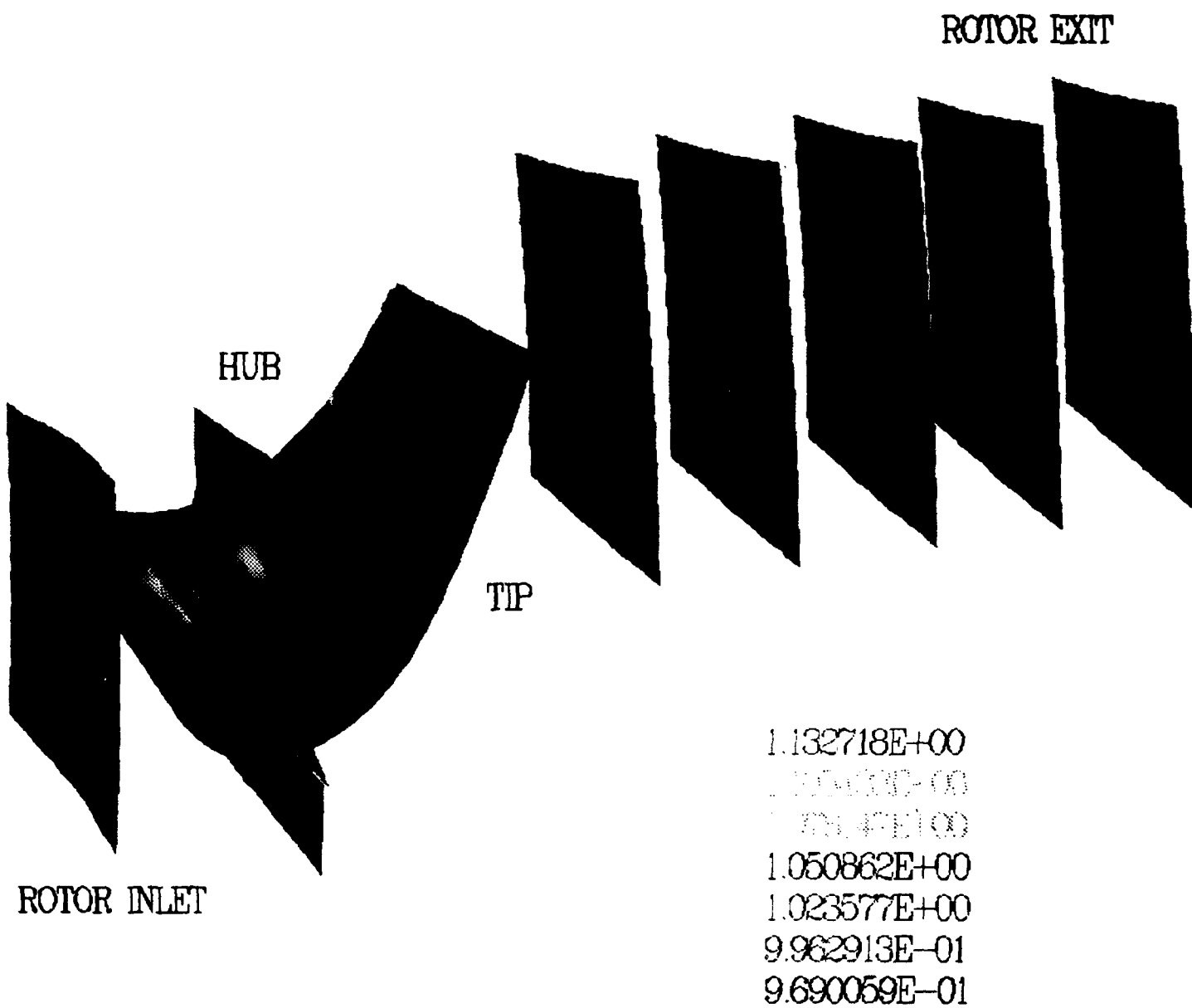


Figure 129: Rotor pressure surface time-averaged temperature contours - 3 rows f.c.

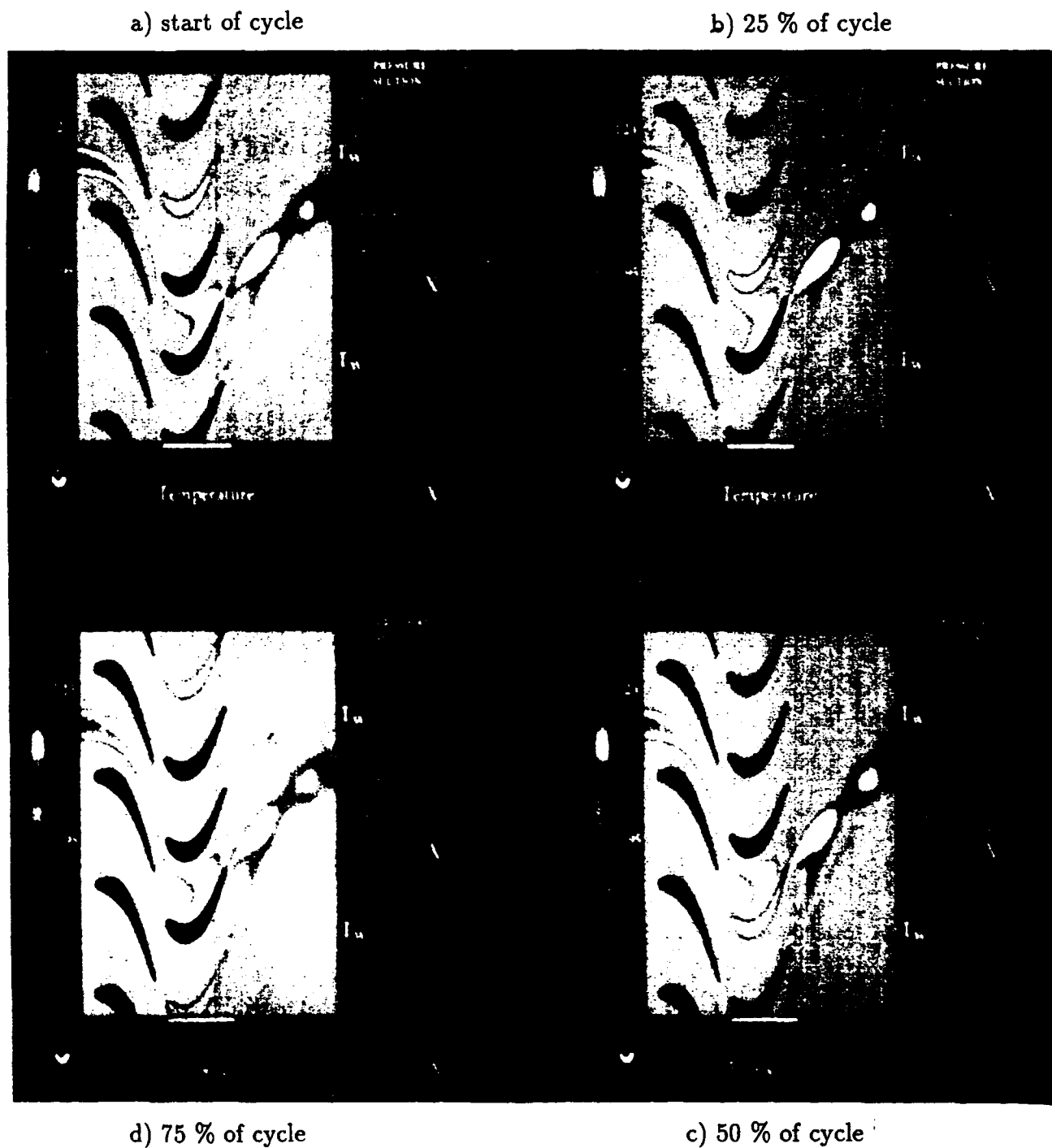
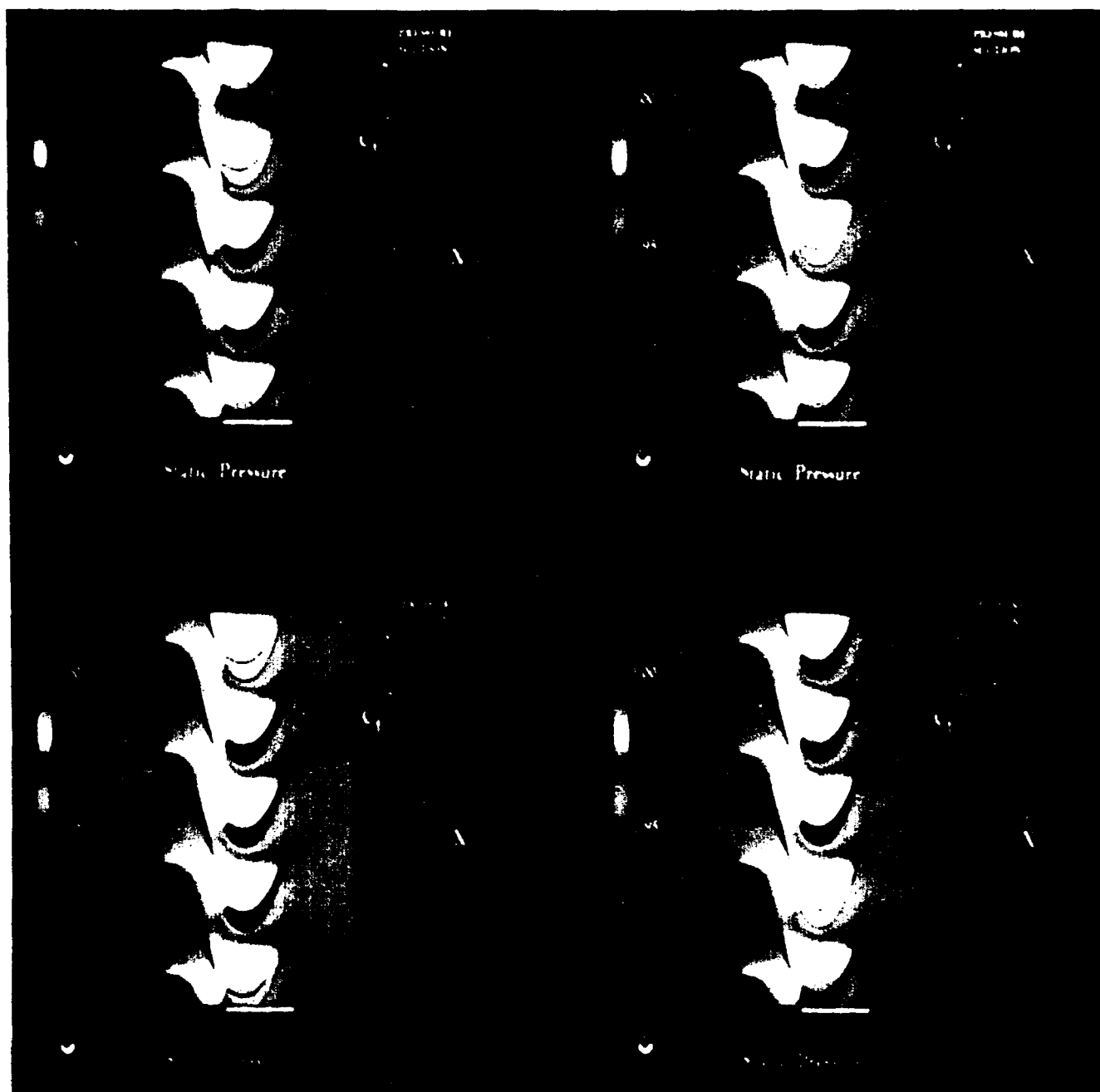


Figure 130: Static temperature contours for 2-D adiabatic hot streak simulation

a) start of cycle

b) 25 % of cycle



d) 75 % of cycle

c) 50 % of cycle

Figure 131: Static pressure contours for 2-D adiabatic hot streak simulation

a) start of cycle

b) 25 % of cycle

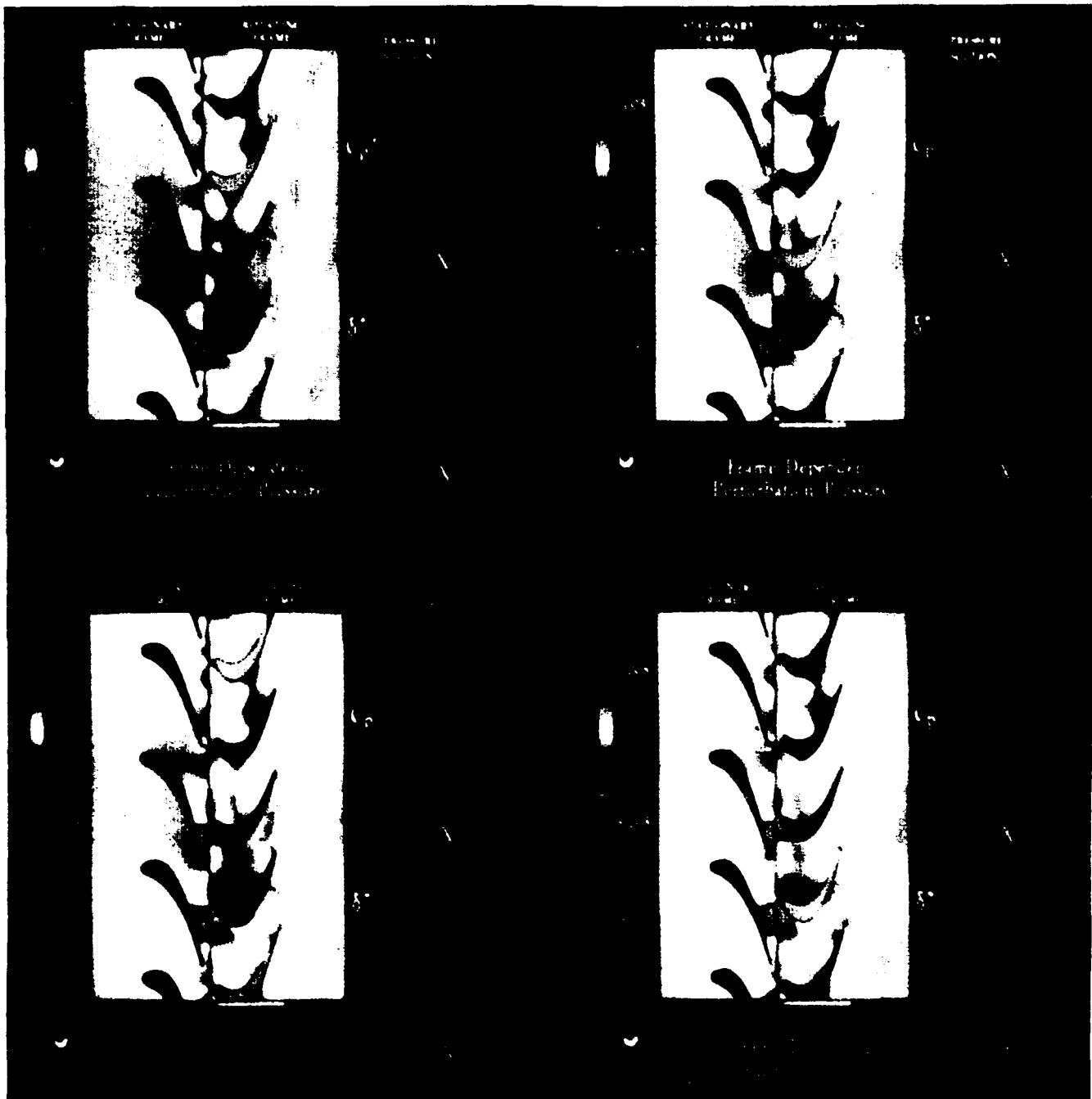


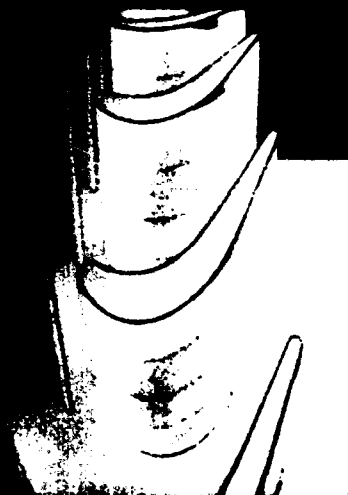
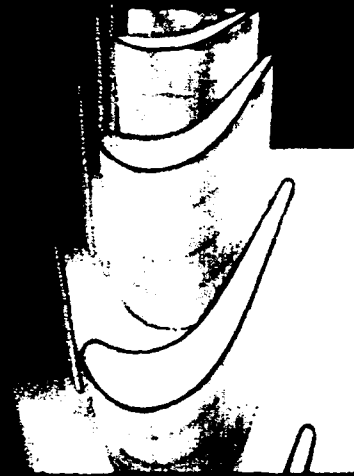
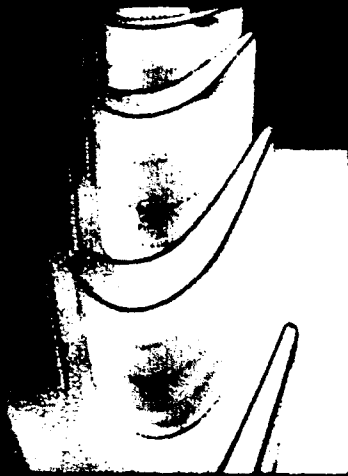
Figure 132: Perturbation pressure contours for 2-D adiabatic hot streak simulation



Figure 133: Magnified perturbation pressure contours for 2-D adiabatic hot streak simulation

a) start of cycle

b) 37.5 % of cycle



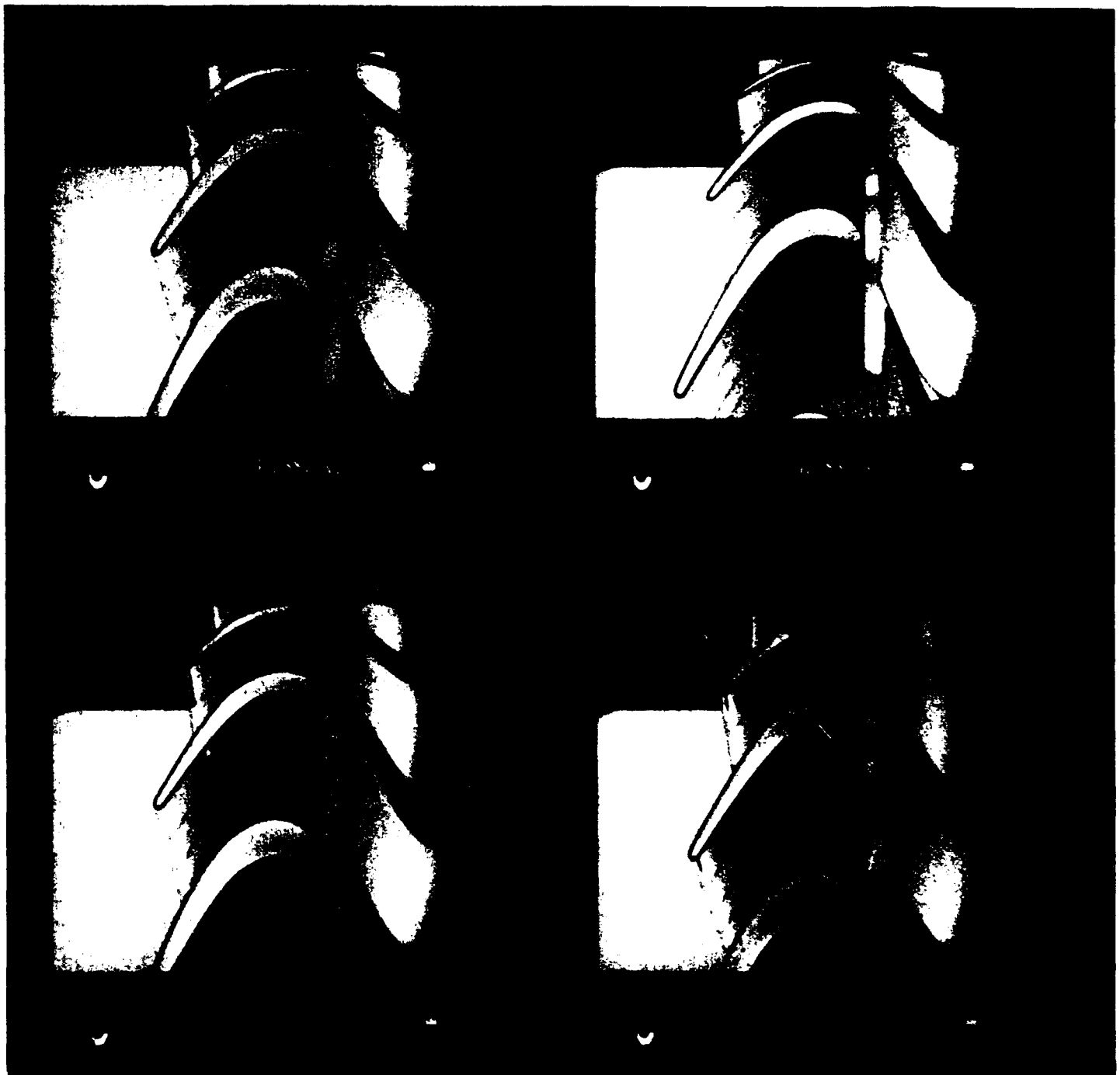
d) end of cycle

c) 75 % of cycle

Figure 134: Surface pressure for 3-D adiabatic hot streak simulation (View - rotor suction side)

a) start of cycle

b) 37.5 % of cycle



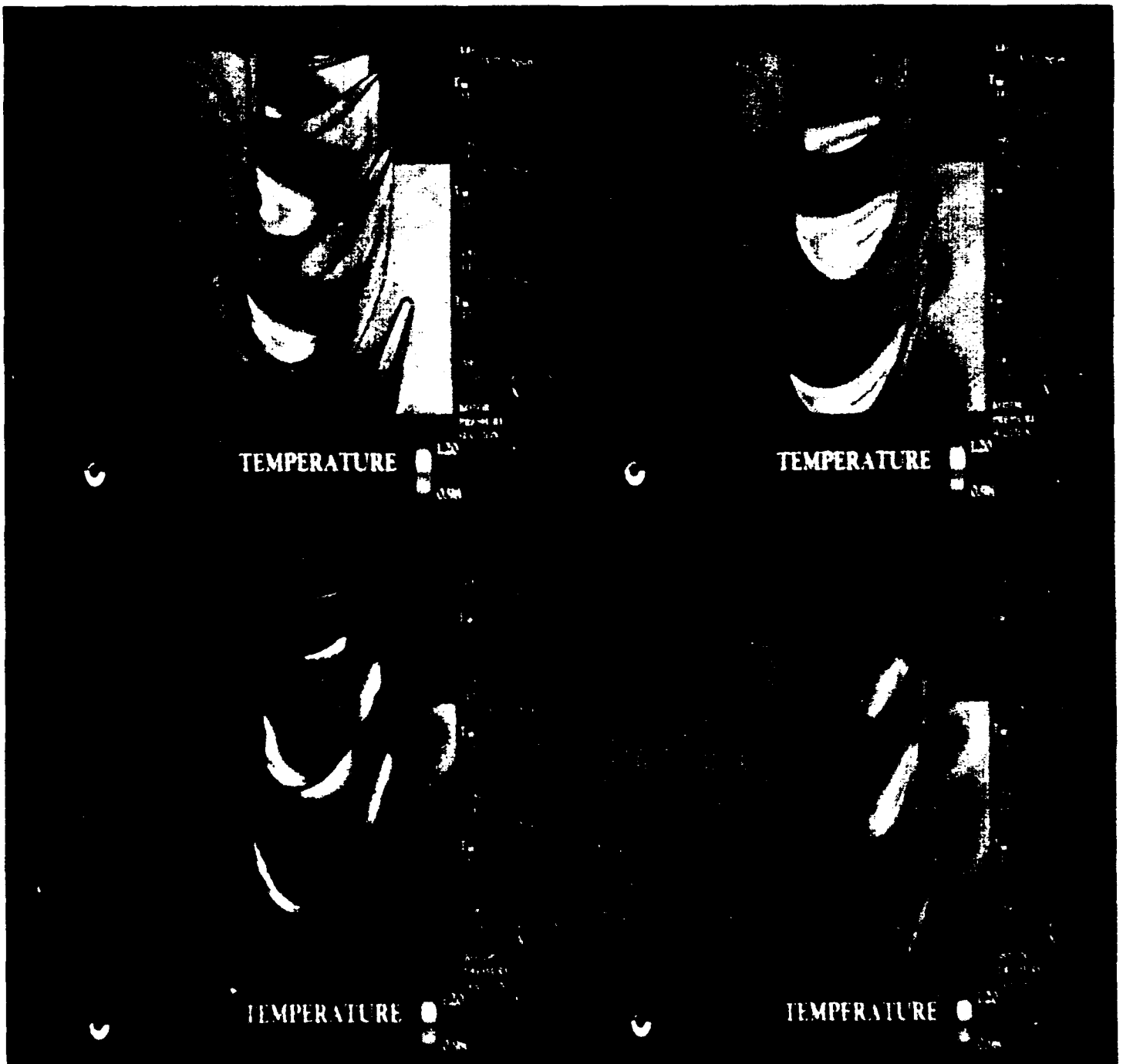
d) end of cycle

c) 75 % of cycle

Figure 135: Surface pressure for 3-D adiabatic hot streak simulation (View - rotor pressure side)

a) start of cycle

b) 37.5 % of cycle



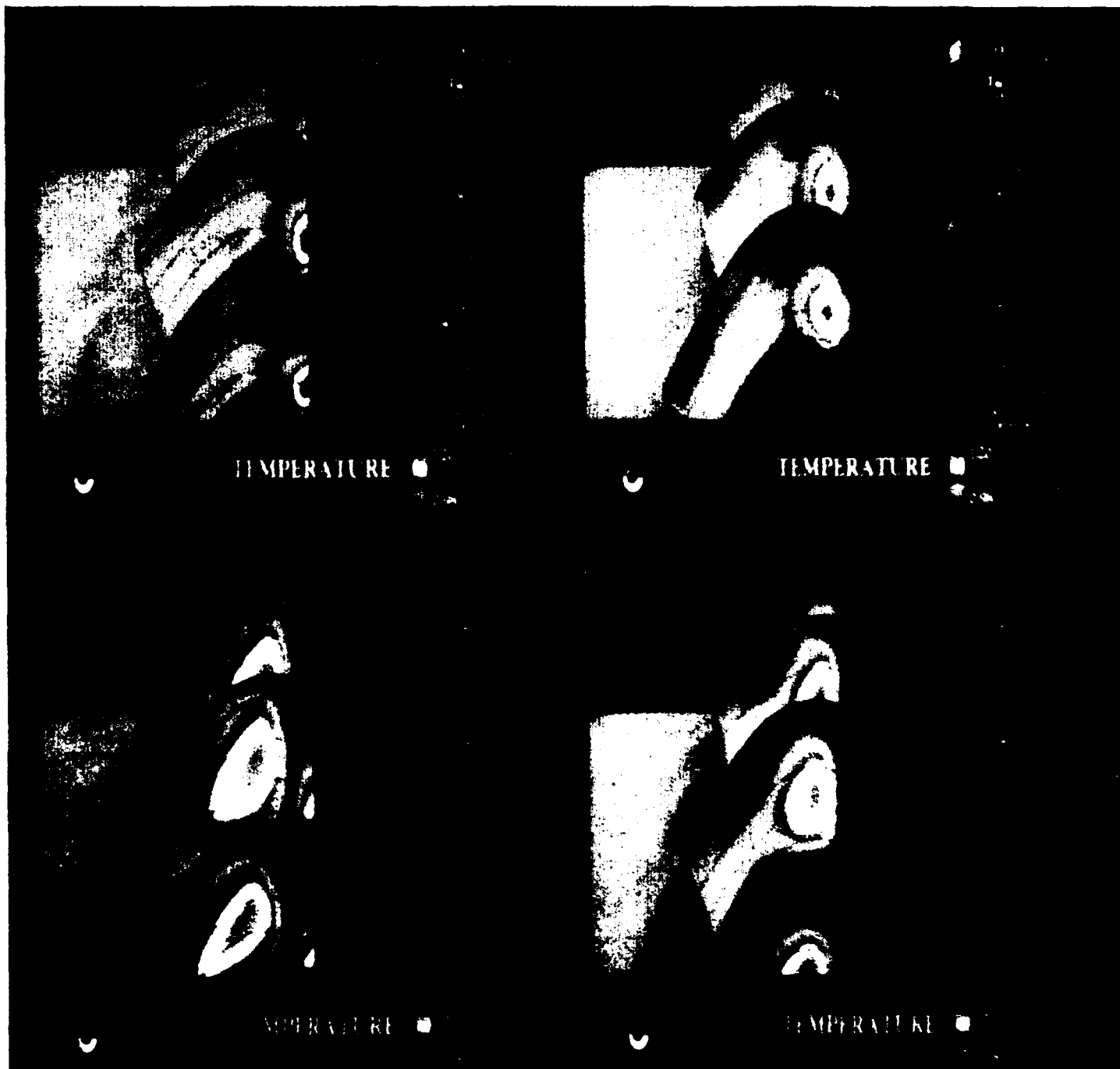
d) end of cycle

c) 75 % of cycle

Figure 136: Surface temperature for 3-D adiabatic hot streak simulation (View - rotor suction side)

a) start of cycle

b) 37.5 % of cycle



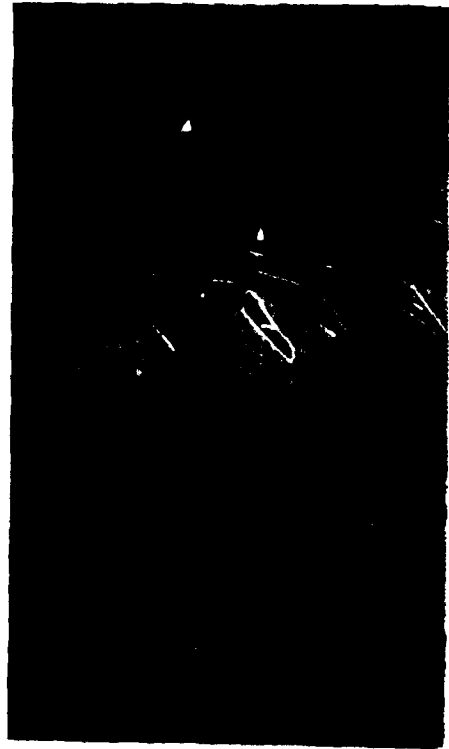
d) end of cycle

c) 75 % of cycle

Figure 137: Surface temperature for 3-D adiabatic hot streak simulation (View - rotor pressure side)



0%



50%



25%



75%

Figure 138: $T = 1.05T_{\infty}$ Isotherm for 3-D adiabatic hot streak simulation (View - rotor suction side)



0%



50%



25%



75%

Figure 139: $T = 1.05T_{\infty}$ Isotherm for 3-D adiabatic hot streak simulation (View - rotor pressure side)



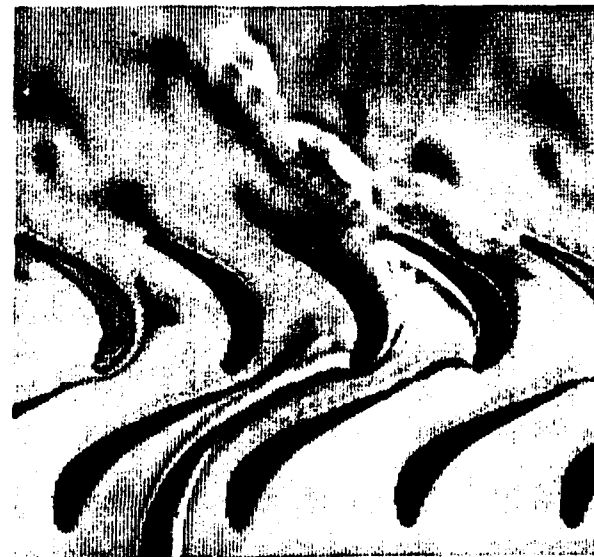
0%



50%



25%



75%

Figure 140: Static temperature contours for 2-D hot streak with film cooling and heat flux



0%



50%



25%



75%

Figure 141: Surface temperature for 3-D hot streak with film cooling and heat flux (View - rotor suction side)



0%



50%



25%



75%

Figure 142: Surface temperature for 3-D hot streak with film cooling and heat flux (View - rotor pressure side)



Figure 143: $T = 0.99, 1.05T_{\infty}$ Isotherms for 3-D hot streak with film cooling and heat flux
(View - rotor pressure side)

Errata AD-A250688

Errata Pages to UTRC Report 91-29

Contract No. N00014-88-C-0677

Investigation of Hot Streak Migration and Film Cooling Effects on Heat Transfer in Rotor/Stator Interacting Flows

N00014-88-C-0677 - Report 1
UTRC Report 91-29

Daniel J. Dorney Roger L. Davis
Computational & Design Methods

David E. Edwards
Physical & Mathematical Modeling
United Technologies Research Center

1 April 1992



ulations can be used to predict when rotor surface heating will exceed allowable structural limits, 3) predict when the adverse effects of hot streaks on rotor surface temperature can be eliminated using film cooling, and 4) use advanced scientific visualization techniques to quickly identify and illustrate the pertinent aerodynamic and thermodynamic features of the flow fields.

This document is organized into eight chapters. Chapter 1 is the introduction and provides background information on the problem of hot streak migration. The three-dimensional numerical procedure, including the governing equations, the integration procedure, the turbulence/transition models, and the boundary conditions is discussed in Chapter 2. The grid generation procedure for the zonal grid topology is explained in Chapter 3. The fourth chapter reviews the visualization technology used in this investigation. Chapter 5 describes the test cases used to validate the numerical procedure. The results of numerous hot streak migration simulations are presented and analyzed in Chapter 6. A video, which was created from the animated results of the numerical simulations, is discussed in Chapter 7. Finally, Chapter 8 presents the conclusions and recommendations of this investigation.

The three-dimensional source code, users manual, and/or video resulting from this investigation may be obtained from

Defense Logistics Agency
Defense Technical Information Center
Building No. 5, Cameron Station
Alexandria, Virginia 22304-6145
(final report AD-A250 688)
(user's manual AD-B164 302)
(source code AD-M200 104)
(video AD-M200 105)

Chapter 7

Scientific Visualization Results

A video tape has been created showing the animated results of the following computer simulations:

- 2-D Adiabatic Hot Streak Migration
- 3-D Adiabatic Hot Streak Migration
- 2-D Hot Streak Migration with Film Cooling
- 3-D Hot Streak Migration with Film Cooling

Details of each of the animations are in the following subsections. Copies of the videotape can be obtained from

Defense Logistics Agency
Defense Technical Information Center
Building No. 5, Cameron Station
Alexandria, Virginia 22304-6145
(NAVAIR video AD-M200 105)